Development of MoSi2-based sacrificial particles for self-healing thermal barrier coatings

Ding, Z.

Development of MoSi2-based sacrificial particles for self-healing thermal barrier coatings

Zhaoying Ding

Development of MoSi$_2$-based sacrificial particles for self-healing thermal barrier coatings

Zhaoying DING

Development of MoSi₂-based sacrificial particles for self-healing thermal barrier coatings

Dissertation

for the purpose of obtaining the degree of doctor
at Delft University of Technology
by the authority of the Rector Magnificus Prof.dr.ir. T.H.J.J. van der Hagen,
chair of the Board for Doctorates,
to be defended publicly on
Tuesday 16 April 2024 at 12:30 o'clock

by

Zhaoying DING
Master of Science in Materials Science and Engineering,
Delft University of Technology, the Netherlands
born in Zhejiang, China

This dissertation has been approved by the promotors.

Composition of the doctoral committee:

Rector Magnificus,   Chairman
Dr.ir. M.J.M. Hermans   Delft University of Technology, promotor
Dr. V.A. Popovich   Delft University of Technology, promotor

Independent members:
Prof.dr.ir. J.M.C. Mol   Delft University of Technology
Prof.dr.ir. S. van der Zwaag   Delft University of Technology
Prof.dr. R. Vaßen   Forschungszentrum Jülich, Germany
Prof.dr. P. Xiao   University of Manchester, UK
Dr. S.J. Garcia Espallargas   Delft University of Technology

Dr.ir. W.G. Sloof has contributed greatly to the preparation of this dissertation.

The research described in this thesis was carried out in the Department of Materials Science and Engineering, Delft University of Technology.

Front cover: Micrograph of self-healing in $MoSi_2$-YSZ composite.
Back cover: Interface between cristobalite and borosilicate.

Contents

Summary

Thermal barrier coatings (TBCs) are applied on the surface of metallic components of modern jet engines such as combustion chambers, blades and vanes, in order to increase the engine efficiency by allowing higher operating temperatures. However, during cooling from the operating temperature (i.e. 1000 °C) to room temperature high stresses develop in the ceramic coating due to mismatch of the coefficient of thermal expansion between the metal substrate and ceramic TBC. Then, micro-cracks are generated which, ultimately, lead to the failure of the TBC system. Yttria partially stabilized zirconia (YSZ) is the state-of-art material in industrial TBCs. Since YSZ does not exhibit any self-repair, it is highly desirable to develop new TBC materials with a prolonged lifetime. This can be achieved by addition of $MoSi_2$ intermetallic particles to the YSZ base material. Upon exposure to high-temperature and an oxidizing environment via the crack-path, these $MoSi_2$ particles decompose into a volumetrically expanding product which fills and seals the crack.

Until now, the concept of self-healing by introducing sacrificial particles has been proven to effectively extend the life of YSZ based TBCs, but optimizing the sacrificial $MoSi_2$ particles remains a demanding challenge. The establishment of a microcapsule system, consisting of a robust alumina shell and a boron-doped $MoSi_2$ core, stands out as a key problem in the ongoing research on self-healing TBCs. To overcome this challenge and improve the feasibility of self-healing TBCs, this study has combined a comprehensive approach that starts from model-based material design and integrates multiple important aspects including material synthesis, gas-solid interactions, oxidation and advanced surface and microstructure analysis.

Firstly, $MoSi_2$-based particles with high circularity and uniform size distribution are desired in the self-healing TBCs system for a more efficient encapsulation and thermal spraying process. However, producing spherical $MoSi_2$ particles by the method of gas atomization is rather difficult and results in a low yield due to the high melting point of $MoSi_2$. To address this challenge, a simple and cost-effective method to prepare spherical $MoSi_2$ based particles has been proposed in this study. Irregular shaped particles obtained by

crunching of spark plasma sintered MoSi$_2$ were spheroidized by a ball milling treatment. The effect of milling time, size of milling balls and the milling media on the geometrical modification of the milled particles was investigated. The results show that a low rotation speed eliminates the sharp edges while minimizing the size reduction of the particles. The circularity compared with the as crunched particle was improved from 0.57 to 0.72, and the flow of the powder was changed from cohesive to free flowing. This spheroidization enables preparation of powders of brittle and high melting materials and make these powders suitable for thermal spraying applications.

For the self-healing TBC system to work reliably under real operating conditions MoSi$_2$ sacrificial particles must remain stable until damage is generated in the ceramic coatings. However, the YSZ matrix is rather transparent to oxygen and, hence, continuous oxidation of the healing particles will occur if these particles are not protected. Partial substitution of Si sites with Al in the MoSi$_2$ lattice improves the oxidation resistance of MoSi$_2$ due to the formation of a protective Al$_2$O$_3$ scale via an in-situ displacement reaction. However, the oxidation mechanism remains yet unclear and most of studies concerns Mo(Al,Si)$_2$ compounds with a relatively low Al substitution. To fill this gap, selective oxidation behaviour of Al in Mo(Si,Al)$_2$ with relatively high Al contents up to about 43 at.% was studied in this work. Mo(Al$_x$Si$_{1-x}$)$_2$ bulk alloys with Al content x varying from 0.35 to 0.65 were prepared by a one-step spark plasma sintering process. To study the exclusive formation of an α-Al$_2$O$_3$ scale, oxidation experiments were conducted in low and high oxygen partial pressure (pO$_2$) ambient at 1100 °C; viz.: 10^{-14} and 0.2 atm. The oxidation kinetics follows a parabolic rate law after a transient period. A counter-diffusion process of O and Al along grain boundaries of the Al$_2$O$_3$ scale is responsible for the equiaxed and columnar grain growth based on a two-layered microstructure. The findings revealed that the formation of a dense equiaxed α-Al$_2$O$_3$ layer contributes to excellent oxidation resistance.

Capitalizing on the remarkable high-temperature oxidation resistance of Mo(Al,Si)$_2$, the material was downsized to particles subsequently. An encapsulation method was introduced based on the selective oxidation of Al with the aim of preventing premature triggering of the healing reaction in the self-healing TBC system. Healing particles of Mo(Al$_x$Si$_{1-x}$)$_2$ is designed in terms of alumina shell thickness, particle size and fraction Al dissolved. By replacing Si by Al in MoSi$_2$ up to the maximum solubility ($x = 0.65$) a strong crack healing ability is maintained (relative volume expansion ≥ 40 %). The formed exclusive α-Al$_2$O$_3$, featuring a two-layered structure, results from a counter-diffusion process along the grain boundaries, and its oxidation kinetics fits well with the 3D diffusion-Jander model. After 16 hours exposure in gaseous ambient with a pO$_2$ of 5×10^{-10} atm. at 1100 °C, a closed and

dense shell of α-Al$_2$O$_3$ is formed with a thickness of about 1.3 μm. The oxide shell produced under this condition provided healing particles with significantly improved stability upon exposure to high pO$_2$ of 0.2 atm. at 1100 °C for 50 hours. The particles after exposure feature an inner core of MoSi$_2$ with Al completely consumed and an oxide shell of α-Al$_2$O$_3$. Therefore, this framework effectively addressed the issue of premature oxidation of sacrificial particles in a self-healing TBC system and these prospective sacrificial particles can be exploited to other high temperature structural ceramics as well.

In the concept of self-healing TBCs, the presence of boron in the MoSi$_2$-based sacrificial particle is paramount for crack healing since it significantly facilitates the formation of borosilicate as crack-filling agent and thereby promotes the subsequent formation of the mechanical load bearing phase of ZrSiO$_4$. However, the effect of boron on the high temperature oxidation of MoSi$_2$ is still debated. The evolution of the microstructure on an atomic scale to reveal the oxidation mechanism of MoSi$_2$ with boron addition is still lacking. In this context, the high temperature (1100 °C) oxidation of B doped MoSi$_2$ in synthetic air has been investigated. Bulk MoSi$_2$ with various boron addition was fabricated by spark plasma sintering. The effect of boron on accelerating the oxidation kinetics and changing the microstructure of the oxide scale was captured by thermogravimetric analyses and high-resolution transmission electron microscopy, respectively. The findings revealed that the growth rate constant of the oxide layer is enhanced by the boron in the alloy by 90 % per at.% B. The increase in growth rate is associated with the effect of boron mitigating the formation of cristobalite thereby promoting the formation of amorphous SiO$_2$.

As MoSi$_2$ was downsized from bulk to particulate form, serving as sacrificial particles in self-healing TBCs, the oxidation process becomes increasingly intricate. This complexity arises from stronger element depletion, larger specific surface area and associated higher defect density of particles. To understand the oxidation behavior, MoSi$_2$ particles with various boron addition across different size ranges and microstructures were fabricated. The effect of boron addition, particle size and microstructure on the oxidation kinetics was captured by thermogravimetric analyses. The oxidation rate constants were quantified by employing a thermal diffusion-based model. The findings reveal that the boron addition to the MoSi$_2$ particles promotes the formation of the desirable amorphous SiO$_2$ and accelerates the oxidation. The role of boron is explained in terms of modification of the oxide microstructure and related oxygen diffusion through the oxide shell.

To validate the optimized features of the sacrificial particles (e.g., Al content, boron content and particle sphericity), a complete self-healing YSZ system designed for self-healing TBCs was fabricated via spark plasma sintering. Evolution of the Al- and B-alloyed

$MoSi_2$ healing particles and their interaction with the YSZ matrix were investigated in both high- and low- pO_2 oxidizing environments at 1100 °C. In-situ encapsulation with $\alpha\text{-}Al_2O_3$ around $Mo(Al,Si)_2$ particles with MoB addition has been realized by annealing the ceramic composite to selectively oxidize aluminum. After oxidation in gaseous ambient with pO_2 of 5×10^{-10} atm. at 1100 °C for 16 hours followed by further exposing the ceramic composite to Ar with 20 vol.% O_2 for another 16 hours, a core of $MoSi_2$ with MoB as fine distributed second phase was enveloped by a robust shell of $\alpha\text{-}Al_2O_3$, effectively eliminating the issue of premature oxidation while depleting Al. A controlled crack is deliberately introduced and crack healing has been identified in the self-healing YSZ composite, which is agreement with the envisaged crack healing mechanism.

Overall, extensive investigations were conducted to develop a $MoSi_2$ based sacrificial particle for self-healing TBCs. This research significantly contributes to the advancement of self-healing TBC systems. The findings hold the potential to be extrapolated to other self-healing structural ceramics designed for high temperature applications.

Samenvatting

Thermische barrièrecoatings (TBC's) worden aangebracht op het oppervlak van metalen componenten van moderne straalmotoren, zoals verbrandingskamers, bladen en schoepen, om de motorefficiëntie te verhogen door hogere bedrijfstemperaturen mogelijk te maken. Tijdens het afkoelen van de bedrijfstemperatuur (d.w.z. ca. 1000 °C) naar kamertemperatuur ontwikkelen zich echter hoge spanningen in de keramische coating door een verschil van de thermische uitzettingscoëfficiënt tussen het metalen substraat en de keramische TBC. Hierdoor ontstaan microscheurtjes die uiteindelijk leiden tot het falen van het TBC-systeem. Gedeeltelijk yttriumoxide-gestabiliseerd zirkoniumoxide (YPSZ) is het materiaal waar de TBC's van zijn gemaakt. Omdat YPSZ geen zelfherstel vertoont, is het zeer wenselijk om een nieuw TBC systeem te ontwikkelen met een langere levensduur. Dit kan worden bereikt door toevoeging van intermetallische $MoSi_2$-deeltjes aan het YPSZ-basismateriaal. Bij blootstelling aan hoge temperaturen en een oxiderende omgeving via het scheurpad vallen deze $MoSi_2$-deeltjes uiteen in een volumetrisch expanderend product dat de scheur opvult en afdicht.

Tot nu toe is bewezen dat het concept van zelfherstel door de introductie van opofferingsdeeltjes de levensduur van de op YPSZ gebaseerde TBC's effectief verlengt, maar het optimaliseren van de $MoSi_2$ opofferingsdeeltjes blijft een veeleisende uitdaging. Het realiseren van een microcapsulesysteem dat bestaat uit een robuuste schil van aluminiumoxide en een met boor gedoteerde $MoSi_2$-kern is een van de belangrijkste uitdaging bij het onderzoek naar zelfherstellende thermische barrièrecoatings. Om deze uitdaging aan te gaan en de haalbaarheid van zelfherstellende TBC's te vergroten, heeft deze studie een alomvattende aanpak gevolgd, dat gebaseerd is op modelmatig materiaalontwerp en verschillende belangrijke aspecten integreert, waaronder materiaalsynthese, gas-vaste stof-interacties, oxidatie alsmede geavanceerde oppervlakte- en microstructuuranalyse.

Ten eerste zijn op $MoSi_2$ gebaseerde deeltjes met hoge circulariteit en uniforme grootteverdeling gewenst in het zelfherstellende TBC-systeem voor een efficiënter inkapselings- en thermisch spuitproces. Het produceren van bolvormige $MoSi_2$-deeltjes door

middel van gasverneveling is echter nogal moeilijk en resulteert in een lage opbrengst door het hoge smeltpunt van $MoSi_2$. Om deze uitdaging aan te pakken, is in deze studie een eenvoudige en kosteneffectieve methode ontwikkeld om bolvormige $MoSi_2$ gebaseerde deeltjes te produceren. Onregelmatig gevormde deeltjes verkregen door het verbrokkelen van gesinterd $MoSi_2$ tabletten, werden vervolgens bolvormig gemaakt door een kogelmaalbehandeling. Het effect van de maaltijd, de grootte van de maalkogels en de maalmedia op de geometrische modificatie van de gemalen deeltjes werd onderzocht. De resultaten laten zien dat een lage rotatiesnelheid de scherpe randen elimineert en tegelijkertijd de verkleining van de deeltjes minimaliseert. De circulariteit vergeleken met het vermalen deeltje werd verbeterd van 0.57 naar 0.72, en de aard van het verstuiven van het poeder werd veranderd van cohesief naar vrij vloeiend. Dit spheroïdisatie proces maakt de bereiding van poeders van brosse en hoogsmeltende materialen mogelijk en maakt deze poeders geschikt voor thermische spuittoepassingen.

Om ervoor te zorgen dat het zelfherstellende TBC-systeem betrouwbaar kan werken onder reële bedrijfsomstandigheden, moeten $MoSi_2$-opofferingsdeeltjes stabiel blijven totdat er schade ontstaat in de keramische coatings. De YPSZ-matrix is echter transparant voor zuurstof en daarom zal continue oxidatie van de $MoSi_2$-opofferingsdeeltjes plaatsvinden als deze deeltjes niet worden beschermd. Gedeeltelijke vervanging van Si door Al verbetert de oxidatieweerstand van $MoSi_2$ door de vorming van een beschermende Al_2O_3-schil. Het oxidatiemechanisme is echter nog onduidelijk en de meeste onderzoeken hebben betrekking op $Mo(Al,Si)_2$-verbindingen met een relatief lage Al-substitutie. Om deze leemte op te vullen, werd in dit werk het selectieve oxidatiegedrag van Al in $Mo(Si,Al)_2$ met relatief hoge Al-gehalten tot ongeveer 43 at.% bestudeerd. $Mo(Al_xSi_{1-x})_2$-bulklegeringen met een Al-gehalte x variërend van 0.35 tot 0.65 werden bereid door een een-stap plasma-sinterproces. Om de exclusieve vorming van een α-Al_2O_3-schil te bestuderen, werden oxidatie-experimenten uitgevoerd in gasatmosferen met lage en hoge partiële zuurstofdruk (pO_2) bij 1100 °C; namelijk: 10^{-14} en 0.2 atm. De oxidatiekinetiek volgt, na een korte initiële periode, een parabolische groeiwet. Een tegendiffusieproces van O en Al langs korrelgrenzen in de Al_2O_3-schil is verantwoordelijk voor de dubbellaag microstructuur. Uit de bevindingen bleek dat de vorming van een gesloten α-Al_2O_3-laag bijdraagt aan een uitstekende oxidatieweerstand.

Voortbouwend op de opmerkelijke oxidatieweerstand bij hoge temperaturen van $Mo(Al,Si)_2$, werd het materiaal vervolgens verkleind tot deeltjes. Er werd een inkapselingsmethode geïntroduceerd, gebaseerd op de selectieve oxidatie van Al, met als doel het voortijdig activeren van de oxidatie van de $MoSi_2$-gebaseerde opofferingsdeeltjes in het zelfherstellende TBC-systeem te voorkomen. De samenstelling van de $Mo(Al_xSi_{1-x})_2$

deeltjes is ontworpen in termen van de dikte van de aluminiumoxideschil, de deeltjesgrootte en de opgeloste fractie Al. Door Si te vervangen door Al in $MoSi_2$ tot de maximale oplosbaarheid (x = 0.65) blijft een sterk vermogen om scheurtjes in de TBC te repareren behouden (relatieve volume-expansie $\geqslant$ 40%). De gevormde exclusieve a-Al_2O_3 schil met een tweelaagse structuur, is het resultaat van een tegendiffusieproces langs de korrelgrenzen, en de oxidatiekinetiek ervan past goed bij het 3D-diffusie-Jander-model. Na 16 uur blootstelling in een gasvormige omgeving met een pO_2 van 5×10^{-10} atm. bij 1100 °C wordt een gesloten en dichte schil van α-Al_2O_3 gevormd met een dikte van ongeveer 1.3 μm. De oxideschil die onder deze omstandigheden werd geproduceerd, zorgde voor helende deeltjes met een aanzienlijk verbeterde stabiliteit bij blootstelling aan een hoge pO_2 van 0.2 atm. bij 1100 °C gedurende 50 uur. De deeltjes hebben na blootstelling een kern van $MoSi_2$ waarbij Al volledig is verbruikt om een oxideschil van α-Al_2O_3 te vormen. Dus het hier voorgestelde concept zorgt er effectief voor om voortijdige oxidatie van opofferingsdeeltjes in een zelfherstellend TBC-systeem te voorkomen. Verwacht wordt dat dit concept ook kan worden toegepast voor nog te ontwikkelen opofferingsdeeltjes voor andere structurele zelfherstellende keramische materialen.

In de beoogde zelfherstellende TBC's is de aanwezigheid van boor in het op $MoSi_2$ gebaseerde opofferingsdeeltje van cruciaal belang voor het repareren van scheuren. Boor bevordert namelijk de vorming van borosilicaat dat vulling van de scheuren aanzienlijk vergemakkelijkt en tevens de vorming van zircon ($ZrSiO_4$), van belang voor het herstellen van de mechanische belastbaarheid. Over het effect van boor op de oxidatie van $MoSi_2$ bij hoge temperatuur is nog veel onduidelijk. Met name de evolutie van de microstructuur op atomaire schaal tijdens de oxidatie van $MoSi_2$ met boortoevoeging is onbekend. In deze context is de oxidatie bij hoge temperatuur (1100 °C) van B-gedoteerd $MoSi_2$ in synthetische lucht onderzocht. Bulk-$MoSi_2$ met diverse boortoevoegingen werd vervaardigd door plasma sinteren. Het effect van boor op het versnellen van de oxidatiekinetiek en het veranderen van de microstructuur van de oxideschaal is onderzocht met thermogravimetrische analyses en hoge resolutie transmissie-elektronenmicroscopie. Uit de meetresultaten bleek dat de groeisnelheidsconstante van de oxidelaag wordt verhoogd door het boor in de legering met 90% per at.% B. De toename van de groeisnelheid houdt verband met het onderdrukken van de vorming van cristobaliet door de aanwezigheid van boor, waardoor de vorming van amorf SiO_2 wordt bevorderd.

De oxidatie van $MoSi_2$ gebaseerde deeltjes is complexer dan dat van bulk materiaal. Deze complexiteit is het gevolg van een sterkere uitputting van elementen, een groter specifiek oppervlak en de daarmee samenhangende hogere defectdichtheid van deeltjes. Om

het oxidatiegedrag van MoSi$_2$-deeltjes te onderzoeken, werden verschillende deeltjes vervaardigd met verschillende hoeveelheid toegevoegd boor, deeltjesgrootte en microstructuur. Thermogravimetrische analyses werden uitgevoerd om de oxidatiekinetiek te bepalen. De oxidatiesnelheidsconstanten werden gekwantificeerd op basis van een thermische diffusie model. Uit de bevindingen blijkt dat de toevoeging van boor aan de MoSi$_2$-deeltjes de vorming van het gewenste amorfe SiO$_2$ bevordert en de oxidatie versnelt. De rol van boor wordt verklaard in termen van modificatie van de oxidemicrostructuur en de daarmee samenhangende diffusie van zuurstof door de oxideschil.

Om de geoptimaliseerde kenmerken van de opofferingsdeeltjes (bijvoorbeeld het Al-gehalte, het boorgehalte en de bolvormigheid van de deeltjes) te valideren, werd een compleet zelfherstellend PYSZ-systeem ontworpen voor een zelfherstellende TBC systeem. De evolutie van de Al- en B-gelegeerde MoSi$_2$-opofferingsdeeltjes en hun interactie met de PYSZ-matrix werden onderzocht in zowel een oxiderende omgeving met hoge als lage pO$_2$ bij 1100 °C. In-situ omhulling met α-Al$_2$O$_3$ rond Mo–Al–Si–B–deeltjes is gerealiseerd door het keramische composiet te oxideren bij hoge temperatuur. Na oxidatie in een gasvormige omgeving met een pO$_2$ van 5×10^{-10} atm. bij 1100 °C gedurende 16 uur, gevolgd door verdere blootstelling van het keramische composiet aan Ar met 20 vol.% O$_2$ gedurende nog eens 16 uur, werd een kern van MoSi$_2$ met MoB als fijn verdeelde tweede fase omhuld door een robuuste schil van α-Al$_2$O$_3$. Hierdoor wordt effectief voortijdige oxidatie van de MoSi2 gebaseerde deeltjes voorkomen, terwijl Al volledig geconsumeerd is door de vorming van de α-Al$_2$O$_3$ schil. In het zelfherstellende PYSZ-composiet is op gecontroleerde wijze een scheur geïntroduceerd. Door vervolgens blootstelling aan hoge temperatuur in en oxiderende omgeving is de geïntroduceerde scheur volledig hersteld.

Omvangrijk onderzoek is uitgevoerd om de MoSi$_2$ gebaseerde opofferingsdeeltjes voor zelfherstellende TBC's te ontwikkelen. Hiertoe werd een gecombineerd theoretisch en experimenteel raamwerk ontwikkeld. Dit omvat o.a. de samenstelling van de deeltjes, het sinterproces, gas-vaste stof-interacties en oxidatiekinetiek, oppervlakte- en microstructuuranalyse. Dit onderzoek draagt aanzienlijk bij aan de ontwikkeling van zelfherstellende TBC-systemen. De bevindingen zijn ook van belang voor de ontwikkeling van andere zelfherstellende structurele keramische materialen voor toepassingen bij hoge temperaturen.

List of abbreviations

TBC	Thermal barrier coating
YSZ/YPSZ	Yttria stabilized zirconia/ Yttria partially stabilized zirconia
HP	Healing particles
CTE	Coefficients of thermal expansion
TGO	Thermally grown oxide
BC	Bond coating
APS	Atmospheric plasma spraying
SPS	Spark plasma sintering
$p\mathrm{O}_2$	Oxygen partial pressure
XRD	X-ray diffractometry
SEM	Scanning electron microscopy
PFIB	Plasma focused ion beam
EPMA	Electron probe X-ray microanalysis
TEM	Transmission electron microscopy
STEM	Scanning transmission electron microscopy
TGA	Thermogravimetric analysis
AE	Acoustic emission

1.

Introduction

1.1. Introduction

Thermal barrier coatings (TBCs) are applied to metallic surfaces of combustion chambers, blades and vanes in gas turbine engines used for propulsion and power generation to allow for higher operation temperatures [1-7]; see Figure 1. 1. This thermal barrier is crucial to enhance the engine's fuel efficiency and consequently translates into cleaner exhaust [2]. The turbines and the TBCs experience severe thermal cycles spanning a range of over 1000 °C due to starts and stops of an engine. During cooling from the operation temperature to room temperature, high stresses develop due to a mismatch between the coefficients of thermal expansion (CTEs) of the metal substrate and the ceramic TBC [2, 3, 6]. In time, these stresses result in the development of crack patterns in the TBC that coalesce and ultimately lead to failure [2, 3, 5, 6]. Cracks that run through the TBC perpendicular to its surface are not detrimental per se, but in conjunction with cracks that develop parallel to the interface they lead to spallation (i.e. fragmentation) of the TBC, directly exposing the substrate to the high-temperature environment.
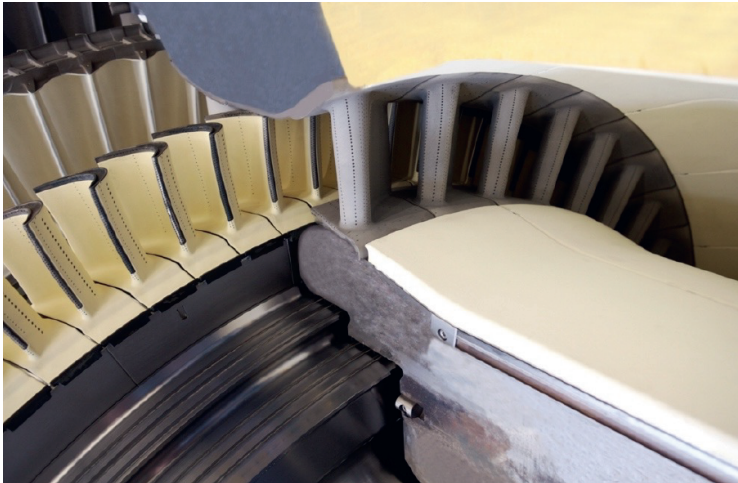
Figure 1. 1. Turbine blades, vanes and combustor liners (from left to right) coated with TBC (white-yellow material) in Alstom's GT26 gas turbine engine [7].

A complete modern high-temperature coating system comprises a TBC on top of a bond coating (BC) applied to a component usually made of a superalloy [1, 2]. A thin thermally grown oxide (TGO) layer is formed during operation between the TBC and BC layers [1, 2].

Yttria partially stabilized zirconia (YSZ) is the most widely used ceramic coating in industrial TBCs because it is one of the lowest ceramic thermal conductors at high temperatures (2.3 $W \cdot m^{-1} \cdot K^{-1}$ at 1000 °C) and has other excellent thermo-mechanical and chemical properties [1-7]. However, stresses as high as several GPa can be generated in the coating during thermal cycling due to the difference in CTEs of the YSZ ($11–13 \times 10^{-6}$ °C^{-1}) and the metallic substrate ($18–20 \times 10^{-6}$ °C^{-1}) [5-8]. As a result, delamination cracks run in the TBC typically close to the interface with the bond coating; see Figure 1. 2. The lifetime of a YSZ-TBC on a turbine engine for a commercial passenger aircraft is limited to a maximum of 2000–4000 thermal cycles which corresponds to around 30,000 hours of flying time [9]. As the lifetime of the (metallic part of the) engine itself is much longer, it means that each turbine engine has to be recoated several times during its life time, which brings about high direct and indirect costs.
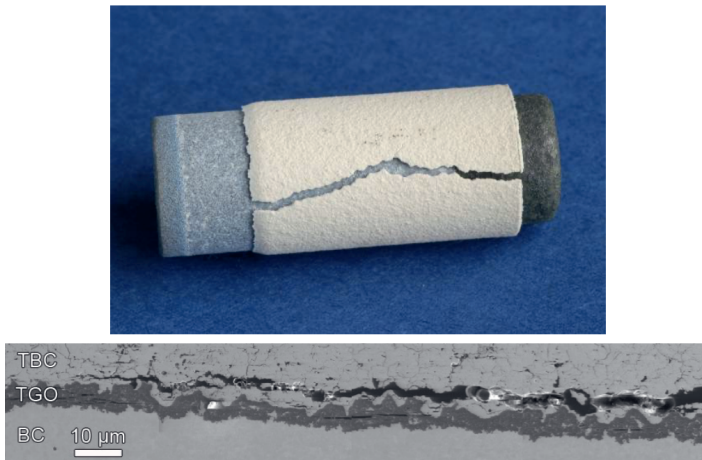
Figure 1. 2. Delamination crack in a TBC close to the interface with the bond coating developed upon thermal cycling [7].

Already in 2008, the concept of a new self-healing thermal barrier coating was proposed [10] based on the oxidation of boron doped molybdenum disilicide (B-MoSi$_2$) particles embedded in ZrO$_2$-based TBCs [11, 12]; see Figure 1.3. The healing particles, namely MoSi$_2$, exhibits a high melting point of 2020 °C, a density of 6.24 g·cm^{-3} and a coefficient of thermal expansion (CTE, 8.1×10^{-6} °C^{-1}) which is close to that of YSZ (6.08 g·cm^{-3} density and 10×10^{-6} °C^{-1} CTE). Upon high-temperature exposure in an oxidising environment the embedded healing particles react to form a viscous silica (SiO$_2$), which fills the cracks, re-

establishes adherence in the TBC and subsequently reacts with the matrix resulting in a load bearing, solid crystalline ceramic phase [13]. To prevent premature triggering of the healing reaction, the concept of self-healing TBC also involves creating an inert and oxygen impenetrable α-Al_2O_3 shell around the sacrificial healing particle ($MoSi_2$); see Figure 1. 3, since this oxide is stable at high temperatures in an oxidizing environment and exhibits a very low permeability of oxygen compared to other oxides [14].

1
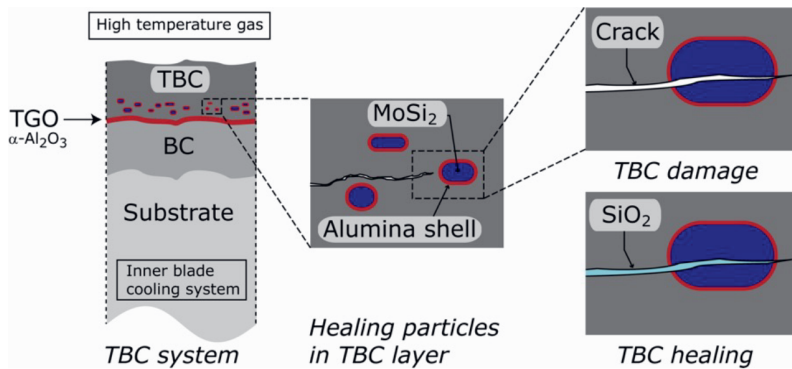
Figure 1. 3. Schematic of crack-healing mechanism in a thermal barrier coating (TBC) with encapsulated Mo–Si based particles [12].

Extensive research into self-healing TBCs has been conducted over the past years, encompassing both experimental investigations and modeling studies. The effects of incorporating $MoSi_2$-based particles into an YSZ ceramic on its thermo-mechanical behavior [15] and thermal conductivity [16, 17] have been investigated in a wide composition range; crack-particle interactions have been simulated and summarized in the form of fracture maps as a guideline for particulate composite system designing [18]; facture behavior of TBCs containing healing particles has been systematically investigated using both cohesive element-based [19, 20] and actual microstructure-based [21] finite element analysis; a numerical model [22] and computationally-efficient surrogate models [23] have been developed to predict the lifetime and quantify the uncertainties of the self-healing TBCs under thermal cyclic conditions. All these findings clearly indicate that the incorporation of $MoSi_2$ sacrificial particles into the YSZ TBC system can autonomously trigger a self-healing reaction, effectively repairing microcracks in TBC without compromising high-temperature performance.

1

The manufacturing of the self-healing top coat with MoSi$_2$ particle has been successfully achieved through atmospheric plasma spraying (APS) [24-26]. In this process, a dual injection system was employed to fabricate a self-healing interlayer in close proximity to the bond coat, the location where crack propagation typically takes place in TBC systems [24]. Furthermore, various methods have been utilized to encapsulate the MoSi$_2$ particles with α-Al$_2$O$_3$ [27, 28]. Among these methods, the in-situ encapsulation, which facilitates the direct formation of α-Al$_2$O$_3$ shell on the healing particle at temperatures comparable to those encountered during the high-temperature operation of TBCs, holds greater promise [25]. When the healing particles are embedded in YSZ, the encapsulation can be performed in-situ by annealing the system in an appropriate ambient before being applied in working conditions, since the YSZ matrix is permeable for oxygen [25, 29]. The feasibility of a complete self-healing TBC system manufactured by APS with all original design features (cf. Figure 1. 3) incorporated has been successfully demonstrated [25]. Although experimental evidence has uncovered characteristic sign of crack healing in the YSZ coating, it is essential to embark on future research endeavours to improve the protectiveness of the α-Al$_2$O$_3$ shell and maximize the crack healing efficiency.

1.2. Challenges and motivations

Prior research has demonstrated that the addition of MoSi$_2$-based sacrificial particles to YSZ-TBCs can indeed lead to the filling of even long cracks, but also revealed an insufficient long-term stability of such particles in the non-cracked condition to allow application of the concept in real engines [14, 25, 30]. The limited stability is due to premature triggering of the healing action of MoSi$_2$ particles via oxygen atoms diffusing through the undamaged TBCs matrix, which activates the reaction, even in the absence of a crack. Establishment of the microcapsule system with a more robust alumina shell is one of the key problems in the research of self-healing thermal barrier coatings. In addition, a prior experimental observation has indicated the necessity for optimizing the shape of the healing particles, as many healing particles in the self-healing APS TBCs exhibit an undesirable "splat" microstructure (tens of microns in length and a few microns in width), which hinders effective crack healing [25].

Furthermore, it was suggested that doping MoSi$_2$ particles with small amounts of boron will increase the fluidity of the healing agent by the formation of borosilicate with lower viscosity than silica [11, 13], making it more effective to fill the cracks. However, the effect of boron on promoting the oxidation kinetics still remains unclear. Up to date, there is no

related literature available reporting the mechanism of the promoted oxidation provided by boron. Further optimization of boron content and distribution in $MoSi_2$ remains challenging.

Until now, the concept of self-healing by introducing sacrificial particle has been proven to effectively extend the life of YSZ based TBCs but optimizing of the sacrificial particles of $MoSi_2$ remains a demanding challenge. The main research question of the present work is to establish a microcapsule system consisting of a robust alumina shell and a boron-doped $MoSi_2$ core that possesses self-healing capacity within a YSZ system. This will be achieved through a combined theoretical and experimental approach of an innovative self-healing concept that relies on tailoring the composition of the healing particles.

1.3. Thesis outline

Chapter 2 presents a novel method to prepare spherical $MoSi_2$ particles with good flowability based on morphological and compositional characteristics. The crushed $MoSi_2$ based particles obtained from dense bulk tablets was processed by a ball milling and a polishing treatment. The flowability of the treated particles was significantly improved according to the results of angle of repose and flow through orifice tests.

$Mo(Al,Si)_2$ alloy with different Al content were fabricated by a one-step spark plasma sintering process in **Chapter 3**. To study the exclusive formation of an α-Al_2O_3 scale, oxidation experiments were conducted in low and high oxygen partial pressure (pO_2) ambient. The oxidation kinetics and mechanism of alumina formation at high temperatures were studied in detail.

Based on the selective oxidation of Al in $Mo(Al,Si)_2$ alloy studied in **Chapter 3**, an encapsulation technique to obtain a thick and dense alumina coating onto $MoSi_2$ based healing particles for high temperature ceramics is presented in **Chapter 4**. This involves a controlled depletion of aluminium in $MoSi_2$ particles by oxidation in a low oxygen partial pressure (pO_2) ambient followed by post annealing in high pO_2 ambient to further exhaust the remnant Al reservoir and thicken the alumina shell. The mechanism of alumina formation and the microcapsule stability at high temperature were studied in detail.

Chapter 5 addresses the effects of boron addition on the high temperature oxidation of $MoSi_2$ alloys. To complement this, $MoSi_2$ with various boron additions were fabricated by spark plasma sintering. The effect of boron on accelerating the oxidation kinetics and changing the microstructure of oxide scale was captured by thermogravimetric analyses and high-resolution transmission electron microscopy, respectively. Subsequently, the study of

high temperature oxidation of MoSi$_2$ particles with boron addition was presented and discussed in **Chapter 6**.

Finally, **Chapter 7** demonstrates the oxidation-induced crack healing ability of α-Al$_2$O$_3$ encapsulated MoSi$_2$ particles doped with B in YSZ ceramic prepared by spark plasma sintering. The crack healing behavior of the material was evaluated by manually introducing controlled cracks. A post-mortem study indicates local healing of cracks via the formation of the glassy borosilicate phase at the fracture surfaces.

Based on the results, **Chapter 8** summarises the main findings and contributions of this research to the self-healing material community, and relevant further developments of self-healing TBCs are proposed in **Chapter 9**.

References

[1] D.R. Clarke, S.R. Phillpot, Thermal barrier coating materials, Materials Today 8(6) (2005) 22-29.

[2] N.P. Padture, M. Gell, E.H. Jordan, Thermal barrier coatings for gas-turbine engine applications, Science 296(5566) (2002) 280-284.

[3] R. Vaßen, M.O. Jarligo, T. Steinke, D.E. Mack, D. Stöver, Overview on advanced thermal barrier coatings, Surface and Coatings Technology 205(4) (2010) 938-942.

[4] X.Q. Cao, R. Vassen, D. Stoever, Ceramic materials for thermal barrier coatings, Journal of the European Ceramic Society 24(1) (2004) 1-10.

[5] T.S. Hille, T.J. Nijdam, A.S.J. Suiker, S. Turteltaub, W.G. Sloof, Damage growth triggered by interface irregularities in thermal barrier coatings, Acta Materialia 57(9) (2009) 2624-2630.

[6] A.G. Evans, D.R. Mumm, J.W. Hutchinson, G.H. Meier, F.S. Pettit, Mechanisms controlling the durability of thermal barrier coatings, Progress in Materials Science 46(5) (2001) 505-553.

[7] W.G. Sloof, Self-Healing Thermal Barrier Coatings (SAMBA), (2012) EU-FP7-NMP-2012-SMALL-6.

[8] L.B. Chen, Yttria-stabilized zirconia thermal barrier coatings — a review, Surface Review and Letters 13(05) (2006) 535-544.

[9] R. Vaßen, S. Giesen, D. Stöver, Lifetime of plasma-sprayed thermal barrier coatings: comparison of numerical and experimental results, Journal of Thermal Spray Technology 18(5) (2009) 835-845.

[10] K. Kochubey, W.G. Sloof, Self healing mechanism in thermal barrier coatings, Proceedings of the International Thermal Spray Conference (DVS Verlag GmbH, Düsseldorf, Germany, ISBN 978-3-87155-979-2) (2008).

[11] Z. Derelioglu, A.L. Carabat, G.M. Song, S.v.d. Zwaag, W.G. Sloof, On the use of B-alloyed $MoSi_2$ particles as crack healing agents in yttria stabilized zirconia thermal barrier coatings, Journal of the European Ceramic Society 35(16) (2015) 4507-4511.

[12] W. Sloof, S. Turteltaub, A. Carabat, Z. Derelioglu, S. Ponnusami, G. Song, 219 Crack healing in yttria stabilized zirconia thermal barrier coatings, Self Healing Materials: Pioneering Research in the Netherlands 219 (2015).

[13] F. Nozahic, A.L. Carabat, W. Mao, D. Monceau, C. Estournes, C. Kwakernaak, S. van der Zwaag, W.G. Sloof, Kinetics of zircon formation in yttria partially stabilized zirconia as a result of oxidation of embedded molybdenum disilicide, Acta Materialia 174 (2019) 206-216.

[14] F. Nozahic, C. Estournès, A.L. Carabat, W.G. Sloof, S. van der Zwaag, D. Monceau, Self-healing thermal barrier coating systems fabricated by spark plasma sintering, Materials & Design 143 (2018) 204-213.

1

[15] J. Kulczyk-Malecka, X. Zhang, J. Carr, F. Nozahic, C. Estournès, D. Monceau, A.L. Carabat, W.G. Sloof, S. van der Zwaag, P.J. Withers, P. Xiao, Thermo–mechanical properties of SPS produced self-healing thermal barrier coatings containing pure and alloyed MoSi$_2$ particles, Journal of the European Ceramic Society 38(12) (2018) 4268-4275.

[16] F. Cernuschi, J. Kulczyk-Malecka, X. Zhang, F. Nozahic, C. Estournès, W.G. Sloof, Thermal conductivity of binary ceramic composites made of insulating and conducting materials comprising full composition range – Applied to yttria partially stabilized zirconia and molybdenum disilicide, Journal of the European Ceramic Society 43(14) (2023) 6296-6307.

[17] J. Kulczyk-Malecka, X. Zhang, J. Carr, A.L. Carabat, W.G. Sloof, S. van der Zwaag, F. Cernuschi, F. Nozahic, D. Monceau, C. Estournès, P.J. Withers, P. Xiao, Influence of embedded MoSi$_2$ particles on the high temperature thermal conductivity of SPS produced yttria-stabilised zirconia model thermal barrier coatings, Surface and Coatings Technology 308 (2016) 31-39.

[18] S.A. Ponnusami, S. Turteltaub, S. van der Zwaag, Cohesive-zone modelling of crack nucleation and propagation in particulate composites, Engineering Fracture Mechanics 149 (2015) 170-190.

[19] S.A. Ponnusami, J. Krishnasamy, S. Turteltaub, S. van der Zwaag, A cohesive-zone crack healing model for self-healing materials, International Journal of Solids and Structures 134 (2018) 249-263.

[20] J. Krishnasamy, S.A. Ponnusami, S. Turteltaub, S. van der Zwaag, Modelling the fracture behaviour of thermal barrier coatings containing healing particles, Materials & Design 157 (2018) 75-86.

[21] S.A. Ponnusami, J. Krishnasamy, S. Turteltaub, S. van der Zwaag, A micromechanical fracture analysis to investigate the effect of healing particles on the overall mechanical response of a self-healing particulate composite, Fatigue & Fracture of Engineering Materials & Structures 42(2) (2019) 533-545.

[22] J. Krishnasamy, S.A. Ponnusami, S. Turteltaub, S. van der Zwaag, Thermal cyclic behavior and lifetime prediction of self-healing thermal barrier coatings, International Journal of Solids and Structures 222-223 (2021) 111034.

[23] A. Kumthekar, S.A. Ponnusami, S. van der Zwaag, S. Turteltaub, Uncertainty quantification of the lifetime of self-healing thermal barrier coatings based on surrogate modelling of thermal cyclic fracture and healing, Materials & Design 221 (2022) 110973.

[24] D. Koch, D.E. Mack, R. Vaßen, Degradation and lifetime of self-healing thermal barrier coatings containing MoSi$_2$ as self-healing particles in thermo-cycling testing, Surface and Coatings Technology 437 (2022) 128353.

[25] H. Chen, Q. Wei, Y. Zhang, F. Chen, Y. Shi, W. Yan, Powder-spreading mechanisms in powder-bed-based additive manufacturing: Experiments and computational modeling, Acta Materialia 179 (2019) 158-171.

[26] D. Koch, G. Mauer, R. Vaßen, Manufacturing of composite coatings by atmospheric plasma spraying using different feed-stock materials as YSZ and $MoSi_2$, Journal of Thermal Spray Technology 26(4) (2017) 708-716.

[27] A.L. Carabat, M.J. Meijerink, J.C. Brouwer, E.M. Kelder, J.R. van Ommen, S. van der Zwaag, W.G. Sloof, Protecting the $MoSi_2$ healing particles for thermal barrier coatings using a sol-gel produced Al_2O_3 coating, Journal of the European Ceramic Society 38(7) (2018) 2728-2734.

[28] A.L. Carabat, S. van der Zwaag, W.G. Sloof, Creating a protective shell for reactive $MoSi_2$ particles in high-temperature ceramics, Journal of the American Ceramic Society 98(8) (2015) 2609-2616.

[29] S.J. Skinner, J.A. Kilner, Oxygen ion conductors, Materials Today 6(3) (2003) 30-37.

[30] F. Nozahic, D. Monceau, C. Estournès, Thermal cycling and reactivity of a $MoSi_2/ZrO_2$ composite designed for self-healing thermal barrier coatings, Materials & Design 94 (2016) 444-448.

1

1

2.

Preparation of MoSi$_2$ based particles

Abstract

A simple and cost-effective method to prepare spherical MoSi$_2$ based particles is presented. Irregular shaped particles obtained by crunching of spark plasma sintered of MoSi$_2$ were spheroidized by a ball milling treatment. The effect of milling time, size of milling balls and the milling media on the geometrical modification of the milled particles was investigated. To this end, the morphologies of the particles were characterized by SEM and image analysis. The circularity and aspect ratio of single particles were extracted. The results show that a low rotation speed eliminates the sharp edges while minimizing the size reduction of the particles. Using small milling balls promotes a higher roundness. However, the milling time seemed to be the most dominant factor determining the circularity of milled particles. The flowability of the powder after the milling treatment was significantly improved according to the results of angle of repose and flow through orifice tests.

2

2.1. Introduction

Molybdenum disilicide (MoSi$_2$) is a high temperature refractory intermetallic compound having a high melting point of 2030 °C. Due to its unique combination of low electrical resistivity, good thermal conductance, excellent strength, creep and oxidation resistance [1-5], MoSi$_2$ is used as high-temperature electric heating elements [5, 6], wear- and oxidation-resistant coatings at high temperature environment [3, 4], and as high-temperature joining material for structural ceramic components [4].

Recently, particles of MoSi$_2$ alloyed with boron have been used as a healing agent in yttria stabilized zirconia (YSZ) thermal barrier coating (TBC) [7-9]. Upon high temperature oxidation these particles form amorphous borosilicate [8, 9]. When embedded in YSZ and cracks occur, the borosilicate fills the crack-gap. Subsequently, the borosilicate reacts with the YSZ at the fracture surfaces forming zircon (ZrSiO$_4$) [8] and restoring the material integrity [8, 9]. For a more efficient and complete encapsulation when manufacturing a self-healing TBC [9], it is advantageous when the MoSi$_2$ based particles show spherical shape and uniform size distribution [10]. Moreover, the shape effect does influence the particles flowability and granular material properties [11-16]. High circularity and uniform size distribution promote the fluidity of the MoSi$_2$ powder which is one of the most importance characteristics of the feedstock when applied with thermal spraying processes [11-18].

The following factors and properties are known as shape descriptors: particle roundness (or circularity), sphericity, roughness, size, aspect ratio, slenderness, solidity and Ferret's

diameter [11, 19]. However, according to Ulusoy *et. al* [20], none of these shape descriptors are universally accepted or standardized. Among the many different definitions for particle roundness [11, 21-23], the so-called Cox roundness [23, 24], is widely accepted. This particle roundness, also known as circularity C, is defined from the from the projected area A and projection perimeter P of the particle, according to:

$$C = 4\pi \cdot \frac{A}{P^2} \qquad (2.1).$$

A high degree of circularity of the particles will reduce the particle contact and interlocking, an thus promote the powder flowability [11, 19]. The aspect ratio, defined as the ratio between major and minor axis of the particle and the above mentioned circularity are found to be the best shape descriptors in this field as both are sensitive to a specific attribute of particle shape [11, 19]. The aspect ratio specifies the elongation of a particle while the circularity indicates the degree in which a particle resembles a sphere. Techniques such as fractal analysis, Fourier methods and image analysis and processing are the main methods to determine the circularity of granular material [11, 21, 23].

Microspheres of metals and their alloys can be produced by gas atomization [25-29]. But utilizing this method in the case of $MoSi_2$ is rather difficult and results in a low yield due to its high melting point [30]. Currently, the radio frequency (RF) plasma technology is reported as a promising method to control the morphology and particle size of for materials with high melting points such as molybdenum and tungsten [30-32]. However, such plasma processes require dedicated equipment and operates at very high temperatures. Hence, the manufacturing of spherical $MoSi_2$ particles along this route is expensive.

As an important preparation step prior to embedding healing particles into a TBC system, the present work describes a simple and cost-effective method to improve the circularity of $MoSi_2$ based particles by a wet ball milling treatment at room temperature. The effect of rotation speed, milling time, as well as the size of the milling balls and milling media on the roundness and flowability of the resulting particles were investigated.

2.2. Experimental procedures

2.2.1. Material preparation

$MoSi_2$ with 2.0 wt% B powder was used as starting material (<45 µm, ChemPUR GmbH, Germany), henceforth denoted as $MoSi_2(B)$. First, this powder was compacted using

spark plasma sintering (FCT SPS system, type KCE-FCT HP D-25-SI, Germany). To this end, 6.5 g powder was loaded into a graphite die with an inner diameter of 20 mm (ISO-68, Toyo Tanso, Japan). Graphite foils (Papyrex, Mersen, France) were used to prevent possible reaction between the powder and the graphite die. A thin layer of BN was sprayed on both sides of the graphite foils to ease the removal of the composite sample from the die and the punches after sintering. The punches and die assembly with the $MoSi_2(B)$ powder was mounted into the spark plasma sintering furnace and a pre-pressure of 5 kN was applied. Then, the SPS furnace was evacuated and flushed with Ar-gas of 5N purity (Linde, The Netherlands) two times. Next, the powder was heated to 1500 ºC with a heating rate of 20 ºC/min while applying a pressure of 50 MPa and flushing with Ar. The sample was kept for 30 min. at the sintering temperature and thereafter naturally cooled to room temperature.

The sintered tablet with a diameter of 20 mm and a thickness of about 3 mm was grinded with SiC emery paper starting with 80 mesh grit size to finally 1500 mesh grit size to remove the attached graphite foils and obtain a smooth surface finish. Hereafter, the $MoSi_2(B)$ tablet was thoroughly cleaned ultrasonically with iso-propanol.

To obtain particles from the SPSed $MoSi_2(B)$ tablet, it was crushed with a Fritsch Pulverisette (type P-0150). Two different size fractions of the particles were prepared by sieving (Analysensieb, DIN-ISO 3310-1, Retsch, Germany), namely fine particles of size D<20 µm and coarse particles of size D>20 µm. The fine powder fraction was discarded.

To polish away the sharp edges of the crushed particles with a size of D>20 µm, a planetary ball mill (PM100, Retsch GmbH, Germany) was used. To this end, a 50 ml zirconia jar with two different groups of zirconia balls with different diameters were used; namely: group 1 with 100 and 8 balls having a diameter of 5 and 10 mm, respectively; and group 2 with 200 and 90 balls having a diameter of 3 and 5 mm, respectively. Three different polishing media were selected including a diamond suspension (3 µm, Struers, Denmark), SiC (99.8%, 1 µm, Alfa Aesar, Germany) and Al_2O_3 (0.05 µm, Buehler, USA). All these polishing media were mixed with about 25 ml iso-propanol. Several batches of about 5.5 g of powder were milled with a rotation speed of 100 rpm. Different milling times were applied, namely: 50 and 100 min, respectively, which was realized by cycles of 25 minutes milling and 5 minutes pause. All milling parameters applied are listed in. Table 2. 1. After the milling, the milled particles were washed with distilled water and sieved with a 20 µm mesh sieve to depose the fine particles and the milling media. The remaining particles were dried in an oven at 80 ºC overnight. Afterwards, the particles were passed through the 50 µm sieve to eliminate the coarse fraction. Ultimately, particles with a size of 20<D<50 µm were obtained.

2

2.2.2. Characterization

The phase composition of the $MoSi_2$ (B) starting material and SPS sintered tablets was determined with X-ray diffractomertry (XRD) using a D8 advance diffractometer (Bruker, Germany) operated with Co Ka radiation. Diffractograms were recorded in the 2θ range of 10 to 110° with a 2θ step size of 0.030° and a counting time per step of 2 s. These diffractograms were evaluated using the Bruker Diffrac EVA software (version 3.1).

The microstructure of the sintered $MoSi_2$(B) tablets and the morphology of the particles after crunching the tablets and subsequently ball milling was observed with scanning electron microscopy (SEM) using a JEOL JSM 6500F (JEOL, Japan). This instrument is equipped with an ultra-dry energy dispersive spectrometer (EDS) for X-ray micro analysis (System 7, Noran, USA). The SEM images of well dispersed particles were analysed with ImageJ software (version 1.48v) to extract the shape parameters using the analyse particles module. The as determined circularity [33] corresponds with Cox roundness as mentioned in Eq. (2.1). Full details of the image processing procedure can be found in [34]. At least 80 particles were analysed for each group of samples.

The particle size distributions were determined with S3500 Microtrack Laser Particle Size Analyzer. The size was characterized using the 10, 50 and 90 % passing size (i.e. D_{10}, D_{50} and D_{90}) in the cumulative distribution. Prior to the measurements, the particles were dispersed in deionized water and agitated ultrasonically for 2 min. to avoid agglomeration.

The flowability of the particles before and after ball milling treatment was evaluated by two indexes, namely: the angle of repose and flow rate through an orifice. The method used to measure the angle of repose α (also known as drained angle of repose) comprises letting the powder pass through a funnel on a horizontal disc with a diameter of 15 mm [35]. The funnel was positioned 40 mm above the disc. The angle is obtained from the height h and base b of the heap carefully built up till the powder flows over the edge of the disc, according to [35]:

$$\tan(\alpha) = \frac{h}{0.5b}$$ (2.2).

The base corresponds to the diameter of the horizontal plate. The height is measured from a picture taken of the front of the heap.

The flow rate was determined over the smallest orifice outlet the powder could pass through. To this end, a tripod holding a brass cone-funnel orifice with an angle of 60°, a well-defined outlet diameter and a metal spatula to close the outlet of the orifice was set-up. The

orifice was closed before the powder was placed into the funnel. Then, the orifice was opened and the time that was needed for the sample to fully pass through was recorded.

The flowability of spherical YSZ powder specifically produced for plasma spraying (Amperit 827.774 ZrO_2-7 wt% Y_2O_3) was also tested for comparison. Prior to the testing, all the powders were dried at 80 °C for 16 hours in order to remove any moisture.

2.3. Results and discussion

2.3.1 Microstructure of MoSi$_2$(B) starting material

As can be seen in Figure 2. 1, the MoSi$_2$(B) sintered tablet features a microstructure consisting of molybdenum-disilicide matrix with precipitates of MoB_2 and inclusions of silica as identified with X-ray microanalysis. According to XRD, the main phase is tetragonal $MoSi_2$ with a minor amount of MoB_2 [36]. Silica is not seen in the diffractogram due to its amorphous structure.
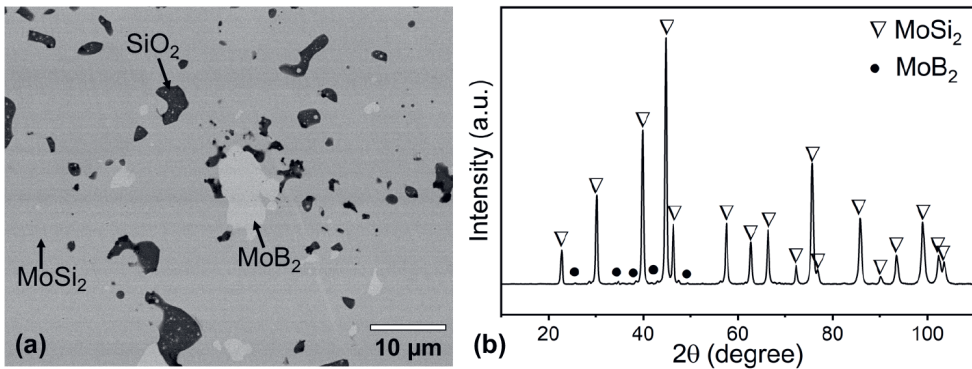
Figure 2. 1. Spark plasma sintered MoSi$_2$(B) tablet. (a) SEM back-scattered electron image and (b) X-ray diffractogram recorded with Co Kα.

2.3.2 Morphology of prepared MoSi$_2$(B) particles

The morphology of the MoSi$_2$(B) particles with a size of 20<D<50 μm after crunching a SPS tablet is shown in Figure 2. 2. These particles exhibit of angular fragments with sharp edges. The morphology of the MoSi$_2$(B) particles milled with different sizes of zirconia

milling balls (corresponding with items 2 and 3 in Table 2. 2, respectively) is shown in Figure 2. 3. It is clear that the MoSi$_2$(B) particles after milling exhibit smoother edges than the particles after crunching; cf. Figure 2. 2. The particles milled with the small zirconia balls (i.e. 200 and 90 balls having a diameter of 3 and 5 mm) show a more uniform particles size distribution than the particles milled with the larger zirconia balls (i.e. 90 and 8 balls having a diameter of 5 and 10 mm); compare Figure 2. 3a with Figure 2. 3b. Hence, the small ZrO$_2$ milling balls were selected for further investigations.

2
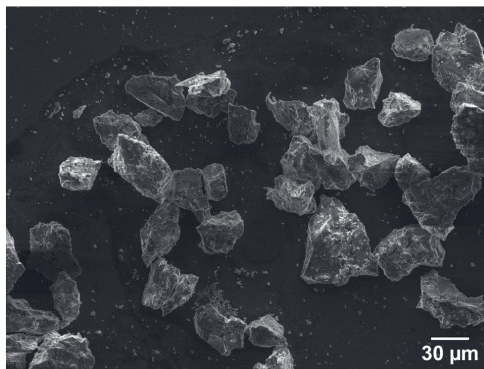
Figure 2. 2. SEM secondary electron image of the MoSi$_2$(B) particles after sieving with a diameter 20<D<50 µm after crunching (correspond with item 1 in Table 2. 2).
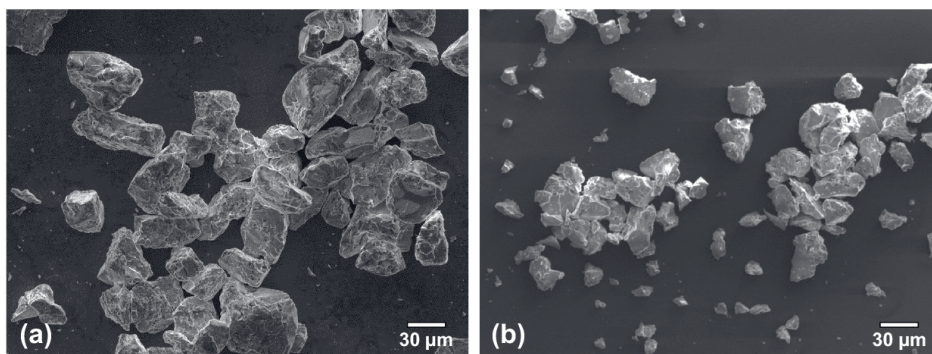

Figure 2. 3. SEM secondary electron images of the MoSi$_2$(B) particles after milling with different sizes of zirconia balls: (a) small zirconia balls (i.e. 200 and 90 balls having a diameter of 3 and 5 mm), (b) large zirconia balls (i.e. 90 and 8 balls having a diameter of 5 and 10 mm).

Table 2. 1. Parameters of ball milling MoSi$_2$(B) particles in 2-propanol with Retch PM 100 using zirconia jar and balls.

No.	Rotation speed (rpm)	Milling time (min.)	Milling[*]	Milling medium[*]
1	/	/	/	/
2	100	50	large balls	/
3	100	50	small balls	/
4	100	50	small balls	SiC
5	100	50	small balls	DP-suspension
6	100	50	small balls	alumina
7	100	100	small balls	SiC

[*] See text for details.

Table 2. 2. The aspect ratio (*AR*) and circularity (*C*) of differently prepared MoSi$_2$(B) particles. The particles were ball milled in 2-propanol with Retch PM 100 using zirconia jar and balls; cf. Table 2. 1.

No.	Additional milling conditions	Aspect ratio (*AR*)	Circularity (C)
1	as crushed	1.52 ± 0.35	0.57 ± 0.09
2	large balls for 50 min	1.56 ± 0.44	0.59 ± 0.16
3	small balls for 50 min	1.64 ± 0.40	0.60 ± 0.13
4	SiC[**] for 50 min	1.47 ± 0.31	0.63 ± 0.12
5	DP-suspension[**] for 50 min	1.58 ± 0.39	0.61 ± 0.10
6	Alumina[**] for 50 min	1.48 ± 0.34	0.66 ± 0.09
7	SiC[**] for 100 min.	1.47 ± 0.29	0.72 ± 0.07

[**] with small balls.

The morphologies of MoSi$_2$(B) particles after milling with different polishing media (corresponding with items 4-6 in Table 2. 2) are shown in Figure 2. 4. A closer look at the particles morphology suggests that using a polishing media result in smoother and rounder particles when compared with the particles milled with only iso-propanol, cf. Figure 2. 3a. Although the differences are small, the particles polished with SiC are relatively the smoothest and roundest; see Figure 2. 4b.
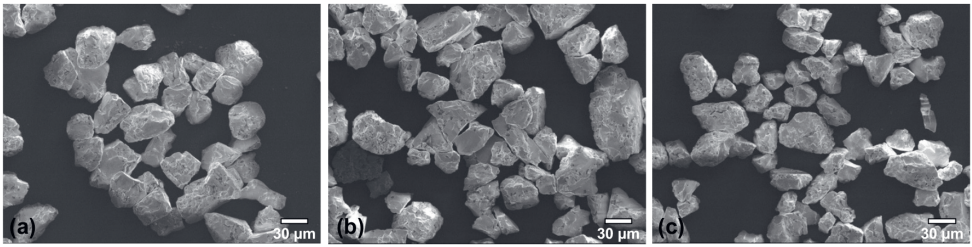
Figure 2. 4. Morphology of the MoSi$_2$(B) particles milled for 50 min. with the following polishing media: (a) 1 µm SiC particles in iso-propanol (b) 3 µm diamond-suspension mix with iso-propanol and (c) 0.05 µm alumina in iso-propanol.

The effect of milling time on the roundness of the MoSi$_2$(B) particles was studied as well. Longer milling of the MoSi$_2$(B) particles with SiC polishing media in isopropanol, i.e. 100 instead of 50 min., results in significantly smoother and rounder particles compared while the overall size is hardly reduced; see Figure 2. 4b and Figure 2. 5.

Figure 2. 5. SEM image of the MoSi$_2$(B) particles after milling with 1 µm SiC particles in iso-propanol for 100 min.

2.3.3 MoSi$_2$(B) particle shape

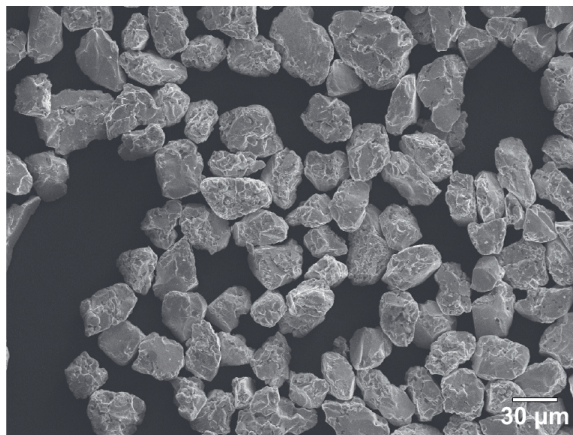Since all the particles have passed through 20 and 50 μm sieves, the particles show a uniform size distribution in all the SEM images. The average values of aspect ratio (AR) and circularity (C) of the differently prepared MoSi$_2$(B) particles are presented in Table 2. 2. The ball milling treatments seems to have hardly any effect on the aspect ratio of the particles, but milling with SiC (items 4 and 7 in Table 2. 2) show the lowest aspect ratio; i.e. the least elongated shape. The circularity of the MoSi$_2$(B) particles is little improved by wet ball milling in 2-propanol; see Table 2. 2 item 1 crushed particles (C is 0.57) versus items 2 and 3 milled particles (C is 0.59 and 0.60, respectively). The circularity of the MoSi$_2$(B) particles milled with the group of small size milling balls is hardly different from the particles milled with the group of big size milling balls; C is on average 0.59 and 0.60, respectively. On the other hand, the circularity of the MoSi$_2$(B) particles is substantially improved by ball milling with a polishing media. Using either silicon carbide, diamond or alumina powder improves the circularity of the crunched MoSi$_2$(B) particles from 0.57 to 0.63, 0.61 and 0.66, respectively; cf. Table 2. 1 and Table 2. 2. However, the milling time has the greatest impact on spherodizing the MoSi$_2$(B) particles. Extending the milling time from 50 to 100 min. increases the circularity from 0.63 to 0.72; cf. Table 2. 1 and Table 2. 2, items 4 and 7, respectively.

2.3.4 MoSi$_2$(B) flowability

The flowability of the roundest MoSi$_2$(B) particles, i.e. having the smallest aspect ratio and highest circularity (1.47 and 0.72, respectively) were tested. These particles were prepared by ball milling with 100 rpm for 100 min. of the crushed particles with small size ZrO$_2$ balls (200 and 90 balls having a diameter of 3 and 5 mm) with 1 μm SiC powder in iso-propanol polishing media. For comparison, the flowability of the as crunched MoSi$_2$(B) particles and spherical YSZ powder were also tested. Since the particle size likely affect the flowability [11], this should be comparable for the three powders analysed. Hence, the size distribution of these powders was measured. Indeed, the size of the powders examined are very similar; see Figure 2. 6 and Table 2. 3.

2
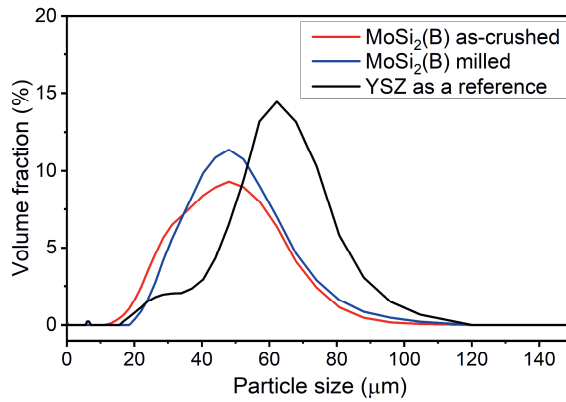
Figure 2. 6. Particle size distribution of $MoSi_2$(B) powder as crunched (red line) and after ball milling with with 1 µm SiC particles in iso-propanol for 100 min. (blue line) as well as spherical yttria stabilized zirconia powder (black line).

Table 2. 3. Particle size of $MoSi_2$(B) and yttria stabilized zirconia at 10, 50 and 90 percent volume fraction.

Particles	Particle size distribution		
	D_{10} (µm)	D_{50} (µm)	D_{90} (µm)
As-crunched $MoSi_2$(B)	28.3	40.3	60.7
Ball milled $MoSi_2$(B)	28.6	43.6	62.9
YSZ	30.6	56.7	75.0

The angle of repose obtained for the three samples and the corresponding classification of flowability [11, 35] are shown in Figure 2. 7 and given in Table 2. 4. As can be seen, the angle of repose of the $MoSi_2$(B) as crushed, i.e. without ball milling, is significantly larger than that of the $MoSi_2$(B) milled and the YSZ powder. The crushed $MoSi_2$(B) powder is classified as cohesive, i.e. poor flowability, while the spherical $MoSi_2$(B) and YSZ powders show free flowability.

Figure 2. 7. Powder heap formed to test the flowability characterized by the repose angle a according to ASTM D6393–99 [35]: (a) $MoSi_2(B)$ powde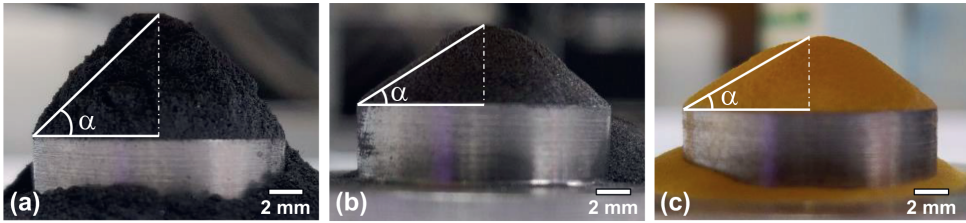r after crunching, (b) $MoSi_2(B)$ powder after ball milling with with 1 µm SiC particles in iso-propanol for 100 min. and (c) spherical yttria stabilized zirconia powder.

2

Table 2. 4. Results for the angle of repose measurements and the respective flowability of powders.

Powder	Angle of repose (º)	Classification of flowability
$MoSi_2(B)$ crunched	49.3 ± 2.9	Cohesive
$MoSi_2(B)$ milled and polished	37.0 ± 1.0	Free flowing
YSZ	34.3 ± 2.0	Free flowing

The results obtained in the flow rate through orifice tests, see Table 2. 5, are consistent with the results for the repose angle. The minimum outlet diameter of the orifice is 9 mm for the crunched $MoSi_2(B)$ powder, while this minimum diameter is only 1.5 mm for the milled $MoSi_2(B)$ and the YSZ powder. The flow rate through the orifice of the YSZ powder is a little higher than that of the milled $MoSi_2(B)$ powder.

Table 2. 5. Results for the flow through an orifice comprising the minimum orifice diameter and flow rate of the powders.

Powder	Orifice Diameter (mm)	Flow rate (g/s)
$MoSi_2(B)$ crunched	9	-
$MoSi_2(B)$ milled and polished	1.5	0.79 ± 0.01
YSZ	1.5	0.86 ± 0.01

2.4. Conclusions

The flowability of MoSi$_2$(B) powder, as prepared by spark plasma sintering and subsequently crunching, was improved by gentle milling with a polishing media. The best result was obtained by ball milling with 100 rpm for 100 min. of crushed particle with small size ZrO$_2$ balls (200 and 90 balls having a diameter of 3 and 5 mm) and with 1 µm SiC powder in iso-propanol as polishing media. The circularity compared with the as crunched MoSi$_2$(B) was improved from 0.57 to 0.72, and the flow of the powder was changed from cohesive to free flowing. This spheroidization enables preparation of powders of brittle and high melting materials and make these powders suitable for thermal spraying applications.

2

References

[1] J.J. Petrovic, Mechanical behavior of MoSi$_2$ and MoSi$_2$ compsites, Materials Science & Engineering A 192/193 (1995) 31-37.

[2] D.A. Berztiss, R.R. Cerchiara, E.A. Gulbransen, F.S. Pettit, G.H. Meier, Oxidation of MoSi$_2$ and comoarisaon with other silicide materials, Materials Science & Engineering A A155 (1992) 165-181.

[3] J. Xu, Z. Li, Z.-H. Xie, P. Munroe, X.L. Lu, X.F. Lan, Novel high damage-tolerant, wear resistant MoSi$_2$-based nanocomposite coatings, Applied Surface Science 270 (2013) 418-427.

[4] J.J. Petrovic, MoSi$_2$-based high-temperature structural silicides, MRS Bulletin 18(7) (2013) 35-41.

[5] A. Costa e Silva, M.J. Kaufman, Applications of in situ reactions to MoSi$_2$-based materials, Materials Science & Engineering A 195 (1995) 75-99.

[6] X. Hou, J. Huang, M. Liu, X. Li, Z. Hu, Z. Feng, M. Zhang, J. Luo, Single-crystal MoO$_3$ micrometer and millimeter belts prepared from discarded molybdenum disilicide heating elements, Scientific Reports 8(1) (2018).

[7] Z. Derelioglu, A.L. Carabat, G.M. Song, S.v.d. Zwaag, W.G. Sloof, On the use of B-alloyed MoSi$_2$ particles as crack healing agents in yttria stabilized zirconia thermal barrier coatings, Journal of the European Ceramic Society 35(16) (2015) 4507-4511.

[8] F. Nozahic, A.L. Carabat, W. Mao, D. Monceau, C. Estournes, C. Kwakernaak, S. van der Zwaag, W.G. Sloof, Kinetics of zircon formation in yttria partially stabilized zirconia as a result of oxidation of embedded molybdenum disilicide, Acta Materialia 174 (2019) 206-216.

[9] F. Nozahic, C. Estournès, A.L. Carabat, W.G. Sloof, S. van der Zwaag, D. Monceau, Self-healing thermal barrier coating systems fabricated by spark plasma sintering, Materials & Design 143 (2018) 204-213.

[10] A.L. Carabat, M.J. Meijerink, J.C. Brouwer, E.M. Kelder, J.R. van Ommen, S. van der Zwaag, W.G. Sloof, Protecting the MoSi$_2$ healing particles for thermal barrier coatings using a sol-gel produced Al$_2$O$_3$ coating, Journal of the European Ceramic Society 38(7) (2018) 2728-2734.

[11] H.M. Beakawi Al-Hashemi, O.S. Baghabra Al-Amoudi, A review on the angle of repose of granular materials, Powder Technology 330 (2018) 397-417.

[12] M.C. Bordes, M. Vicent, A. Moreno, R. Moreno, A. Borrell, M.D. Salvador, E. Sánchez, Microstructure and photocatalytic activity of APS coatings obtained from different TiO$_2$ nanopowders, Surface and Coatings Technology 220 (2013) 179-186.

[13] E. Cañas, M. Vicent, E. Bannier, P. Carpio, M.J. Orts, E. Sánchez, Effect of particle size on processing of bioactive glass powder for atmospheric plasma spraying, Journal of the European Ceramic Society 36(3) (2016) 837-845.

2

[14] K. Nishii, M. Horio, Granulation of a hardmetal powder for spark plasma sintering, Powder Technology 130(1-3) (2003) 199-202.

[15] M. Vicent, E. Bannier, R. Benavente, M.D. Salvador, T. Molina, R. Moreno, E. Sánchez, Influence of the feedstock characteristics on the microstructure and properties of Al_2O_3–TiO_2 plasma-sprayed coatings, Surface and Coatings Technology 220 (2013) 74-79.

[16] L. Wang, Y. Wang, X.G. Sun, J.Q. He, Z.Y. Pan, L.L. Yu, Preparation and characterization of nanostructured $La_2Zr_2O_7$ feedstock used for plasma spraying, Powder Technology 212(1) (2011) 267-277.

[17] J.-h. Yan, X. Jian-jian, d. Rafi ud, Y. Wang, L.-F. Liu, Preparation of agglomerated powders for air plasma spraying $MoSi_2$ coating, Ceramics International 41(9) (2015) 10547-10556.

[18] D. Koch, G. Mauer, R. Vaßen, Manufacturing of composite coatings by atmospheric plasma spraying using different feed-stock materials as YSZ and $MoSi_2$, Journal of Thermal Spray Technology 26(4) (2017) 708-716.

[19] A. Bodhmage, Correlation between physical properties and flowability indicators for fine powders, (2006).

[20] U. Ulusoy, M. Yekeler, C. Hiçyılmaz, Determination of the shape, morphological and wettability properties of quartz and their correlations, Minerals Engineering 16(10) (2003) 951-964.

[21] R.D. Hryciw, J. Zheng, K. Shetler, Particle roundness and sphericity from images of assemblies by chart estimates and computer methods, Journal of Geotechnical and Geoenvironmental Engineering 142(9) (2016) 04016038.

[22] H. Wadell, Volume, shape, and roundness of rock particles, The Journal of Geology Vol. 40, No. 5 (1932) 443-451.

[23] Y. Takashimizu, M. Iiyoshi, New parameter of roundness R: circularity corrected by aspect ratio, Progress in Earth and Planetary Science 3(1) (2016).

[24] E.P. Cox, A method of assigning numerical and percentage values to the degree of roundness of sand grains, Journal of Paleontology Vol. 1, No. 3 (1927) 179-183.

[25] Z.Z. Fang, J.D. Paramore, P. Sun, K.S.R. Chandran, Y. Zhang, Y. Xia, F. Cao, M. Koopman, M. Free, Powder metallurgy of titanium – past, present, and future, International Materials Reviews 63(7) (2017) 407-459.

[26] X.-g. Li, Q. Zhu, S. Shu, J.-z. Fan, S.-m. Zhang, Fine spherical powder production during gas atomization of pressurized melts through melt nozzles with a small inner diameter, Powder Technology 356 (2019) 759-768.

[27] A. Allimant, M.P. Planche, Y. Bailly, L. Dembinski, C. Coddet, Progress in gas atomization of liquid metals by means of a De Laval nozzle, Powder Technology 190(1-2) (2009) 79-83.

[28] S. Ozbilen, Influence of atomising gas pressure on particle shape of Al and Mg powders, Powder Technology 102 (1999) 109-119.

[29] S. Lagutkin, L. Achelis, S. Sheikhaliev, V. Uhlenwinkel, V. Srivastava, Atomization process for metal powder, Materials Science and Engineering: A 383(1) (2004) 1-6.

[30] Z. Károly, J. Szépvölgyi, Plasma spheroidization of ceramic particles, Chemical Engineering and Processing: Process Intensification 44(2) (2005) 221-224.

[31] X.-p. Liu, K.-s. Wang, P. Hu, Q. Chen, A.A. Volinsky, Spheroidization of molybdenum powder by radio frequency thermal plasma, International Journal of Minerals, Metallurgy, and Materials 22(11) (2015) 1212-1218.

[32] J.-J. Wang, J.-J. Hao, Z.-M. Guo, Y.-M. Wang, Preparation of spherical tungsten and titanium powders by RF induction plasma processing, Rare Metals 34(6) (2014) 431-435.

[33] T.F.W. Rasband, ImageJ User Guide IJ 1.46r, (2012).

[34] A. Mazzoli, O. Favoni, Particle size, size distribution and morphological evaluation of airborne dust particles of diverse woods by Scanning Electron Microscopy and image processing program, Powder Technology 225 (2012) 65-71.

[35] D. ASTM, Standard test method for bulk solids characterization by Carr indices, (2006).

2

2

3.

Selective oxidation of aluminium in Mo(Al,Si)$_2$

Abstract

$Mo(Al_xSi_{1-x})_2$ alloy with x in the range of 0.35–0.65 were prepared by a one-step spark plasma sintering. To study the exclusive formation of an $\alpha-Al_2O_3$ scale, oxidation experiments were conducted in low and high oxygen partial pressure ambient at 1373 K; viz.: 10^{-14} and 0.2 atm. The oxidation kinetics follows a parabolic rate law after a transient period. A counter-diffusion process of O and Al along grain boundaries of Al_2O_3 scale is responsible for the equiaxed and columnar grain growth based on a two-layered microstructure. The formation of a dense equiaxed $\alpha-Al_2O_3$ layer contributes to excellent oxidation resistance.

3.1. Introduction

3

Molybdenum disilicide ($MoSi_2$), is an attractive material for structural high-temperature applications due to its high melting point (above 2273 K) in combination with a moderate density (6.24 g/cm^3) and an excellent oxidation resistance in the temperature up to approximately 2000 K [1-4]. Currently, potential applications of $MoSi_2$ include furnace elements and components for high-temperature heat exchangers and filters, gas burners, components for hot-section jet engines and gas turbines [5, 6]. However, a high creep rate at elevated temperatures [1, 2] and the so-called 'pesting' phenomena whereby disintegration occurs during oxidation at temperatures in the range of 650 to 800 K [1-3] have inhibited practical application of this compound, but initiated an intensified research in $MoSi_2$-based alloys [1, 2, 4-7].

High-temperature oxidation resistance can be realized with suitable alloying elements, typically Al, Si and Cr [8], whose preferential oxidation can create a diffusion barrier to oxygen permeation [9-11]. The effect of third elements in Mo–Si–X (with X as Al, Ta, Ti, Zr and Y) intermetallics on the high-temperature oxidation [12, 13] and pesting behaviour [14, 15] has been investigated. Among these alloys, the Mo–Si–Al intermetallic has proven to be the most promising [1, 6, 15].

Partial substitution of Si with Al improves the oxidation resistance of $MoSi_2$ due to the formation of a protective alumina scale via an *in-situ* displacement reaction [11, 16, 17]. The alumina scale formed from $Mo(Al,Si)_2$ is stable and adherent with a close match of thermal expansion coefficient between the bulk material and Al_2O_3 [8, 18], viz.: 7.4–8.6 × 10^{-6} K^{-1} [19] and 8.1–8.9 × 10^{-6} K^{-1} [20], respectively. This is a major advantage compared to silica forming $MoSi_2$, which exhibits evaporation in reducing environments and spalling of the oxide scale [11, 12, 17, 18].

Several studies have been carried out to assess the properties of Mo(Al,Si)$_2$ materials including their mechanical behaviour [4], thermo-physical properties [21] and oxidation behaviour [1, 6, 11, 13, 15, 17, 22]. However, the oxidation mechanism remains yet unclear and most of these studies concerns Mo(Al,Si)$_2$ compounds with a relatively low Al substitution. This work, however, focusses on the selective oxidation behaviour of Al in Mo(Si,Al)$_2$ with relatively high Al contents up to about 43 at.%.

3.2. Materials and methods

3.2.1. Materials design and sample preparation

To obtain single phase Mo(Al,Si)$_2$ with different high Al content, six batches of elemental powder mixtures were prepared; see Table 3. 1. The target compositions of Mo(Al$_x$Si$_{1-x}$)$_2$ were x equal to 0.40, 0.45, 0.50, 0.55, 0.60 and 0.65; respectively. Elemental powder of molybdenum (2–5 µm 99.95+% purity, Chempur, Germany), silicon (45 µm 99.99 % purity, TLS Technik GmbH & Co, Germany) and aluminium (45 µm 99.8 % purity, TLS Technik GmbH & Co, Germany) were mixed in the desired molar ratios for 3 hours with a Turbula mixer (Willy A. Bachofen AG Maschinenfabrik, Type T2C, Switzerland) using ZrO$_2$ balls with a diameter of 5 mm. Next, the powder mixtures were densified and sintered in a spark plasma sintering (SPS) furnace (FCT SPS system, type KCE-FCT HP D-25-SI, Germany). To this end, 6.5 g of the powder mixture was loaded into a graphite die with an inner diameter of 20 mm (ISO-68, Toyo Tanso, Japan). Graphite foils (Permafoil, PF20-HP, Toyo Tanso, Thailand) was used to prevent possible reaction between the powder and the graphite die and punches. Thin layers of BN (Henze, Lauben, Germany) were sprayed onto both sides of the graphite foils for easy removal of the composite sample from the die and punches after sintering. The punches and die assembly with the elemental powder mixture was mounted into the SPS furnace. Then, this furnace was evacuated and flushed two times with Ar-gas of 5N purity (Linde, The Netherlands). Next, the furnace was heated up to 1773 K with a heating rate of 20 K/min. The electric current was applied following 15/5 on/off 3 ms pulse sequence. First, a pressure of 50 MPa was applied till the temperature reached 873 K. Next, the pressure was released to avoid leakage of melted Al. When the temperature reached to 1773 K, a pressure of 50 MPa was applied again to promote alloying and densification. The sample was kept for 30 minutes at the sintering temperature and thereafter cooled naturally to room temperature. The sintered tablet with a diameter of 20 mm and a thickness of about 3 mm was ground with SiC emery paper starting with 80 mesh

grit size to finally 1500 mesh grit size to obtain a smooth surface finish. Hereafter, the disc was thoroughly cleaned ultrasonically with isopropanol.

Finally, the sintered discs were cut into rectangular bars of $15 \times 8 \times 2$ mm via electric discharge machining (EDM) for thermogravimetric analysis. The surfaces of these bars were ground with SiC emery paper starting with 800 mesh grit size to finally 4000 mesh grit size. Next, these surfaces were polished subsequently with 3 and 1 μm grains diamond paste on soft cloths. The samples were cleaned ultrasonically in isopropanol and dried by blowing with pure nitrogen (purity better than 5N) before storing into airtight membrane boxes (Agar Scientific G3319, UK).

3.2.2. Isothermal oxidation

The isothermal oxidation of bulk $Mo(Al_xSi_{1-x})_2$ material was performed in a low oxygen partial pressure (pO_2) of 10^{-14} atm. gas environment at 1373 K to promote the selective oxidation of Al and to avoid possible formation of volatile Mo-oxide species.

The low oxygen partial pressure of 10^{-14} atm. at 1373 K in the gas ambient was realized with a gas mixture of Ar with 8 vol.% CO_2 and 50 vol.% CO; see Appendix A. The oxidation kinetics was monitored with thermogravimetric analysis (TGA) using a dual furnace balance (Setaram TAG 16/18, Caluire, France), which allows automatic correction for buoyancy effects. The alumina furnace tubes have an inner diameter of 15 mm. This analyser is equipped with Pt/Pt-10%Rh (S-type) thermocouples. The gas mixture was admitted to the TGA analyser via mass flow controllers (Bronkhorst, The Netherlands) operated with Labview (version 2020) such that the total gas flow matches 100 sccm, which was equally divided over both furnace tubes. The gases Ar, CO and CO_2 were supplied from Linde Gas Benelux BV with a purity better than 5N. Prior to admitting the gas mixtures to the furnaces, Ar was filtered to remove any residual moisture and hydrocarbons, with SGT click on oxygen trap (< 5 ppb O_2, SGT Middelburg, The Netherlands), Hydrosorb (< 20 ppb H_2O) and Accosorb (< 10 ppb hydrocarbons) filters (Messer Griesheim, Germany); respectively.

The sample was mounted onto a sapphire rod with an alumina pin having a diameter of 2.2 mm through a hole of diameter of 2.5 mm in the sample. The initial mass of the sample was weighed using a Mettler Toledo balance (accuracy ± 1 μg). A dummy sample of alumina with the same dimensions was mounted onto a sapphire rod of the counter part of the balance to eliminate any buoyancy effect. To flush the gas lines, balance and furnaces, the TGA system was pumped to vacuum (< 50 Pa) and refilled with Ar three times. Then, the dual

furnaces were heated up from room temperature to the target temperature with 10 K/min, while purging with 100 sccm Ar, i.e., 50 sccm gas in each furnace. When the target temperature for isothermal oxidation was reached, the gas composition was switched to the oxidation atmosphere while maintaining a total gas flow of 100 sccm for 16 hours. After oxidation, the furnace was cooled down to room temperature with 10 K/min while flushing with pure Ar. The short-term oxidation experiments of 1 hour holding time were conducted using the same condition.

The oxidation behaviour of $Mo(Al_xSi_{1-x})_2$ material at 1373 K was also investigated by direct exposure to a dry synthetic air environment and after pre-oxidation under low oxygen partial pressure condition. Also, in these cases the oxidation kinetics was monitored with thermogravimetric analysis using a dual furnace balance. After 16 hours pre-oxidation under low oxygen partial pressure of 10^{-14} atm. at 1373 K, the gas was switched directly to Ar with 21 vol.% O_2 for another 50 hours. Afterwards, the furnace was cooled to room temperature flushing with pure Ar.

3.2.3. Characterization

The phase composition of the alloy samples before and after oxidation were determined with X-ray diffractometry (XRD) using a D8 advance diffractometer (Bruker, Germany) in the Bragg-Brentano geometry operated with Cu-Kα radiation. Diffractograms were recorded in the 2θ range of 10 to 130° with a step size of 0.030° and a counting time of 2 s per step. XRD measurements in the grazing incidence geometry were performed with the same diffractometer with Co-Kα radiation in the 2θ region between 10 and 110° with a fixed observation angle of 3°. The incident beam had a height of 5 mm and a width of 1 mm. A step size of 0.030° 2θ and a counting time of 5 s per step were applied to identify the oxide phases present at the sample surface. These diffractograms were evaluated using the Bruker Diffrac EVA software (version 3.1). Quantitative phase composition analysis and lattice parameters determination were performed with Rietveld refinement [23] using MAUD software (version 2.93).

The surface morphology of the samples was observed with scanning electron microscopy (SEM) using a JEOL JSM 6500F (JEOL, Japan). This instrument is equipped with an ultra-dry energy dispersive spectrometer (EDS) for X-ray micro analysis (XMA, System 7, Noran, USA). Cross-sections of the samples were prepared and analysed with a dual beam scanning electron microscope (Helios G4 PFIB UXe, Thermo Fisher Scientific,

USA) equipped with a xenon plasma focused ion beam (PFIB). This instrument is provided with an EDAX system (USA) for energy dispersive X-ray micro analysis with Octane Elite plus detector, using TEAM acquisition and analysis software (version 4.5). First, the surface of the sample was covered with about 2 µm layer of Pt added with C. Next, a trench was cut with the Xe PFIB operated at 30 keV. Then, the surface of the cross-section was polished with a low current Xe PFIB. SEM images and X-ray spectra were recorded using a 10 keV focused electron beam. The thickness of the oxide layer was measured at the cross-section exposed by PFIB milling.

The concentration of Mo, Si, Al and O was determined with electron probe X-ray microanalysis (EPMA). The analysis was performed with a JXA 8900R (JEOL, Japan) microprobe employing Wavelength Dispersive Spectrometry (WDS). A focussed electron beam was used with an energy of 10 keV and a current of 50 nA. The composition at each analysis location of the sample was determined using the X-ray intensities of the constituting elements after background correction relative to the corresponding intensities of reference materials. In this case, the X-ray intensities of Mo-Lα, Si-Kα, Al-Kα and O-Kα were measured and pure Mo, Si, Al and SiO_2, respectively, were used as references. The thus obtained intensity ratios were processed with a matrix correction program CITZAF [24]. The concentration of each element was obtained from the average of at least 80 measurement points.

3.3. Results and Discussion

3.3.1. Composition and microstructure of sintered Mo–Si–Al alloys

The Mo–Al–Si ternary phase diagram at different temperatures was constructed with Thermo-Calc software (version 2022a, Thermo-Calc, Stockholm, Sweden) using the thermodynamic database of Al–Si–Mo / Al–Mo–Si–U [25] to investigate the amount of Al that can be dissolved in $Mo(Al,Si)_2$. Figure 3. 1 shows as examples, the section of the Mo–Al–Si ternary phase diagram at 1773 K and 1373 K as well as the calculated maximum amount of Al dissolved in $Mo(Al_xSi_{1-x})_2$ as a function of temperature.
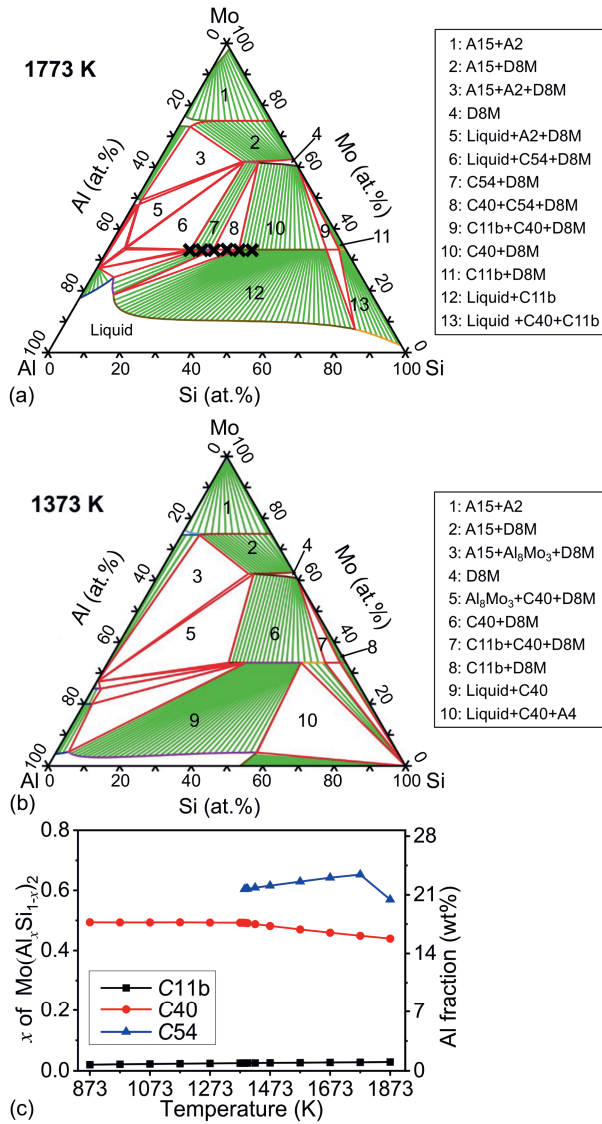
Figure 3. 1. (a) Mo–Al–Si ternary phase diagram at 1773 K calculated by Thermo-Calc software. The black crosses denote the compositions of the alloys prepared in the present work; (b) Mo–Al–Si ternary phase diagram at 1373 K calculated by Thermo-Calc software; (c) the maximum amount of Al dissolved in Mo(Al_xSi_{1-x})$_2$ as a function of temperature. The C11b, C40 and C54 are Mo(Al,Si)$_2$ in tetragonal, hexagonal and orthorhombic crystal lattice, respectively; D8M is Mo$_5$(Al,Si)$_3$ with tetragonal crystal lattice; A15 is Mo$_3$(Al,Si), A2 is AlMo, and A4 is Si with diamond structure.

Mo(Al,Si)$_2$ appears with three different crystal lattice structures depending on the Al to Si ratio, which include: the tetragonal ($C11b$) structure, the hexagonal ($C40$) structure and the orthorhombic ($C54$) structure. MoSi$_2$ exhibits the tetragonal ($C11b$) structure, which has a small solubility of Al (1.9 at.% at 1773 K). Further substitution of Si with Al results in Mo(Al,Si)$_2$ with hexagonal ($C40$) crystal lattice structure which exists over a wide composition range up to about 30 at.% Al at 1773 K. Beyond this composition, Mo(Al,Si)$_2$ takes the orthorhombic ($C54$) crystal lattice structure. As can be seen in Figure 3. 1c, the largest amount of Al that can be dissolved in Mo(Al,Si)$_2$ at a temperature of about 1773 K occurs when the material features the orthorhombic ($C54$) crystal lattice.

The actual compositions of the fabricated alloy bulk samples determined by EPMA analysis are listed in Table 3. 1. The Al content of the alloys is slightly lower but still very close to the nominal value. The loss of the small amount of Al results from the formation of alumina inclusions.

3

XRD patterns of the alloys reveal that with increasing amount of Al substituting Si, denoted as x in Mo(Al$_x$,Si$_{1-x}$)$_2$, the crystal lattice changes from a hexagonal type $C40$ to a orthorhombic type $C54$; see Figure 3. 2. The phase fractions and lattice parameters as determined by the Rietveld refinement are listed in Table 3. 1. These results show that a small fraction of the orthorhombic phase (7.2 %) starts to appear when the Al content is 31.9 at.% in Mo(Al$_x$Si$_{1-x}$)$_2$ and becomes the dominant phase when the Al content is further increased up to 38.9 at.%. This phase change as a function of the composition is in agreement with the ternary phase diagram of Mo–Al–Si at 1773 K (cf. Figure 3. 1a) suggesting that the phases are in thermodynamic equilibrium after sintering and stay stable upon cooling to room temperature. Mo(Al,Si)$_2$ is the main phase in the alloy samples. XRD lines of Mo$_5$Si$_3$ and small peaks Mo$_3$Al$_8$ were also detected for samples with high Al content; see Figure 3. 2. The Mo$_5$Si$_3$ phase can be present already at the synthesis temperature, whereas the Mo$_3$Al$_8$ can only be formed during cooling; see the Mo–Al–Si ternary phase at 1773 K in Figure 3. 1a and at 1373 K in Figure 3. 1b.

3

Table 3. 1. Chemical composition, constituting phases fractions and lattice parameters of Mo(Al$_x$Si$_{1-x}$)$_2$ samples prepared by spark plasma sintering.

Nominal x (-)	Actual x (-)	Al fraction* (at.%)	Phase (wt%)	Crystal lattice** (-)	Lattice parameter				
					a (pm)	b (pm)	c (pm)	c/a (-)	b/a (-)
0.40	0.35	23.5±0.5	H: 100.0	C40	472.15(1)	-	657.65(2)	1.393	-
0.45	0.40	26.4±0.4	H: 100.0	C40	472.06(1)	-	657.57(3)	1.393	-
0.50	0.48	31.9±0.1	H: 92.8	C40	474.198(4)	-	660.08(1)	1.392	-
			O: 7.2	C54	826.5(3)	481.2(2)	877.5(3)	1.062	0.582
0.55	0.52	34.9±3.6	H: 85.4	C40	474.78(2)	-	660.90(4)	1.392	-
			O: 14.6	C54	827.0(1)	480.1(1)	879.1(2)	1.063	0.581
0.60	0.58	38.9±0.3	H: 5.7	C40	474.47(3)	-	660.32(7)	1.392	-
			O: 90.2 T: 4.1	C54	826.25(2)	479.93(2)	877.77(3)	1.062	0.581
0.65	0.65	43.1±0.5	O: 92.7 T: 7.3	C54	826.86(2)	481.88(3)	879.19(4)	1.063	0.583

H: hexagonal Mo(Al,Si)$_2$; O: orthorhombic Mo(Al,Si)$_2$; T: tetragonal Mo$_5$(Al,Si)$_3$

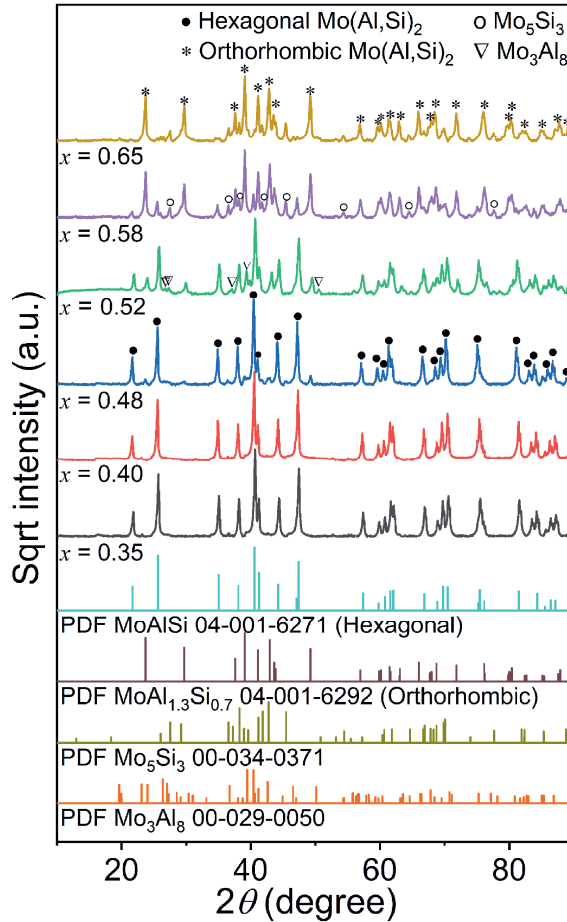*As determined with EPMA, cf. Section 3.2.3.

**In terms of Mo(Al,Si)$_2$

Figure 3. 2. XRD patterns of Mo(Al$_x$Si$_{1-x}$)$_2$ bulk alloys fabricated by spark plasma sintering.

It may be expected that with increasing substitution of Si by Al in Mo(Al,Si)$_2$ the lattice parameters change due to the larger atomic radius of Al atoms (143 pm) compared to Si (117 pm) [21]. However, the variations of lattice parameters for the composition range considered here (i.e., x from 0.35 to 0.65) are very small with increasing amount of Al; see Table 3. 1. This is in agreement with the work of Tabaru et al. [21], who provided a detailed explanation. The crystal lattice structure of Mo(Al$_x$Si$_{1-x}$)$_2$ is hexagonal (C40) from x is 0.35 till 0.40 when the maximum solubility of Al in this crystal lattice is reached. When the Al content is further increased, the crystal lattice changes from hexagonal (C40) to orthorhombic (C54).

The alloys fabricated by sintering of elemental powder mixtures exhibit uniform microstructures albeit some patches of alumina were observed, except in the alloy with 43.1 at.% Al ($x = 0.65$); see Figure 3. 3. Local composition analysis with XMA revealed regions where three phases coexist; see Figure 3. 3f. These regions comprise $Mo_5(Al,Si)_3$, Mo_3Al_8 and $Mo(Si,Al)_2$, which is formed upon cooling (cf. phase diagram in Figure 3. 1b) and is consistent with the XRD results (see above).
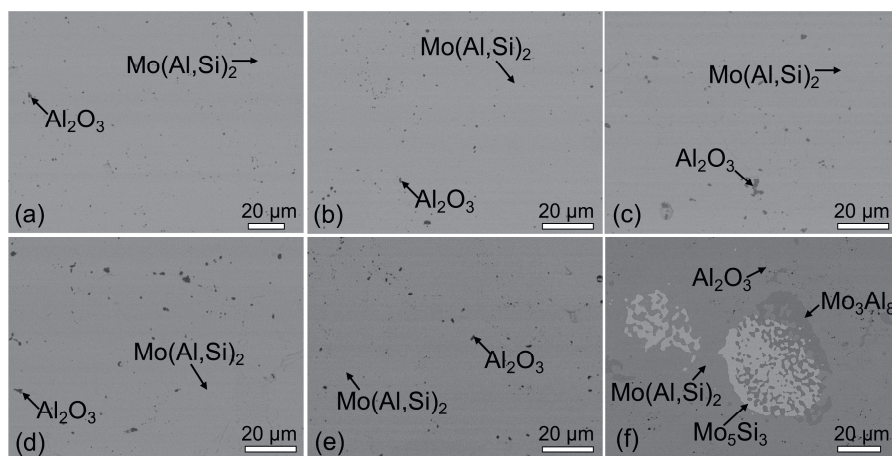

Figure 3. 3. Microstructures of $Mo(Al_xSi_{1-x})_2$ bulk alloys fabricated by spark plasma sintering of elemental powder mixtures with composition of (a) $x = 0.35$; (b) $x = 0.40$; (c) $x = 0.48$; (d) $x = 0.52$; (e) $x = 0.58$; (f) $x = 0.65$.

3.3.2. Low oxygen partial pressure oxidation of Mo–Si–Al alloys

Isothermal oxidation of bulk $Mo(Al_xSi_{1-x})_2$ material was performed in a low oxygen partial pressure (pO_2) of 10^{-14} atm. gaseous ambient at 1373 K, which is slightly lower than the dissociation pressure of Mo-oxides, but far above the dissociation pressure of Si- and Al-oxides according to the metal/oxide stability diagrams; see Figure 3. 4a-d. SiO(g) possesses the highest vapour pressure of about 10^{-10} atm. at the target pO_2 of 10^{-14} atm.; see Figure 3. 4d. The vapour pressure magnitudes will slightly differ for the $Mo(Al,Si)_2$ material since unit activities are assumed for the calculation of this kind of diagram [26-28]. However, when considering ideal thermodynamic behaviour of the $Mo(Al_xSi_{1-x})_2$ alloys, the activity has no

influence on the slope of the lines in the oxide stability diagram (Figure 3. 4) but only make a very small difference on the intercept.
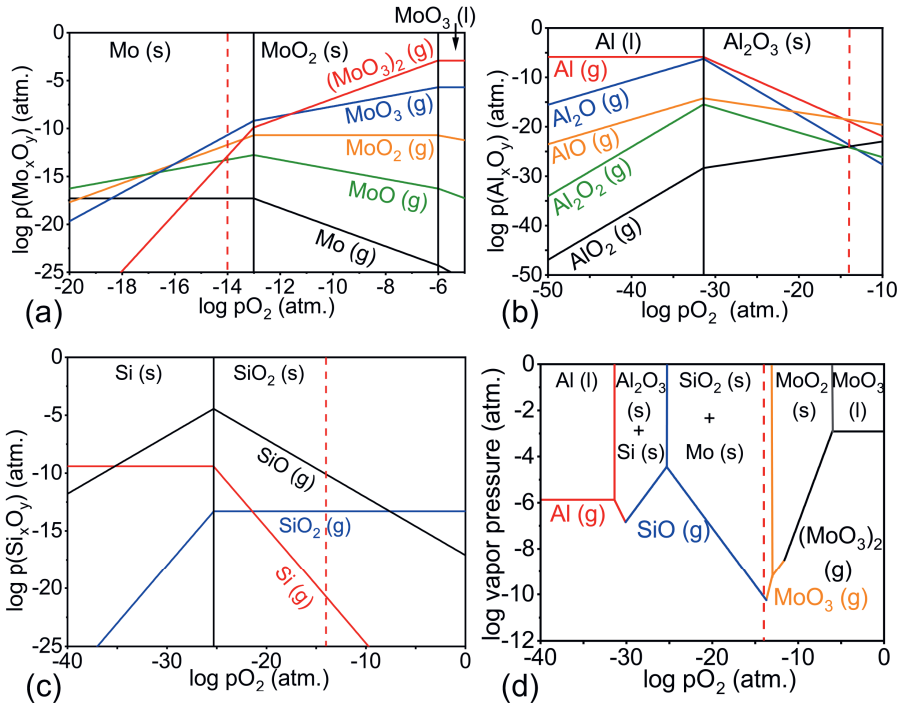

Figure 3. 4. Stability diagrams at 1373 K for: (a) Mo–O; (b) Al–O; (c) Si–O; and (d) combined diagram presenting the species with the highest vapour pressure as a function of pO_2. Vertical dashed red line indicates an oxygen partial pressure of 10^{-14} atm..

During the oxidation process in such a low pO_2 ambient condition, the solid oxide MoO_2 cannot be formed and the vapour pressures of the volatile Mo-oxides are very low (less than 10^{-10} atm.), according to the oxide stability diagram; cf. Figure 3. 4. Once the surface of the alloy is covered with a closed layer of either solid silica or alumina, volatile Mo-oxides will likely cease to form. Since the dissociation pressure of Al_2O_3 is much lower than that of SiO_2 (10^{-31} versus 10^{-25} atm., respectively, see Figure 3. 4b and c), alumina will be formed preferentially [29, 30].

3.3.2.1. Oxide scale composition and microstructure

After oxidation in the low pO_2 ambient at 1373 K for 16 hours, $Mo(Al_xSi_{1-x})_2$ alloys with x in the range of 0.35 to 0.65 feature the same surface morphology. As an example, the surface morphology of the oxide scale is shown in Figure 3. 5a. The surface of the substrate is fully covered with a "grass like" oxide scale. A cross-section of the same sample reveals that the oxide scale is composed of α-Al_2O_3 exclusively with an Al depletion layer beneath corresponding with $Mo_5(Al,Si)_3$; see Figure 3. 5b.
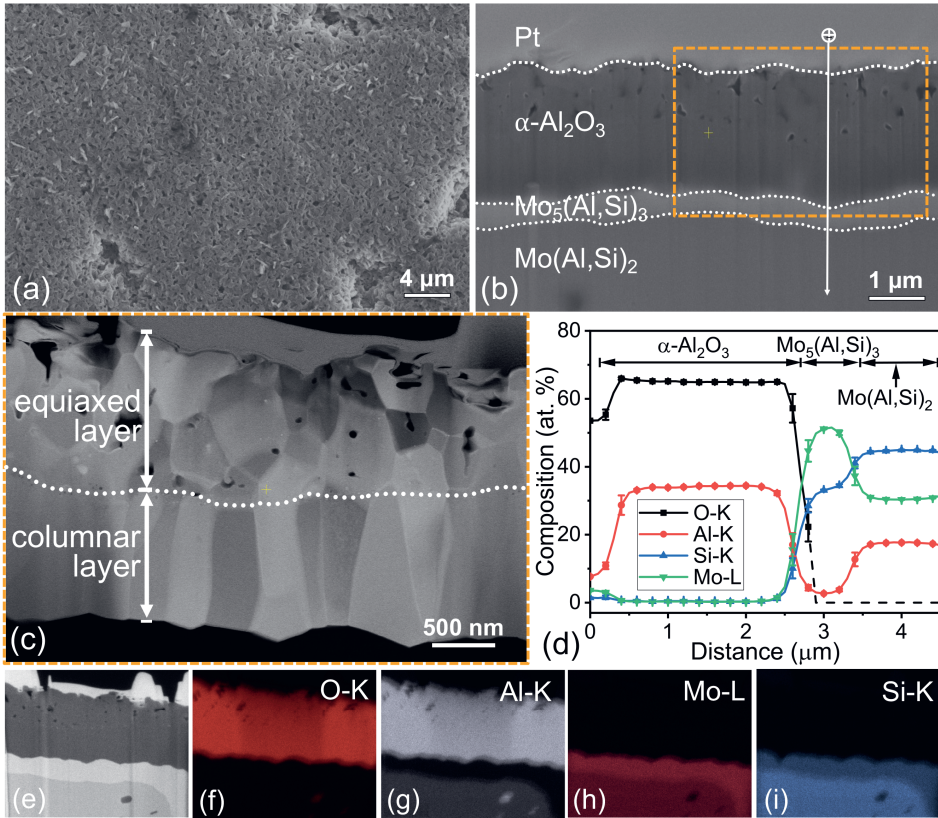

Figure 3. 5. SEM surface and cross-section observation of the $Mo(Al_{0.40}Si_{0.60})_2$ after oxidation in low pO_2 (10^{-14} atm.) gaseous ambient at 1373 K for 16 hours: (a) surface morphology; (b) cross-section with position of the composition line scan across the oxide scale, $Mo_5(Al,Si)_3$ layer and $Mo(Al,Si)_2$ substrate; (c) cross-section (STEM image); (d) composition depth profile; (f)–(i) X-ray maps of region (e).

The microstructure of the alumina scale formed exhibits a distinctive two-layer microstructure; see Figure 3. 5c. In the outer layer near the surface the grains are equiaxed whereas in the inner layer adjacent to the alloy the grains are columnar. The lateral grain size in the columnar layer is about 0.31 ± 0.10 µm; see Table 3. 2. The elemental mapping in Figure 3. 5e till i confirms that the oxide scale consists of only Al and O while the adjacent region has a higher Mo to Si ratio than the substrate and contains little Al.
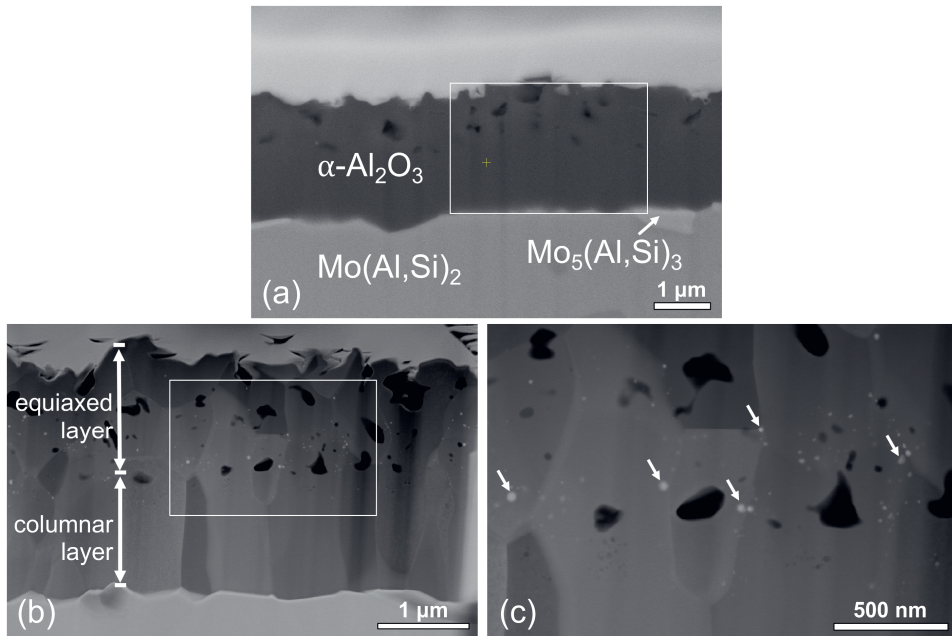

Figure 3. 6. SEM cross-section observation of the $Mo(Al_{0.65}Si_{0.35})_2$ after oxidation in low pO_2 (10^{-14} atm.) gaseous ambient at 1373 K for 16 hours: (a) cross-section (BSE image); (b) cross-section (STEM image) of the area indicated with the white frame in (a); (c) details (STEM image) of the area indicated with the white frame in (b). White arrows in (c) indicate particles of $Mo_5(Al,Si)_3$.

A composition depth profile confirms the presence of the different layers in the $Mo(Al_{0.40}Si_{0.60})_2$ alloy after oxidation; see Figure 3. 5d. The atomic ratio in the oxide scale represents the exclusive formation of Al_2O_3. The depletion layer composed of $Mo_5(Al,Si)_3$ contains 3.0 at.% Al, which is in agreement with the phase diagram at 1373 K (cf. Figure 3.

1b) and also with Ref. [18]. No Al gradient was observed within the $Mo_5(Si,Al)_3$ layer, suggesting that the diffusion of aluminium in this phase is rapid compared with rate of Al consumption as a result of alumina formation. In the $Mo(Si,Al)_2$ phase adjacent to the $Mo_5(Al,Si)_3$ layer also hardly an Al gradient occurs, which implies that also in the $Mo(Si,Al)_2$ phase the diffusion of Al is fast.

In a cross-section of the sample with the highest Al content, i.e., $Mo(Al_{0.65}Si_{0.35})_2$, an exclusive α-Al_2O_3 scale with the layered microstructure and small patches of $Mo_5(Al,Si)_3$ at the interface with the oxide scale were observed; see Figure 3. 6a and 3. 6b. The lateral grain size in the columnar layer is about 0.39 ± 0.20 µm; see Table 3. 2.

The small bright spots having a size of 10–30 nm seen in the STEM image of the alumina scale, see Figure 3. 6c, are likely composed of $Mo_5(Al,Si)_3$ according to XMA. Small pores can be observed in the equiaxed layer of the α-Al_2O_3 scale; see Figure 3. 5 and 3. 6.

The α-Al_2O_3 and $Mo_5(Al,Si)_3$ phases were also identified in XRD patterns recorded with Bragg-Brentano geometry; see Figure 3. 7. Comparing the XRD patterns before and after oxidation (cf. Figure 3. 3 and 3. 7), shows that transformation of $Mo(Al,Si)_2$ from the orthorhombic ($C54$) to the hexagonal ($C40$) crystal lattice structure occurred. This transformation can also be derived from the Mo–Al–Si phase diagram; viz.: the initial $Mo(Al,Si)_2$ phase with an orthorhombic crystal lattice structure at 1773 K lies in the three-phase region of $C40$, $Mo_5(Al,Si)_3$ and Mo_3Al_8 in the phase diagram at 1373 K when $x > 0.45$; see Figure 3. 1a and 3. 1b.

Table 3. 2. Parabolic growth rate constant (k_p) of the oxidation, thicknesses and lateral grain size of the oxide scale.

Isothermal oxidation	pO_2 (atm.)	Gas flow (sccm) *	Al_2O_3 thickness (µm)	k_p ($g^2m^{-4}h^{-1}$)	$h_{columnar}/h_{total}$ ** (-)	Lateral grain size (µm)
16 h low pO_2	10^{-14}	100	2.27 ± 0.11	0.66	0.48	0.31 ± 0.10
16 h low pO_2	10^{-14}	80	4.19 ± 0.14	0.45	0.37	0.49 ± 0.14
then 50 h dry syn. air	0.21			0.70		
50 h in syn. air	0.21	80	2.30 ± 0.33	0.25	0.34	0.33 ± 0.07

* A total gas flow of 80 sccm was applied for the oxidation experiment with dry synthetic air.

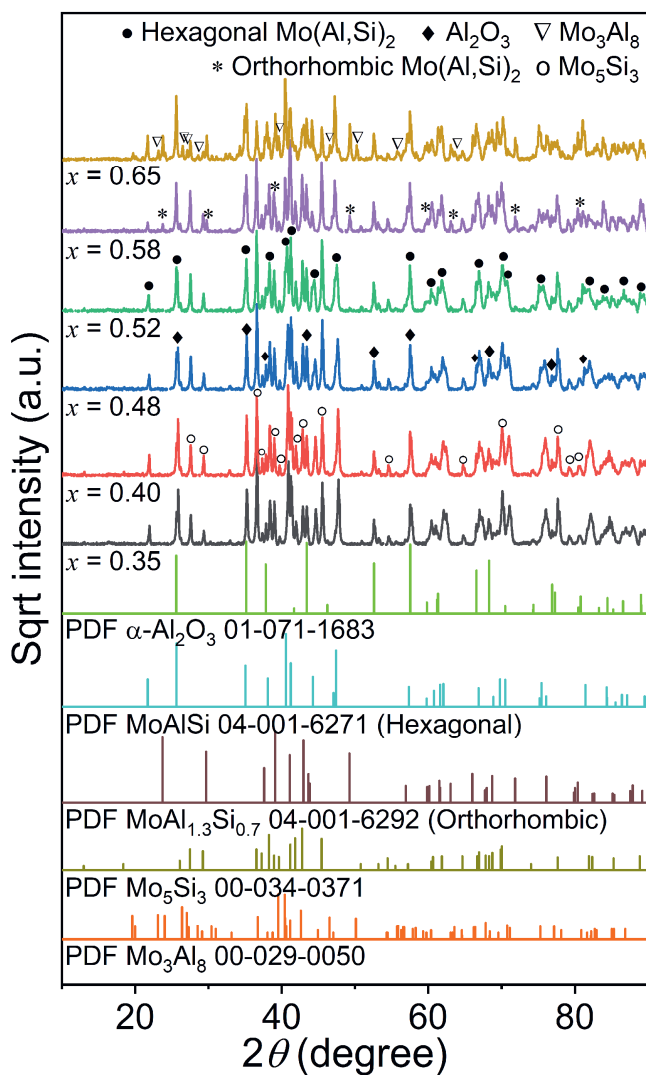**Thickness ratio of columnar layer to the total oxide scale.

3

Figure 3. 7. XRD patterns of Mo(Al$_x$Si$_{1-x}$)$_2$ after 16 hours oxidation in low pO$_2$ (10^{-14} atm.) gaseous ambient at 1373 K recorded with Bragg–Brentano geometry.

3.3.2.2. Oxidation kinetics

The weight gain per unit surface area of the $Mo(Al_xSi_{1-x})_2$ specimens recorded during oxidation at 1373 K in a gaseous ambient with a low pO_2 of 10^{-14} atm. is shown in Figure 3. 8a. Although the weight gain during this oxidation process is rather small, a slight dependence of the oxidation rate on the Al content of $Mo(Al_xSi_{1-x})_2$ is observed. The oxidation rate increases with increasing Al content of $Mo(Al_xSi_{1-x})_2$.
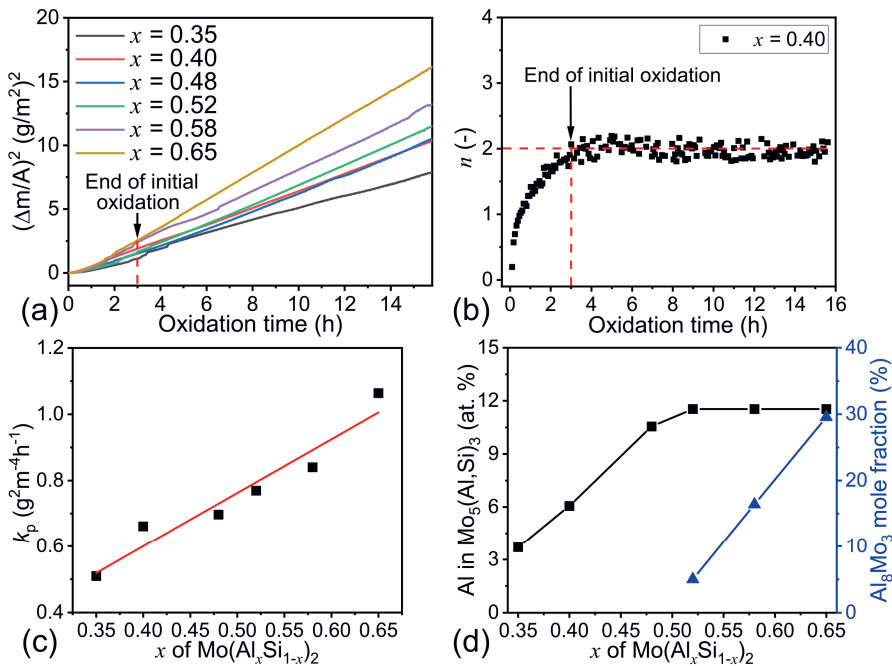

Figure 3. 8. (a) Thermogravimetric analysis of the oxidation of $Mo(Al_xSi_{1-x})_2$ in low pO_2 (10^{-14} atm.) gaseous ambient at 1373 K in terms of square weight gain per unit area $(\Delta m/A)^2$ versus oxidation time; (b) Change of the exponent n with time in a power law (cf. Eq. (3.1)); (c) parabolic growth rate constant k_p of the oxidation of $Mo(Al_xSi_{1-x})_2$ (red line: only to guide the eye); (d) Al fraction in the $Mo_5(Al,Si)_3$ (D8M) and the fraction of Al rich phase of Mo_3Al_8 after 16 hours oxidation as determined from the Mo–Al–Si phase diagram at 1373 K.

To describe the oxidation process quantitatively, the oxidation kinetics was formulated as a power law with exponent n:

$$\left(\frac{\Delta m}{A}\right)^n = k_m t \tag{3.1},$$

where Δm is the weight change; A is the surface area of the sample and t the isothermal oxidation time; k_m denotes the oxidation rate constant measured by thermogravimetric analysis. The exponent n versus time t can be derived from the mass change data with [31, 32]:

$$\frac{1}{n} = \frac{\partial(\log(\frac{\Delta m}{A}))}{\partial(\log(t))} \tag{3.2}.$$

Analysis of the exponent n as a function of oxidation time of the oxide growth curves shows that after an initial transient oxidation period of about 3 hours (practically independent of the Al content), the oxide growth proceeds with a steady state regime obeying a parabolic growth rate law; see Figure 3. 8b. In the case of exclusive scale formation and the scaling rate controlled by diffusion in the scale, the parabolic rate constant (k_p) can be derived from k_m. The parabolic rate constant (k_p) increases slightly with the increasing Al content of $Mo(Al_xSi_{1-x})_2$; see Figure 3. 8c.
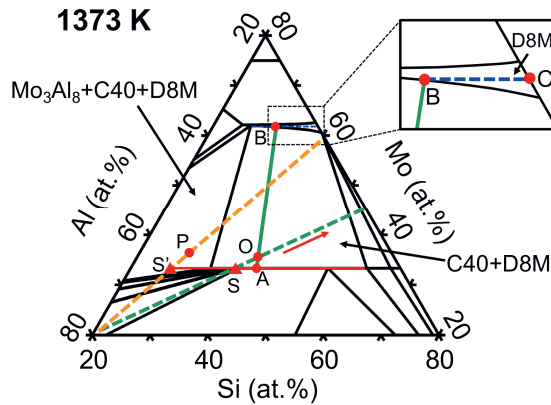

Figure 3. 9. Partial phase diagram of Mo–Si–Al system at 1373 K, where point S and S' are the starting compositions of $Mo(Al_{0.40}Si_{0.60})_2$ and $Mo(Al_{0.65}Si_{0.35})_2$ before oxidation, respectively; point O and P are the final compositions of $Mo(Al_{0.40}Si_{0.60})_2$ and $Mo(Al_{0.65}Si_{0.35})_2$ after oxidation; point A and point B are the compositions at Al-rich region and Al-poor region at the equilibrium of point O. $C40$ pertains to hexagonal $Mo(Al,Si)_2$ and D8M to $Mo_5(Al,Si)_3$.

After the initial transient oxidation period, a layer of $Mo_5(Al,Si)_3$ forms beneath the Al_2O_3 scale and the alloy composition changes along the dashed lines in Figure 3. 9. The phase constitution and composition can be derived from the tie-lines joining Al-rich region ($C40$) and Al-poor region (D8M); see Figure 3. 9. For those $Mo(Al_xSi_{1-x})_2$ alloys with $x < 0.5$, the alloy composition changes from a single phase position $Mo(Al_xSi_{1-x})_2$ with $C40$ crystal lattice to the two-phase region of $Mo(Al_xSi_{1-x})_2$ ($C40$) and $Mo_5(Al,Si)_3$ (D8M); while for those $Mo(Al_xSi_{1-x})_2$ alloys with $x > 0.5$, the composition changes from $Mo(Al_xSi_{1-x})_2$ with $C54$ crystal lattice (formed at 1773 K) into a three-phase region of $Mo(Al_xSi_{1-x})_2$ with $C40$ crystal lattice, Mo_3Al_8 and $Mo_5(Al,Si)_3$ after 16 hours oxidation at 1373 K. For the $Mo(Al_xSi_{1-x})_2$ alloys with $x < 0.5$, the Al content in the $Mo_5(Al,Si)_3$ phase increases with increasing x in $Mo(Al_xSi_{1-x})_2$ (see Figure 3. 8d). And for $Mo(Al_xSi_{1-x})_2$ alloys with $x > 0.5$, the fraction of Al rich phase of Mo_3Al_8 also increases with increasing x in $Mo(Al_xSi_{1-x})_2$ after 16 hours oxidation (see Figure 3. 8d), both of which will accelerate the supply of Al.

To observe the oxide morphology on the surface of the $Mo(Al_xSi_{1-x})_2$ alloys during the fast-initial oxidation state, a short term oxidation of $Mo(Al_{0.40}Si_{0.60})_2$ was executed at 1373 K in a low pO_2 (10^{-14} atm.) gaseous ambient for 1 hour. After this exposure, a discontinuous oxide scale with dimples was observed; see Figure 3. 10a and b. In these dimples a kind of 'filiform' oxide is seen; see Figure 3. 10c and d. The thickness of the oxide scale in the dimples vary between 200 and 400 nm, while the thickness of the continuous part of the oxide scale is about 1 μm; see Figure 3. 10e and f. The distance between the 'filiform' oxide is comparable with the width of the lateral grain size in the columnar layer. Therefore, the 'filiform' oxide is considered as the new oxide grown on top of the grain boundary of the columnar layer. These so-called 'grain boundary ridges' were also observed in wedge experiments with various types of alumina forming materials [33-36] and was considered as *prima-facie* evidence of oxide formed by outward diffusion of Al along grain boundaries [34].

3
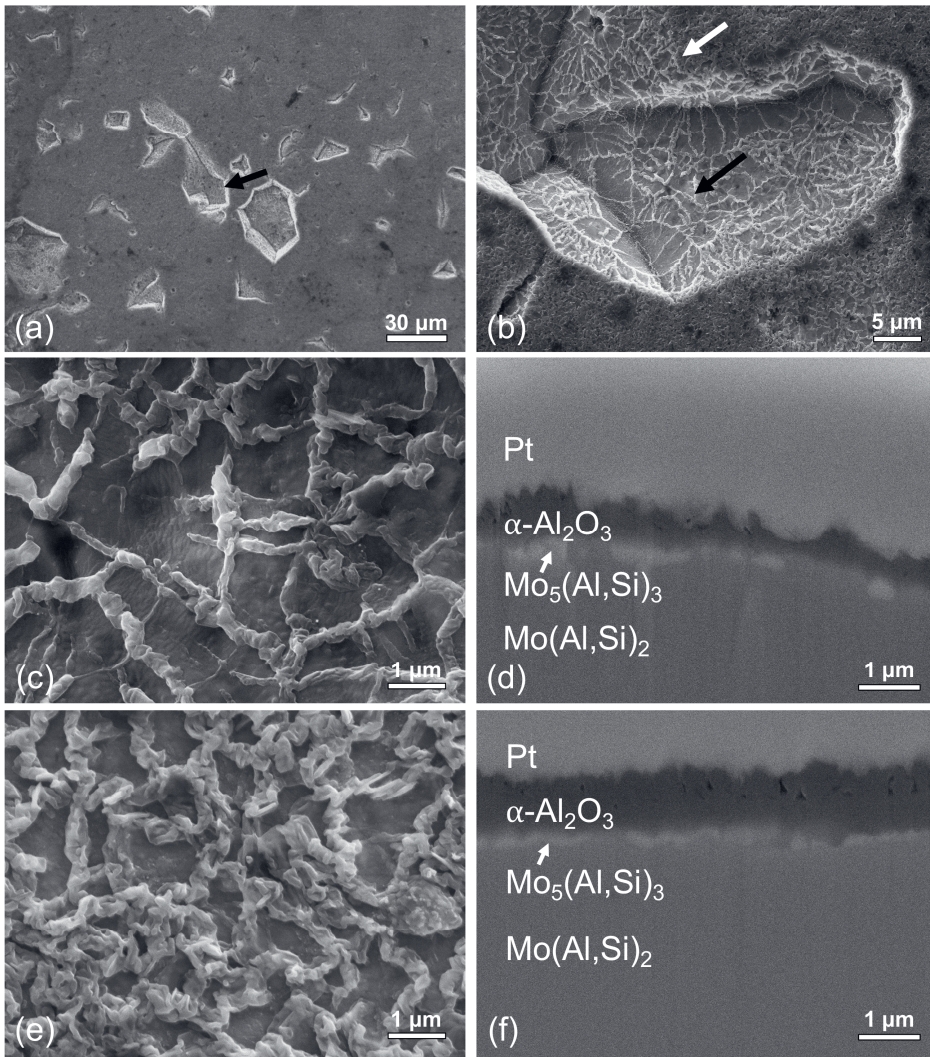
Figure 3. 10. Morphology of the $Mo(Al_{0.40}Si_{0.60})_2$ bulk material after a short term oxidation of 1 hour at 1373 K in low pO_2 (10^{-14} atm.) gaseous ambient: (a) SEM image of the surface; (b) detail image of the area indicated with the black arrow in (a); (c) detail image of the dimples indicated with the black arrow in (b); (d) cross-section of the dimples in (c); (e) detail image of the area indicated with the white arrow in (b); (f) cross-section of the area in (e).

3.3.2.3. Oxide scale growth mechanism

It is generally accepted that alumina growth relies on inward and outward diffusion, whereby the relative contributions depend on material, dopants, *etc*. [37, 38], whereas the oxidation of chromia formers, for example, the oxide scale is formed primarily by outward diffusion of the metal [34]. There are numerous examples that pointed out that grain-boundary transport of both aluminium and oxygen appears to be the rule in Al_2O_3 scale-forming Fe-base and Ni-base alloys and the donor or acceptor states of importance must be those associated with the grain boundaries and not with those of the crystal lattice [34, 36, 39].

The microstructure of the oxide scale on alumina forming alloys and compounds is columnar near the alloy/oxide interface, while equiaxed near the oxide/gas interface [32, 34-36, 40]. It has been shown by wedge experiments [33-36] that the two-layered microstructure of the grown Al_2O_3 scale is the result of a so-called "counter-diffusion process" along the grain boundaries, where the inner columnar layer is formed by epitaxial thickening of oxide grains due to inward diffusion of oxygen and the outer equiaxed layer is formed by new oxide growing on top of the grain boundaries of the columnar oxide with repeated coalescence and new oxide creation as a result of the outward diffusion of Al. In the case of $Mo(Al_xSi_{1-x})_2$, the same counter-diffusion mechanism is considered to be responsible for the two-layer microstructure of Al_2O_3 scale formed after oxidation at 1373 K in a low pO_2 gaseous ambient; see Figure 3. 5 and 3. 6.

The growth of an α-Al_2O_3 layer by selective oxidation of Al in an alloy relies on ionic and electronic transport. In what follows, defect notation of Kroger and Vink [41] is used, wherein the principal lattice species in Al_2O_3 are represented by $O_O^\times$ and $Al_{Al}^\times$.

For the scale growth dominated by inward oxygen transport (outward oxygen vacancies diffusion), i.e., the formation of the columnar layer, oxygen vacancies ($V_O^{\bullet\bullet}$) must be annihilated at the scale-gas interface [39] according to:

$$O_2 + 2V_O^{\bullet\bullet} \rightarrow 2O_O^\times + 4h^\bullet \tag{3.3}$$

and the growth of new oxide and consumption of substrate metal occurring at the scale-alloy interface follows [39]:

$$2Al_M \rightarrow 3V_O^{\bullet\bullet} + 2Al_{Al}^\times + 2V_{Al}' + 6e' \tag{3.4},$$
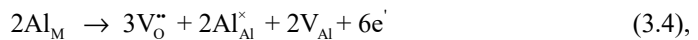
where Al_M and V_{Al} represent an Al atom and Al vacancy in the Mo–Al–Si alloy. In this case, new oxide develops at the scale-alloy interface and the created Al vacancies must be annihilated at the scale-alloy interface (see Eq. (3.4)), which is related to the recession of the scale-alloy interface during oxidation.

For the new oxide appearing at the scale-gas interface when outward Al transport (inward diffusion of Al vacancies) dominates, the defect reaction at scale-gas interface can be described as [39]:

$$3O_2 + 12e^{'} \rightarrow 4V_{Al}^{'''} + 6O_O^{\times} \tag{3.5},$$

while consumption of alloy at the scale-metal interface follows [39]:

$$Al_M + V_{Al}^{'''} \rightarrow Al_{Al}^{\times} + V_{Al} + 3e^{'} \tag{3.6}.$$
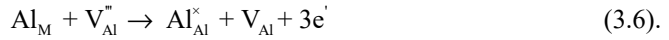
Similarly, vacancy sinks in the substrate must be available as Al vacancies (V_{Al}) are injected into the alloy substrate (Eq. (3.6)).

The α-Al_2O_3 oxide scale growth rate in the steady state stage (i.e., after the transient oxidation stage (see Figure 3. 8b) depends on the Al fraction x of the $Mo(Al_xSi_{1-x})_2$ alloy; see Figure 3. 8a and c. This is likely related to the scale/alloy interface concentration which increases with the Al content x of the $Mo(Al_xSi_{1-x})_2$ alloy. The Al activity as the driving force for transport across the scale strongly depends on the Al concentration. An increased activity of Al will result in an enhanced oxidation kinetics due to the accelerated annihilation of cation vacancies [39], cf. Eq. (3.4) and (3.6). The increase of the Al fraction in the $Mo_5(Al,Si)_3$ depletion layer adjacent to the α-Al_2O_3 oxide scale as a function of the Al fraction x of the $Mo(Al_xSi_{1-x})_2$ alloy (see Figure 3. 8d) points in this direction as well; see also Section 3.3.2.2.

3.3.3. High oxygen partial pressure and long-term oxidation

When exposing $Mo(Al_{0.40}Si_{0.60})_2$ bulk alloy in dry synthetic air for another 50 hours after low pO_2 pre-oxidation for 16 hours, a thickened exclusive α-Al_2O_3 scale is formed on the surface; see the XRD result in Figure 3. 11a and the cross section in Figure 3. 11b. After pre-oxidation in the low pO_2 ambient at 1373 K for 16 hours, the oxidation of the $Mo(Al_{0.40}Si_{0.60})_2$ in dry synthetic air proceeds similarly as during the pre-oxidation; see Section 3.3.2.3. The composition depth profile in Figure 3. 12a and b confirms that the oxide layer is composed of α-Al_2O_3 with adjacent a $Mo_5(Al,Si)_3$ depletion layer. The two-layered microstructure of the Al_2O_3 scale on $Mo(Al_{0.40}Si_{0.60})_2$ can still be observed; see Figure 3. 12c. The equiaxed

layer is significantly thickened and densified, while there is only a slight increase in the thickness of the columnar layer; see Table 3. 2. This indicates that the outward diffusion of aluminium ions becomes dominating over the inward diffusion of oxygen during the prolonged oxidation process in the high pO_2 gaseous ambient. A similar observation was also made in FeCrAl-based alloys that the Al outward flux contributes significantly to the oxide thickening [34]. After increasing the pO_2 from 10^{-14} to 0.21 atm. (dry synthetic air), the weight change shows a continuous steady state regime obeying a parabolic growth rate law; see Figure 3. 13.
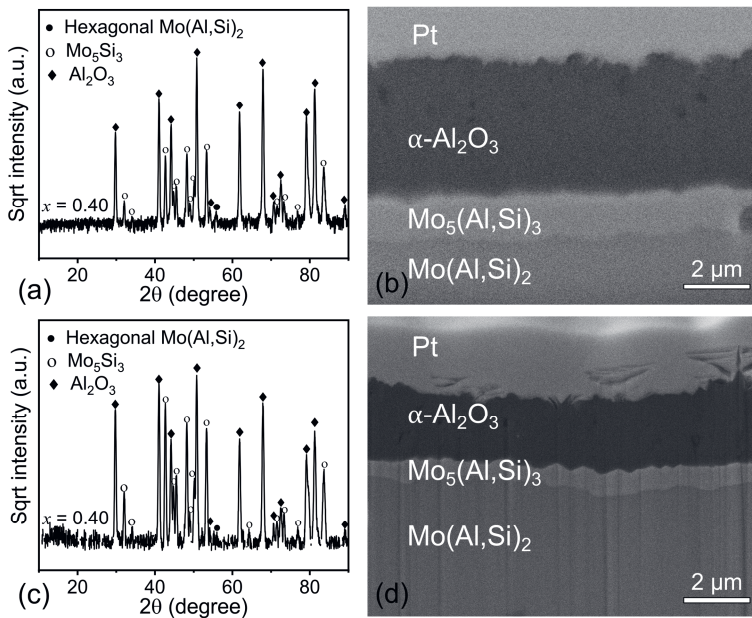

Figure 3. 11. (a) XRD pattern recorded with grazing incidence geometry; (b) cross-section of Mo(Al$_{0.40}$Si$_{0.60}$)$_2$ alloy material after oxidation resistance test (first pre-oxidation in low pO_2 (10^{-14} atm.) for 16 hours and then oxidation in dry synthetic air for 50 hours at 1373 K); (c) XRD pattern recorded with grazing incidence geometry; (d) cross-sectional morphology of Mo(Al$_{0.40}$Si$_{0.60}$)$_2$ bulk alloy after direct oxidation in dry synthetic air at 1373 K for 50 hours.

Direct exposure of the Mo(Al$_{0.40}$Si$_{0.60}$)$_2$ alloy to dry synthetic air (pO_2 is 0.21 atm.) for 50 hours, i.e., without pre-oxidation in low pO_2 ambient, also α-Al$_2$O$_3$ is exclusively formed. XRD analysis (Figure 3. 11c) and analysis of the cross section (Figure 3. 11d and Figure 3.

14b and 14c) confirm the formation of an exclusive α-Al$_2$O$_3$ scale with adjacent a Mo$_5$(Al,Si)$_3$ depletion layer. Again, the oxide scale exhibits an equiaxed layer on top of a columnar layer; see Figure 3. 14a. However, this oxide scale formed by direct exposure to dry synthetic air at 1373 K for 50 hours is thinner and denser than the oxide scale formed after first a pre-oxidation in a low pO_2 (10^{-14} atm.) gaseous ambient; cf. Figure 3. 11d and 3. 14a; see Table 3. 2. The fully dense oxide scale formed, i.e., the equiaxed grained layer without porosity, will effectively inhibit the diffusion process in the oxide scale and thus results in an overall reduction of the oxidation kinetics, which is supported by the lower weight gain and smaller parabolic rate constant (0.25 g^{2}m^{-4}h^{-1} direct exposure vs. 0.70 g^{2}m^{-4}h^{-1} with pre-oxidation); see Figure 3. 13 and Table 3. 2. Apparently, a closed α-Al$_2$O$_3$ layer is formed at the start of the oxidation preventing the development of volatile Mo-oxide species, because the lower mass gain (see Figure 3. 13) is not related to material loss but to a slower growth of the oxide scale. Hence, a pre-oxidation of the Mo(Al$_x$Si$_{1-x}$)$_2$ alloys is not required in practice.
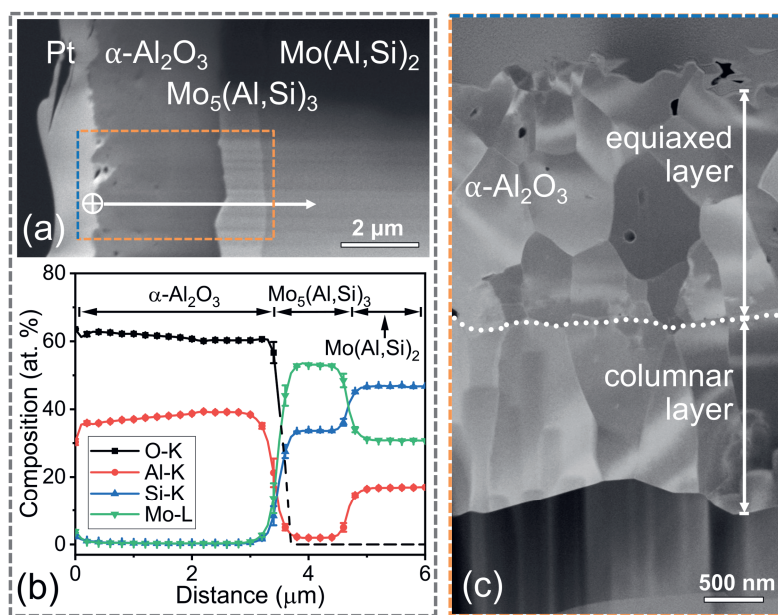

Figure 3. 12. (a) Position of the composition line scan across the oxide scale, Mo$_5$(Al,Si)$_3$ layer and Mo(Al,Si)$_2$ substrate after 66 hours oxidation (first pre-oxidation in low pO_2 of 10^{-14} atm. for 16 hours and then oxidation in dry synthetic air for 50 hours at 1373 K); (b) composition depth profile of Mo(Al$_{0.40}$Si$_{0.60}$)$_2$ bulk alloy after 66 hours oxidation; (c) cross-section (STEM image) of oxide scale on Mo(Al$_{0.40}$Si$_{0.60}$)$_2$ bulk alloy after 66 hours oxidation.
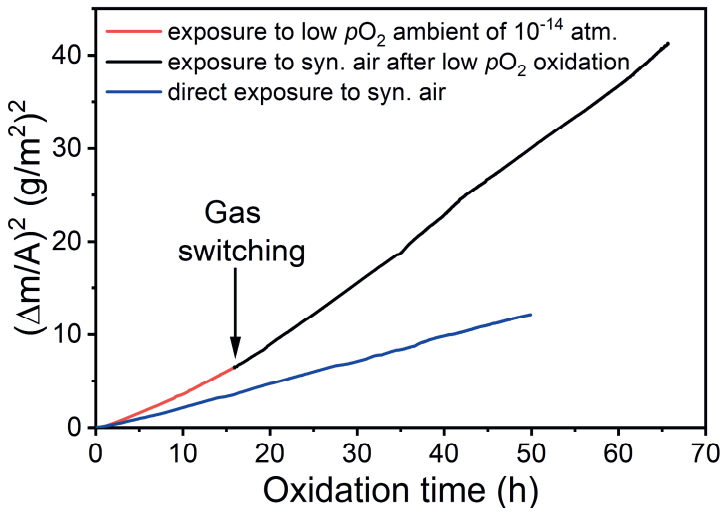
Figure 3. 13. Thermogravimetric analysis of the oxidation of $Mo(Al_{0.40}Si_{0.60})_2$ in terms of square weight gain per unit area $(\Delta m/A)^2$ versus oxidation time: first in low pO_2 atmosphere $(10^{-14}$ atm.) at 1373 K for 16 hours and then exposed to dry synthetic air for another 50 hours.

After exposure to dry synthetic air for 50 hours, the thickness ratio of the columnar layer to the total oxide scale (0.34) is smaller than that when exposed to low pO_2 ambient for 16 hours, 0.34 versus 0.48; see Table 3. 2. The dependence of the growth of the α-Al_2O_3 scale on the pO_2 of the gaseous ambient was demonstrated by a study of the oxygen permeability in non-doped polycrystalline Al_2O_3 wafers under steep pO_2 gradients [42-44]. It was shown that the α-Al_2O_3 scale exhibits a n-type ionic behaviour at the low pO_2 side and a p-type ionic behaviour at high pO_2 side, which is correlated with the growth of columnar and equiaxed grains, respectively [42-44]. The n-type behaviour prevails throughout the scale if oxidation occurs at a sufficiently low oxygen partial pressure [42, 43]. This explains the thicker columnar layer that was developed when oxidizing $Mo(Al_{0.40}Si_{0.60})_2$ in a low pO_2 ambient of 10^{-14} atm. as compared with oxidation of this alloy in dry synthetic air ($pO_2 = 0.21$ atm.).
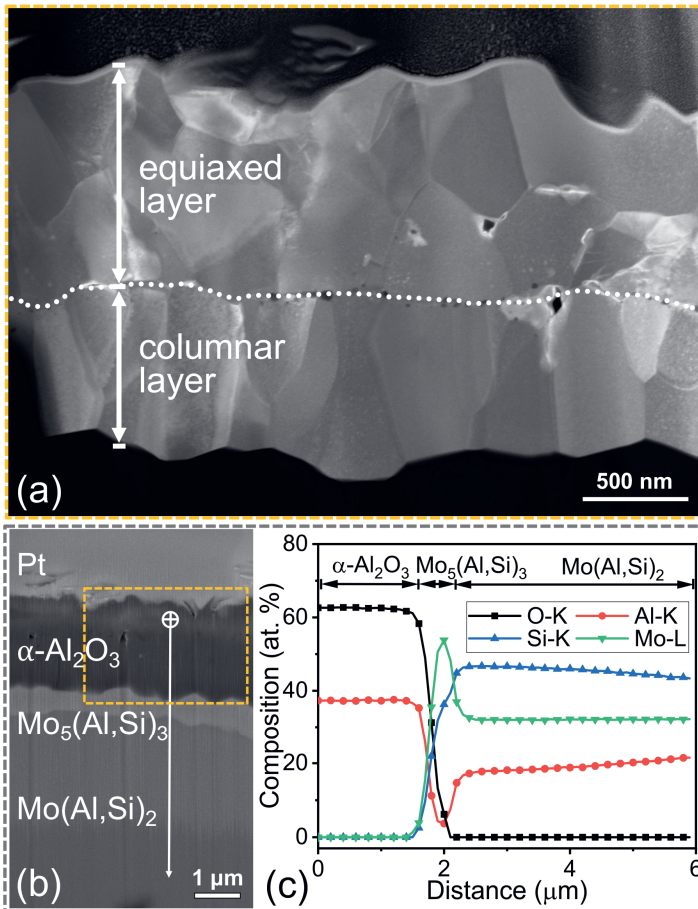
3

Figure 3. 14. (a) Cross-section (STEM image) of oxide scale on $Mo(Al_{0.40}Si_{0.60})_2$ bulk alloy after oxidation in dry synthetic air at 1373 K for 50 hours; (b) position of the composition line scan across the oxide scale, $Mo_5(Al,Si)_3$ layer and $Mo(Al,Si)_2$ substrate; (c) composition depth profile of $Mo(Al_{0.40}Si_{0.60})_2$ bulk alloy after oxidation in dry synthetic air at 1373 K for 50 hours.

3.4. Conclusions

$Mo(Al_xSi_{1-x})_2$ bulk alloys with Al content x varying from 0.35 to 0.65 were prepared by a one-step spark plasma sintering process at 1773 K. The crystal lattice changes from a hexagonal type $C40$ to a orthorhombic type $C54$ with increasing amount of Al substituting Si; i.e, x in $Mo(Al_x,Si_{1-x})_2$.

Upon thermal oxidation of the $Mo(Al_xSi_{1-x})_2$ alloys in low oxygen partial pressure atmosphere at 1373 K an oxide scale of exclusively α-Al_2O_3 was formed with adjacent an Al depleted layer consisting of $Mo_5(Al,Si)_3$. A two-layered structure was observed in the α-Al_2O_3 scale, where the outer layer near the surface consists of grains which are equiaxed whereas in the inner layer adjacent to the alloy the grains are columnar. Phase transformation from orthorhombic ($C54$) to hexagonal ($C40$) crystal lattice occurred due to Al depletion in the $Mo(Al,Si)_2$ as a result of the oxidation process.

The oxidation kinetics obeys an ideal parabolic growth rate law after a short transient oxidation period. The parabolic growth rate constant increased only slightly with the increasing Al content in the $Mo(Al_xSi_{1-x})_2$ alloy. A counter-diffusion process of O and Al along grain boundaries of the oxide scale is considered to be responsible for the growth of the α-Al_2O_3 scale. Dominant inward diffusion of oxygen results in a columnar layer in contact with the alloy, while dominant outward diffusion of Al along grain boundaries of the columnar layer results in formation of the equiaxed layer in contact with the gaseous ambient. During long-term exposure in dry synthetic air after a low oxygen partial pressure oxidation treatment of the $Mo(Al_xSi_{1-x})_2$ alloys, outward diffusion of Al contributes significantly to the oxide layer growth.

When the $Mo(Al_xSi_{1-x})_2$ alloys are exposed directly to dry synthetic air (high oxygen partial pressure), the α-Al_2O_3 scale is denser and grows slower as compared to oxidation in a low oxygen partial pressure gaseous ambient. The thickness ratio of the columnar layer to the total oxide scale is smaller than that when exposed to low oxygen partial pressure. Thereby, the formation of dense equiaxed α-Al_2O_3 layer contributes to excellent oxidation resistance. A low oxygen partial pressure pre-oxidation treatment is not required to mitigate the formation of volatile Mo-oxide species.

3

Appendix A

For a gas mixture of CO_2 and CO is used, the oxygen partial pressure pO_2 follows from the equilibrium:

$$CO + \frac{1}{2}O_2 \rightarrow CO_2 \qquad (A1),$$

with the standard Gibbs free energy expressed as [45]:

$$\Delta G^0 = -282420 + 86.8T \quad (J/mol) \qquad (A2),$$

where T is the temperature in degree Kelvin. Next, the pO_2 of the gas mixture is related to the ratio of the partial pressures of CO and CO_2, pCO and pCO_2 respectively, according to:

$$pO_2 = (\frac{pCO_2}{pCO})^2 \exp(\frac{2\Delta G^0}{RT}) \qquad (A3).$$

References

[1] T. Maruyama, K. Yanagihara, High temperature oxidation and pesting of Mo(Si,Al)$_2$, Materials Science and Engineering A (1997) 828-841.

[2] A.K. Vasudevan, A comparative overview of molybdenum disilicide composites, Materials Science and Engineering A 155 (1992) 1-17.

[3] T.C. Chou, T.G. Nieh, Mechanism of MoSi$_2$ pest during low temperature oxidation, Journal of Materials Research 8(1) (1993) 214 - 226.

[4] A.A. Sharif, A. Misra, J.J. Petrovic, T.E. Mitchell, Alloying of MoSi$_2$ for improved mechanical properties, Intermetallics 9 (2001) 869-873.

[5] J.J. Petrovic, Mechanical behavior of MoSi$_2$ and MoSi$_2$ composites, Materials Science and Engineering A 192/192 (1995) 31-37.

[6] R. Mitra, R.R. V.V., Effect of minor alloying with Al on oxidation behaviour of MoSi$_2$ at 1200 °C, Materials Science and Engineering A 260 (1999) 146-160.

[7] J.A. Lemberg, R.O. Ritchie, Mo-Si-B alloys for ultrahigh-temperature structural applications, Advanced Materials 24(26) (2012) 3445-80.

[8] M. Sundberg, G. Malmqvist, A. Magnusson, T. El-Raghy, Alumina forming high temperature silicides and carbides, Ceramics International 30(7) (2004) 1899-1904.

[9] I.M. Wolff, L.E. Iorio, T. Rumpf, S. P.V.T., J.H. Potgieter, Oxidation and corrosion behaviour of Fe–Cr and Fe–Cr–Al alloys with minor alloying additions, Materials Science and Engineering A 241 (1998) 264-276.

[10] B. Bakhit, J. Palisaitis, J. Thörnberg, J. Rosen, P.O.Å. Persson, L. Hultman, I. Petrov, J.E. Greene, G. Greczynski, Improving the high-temperature oxidation resistance of TiB$_2$ thin films by alloying with Al, Acta Materialia 196 (2020) 677-689.

[11] C.E. Ramberg, W.L. Worrell, Oxidation kinetics and composite scale formation in the system Mo(Al,Si)$_2$, Journal of the American Ceramic Society 85(2) (2002) 444-452.

[12] K. Yanagihara, T. Maruyama, K. Nagata, High temperature oxidation of Mo-Si-X intermetallics (X = Al, Ti, Ta, Zr and Y), Intermetallics 3 (1995) 243-251.

[13] T. Maruyama, K. Yanagihara, K. Nagata, High temperature of oxidation of intermetallic compounds of Mo(Si$_{1-x}$Al$_x$)$_2$, Corrosion Science 35 (1993) 939-944.

[14] K. Yanagihara, T. Maruyama, K. Nagata, Effect of third elements on the pesting suppression of Mo-Si-X intermetallics (X = AI, Ta, Ti, Zr and Y), Intermetallics 4 (1996) 133-139.

[15] A. Stergiou, P. Tsakiropoulos, A. Brown, The intermediate and high-temperature oxidation behaviour of Mo(Si$_{1-x}$,Al$_x$)$_2$, intermetallic alloys Intermetallics 5 (1997) 69-81.

[16] S. Majumdar, I.G. Sharma, S. Raveendra, I. Samajdar, P. Bhargava, In situ chemical vapour co-deposition of Al and Si to form diffusion coatings on TZM, Materials Science and Engineering: A 492(1-2) (2008) 211-217.

3

[17] L. Ingemarsson, K. Hellström, S. Canovic, T. Jonsson, M. Halvarsson, L.G. Johansson, J.E. Svensson, Oxidation behavior of a Mo(Si,Al)$_2$ composite at 900–1600 °C in dry air, Journal of Materials Science 48(4) (2012) 1511-1523.

[18] L. Ingemarsson, K. Hellström, L.G. Johansson, J.E. Svensson, M. Halvarsson, Oxidation behaviour of a Mo(Si,Al)$_2$ based composite at 1500 °C, Intermetallics 19(9) (2011) 1319-1329.

[19] T. Dasgupta, A.M. Umarji, Thermal properties of MoSi$_2$ with minor aluminum substitutions, Intermetallics 15(2) (2007) 128-132.

[20] J.B. Wachman, T.G. Scuderi, G.W. Cleek, Linear thermal expansion of aluminum oxide and thorium oxide from 100 to 1100 K, Journal of American Ceramic Society 45(7) (1962) 319-323.

[21] T. Tabaru, K. Shobu, M. Sakamoto, S. Hanada, Effects of substitution of Al for Si on the lattice variations and thermal expansion of Mo(Si,Al)$_2$, Intermetallics 12(1) (2004) 33-41.

[22] T. Tabaru, K. Shobu, H. Hirai, S. Hanada, Influences of Al content and secondary phase of Mo$_5$(Si,Al)$_3$ on the oxidation resistance of Al-rich Mo(Si,Al)$_2$-base composites, Intermetallics 11(7) (2003) 721-733.

[23] D.L. Bish, S.A. Howard, Quantitative phase analysis using the Rietveld method, Journal of Applied Crystallography 21(2) (1988) 86-91.

[24] J.T. Armstrong, Quantitative elemental analysis of individual microparticles with electron beam instruments, in: Electron Probe Quantitation, Springer US, Boston (1991) 261-315.

[25] P.E.A. Turchi, A.L. Landa, Thermodynamic database, lower length scale, part II: thermodynamic assessment of Al-Mo-Si-U (M3MS-12LL0602092), Lawrence Livermore National Laboratory Tech. Rep. LLNL-TR-603054, (2012).

[26] M.M. Opeka, I.G. Talmy, J.A. Zaykoski, Oxidation-based materials selection for 2000 ∘C+ hypersonic aerosurfaces: Theoretical considerations and historical experienc, Journal of Materials Science 39 (2004) 5887-5904.

[27] H. Li, L. Zhang, Q. Zeng, L. Cheng, Thermodynamic calculation of HfB$_2$ volatility diagram, Journal of Phase Equilibria and Diffusion 32(5) (2011) 422-427.

[28] R. Inoue, Y. Arai, Y. Kubota, Y. Kogo, K. Goto, Oxidation of ZrB$_2$ and its composites: a review, Journal of Materials Science 53(21) (2018) 14885-14906.

[29] T.J. Nijdam, L.P.H. Jeurgens, W.G. Sloof, Modelling the thermal oxidation of ternary alloys—compositional changes in the alloy and the development of oxide phases, Acta Materialia 51(18) (2003) 5295-5307.

[30] T.J. Nijdam, L.P.H. Jeurgens, W.G. Sloof, Promoting exclusive α-Al$_2$O$_3$ growth upon high-temperature oxidation of NiCrAl alloys: experiment versus model predictions, Acta Materialia 53(6) (2005) 1643-1653.

[31] G.M. Song, V. Schnabel, C. Kwakernaak, S. van der Zwaag, J.M. Schneider, W.G. Sloof, High temperature oxidation behaviour of Ti_2AlC ceramic at 1200 °C, Materials at High Temperatures 29(3) (2014) 205-209.

[32] D. Naumenko, B. Gleeson, E. Wessel, L. Singheiser, W.J. Quadakkers, Correlation between the microstructure, growth mechanism, and growth kinetics of alumina scales on a FeCrAlY alloy, Metallurgical and Materials Transactions A 38(12) (2007) 2974-2983.

[33] H.J. Yang, Y.T. Pei, J.T.M. De Hosson, Oxide-scale growth on Cr_2AlC ceramic and its consequence for self-healing, Scripta Materialia 69(2) (2013) 203-206.

[34] J.A. Nychka, D.R. Clarke, Quantification of aluminum outward diffusion during oxidation of FeCrAl alloys, Oxidation of Metals 63(5-6) (2005) 325-352.

[35] V.K. Tolpygo, D.R. Clarke, Microstructural evidence for counter-diffusion of aluminum and oxygen during the growth of alumina scales, Materials at High Temperatures 20(3) (2014) 261-271.

[36] A.H. Heuer, D.B. Hovis, J.L. Smialek, B. Gleeson, Alumina scale formation: a new perspective, Journal of the American Ceramic Society 94 (2011) s146-s153.

[37] W.J. Quadakkers, H. Holzbrecher, K.G. Briefs, H. Beske, Differences in growth mechanisms of oxide scales formed on ODS and conventional wrought Alloys, Oxidation of Metals 32 (1989) 67-88.

[38] J.L. Smialek, Oxygen diffusivity in alumina scales grown on Al-MAX phases, Corrosion Science 91 (2015) 281-286.

[39] A.H. Heuer, T. Nakagawa, M.Z. Azar, P.B. Hovis, J.L. Smialek, B. Gleeson, N.D.M. Hine, H. Guhl, H.S. Lee, P. Tangney, W.M.C. Foulkes, M.W. Finnis, On the growth of Al_2O_3 scales, Acta Materialia 61(18) (2013) 6670-6683.

[40] F.A. Golightly, F.H. Stott, G.C. Wood, The relationship between oxide grain morphology and growth mechanisms for Fe-Cr-Al and Fe-Cr-Al-Y alloys, Journal of the Electrochemical Society 126(6) (1979) 1035-1042.

[41] D.J. Young, High temperature oxidation and corrosion of metals, Elsevier2008.

[42] M. Wada, T. Matsudaira, S. Kitaoka, Mutual grain-boundary transport of aluminum and oxygen in polycrystalline Al_2O_3 under oxygen potential gradients at high temperatures, Journal of the Ceramic Society of Japan 119(11) (2011) 832-839.

[43] T. Matsudaira, M. Wada, T. Saitoh, S. Kitaoka, The effect of lutetium dopant on oxygen permeability of alumina polycrystals under oxygen potential gradients at ultra-high temperatures, Acta Materialia 58(5) (2010) 1544-1553.

[44] S. Kitaoka, T. Matsudaira, M. Wada, Mass-transfer mechanism of alumina ceramics under oxygen potential gradients at high temperatures, Materials Transactions 50(5) (2009) 1023-1031.

3

3

4.

Mo(Al$_x$Si$_{1-x}$)$_2$ healing particles for high temperature ceramics and encapsulation by selective oxidation of aluminium

Abstract

To prevent premature triggering of the healing reaction in Mo–Si containing self-healing thermal barrier coating system, an oxygen impenetrable shell (α-Al$_2$O$_3$) around the sacrificial healing particles (MoSi$_2$) is desired. Here an encapsulation method is presented through selective oxidation of Al in Mo(Al$_x$Si$_{1-x}$)$_2$ particles. Healing particles of Mo(Al$_x$Si$_{1-x}$)$_2$ is designed in terms of alumina shell thickness, particle size and fraction Al dissolved. By replacing Si by Al in MoSi$_2$ up to the maximum solubility ($x = 0.65$) a strong crack healing ability is maintained (relative volume expansion ≥ 40 %). The formed exclusive α-Al$_2$O$_3$, featuring a two-layered structure, results from a counter-diffusion process along the grain boundaries, and its oxidation kinetics fits well with the 3D diffusion-Jander model. After 16 hours exposure in gaseous ambient with a pO$_2$ of 5×10^{-10} atm. at 1100 ^{o}C, a closed and dense shell of α-Al$_2$O$_3$ is formed with a thickness of about 1.3 μm. The oxide shell produced under this condition provided healing particles with significantly improved stability upon exposure to high pO$_2$ of 0.2 atm. at 1100 ^{o}C for 50 hours. The particles after exposure feature an inner core of MoSi$_2$ with Al completely consumed and an oxide shell of α-Al$_2$O$_3$.

4

4.1. Introduction

Thermal barrier coatings (TBC) systems are applied on the metallic components to provide thermal insulation from the hot gas stream in gas-turbine and jet engines [1-5]. With the use of a TBC, the modern gas-turbine engines are enabled to operate at gas temperatures well above the melting temperature of the nickel- or cobalt-based structural superalloys (~1300 ^{o}C), thereby improving engine efficiency and performance [1-5]. Yttria Partially Stabilized Zirconia (YPSZ) is the most widely used ceramic for TBCs because of its low thermal conductivity at high temperatures (2.3 W·m^{-1}·^{o}C^{-1} at 1000 ^{o}C) in conjunction with high "strain tolerance" and chemical stability [1-5]. However, high stresses (2–6 GPa) are generated in these coatings when applied in *e.g.* gas turbine and jet engines where they are exposed to thermal cycles between operating and room temperature [1, 4]. These stresses arise due to the difference in thermal expansion coefficients (CTEs) of the ceramic coating of YPSZ (11–13 $\times$ 10^{-6} ^{o}C^{-1}) and the metal substrate (18–20 $\times$ 10^{-6} ^{o}C^{-1}) [5] and give rise to the formation of microcracks, which propagate and eventually coalesce, and ultimately leading to TBC spallation [1, 2, 4-10]. The Mo(Al$_x$Si$_{1-x}$)$_2$ particles are envisioned to be embedded in the bottom part of the TBC [7, 11] near the interface with the bond coating where delamination cracks usually initiate [12, 13].

A new self-healing TBC system was proposed to extend the lifetime [8, 9, 11, 14] and has been applied successfully in a real TBC system [7, 15, 16] based on the oxidation of boron doped molybdenum disilicide ($MoSi_2$-B) particles embedded in ZrO_2-based TBC [4, 7, 15]. When intercepted by cracks [8, 9], the $MoSi_2$ healing particles oxidize preferentially and lead to the formation of amorphous SiO_2, which fills the crack gap and establishes direct contact with the crack faces [4]. The amorphous SiO_2 subsequently reacts with the ZrO_2 of the matrix to form a load bearing $ZrSiO_4$ phase, whereby wetting of the crack faces is achieved [4, 17]. This prospective self-healing concept can be exploited to other high temperature structural ceramics as well [18, 19].

The concept of self-healing TBC involves creating an inert and oxygen impenetrable shell around the sacrificial healing particle ($MoSi_2$), which prevents premature triggering of the healing reaction [7, 15]. A shell composed of α-Al_2O_3 is the most promising, since this oxide is stable at high temperatures in an oxidizing environment and exhibit a very low permeability of oxygen compared to other oxides [20-22]. Moreover, the α-Al_2O_3 shell exhibits a close match of thermal expansion coefficient between the core material and α-Al_2O_3, viz.: 7.4–8.6 × 10^{-6} K^{-1} and 8.1–8.9 × 10^{-6} K^{-1}, respectively. The encapsulation of $MoSi_2$ particles with α-Al_2O_3 has been realized by a precipitation [23] and a sol-gel [24] method followed by a calcining process. Both these encapsulation methods are applicable prior to embedding the healing particles into the YPSZ matrix as for example when manufacturing a self-healing TBC by spark plasma sintering [15].

Here an alternative method, based on selective oxidation [25, 26] of Al in $Mo(Al_xSi_{1-x})_2$, is explored to encapsulate the $MoSi_2$ sacrificial particles for self-healing TBCs. This method has already been applied successfully when manufacturing a self-healing TBC by plasma spraying [7, 16]. The advantage of this encapsulation by selective oxidation of Al in $Mo(Al_xSi_{1-x})_2$ is that the alumina shell on the healing particle is directly formed at temperatures comparable to those during high temperature operation of TBCs [1]. When the $Mo(Al_xSi_{1-x})_2$, healing particles are embedded in YPSZ, the encapsulation can be performed *in-situ* by annealing the system in an appropriate ambient before applied in working conditions, since the YPSZ matrix is permeable for oxygen [17]. Moreover, TBCs usually are porous [1-5].

In this work, for the encapsulation of $Mo(Al_xSi_{1-x})_2$, healing particles is designed in terms of alumina shell thickness, particle size and fraction Al dissolved. The conditions for the selective oxidation of Al to form a dense α-Al_2O_3 shell such as temperature and oxygen partial pressure are determined based on thermodynamic and kinetic data.

4.2. Theory and experimental procedures

4.2.1. Selective oxidation of Al in Mo(Al$_x$Si$_{1-x}$)$_2$ particles

4.2.1.1. Composition and crystal structure

Mo(Al,Si)$_2$ appears with three different crystal lattice structures depending on the ratio of Al to Si ratio, which include: tetragonal (*C*11b), hexagonal (*C*40) and orthorhombic (*C*54) structures; see the Mo–Al–Si ternary phase diagram at 1500 ºC in Figure 4. 1a. MoSi$_2$ exhibits the tetragonal (*C*11b) crystal structure, which has a small solubility of Al (1.9 at.% at 1500 ºC). Further substitution of Si with Al results in Mo(Al,Si)$_2$ with a hexagonal (*C*40) crystal lattice structure, which exists over a wide composition range (up to about 30 at.% Al at 1500 ºC). Beyond this composition, Mo(Al,Si)$_2$ takes the orthorhombic (*C*54) crystal lattice structure.

4.2.1.2. Oxidation

4

The temperature of 1100 ºC at which the oxidation experiments are executed, is chosen in view of the application in thermal barrier coating systems [1, 27, 28]. In order to define the conditions for selective oxidation of Al of Mo(Al,Si)$_2$ at 1100 ºC, the stability of the constituting elements and their oxides as a function of the oxygen partial pressure in a gaseous ambient is considered; see Figure 4. 2. The oxygen partial pressure (*p*O$_2$) of 10^{-14} atm. lies just below the dissociation oxygen partial pressure of Mo-oxides at 1100 ºC, but far above the dissociation oxygen partial pressure of Si- and Al-oxides according to the metal/oxide stability diagrams; see Figure 4. 2a–d. SiO(g) exist as the highest vapor pressure of about 10^{-10} atm. with a *p*O$_2$ of 10^{-14} atm. in the gas ambient; see Figure 4. 2. During oxidation of Mo(Al,Si)$_2$ at 1100 ºC with a *p*O$_2$ of 10^{-14} atm., the solid oxide of MoO$_2$ cannot be formed and the vapour pressures of the volatile Mo-oxides are very low (less than 10^{-10} atm.). While the *p*O$_2$ of 5×10^{-10} atm. lies above the dissociation oxygen partial pressure of solid MoO$_2$ with the highest vapor pressure of gaseous (MoO$_3$)$_2$ is only about 10^{-6} atm. at 1100 ºC. However, once the surface of the alloy is covered with a close layer of either silica or alumina, volatile Mo-oxides will likely cease to form. Since the dissociation oxygen partial pressure of Al$_2$O$_3$ is much lower than that of SiO$_2$ (10^{-31} atm. versus 10^{-25} atm., see Figure 4. 2b and c), alumina will be formed preferentially.
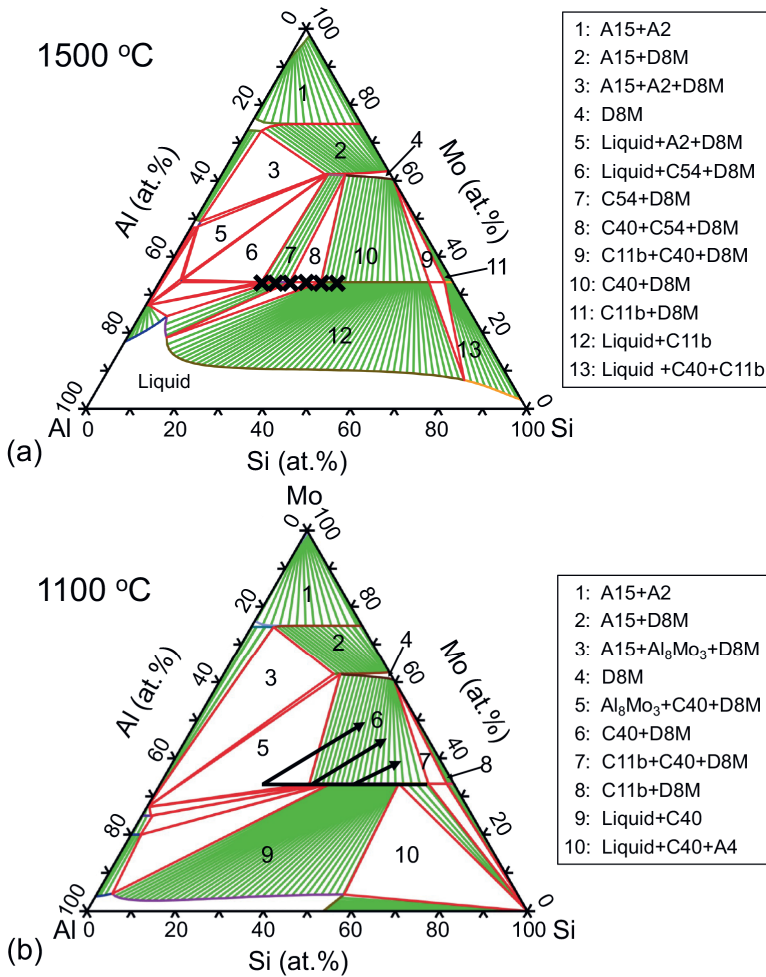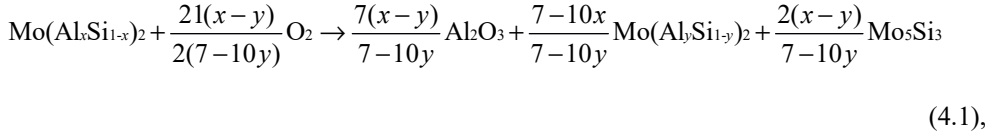
Figure 4. 1. Mo–Al–Si ternary phase diagram at (a) 1500 °C and (b) 1100 °C as calculated with Thermo-Calc software. The composition of the prepared alloys is indicated with crosses in (a) and the Al depletion paths upon oxidation are identified with arrows in (b). The $C11b$, $C40$ and $C54$ represent $Mo(Al,Si)_2$ having a tetragonal, hexagonal and orthorhombic crystal lattice, respectively. D8M is $Mo_5(Al,Si)_3$ with a tetragonal crystal lattice. A15 is $Mo_3(Al,Si)$ with a cubic crystal system, A2 is AlMo with a body-centered cubic crystal lattice, and A4 is Si with diamond crystal structure.

The selective oxidation of Al in Mo(Al,Si)$_2$, proceeds according to the following chemical reaction under a low pO_2 of 10^{-14} atm. at 1100 °C [29]:

$$Mo(Al_xSi_{1-x})_2 + \frac{21(x-y)}{2(7-10y)} O_2 \rightarrow \frac{7(x-y)}{7-10y} Al_2O_3 + \frac{7-10x}{7-10y} Mo(Al_ySi_{1-y})_2 + \frac{2(x-y)}{7-10y} Mo_5Si_3$$

(4.1),

where Mo(Al$_y$Si$_{1-y}$)$_2$ is the intermediate product with $y \leq x$. The Al depletion path according to this reaction (Eq. (4.1)) is identified in the Mo–Si–Al phase diagram at 1100 °C; see Figure 4. 1.
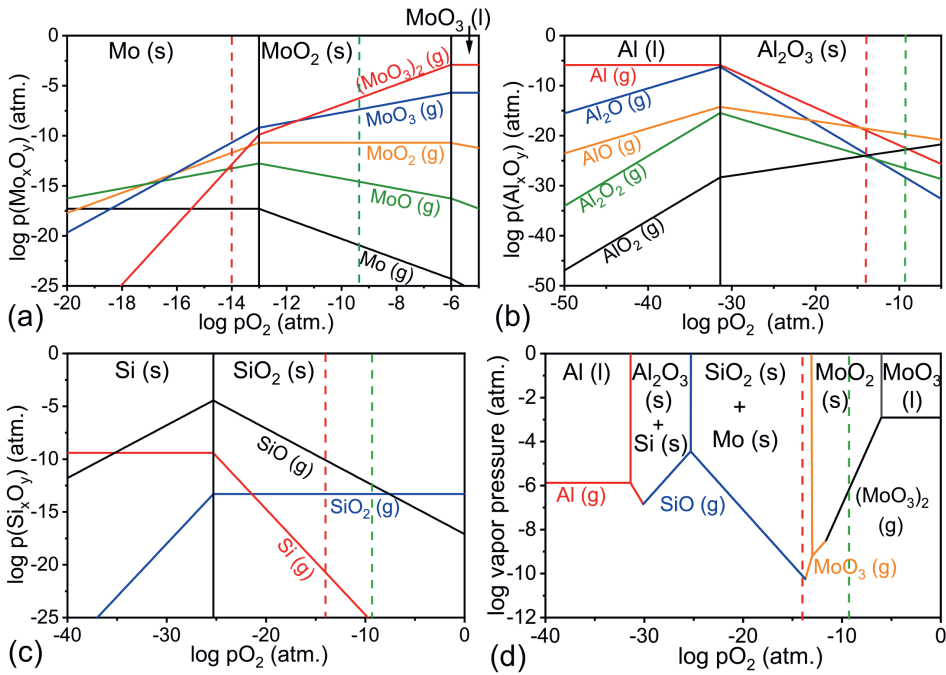

Figure 4. 2. Stability diagrams at 1100 °C for: (a) Mo–O; (b) Al–O; (c) Si–O; and (d) combined volatility diagram, illustrating the highest vapor pressure of the various gaseous species as a function of different pO_2. The dashed red and green lines indicate an oxygen partial pressure of 10^{-14} atm. and 5×10^{-10} atm., respectively.

4.2.1.3. Kinetics

The kinetics of selective oxidation of the $Mo(Al_xSi_{1-x})_2$ is described in terms of its conversion according to Eq. (4.1) expressed as:

$$\alpha = \frac{m_t - m_0}{m_\infty - m_0} \Rightarrow \alpha = \frac{\Delta m / m_0}{(m_\infty / m_0) - 1} \tag{4.2},$$

where α is the converted fraction as a function of time, m_0 denotes the initial mass, m_t is the mass at time t, and m_∞ is the mass after full conversion.

When all Al is consumed (i.e., $y = 0$), then according to Eq. (4.1) it holds that:

$$Mo(Al_xSi_{1-x})_2 + \frac{3x}{2}O_2 \rightarrow xAl_2O_3 + \frac{7-10x}{7}MoSi_2 + \frac{2x}{7}Mo_5Si_3 \tag{4.3}.$$
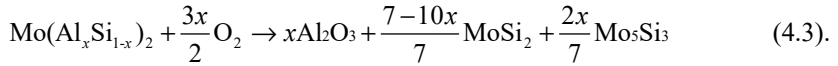
Hence:

$$m_\infty / m_0 = \frac{(\frac{7-10x}{7}M_{MoSi_2} + xM_{Al_2O_3} + \frac{2x}{7}M_{Mo_5Si_3})}{M_{Mo(Al_xSi_{1-x})_2}} \tag{4.4},$$

where M is the corresponding molar mass.

The rate of conversion into oxides upon thermal oxidation of the solid particles can be described with [30]:

$$\frac{d\alpha}{dt} = Ae^{-(\frac{E_a}{RT})}f(\alpha) \tag{4.5},$$

where, A is the pre-exponential factor of the Arrhenius relation, E_a is the activation energy (J/mol), T is the absolute temperature (K), R is the gas constant, $f(\alpha)$ represents the reaction model, and α is the fraction converted, which is derived from gravimetric measurements; see Eq. (4.2) and (4.4). Separating variables and integrating Eq. (4.5) gives the integral form of the isothermal rate law [30]:

$$g(\alpha) = kt \tag{4.6},$$

$$\text{where } g(\alpha) = \int_0^\alpha \frac{d(\alpha)}{f(\alpha)} \tag{4.7},$$

$$\text{and} \quad k = Ae^{(\frac{-E_a}{RT})} \tag{4.8},$$

in which $g(\alpha)$ is the integral reaction model and k being the rate constant. An experimental value for the rate constant k at different temperatures can be obtained from plotting $g(\alpha)$ versus t.

The appropriate reaction model can be ascertained by plotting the experimentally determined converted fraction α as a function of a reduced time variable t/t_α, where t_α is the time required to reach a specified conversion (e.g., $\alpha = 0.25$); the so-called reduced-time plot [30, 31]. Next, the experimental data are compared with theoretical reaction models [30], viz.: diffusion (D), Avrami-Erofeyev (A), order-based (F) or geometrical contraction (R) reaction models; see Table 4. 1 for the solid-state kinetic models and their integral expressions. The reaction model that resembles the experimental data best is selected.

Table 4. 1. Solid-state rate and integral expressions for the selected reaction models [30].

Model	Differential form $f(\alpha) = \dfrac{1}{k}\dfrac{d\alpha}{dt}$	Integral form $g(\alpha) = kt$
3-D diffusion – Jander (D3)	$[3(1-\alpha)^{2/3}]/[2(1-(1-\alpha)^{1/3}]$	$(1-(1-\alpha)^{1/3})^2$
Avrami-Erofeyev (A3)	$3(1-\alpha)[-\ln(1-\alpha)]^{2/3}$	$[-\ln(1-\alpha)]^{1/3}$
Third-order (F3)	$(1-\alpha)^3$	$(1/2)[(1-\alpha)^{-2}-1]$
Contraction volume (R3)	$3(1-\alpha)^{2/3}$	$1-(1-\alpha)^{1/3}$

4

4.2.2. Experimental procedures

4.2.2.1. Synthesis of Mo–Si–Al alloys

Single phase $Mo(Al_xSi_{1-x})_2$ alloys were prepared by a one-step sintering process. Elemental powder of molybdenum (2-5 μm 99.95+% purity, Chempur, Germany), silicon (45 μm 99.99% purity, TLS Technik GmbH, Germany) and aluminium (45 μm 99.8% purity, TLS Technik GmbH, Germany) were mixed in the desired molar ratios for 3 hours with a Turbula mixer (Willy A. Bachofen AG Maschinenfabrik, Type T2C, Switzerland) using ZrO_2 balls with a diameter of 5 mm. Next, the powder mixtures were densified and sintered in a spark plasma sintering (SPS) furnace (FCT SPS system, type KCE-FCT HP D-25-SI, Germany) at 1500 ºC with a heating rate of 20 ºC·min.$^{-1}$. A pressure of 50 MPa was applied till the temperature reached 600 ºC. Then, the pressure was released to avoid leakage of melted Al. When the temperature reached to 1500 ºC, the pressure of 50 MPa was applied

again to promote alloying and densification. The sample was kept for 30 min. at the sintering temperature and thereafter naturally cooled to room temperature.

The sintered $Mo(Al_xSi_{1-x})_2$ alloys exhibit crystal lattice changes from hexagonal type $C40$ to orthorhombic type $C54$ with increasing Al content; see Section 4.2.1. The actual composition and the phase fractions of the alloy bulk samples analysed with electron probe X-ray microanalysis (EPMA) and X-ray diffractometry (XRD) are listed in Table 4. 2.

Table 4. 2. Chemical composition and constituting phases of $Mo(Al_x,Si_{1-x})_2$ materials prepared by SPS.

Actual x	Al fraction[*] (at.%)	Phase fraction (wt%)	Crystal lattice (-)
0.35	23.5±0.5	H: 100.0	$C40$
0.40	26.4±0.4	H: 100.0	$C40$
0.48	31.9±0.1	H: 92.8	$C40$
		O: 7.2	$C54$
0.52	34.9±3.5	H: 5.4	$C40$
		O: 14.6	$C54$
0.58	38.9±0.3	H: 5.7	$C40$
		O: 90.2	$C54$
		T: 4.1	D8M
0.65	43.1±0.5	O: 92.7	$C54$
		T: 7.3	D8M

H: hexagonal $Mo(Al,Si)_2$; O: orthorhombic $Mo(Al,Si)_2$; T: tetragonal Mo_5Si_3; analysed by Rietveld refinement with MAUD software.

[*]As determined with EPMA, cf. Section 4.3.1.

4.2.2.2. Preparation of Mo(Al$_x$Si$_{1-x}$)$_2$ particles

After sintering, the discs (20 mm diameter and 3 mm thickness) were crushed with a Fritsch Pulverisette (type P-0150, Germany). Two different size fractions of the particles were prepared by sieving (Analysensieb, DIN-ISO 3310-1, Retsch, Germany), namely fine particles of size $D < 20$ μm and coarse particles of size $D > 20$ μm. The fine powder fraction was discarded due to the manufacturing constraints when using plasma spraying to fabricate the self-healing TBC [16]. Then, small particles will evaporate during plasma spraying and

large particles will not be melted. Moreover, small particles do not contain sufficient amount of Al for encapsulation; see Section 4.3.1. To polish away the sharp edges of the crushed particles with a size of $D > 20$ µm, a planetary ball mill (PM100, Retsch GmbH, Germany) was used. To this end, a 50 ml zirconia jar with 200 and 90 balls with diameters of 3 and 5 mm zirconia balls were used. As polishing medium SiC (99.8%, 1 µm, Alfa Aesar, Germany) was used and mixed with about 25 ml iso-propanol. Several batches of about 5.5 g of powder were milled with a rotation speed of 100 rpm for 100 minutes which was realized by cycles of milling and pause for 25 and 5 minutes, respectively. Next, the milled particles were washed with deionized water (Milli Q, 18.2 MΩ.cm at 25 °C) and sieved with a 20 µm mesh sieve to remove the fine particles and the milling media. The remaining particles were dried in an oven at 80 °C overnight. Then, the particles were passed through a 50 µm sieve to eliminate the coarse fraction. Finally, the particles with a size of $20 < D < 50$ µm were obtained. The morphology of the as prepared particles is shown in Figure 4. 3.
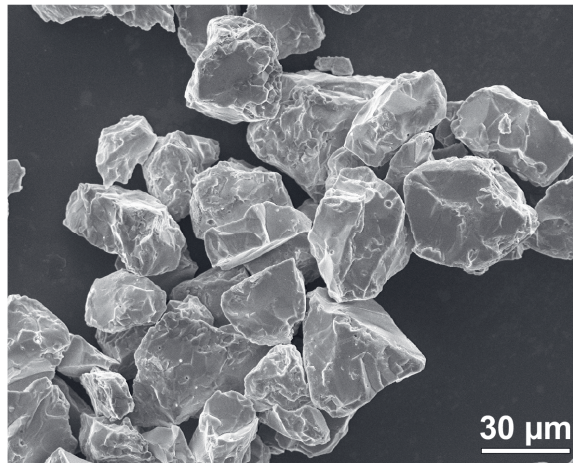

Figure 4. 3. SEM image showing morphology of the $Mo(Al,Si)_2$ particles after milling, sieving and polishing treatment.

4.2.2.3. Oxidation experiments

The $Mo(Al_xSi_{1-x})_2$ particles were oxidized in gas mixtures of Ar + 8 vol.% CO_2 + 50 vol.% CO and Ar + 95 vol.% CO_2 + 2.5 vol.% CO at 1100 °C, corresponding with oxygen partial pressures (pO_2) of 10^{-14} and 5×10^{-10} atm., respectively. Also, oxidation of the as-

prepared $Mo(Al_xSi_{1-x})_2$ particles was conducted in dry synthetic air. The kinetics of isothermal oxidation were monitored with thermogravimetric analysis (TGA) using a dual furnace balance (Seteram TAG 16/18, France), which allows automatic correction for buoyancy effects. The alumina furnace tubes have an inner diameter 15 mm. This analyser is equipped with Pt/Pt-10%Rh (S-type) thermocouples. The gas mixture was admitted to the TGA analyser via mass flow controllers (Bronkhorst, the Netherlands) operated with Labview (version 2020) such that the total gas flow matches 80 sccm[1] which was equally divided over both furnace tubes. The gases Ar, CO and CO_2 were supplied Linde Gas Benelux BV (purity better than 5N). Prior to admitting the gas mixture, Ar was filtered to remove any residual moisture and hydrocarbons, with an SGT click on oxygen trap (< 5 ppb O_2, SGT Middelburg, The Netherlands), Hydrosorb (< 20 ppb H_2O) and Accosorb (< 10 ppb hydrocarbons) filters (Messer Griesheim, Germany), respectively.

The as-prepared alloy particles were mixed with yttria partially stabilized zirconia (YPSZ, Amprit 827, H.C. Starck, Germany) with a mass ratio of 1:3 to avoid bonding and sintering at high temperature ensuring uniform oxidation of all particles in a 100 μL alumina crucible. The alumina crucible was first filled with about 50 mg of the free alloy particles using a Mettler Toledo mechanical balance (AG-204, Switzerland, accuracy ± 1 μg). Next, the YPSZ particles were added to the crucible until the total mass reached 200 mg. Then, this crucible with the powder mixture was placed onto a vibrator (Henry Schein, Vibrator L, Germany) to attain a homogeneous distribution of the particles. Finally, the crucible with the particles was mounted at one side of the TGA balance and an identical but empty crucible at the other side of the balance. To flush the gas lines, balance and furnaces, the TGA system was pumped to vacuum (< 50 Pa) and refilled with Ar, which was repeated three times. Thereafter, the dual furnaces were heated from room temperature to the target temperature with 10 °C·min.$^{-1}$, while purging with 80 sccm Ar, i.e., 40 sccm gas through each furnace. When the target temperature for isothermal oxidation was reached, the gas composition was switched to the oxidation atmosphere (see above) while maintaining a total gas flow of 80 sccm for 16 hours. After oxidation, the furnace was cooled to room temperature with 20 °C·min.$^{-1}$ while flushing with pure Ar.

With the same procedure as described above, isothermal oxidation of the particles at different temperatures, i.e., 1050 and 1075 °C, were performed in order to evaluate the activation energy of oxidation with pO_2 of 10^{-14} and 5×10^{-10} atm., respectively. The

---

[1] standard cubic centimetres per minute

Mo(Al$_x$Si$_{1-x}$)$_2$ particles were oxidized in gas mixtures of: Ar + 21 vol.% CO$_2$ + 50 vol.% CO at 1050 ºC and Ar + 13 vol.% CO$_2$ + 50 vol.% CO at 1075 ºC corresponding to a pO_2 of 10^{-14}, and Ar + 97.9 vol.% CO$_2$ + 1.06 vol.% CO at 1050 ºC and Ar + 96.7 vol.% CO$_2$ + 1.7 vol.% CO at 1075 ºC corresponding to a pO_2 of 5 × 10^{-10} atm.

The high temperature stability of the encapsulated particles (with a low pO_2 oxidation) was investigated by exposure to a high pO_2 (Ar with 20 vol.% O$_2$) at 1100 ºC. For this purpose, TGA was employed as well. When the encapsulation in Ar/CO/CO$_2$ atmosphere was completed, the gas was switched directly to Ar + 20 vol.% O$_2$, for another 50 hours. Finally, the furnace was cooled to room temperature in pure Ar.

4.2.2.4. Characterization

The phase composition of the materials was determined with X-ray diffractometry (XRD) using a D8 advance diffractometer (Bruker, Germany) operated with Cu Kα radiation. Particles were deposited on a Si-$\langle 510 \rangle$ single crystal wafer (University Wafer, USA). Diffractograms were recorded in the 2θ range of 10 to 110° with a 2θ step size of 0.030° and a counting time per step of 2 s. These diffractograms were evaluated using the Bruker Diffrac EVA software (version 3.1).

The microstructure and the morphology of the particles was observed with scanning electron microscopy (SEM) using a JEOL JSM 6500F (JEOL, Japan). This instrument is equipped with an ultra-dry energy dispersive spectrometer (EDS) for X-ray micro analysis (XMA) using System 7, Thermo Fisher Noran, USA. In addition, SEM combined with a xenon plasma focused ion beam (Helios G4 PFIB UXe, Thermo Fisher Scientific, USA) was performed to create cross-sections of the oxidized particles. This instrument is equipped with an EDAX system for energy dispersive X-ray micro analysis (XMA) with an Octane Elite plus detector, using TEAM acquisition and analysis software (version 4.5). First, the particles to be investigated were placed on a single crystal silicon wafer (Si-$\langle 001 \rangle$ p-type, University Wafer, USA). Subsequently, one of the particles was covered with about 2 µm layer of Pt doped with C. Then, the particle was cut with the xenon plasma focused ion beam (PFIB) operated at 30 keV. Finally, the surface of the particle cross-section was polished with a low current Xe ion beam. Transmission electron microscopy (TEM) lamella from selected area in the oxide scale prepared with the plasma focused ion beam were lifted. The grain morphology was observed with scanning transmission electron microscopy (STEM) within the dual beam microscope (Helios G4 PFIB UXe, Thermo Fisher Scientific, USA) operated

4

with a 30 keV electron beam. Subsequently, the thin lamellas were analysed with TEM using a JEOL JEM-1400 plus (JEOL, Japan) operated with a 120 keV electron beam.

4.3. Results and discussion

4.3.1. Design of Mo(Al$_x$Si$_{1-x}$)$_2$ as healing particles

It is conceived that by oxidation of Mo(Al$_x$Si$_{1-x}$)$_2$ a closed shell of alumina (α-Al$_2$O$_3$) with a core of Mo–Si will be formed. For the application on hand, design of these particles is prerequisite.

4.3.1.1. Shell thickness

Assuming that the Mo(Al$_x$Si$_{1-x}$)$_2$ particle has a spherical shape with a diameter d, the Al$_2$O$_3$ shell has a uniform thickness δ and considering that all Al is consumed by selective oxidation, then the thickness of the alumina shell can be calculated according to [7]:

$$\delta = \frac{d}{2}\left[(1+\frac{xM_s\rho_p}{M_p\rho_s})^{\frac{1}{3}} - 1\right]$$

(4.9),

where M_p and M_s denote the molecular weights, ρ_p and ρ_s the densities of the particle and the shell, respectively.

The explicit relation between the alumina shell thickness δ and the diameter d of the healing particle is displayed in Figure 4. 4a for different fractions x of Al. When applying a TBC with plasma spraying, the diameter of the healing particle should be about 20 to 50 μm due to manufacturing constraints [16, 32-34]. For example, when targeting for a minimum alumina shell thickness of 1 μm by full Al depletion of the particles with a diameter of 30 μm, then the minimum Al fraction x according to Eq. (4.9) should be 0.2; see Figure 4. 4a.
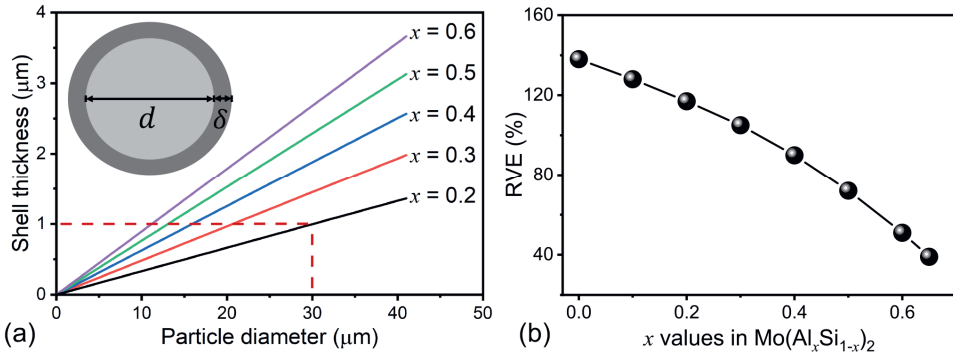
Figure 4. 4. (a) Relationship between the alumina shell thickness and the size of $Mo(Al_xSi_{1-x})_2$ spherical healing particle for different compositions; (b) relationship between the Al content in $Mo(Al,Si)_2$ and the relative volume expansion in the healing reaction.

4.3.1.2. Volume expansion

After alloying $MoSi_2$ with Al by replacing Si, part of the volume expansion associated with the healing reaction is sacrificed. The relative volume expansion (RVE) of the healing particle, after all the Al is consumed by selective oxidation of $Mo(Al_xSi_{1-x})_2$, cf. Section 4.2.1, can be estimated by considering the oxidation induced healing reaction:

$$(7-10x)MoSi_2 + 2xMo_5Si_3 + (49-28x)O_2(g) \rightarrow 7MoO_3(g) + (14-14x)SiO_2 \quad (4.10).$$
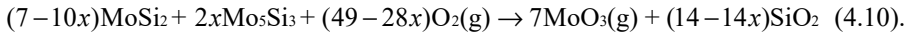
Then, for associated relative volume expansion can be written:

$$RVE = \left[\frac{(14-14x)V_{SiO_2}}{(7-10x)V_{MoSi_2} + 2xV_{Mo_5Si_3}} - 1 \right] \times 100\% \quad (4.11),$$

where V_{SiO_2} is the molar volume of 28.9 cm^3 for amorphous SiO_2, $V_{Mo(Al,Si)_2}$ of 24.3 cm^3 for $Mo(Al,Si)_2$ and $V_{Mo_5Si_3}$ of 68.8 cm^3 for Mo_5Si_3. Although the RVE decreases with increasing Al content, the oxidation reaction still exhibits a large positive volume expansion, i.e., RVE $\geqslant$ 40 % for $x \leqslant 0.65$, which indicates a strong healing ability; see Figure 4. 4b.

4.3.2. Direct exposure of Mo(Al,Si)₂ particles to dry air at 1100 °C

When particles with the composition of $Mo(Al_{0.40}Si_{0.60})_2$ are exposed to dry synthetic air at 1100 °C for 16 hours, the oxidation results in a rather porous oxide scale; see Figure 4. 5a. Besides Al_2O_3 also SiO_2 is formed according to XMA. Initially, a rapid mass gain was recorded, which is associated with the formation of both Al_2O_3 and SiO_2; see Figure 4. 5b. However, the predicted mass gain for full oxidation of Al according to Eq. (4.1) is much larger than recorded as indicated in Figure 4. 5b, which suggests that the mass change is accompanied by the formation of volatile MoO_3 [35]; cf. Figure 4. 2. Subsequently, the mass loss due to the formation of volatile MoO_3 was recorded. Thus, the porous oxide shell structure does not protect the core of the particle from oxidation. Hence, oxidation in a low pO_2 ambient as a precursor for the formation of an exclusive Al_2O_3 scale was performed. In the sequel, the results of this work are reported.

It is noted that the oxidation behaviour of the particle is completely different compared with oxidation of bulk $Mo(Al_{0.40}Si_{0.60})_2$ under the same conditions [36]. Then, a closed and protective scale of α-Al_2O_3 is formed under these conditions. In that case the 'reservoir' of Al is virtually infinite and the diffusion of Al in the alloy is sufficiently fast.
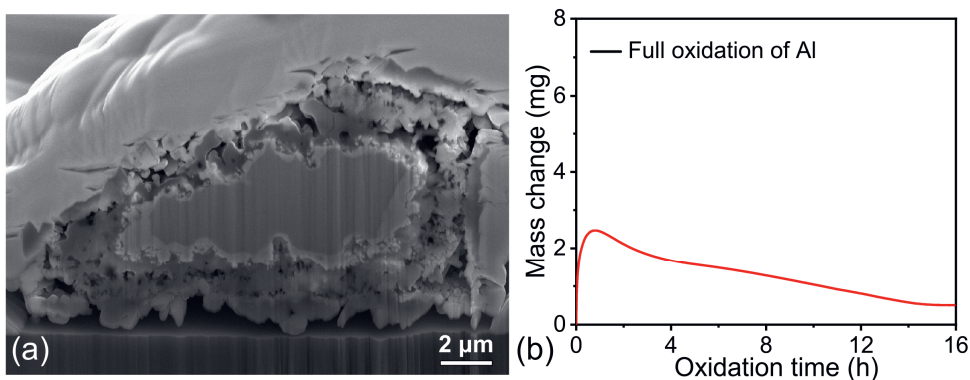

Figure 4. 5. $Mo(Al_{0.40}Si_{0.60})_2$ particle after oxidation in Ar with 20 vol.% O_2 at 1100 °C for 16 hours: (a) SEM image of a cross-section; (b) mass change. The mass gain corresponding with full oxidation of Al only is indicated.

4.3.3. Encapsulation of Mo(Al$_x$Si$_{1-x}$)$_2$ particles by oxidation with low pO_2

The X-ray diffraction patterns of the Mo(Al$_x$Si$_{1-x}$)$_2$ particles mixed with YPSZ granules after oxidation at 1100 ºC with a pO_2 of 10^{-14} atm. and 5×10^{-10} atm. for 16 hours are shown in Figure 4. 6a and Figure 4. 6b, respectively. Although peaks from YPSZ are dominant in the patterns, lines pertaining to α-Al$_2$O$_3$ and Mo$_5$Si$_3$ were identified. These two phases are the result of thermal oxidation of the Mo(Al$_x$Si$_{1-x}$)$_2$ particles. Also remanent Mo(Al$_x$Si$_{1-x}$)$_2$ was recognized in the XRD patterns. However, this phase exhibits a hexagonal crystal lattice. Thus, the initially present orthorhombic Mo(Al$_x$Si$_{1-x}$)$_2$ phase in the high Al containing particles (cf. Table 4. 2) is transformed into hexagonal Mo(Al$_x$Si$_{1-x}$)$_2$ due to Al depletion upon high temperature oxidation.

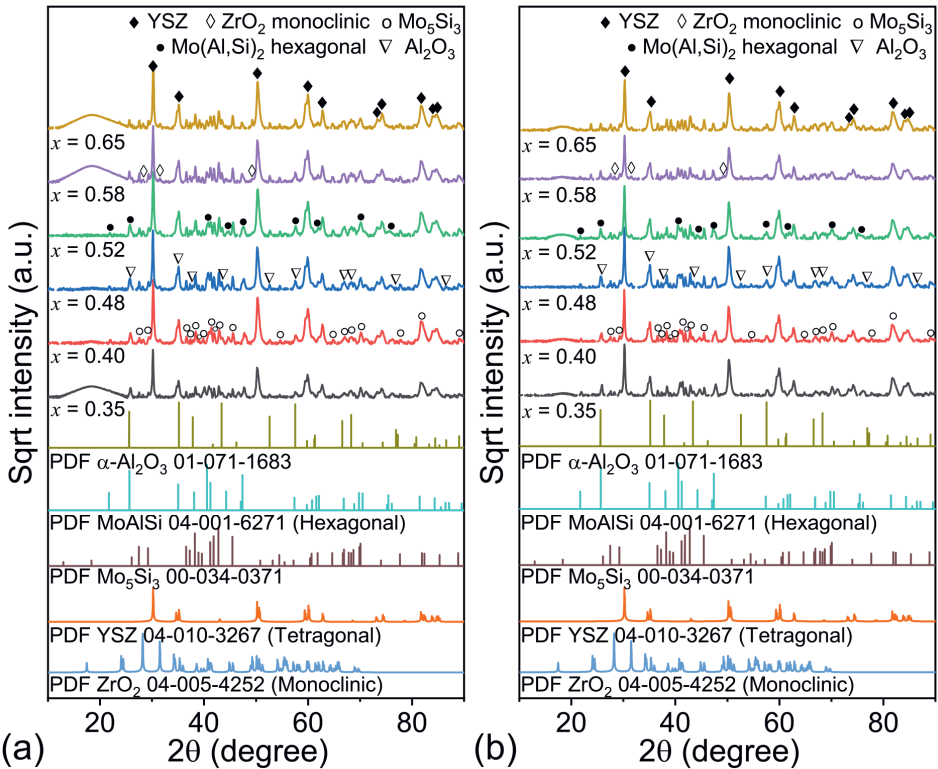
Figure 4. 6. XRD patterns of the Mo(Al$_x$Si$_{1-x}$)$_2$ free particles mixed with YSZ after oxidation with an oxygen partial pressure of (a) 10^{-14} atm. and (b) 5×10^{-10} atm. at 1100 ºC for 16 hours.

4. Mo(Al$_x$Si$_{1-x}$)$_2$ healing particles for high temperature ceramics and encapsulation by selective oxidation of aluminium

All Mo(Al$_x$Si$_{1-x}$)$_2$ particles with different Al content features the same surface morphology after oxidation at 1100 °C with a pO$_2$ of 10^{-14} atm. for 16 hours. As an example, the surface morphology of a free particle covered with thermally grown oxide is shown in Figure 4. 7. The oxide scale is exclusively composed of α-Al$_2$O$_3$ according to XMA and XRD. Two different oxide morphologies can be observed (see Figure 4. 7a): flaky oxides forming network shaped ridges (see Figure 4. 7b), and in between compact oxides (see Figure 4. 7c). The particles are fully covered with an alumina shell with a thickness of about 0.8 ± 0.3 μm after oxidation at 1100 °C with a pO$_2$ of 10^{-14} atm. for 16 hours, as can be seen in a cross section of a free particle; see Figure 4. 8a. The Al depletion layer composed of Mo$_5$(Al,Si)$_3$ adjacent to the alumina layer can also be observed; see Figure 4. 8b. A composition depth profile confirms the presence of the different layers from the surface to the core of the particles after oxidation in the low pO$_2$ ambient at 1100 °C for 16 hours; see Figure 4. 8c. The atomic ratio in the oxide scale represents the exclusive formation of Al$_2$O$_3$. The Mo$_5$(Al,Si)$_3$ depletion layer contains about 3.6 at.% Al, while the core contains still high Al fraction; cf. Figure 4. 8c. The formation of Mo$_5$(Al,Si)$_3$ phase is due to the oxidation reaction of Al at the alloy/gas interface, viz. Eq. (4.1), which is consistent with the depletion path indicated in Figure 4. 1b, and the content of Al in the Mo$_5$(Al,Si)$_3$ depletion layer is in agreement with the Mo–Al–Si phase diagram at 1100 °C; see Figure 4. 1b. The microstructure of the alumina scale formed exhibits a two-layer microstructure; see Figure 4. 8d. A thin layer of columnar grains is grown adjacent to the core of the particle, while a layer of equiaxed grains is formed at the surface in contact with the gaseous ambient. A combination of selected-area electron diffraction patterns (SAEDPs, Figure 4. 8e) and X-ray elemental mapping (Figure 4. 8f) confirms the exclusive formation of a continuous α-Al$_2$O$_3$ layer encapsulating the Mo(Al$_x$Si$_{1-x}$)$_2$ particles.
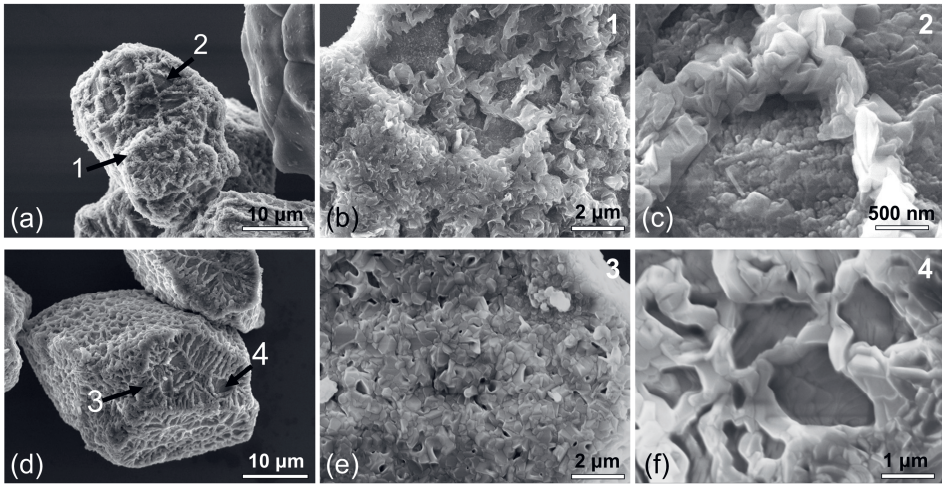
4

Figure 4. 7. SEM images showing morphology of a Mo(Al$_{0.40}$Si$_{0.60}$)$_2$ particle after oxidation with an oxygen partial pressure of (a)–(c) 10^{-14} atm. and (d)–(f) 5×10^{-10} atm., both at 1100 ºC for 16 hours: (a) a whole particle; (b) flaky oxide location indicated with arrow 1 in (a); (c) compact oxide location indicated with arrow 2 a in (a); (d) a whole particle; (e) flaky oxide location indicated with arrow 3 in (c); (f) compact oxide location indicated with arrow 4 in (c).

4

Figure 4. 8. Cross-section of Mo(Al$_{0.40}$Si$_{0.60}$)$_2$ particle after oxidation with an oxygen partial pressure of 10^{-14} atm. at 1100 °C for 16 hours: (a) SEM image; (b) detail BSE image of the shell and adjacent matrix of the particle with α-Al$_2$O$_3$ being the oxide shell, Mo$_5$(Al,Si)$_3$ being the depleted layer and Mo(Al,Si)$_2$ being the core; (c) composition profile along the path indicated by the red arrow in (f); (d) STEM image of the oxide shell of α-Al$_2$O$_3$ (the dotted curve is to distinguish the grain morphologies in the upper and lower part of the oxide shell). The lower part of the oxide shell exhibits an equiaxed grain morphology and the upper part has columnar grains, which correspond to Al outward-diffusion dominant and O inward-diffusion dominant growth, respectively; (e) selected-area electron diffraction pattern (SAEDP) of corresponding area indicated in (d); (f) X-ray emission maps of O, Al, Si and Mo, respectively; location indicated with the frame box in (a).
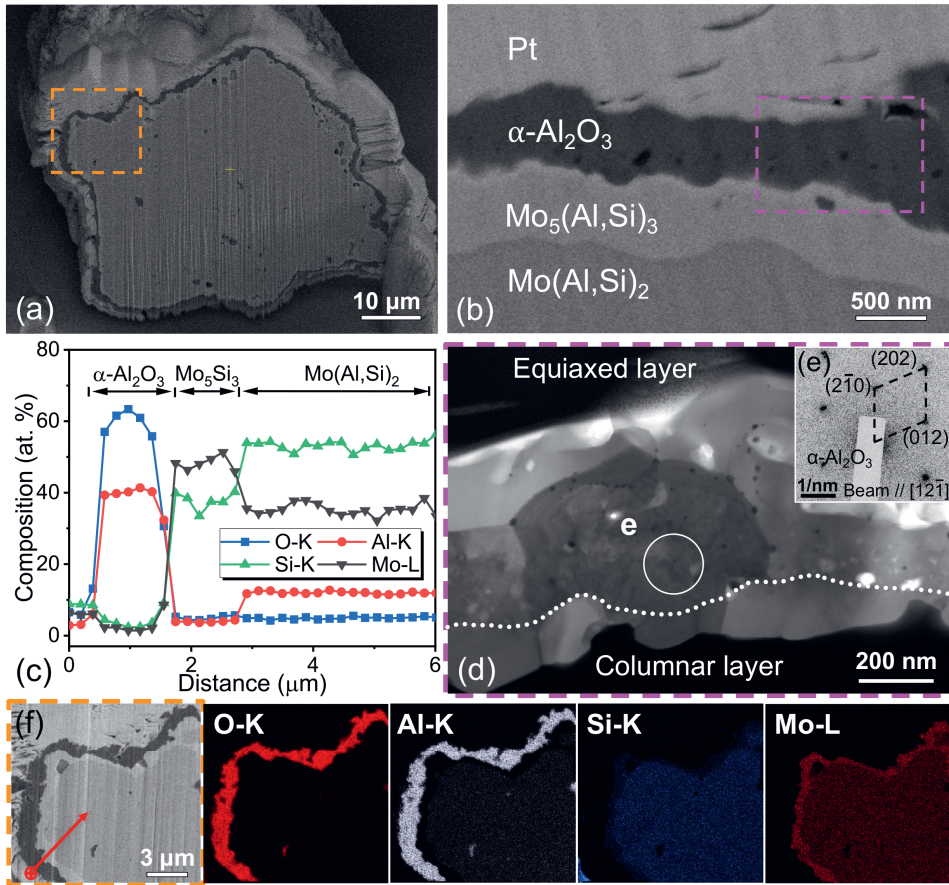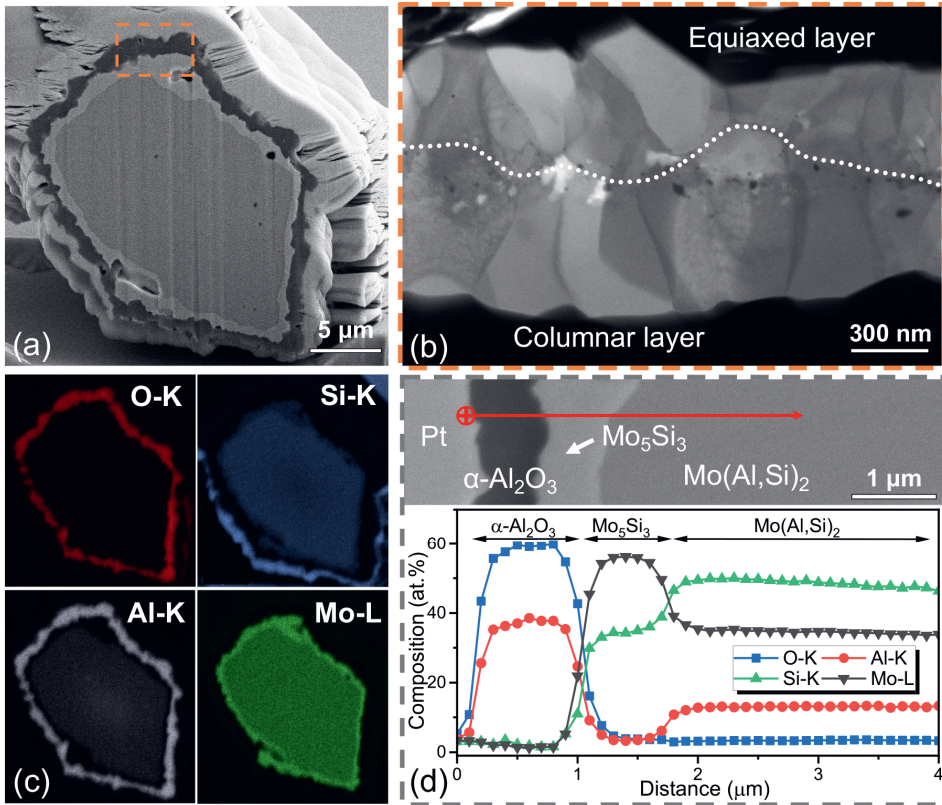
Figure 4. 9. Cross-section of $Mo(Al_{0.40}Si_{0.60})_2$ particle after oxidation with an oxygen partial pressure of 5×10^{-10} atm. at 1100°C for 16 hours: (a) SEM image; (b) STEM image of the oxide shell of α-Al_2O_3 (the dotted curve is to distinguish the grain morphologies in the upper and lower part of the oxide shell). The lower part of the oxide shell exhibits an equiaxed grain morphology and the upper part has columnar grains, which correspond to Al outward-diffusion dominant and O inward-diffusion dominant growth, respectively; (c) X-ray emission maps of O, Al, Si and Mo, respectively; (d) composition profile along the path indicated by the red arrow.

A similar surface morphology was observed when the $Mo(Al_xSi_{1-x})_2$ particles were oxidized at 1100 °C with a pO_2 of 5×10^{-10} atm. for 16 hours; see Figure 4. 7d–f. As compared to oxidation with a pO_2 of 1×10^{-14} atm., the ridges on top of the compact oxides can still be observed (see Figure 4. 7d) and the flaky oxides appear denser (see Figure 4. 7e and f). The oxidation of the $Mo(Al_xSi_{1-x})_2$ particles with a pO_2 of 5×10^{-10} atm. at 1100 °C,

which is beyond the dissociation oxygen partial pressure of solid MoO_2 (see Figure 4. 2a), results also in exclusive formation of a continuous α-Al_2O_3 shell; see Figure 4. 9a–d. Apparently, under these oxidation condition the formation of the volatile species MoO_3 or $(MoO_3)_2$ are mitigated once the surface of the $Mo(Al_xSi_{1-x})_2$ particles is completely covered with α-Al_2O_3. The alumina layer of $Mo(Al_{0.40}Si_{0.60})_2$ particle is thicker when oxidized in an ambient with pO_2 of 5×10^{-10} atm. as compared with oxidation with pO_2 of 10^{-14} atm. at 1100 °C for 16 hours, i.e., about 1.3 ± 0.2 versus 0.8 ± 0.3 μm. The Al depletion layer composed of $Mo_5(Al,Si)_3$ can be observed clearly; see Figure 4. 9. The exclusive formation of continuous α-Al_2O_3 layer encapsulating the $Mo(Al_{0.40}Si_{0.60})_2$ particles is confirmed by X-ray elemental mapping; see Figure 4. 9c. This oxide layer features a distinct two-layered structure, viz. a dense equiaxed layer on top of a dense columnar layer; see Figure 4. 9b. Composition analysis with XMA shows that still a high amount of Al is present in the centre of the particle (Figure 4. 9d), namely 22.3 at.% compared with 26.4 at.% initially.

4.3.4. The growth kinetics of the alumina scale

The converted fraction of $Mo(Al_xSi_{1-x})_2$ particles into Al_2O_3 due to oxidation at 1100 °C with a pO_2 of 10^{-14} atm. as a function of time is displayed in Figure 4. 10a. Fast oxidation during the initial stage of oxidation can be observed for all the $Mo(Al_xSi_{1-x})_2$ particle compositions and then followed by a slow steady conversion. The fast initial oxidation is likely associated with a not yet continuous oxide shell around the particle.

A higher conversion rate was observed during the steady oxidation stage when oxidized with a pO_2 of 5×10^{-10} atm., as compared with oxidation with a pO_2 of 10^{-14} atm.; see Figure 4. 10a and 10b. For both cases it holds that the converted fraction is practically independent of the aluminium content (x) of the original particles. This is somewhat different from the oxidation of bulk $Mo(Al,Si)_2$ under the same conditions [36]. Then, the oxidation was slightly accelerated with increasing Al content in the original material. This difference may be attributed to the infinite supply of Al to the surface of the bulk alloys maintain a high Al interface concentration depending on the alloy's Al content, while the particles become depleted of Al resulting in a relatively low Al interface concentration virtually independent of the original Al content.
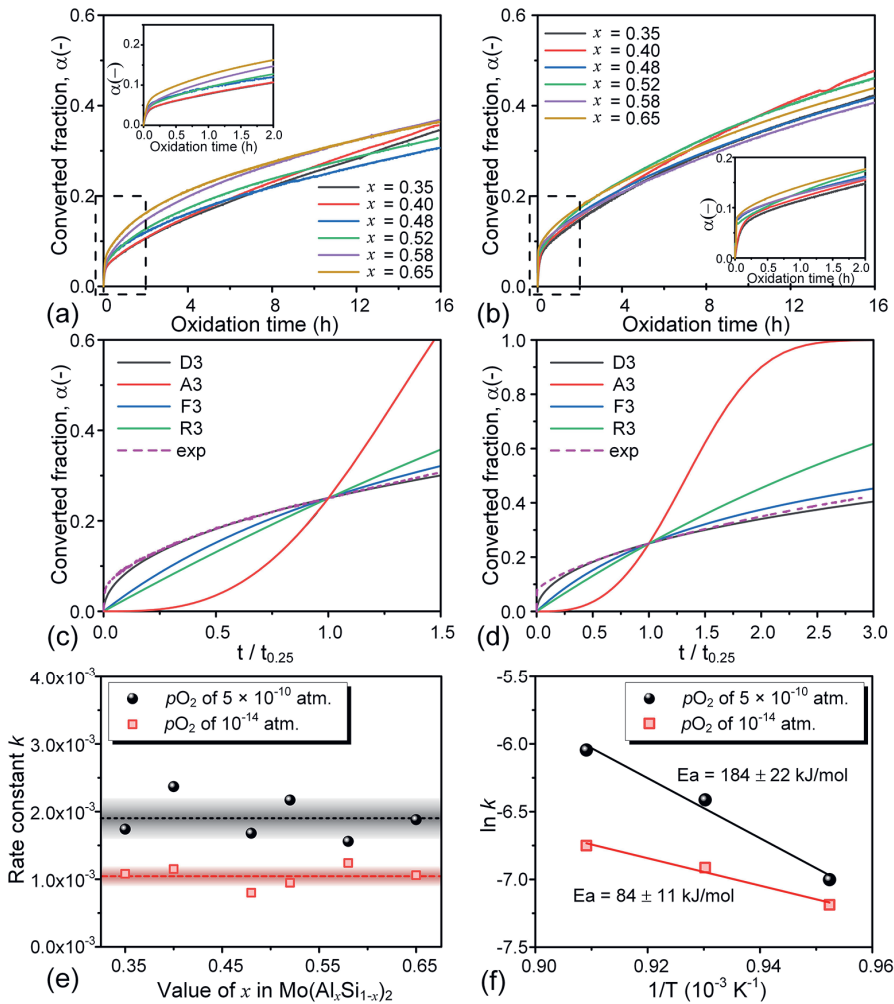
Figure 4. 10. Oxidation kinetics in terms of converted fraction versus oxidation time of (a) Mo(Al$_x$Si$_{1-x}$)$_2$ particles with an oxygen partial pressure of 10^{-14} atm. at 1100 ºC for 16 hours, and (b) Mo(Al$_x$Si$_{1-x}$)$_2$ particles with an oxygen partial pressure of 5×10^{-10} atm. at 1100 ºC for 16 hours. Reduced time plots of the converted fraction a for various reaction models (cf. Table 4. 1) and experimental data of Mo(Al$_{0.48}$Si$_{0.52}$)$_2$ particles oxidized with an oxygen partial pressure of 10^{-14} atm. (c) and 5×10^{-10} atm. (d), respectively. (e) Rate constant of Mo(Al$_x$,Si$_{1-x}$)$_2$ particles oxidized with an oxygen partial pressure of 10^{-14} atm. and 5×10^{-10} atm. (f) Rate constant of Mo(Al$_{0.4}$Si$_{0.6}$)$_2$ particles oxidized with an oxygen partial pressure of 10^{-14} atm. and 5×10^{-10} atm. at temperature of 1050 ºC, 1075 ºC and 1100 ºC for 16 hours with the activation energies indicated.

The prevailing reaction model was determined from the reduced-time plot (cf. Section 4.2.1.3) made for the converted fraction of $Mo(Al_{0.48}Si_{0.52})_2$ particles oxidized with pO_2 of 10^{-14} atm. and 5×10^{-10} atm. at 1100 °C; see Figure 4. 10c and 10d. Out of the various reaction models, the 3-D diffusion-Jander (D3) model closely resembles the experimental data (R^2 equals to 0.9933 and 0.9827 for pO_2 of 10^{-14} atm. and 5×10^{-10} atm., respectively), demonstrating a diffusion-controlled oxidation process. The integral form of this model is defined as:

$$g(\alpha) = (1-(1-\alpha)^{1/3})^2 \qquad (4.12).$$

When combining Eq. (4.5)–(4.8) and (4.12), an expression representing the conversion α can be formulated as:

$$\alpha = 1-(1-\sqrt{kt})^3 \qquad (4.13).$$

The rate constant k has been determined form a linear least-square fitting of Eq. (4.6) to the isothermal oxidation kinetic data for each $Mo(Al_xSi_{1-x})_2$ particle composition with x from 0.35 to 0.65; see Figure 4. 11. The oxidation rate constant as a function of the Al content of the original particles (cf. Figure 4. 10e) confirms the faster oxidation kinetics with a pO_2 of 5×10^{-10} atm. as compared to that with a pO_2 of 10^{-14} atm. The oxidation rate constant k is practically independent of the Al content of the original particles regardless the pO_2 of the gas ambient (see above).

4
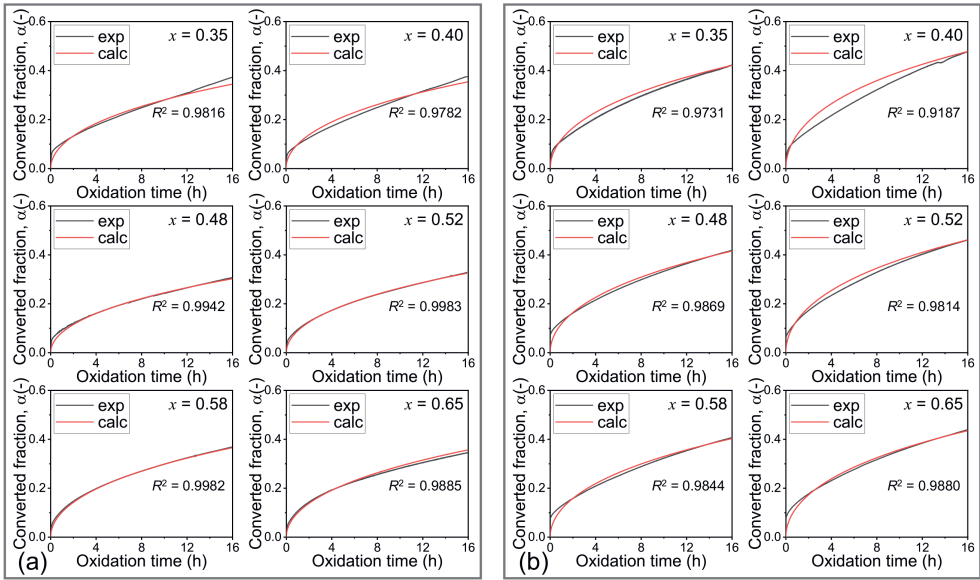
Figure 4. 11. Converted fraction (α) of Mo(Al$_x$,Si$_{1-x}$)$_2$ into a-Al$_2$O$_3$ by oxidation with an oxygen partial pressure of (a) 10^{-14} atm. and (b) 5×10^{-10} atm. at 1100 °C as function of oxidation time. The black curves are the experimental data and the red curve represents the 3-D diffusion-Jander (D3) model fitted to the experimental data.

Activation energy of the oxidation in the pO_2 of 10^{-14} atm. and 5×10^{-10} atm. were evaluated according to Eq. (4.8); see Figure 4. 10f. The activation energy equals to 184 ± 22 kJ/mol and 83 ± 11 kJ/mol for the oxidation in the pO_2 of 5×10^{-10} atm. and 10^{-14} atm., respectively. These activation energies for the thermal oxidation of the Mo(Al,Si)$_2$ particles are lower than that for the thermal oxidation of the bulk Mo(Al,Si)$_2$ alloys (310 kJ/mol [29, 37]) and other high temperature alumina forming alloys, $e.g.,$ Ti$_2$AlC (250 kJ/mol [38]), FeCrAl and Ni$_3$Al alloys (240 kJ/mol [39]). The lower activation energy for the thermal oxidation of the Mo(Al,Si)$_2$ particles is likely due to the large number of surface defects (such as: dislocations, grain boundaries, steps and kinks, roughness, etc.), of which their number increases with surface area [40, 41]. These surface defects promote the nucleation and growth of the oxide [40].

4.3.5. Growth mechanism of the alumina shell

The selective oxidation of Al in $Mo(Al_xSi_{1-x})_2$ created an α-Al_2O_3 shell for the inner core material. The exclusive Al_2O_3 scale formed on $Mo(Al_xSi_{1-x})_2$ via selective oxidation process exhibits a distinct two-layered microstructure, which features a similar microstructure as observed in scales developed during oxidation of alumina forming alloys [20, 42-44]. On the surface of the alloy, an oxide layer with columnar grains and equiaxed grains on top in contact with the gas ambient forms by selective oxidation of aluminium. A wedge-section technique was used first to illustrate the microstructure of Al_2O_3 scale formed on Fe-Cr-Al alloys [43]. In this oxide scale, the two-layered microstructure is due to a so-called "counter-diffusion process" along the grain boundaries [43, 45]. The outward diffusion of aluminium governs the growth of the outer equiaxed layer, while the inward diffusion of oxygen determines the growth of the inner columnar layer interface [20, 42-45].

In the present work, the same counter-diffusion mechanism is considered to be responsible for the growth of the alumina scale. The observed flaky oxide at the surface creating network shaped bridges (cf. Figure 4. 7b and 7e), resembles to the equiaxed layer. This oxide is formed due to outward diffusion of Al along the grain boundaries. The inner oxide layer, adjacent to the particle core, has a columnar grain structure and is formed by inward diffusion of oxygen. Comparing the oxide scale formed in the pO_2 of 10^{-14} atm. and 5×10^{-10} atm., it can be observed that the increase of oxygen partial pressure promotes the growth of both equiaxed and columnar grains; see Figure 4. 8d versus Figure 4. 9b. As a result, a denser oxide scale is formed in the pO_2 of 5×10^{-10} atm. compared to that formed in the pO_2 of 10^{-14} atm., which is the key for acting as a protective shell for the core of the particles.

4.3.6. Oxide shell stability

In typical applications, the oxygen partial pressure is high comparable to the air at atmospheric pressure (0.2 atm.) and can reach the embedded particles because the TBC exhibits an interconnected network of pores (about 20 vol.%) [1]. Therefore, particles were exposed at 1100 °C to Ar with 20 vol.% O_2 for 50 hours to assess their long-term stability after pre-oxidation in a gas ambient with a pO_2 of 10^{-14} and 5×10^{-10} atm., respectively, for 16 hours to form an exclusive alumina shell (cf. Section 4.3). For studying the oxide shell stability, particles of $Mo(Al_{0.40}Si_{0.60})_2$ were selected. The $Mo(Al_{0.40}Si_{0.60})_2$ has a single hexagonal crystal lattice structure; see Table 4. 1.

4.3.6.1. Encapsulation with pO$_2$ of 10^{-14} atm.

The surface morphology shown in Figure 4. 12a confirms that the particles encapsulated with pO$_2$ of 10^{-14} atm. preserved their integrity after exposure in Ar plus 20 vol.% O$_2$ at 1100 °C for 50 hours. At the surface a granular oxide with needles and some cracks is observed; see Figure 4. 12a–c. The needle oxide is composed of Al$_2$O$_3$-SiO$_2$ according to XMA and corresponds with 3Al$_2$O$_3$·2SiO$_2$ according to the atomic ratio of the elements. This is confirmed by the XRD analysis, showing diffraction lines pertaining to mullite (3Al$_2$O$_3$·2SiO$_2$) with an orthorhombic crystal lattice; see Figure 4. 13. XRD analysis also showed diffraction lines corresponding with tetragonal MoSi$_2$, Mo$_5$Si$_3$ and α-Al$_2$O$_3$; but no lines corresponding with crystalline SiO$_2$. The tetragonal crystal lattice of MoSi$_2$ indicates that practically all Al in Mo(Al$_x$Si$_{1-x}$)$_2$ has been consumed during oxidation, since Al can hardly be dissolved in the tetragonal MoSi$_2$; cf. Figure 4. 1. Further, due to the mixing of the Mo(Al$_x$Si$_{1-x}$)$_2$ with yttria partially stabilized zirconia (cf. Section 2.2), small amounts of zircon (ZrSiO$_4$) [13] and yttrium aluminosilicate (YAS) [46, 47] were formed on the surface of the particles during oxidation. These oxide phases can be recognized as island shaped species; see Figure 4. 12b and c.
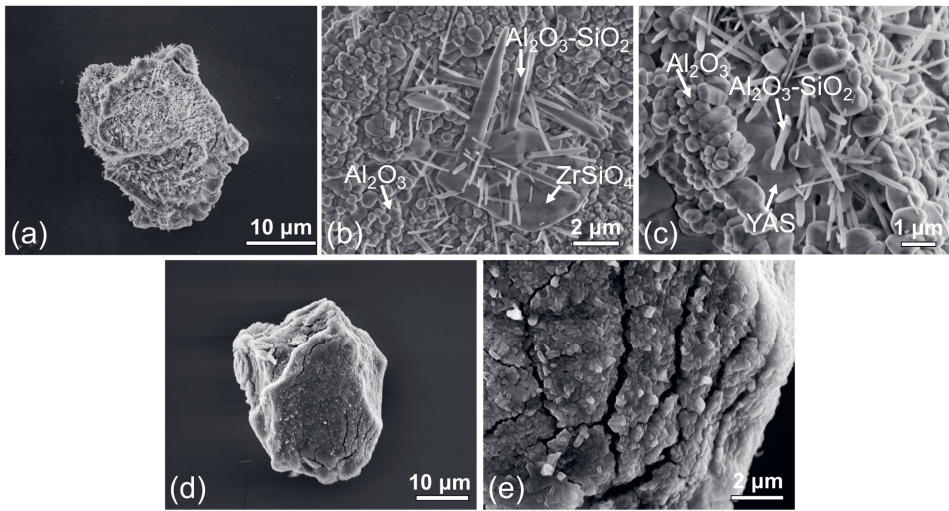
4

Figure 4. 12. SEM images of Mo(Al$_{0.40}$Si$_{0.60}$)$_2$ particle after isothermal exposure at 1100 °C of Mo(Al$_{0.40}$Si$_{0.60}$)$_2$ first with an oxygen partial pressure of (a)–(c) 10^{-14} atm. and (d)–(e) 5 × 10^{-10} atm. for 16 hours followed with an high oxygen partial pressure (i.e., Ar with 20 vol.% O$_2$) for 50 hours: (a) and (d) particle morphology; (b), (c) and (e) detail observation of surface oxides.
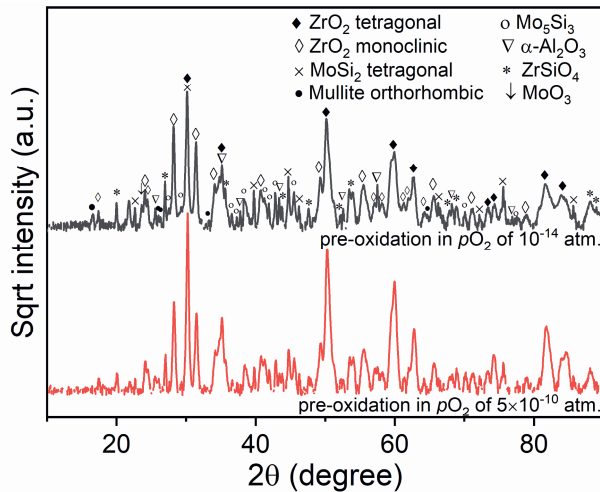

Figure 4. 13. XRD patterns of encapsulated Mo(Al$_{0.40}$Si$_{0.60}$)$_2$ free particles after exposure to high oxygen partial pressure (i.e., Ar with 20 vol.% O$_2$) at 1100 °C for 50 hours.
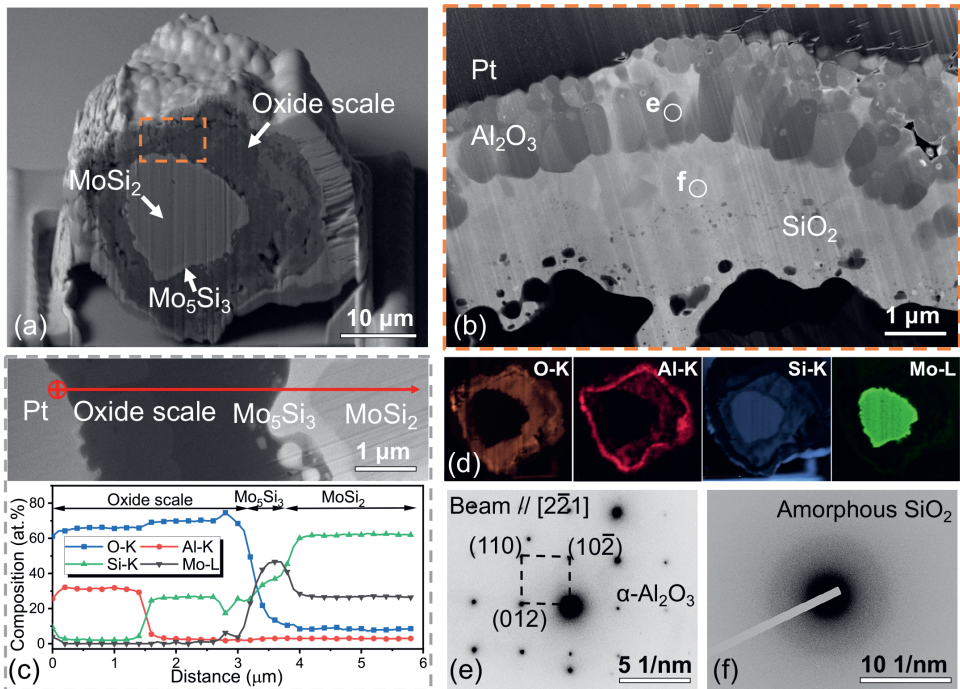
Figure 4. 14. Cross section of $Mo(Al_{0.40}Si_{0.60})_2$ particle after isothermal exposure at 1100 °C first with an oxygen partial pressure of 10^{-14} atm. for 16 hours followed with an high oxygen partial pressure (i.e., Ar with 20 vol.% O_2) for 50 hours. (a) SEM image; (b) STEM image on oxide scale; (c) composition profile along the path across the oxide scale, Mo_5Si_3 layer and $MoSi_2$ substrate indicated by the red arrow; (d) X-ray emission maps of O, Al, Si and Mo, respectively; SAEDPs of corresponding areas indicated in (b): (e) α-Al_2O_3 and (f) amorphous SiO_2.

After exposure in Ar plus 20 vol.% O_2 at 1100 °C for 50 hours, a thick thermally grown oxide shell (about 7 µm) envelops the free particles encapsulated with a pO_2 of 10^{-14} atm. at 1100 °C for 16 hours; see Figure 4. 14a. Composition analysis, elemental mapping and selected-area diffraction patterns confirm that oxide scale consists of an outer rim of α-Al_2O_3 and an inner rim of amorphous SiO_2; see Figure 4. 14b–f. The α-Al_2O_3 outer rim still exhibits a two-layered structure, but with significantly thickened columnar and equiaxed layer compared to the oxide shell formed after encapsulation in the pO_2 of 10^{-14} atm. for 16 hours; see Figure 4. 8and Figure 4. 14b. The SiO_2 underneath fills the gaps in the α-Al_2O_3 layer (Figure 4. 14b) and reacts with Al_2O_3 resulting into mullite ($3Al_2O_3{\cdot}2SiO_2$) as mentioned

above. The core of the remnant particle is fully depleted of Al and is composed of pure MoSi$_2$ with a rim of Mo$_5$Si$_3$; see Figure 4. 14c and Figure 4. 14d. The two-layered structure of the α-Al$_2$O$_3$ in the outer rim indicates that the growth of Al$_2$O$_3$ still follows the counter diffusion mechanism when oxidizing in Ar with 20 vol.% O$_2$ after encapsulation. However, the SiO$_2$ formed by oxidation of the MoSi$_2$ core due to oxygen penetrating through the Al$_2$O$_3$ outer rim, indicates a limited protection provided by the Al$_2$O$_3$ shell formed by oxidation with a pO$_2$ of 10^{-14} atm. The Pilling-Bedworth ratio (PBR) of SiO$_2$/Si (2.26) is much larger than that of Al$_2$O$_3$/Al (1.28) [48]. Therefore, the formation of silica is associated with a large volume expansion, which may have caused cracking of the Al$_2$O$_3$ shell [7]; see Figure 4. 12.

4.3.6.2. Encapsulation with pO$_2$ of 5×10^{-10} atm.

The integrity of the particles encapsulated with a pO$_2$ of 5×10^{-10} atm. and exposed to Ar plus 20 vol.% O$_2$ at 1100 °C for 50 hours is preserved; see Figure 4. 12d. As compared with the particles encapsulated with a pO$_2$ of 10^{-14} atm., no needle shaped oxide was observed at the surface (Figure 4. 12e) and the diffraction lines pertaining to mullite are very weak; see Figure 4. 13.

An about 4 μm thick thermally grown oxide scale envelops the free particles encapsulated with pO$_2$ of 5×10^{-10} atm. after exposure in Ar plus 20 vol.% O$_2$ at 1100 °C for 50 hours; see Figure 4. 15a. This shell is significantly thinner (4 versus 7 μm) than the shell formed on the particles pre-oxidized with a pO$_2$ of 10^{-14} atm. Composition analysis and elemental mapping confirm that the oxide scale consists almost exclusively of Al$_2$O$_3$, and that the core of the remnant particle is fully depleted of Al and is composed of pure MoSi$_2$ with a rim of Mo$_5$Si$_3$; see Figure 4. 15c and e. The formation of an exclusive Al$_2$O$_3$ scale suggests that the encapsulation with pO$_2$ of 5×10^{-10} atm. at 1100 °C for 16 hours (cf. Section 4.3.3) acts as a strong barrier between the particle core material and the gaseous ambient at high temperatures. Two layers of Al$_2$O$_3$ are observed in the oxide scale formed after exposure in Ar with 20 vol.% O$_2$ at 1100 °C for 50 hours; see Figure 4. 15b. The Al$_2$O$_3$ outer layer still exhibits the two-layered structure formed by encapsulation with pO$_2$ of 5×10^{-10} atm. at 1100 °C for 16 hours (cf. Section 4.3.3) and the thickness of this layer remained the same after exposure to Ar with 20 vol.% O$_2$ at 1100 °C for 50 hours; see Figure 4. 15b and Figure 4. 9b. In addition to the outer layer of alumina, an inner layer of alumina composed fine grains is formed after exposure in Ar with 20 vol.% O$_2$ at 1100 °C for 50 hours; see Figure 4. 15d. This layer is formed by the inward diffusion of oxygen through the outer layer of alumina. A very small amount of needle like oxides can be observed in between the outer and inner

alumina layer, which is composed of Al_2O_3-SiO_2 according to the composition analysis and elemental mapping; see Figure 4. 15c and e.
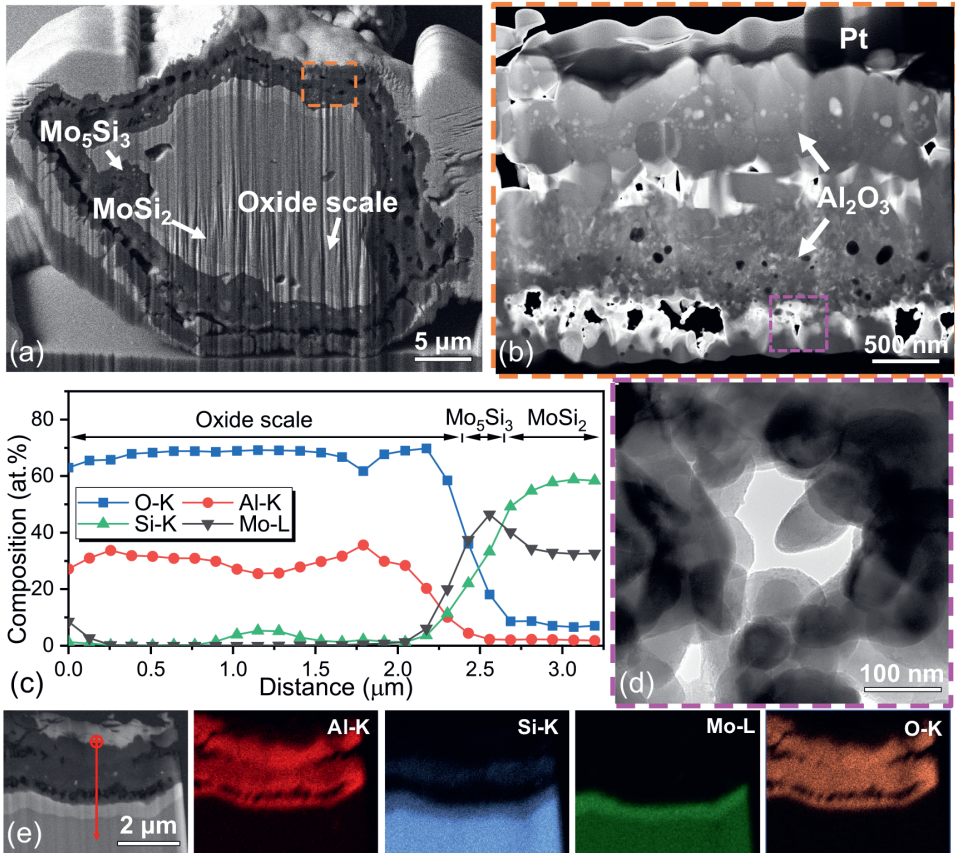
Figure 4. 15.Cross section of $Mo(Al_{0.40}Si_{0.60})_2$ particle after isothermal exposure at 1100 °C first with an oxygen partial pressure of 5×10^{-10} atm. for 16 hours followed with an high oxygen partial pressure in dry synthetic air (i.e., Ar with 20 vol.% O_2) for 50 hours. (a) SEM image; (b) STEM image of the oxide scale; (c) composition profile along the path indicated by the red arrow in (e); (d) bright-field TEM image of the oxide scale composed of fine grains; (e) X-ray emission maps of O, Al, Si and Mo, respectively.

4.3.6.3. Oxidation kinetics after encapsulation

The mass change during exposure of the Mo(Al$_{0.40}$Si$_{0.60}$)$_2$ particles to Ar with 20 vol.% O$_2$ at 1100 ℃ recorded with TGA is shown in Figure 4. 16. An instant weight gain occurred after switching the gas composition to Ar with 20 vol.% O$_2$, followed by a gradual weight loss. Note that the mass change amplitude caused by only switching of the gas composition is neglectable; see insert a of Figure 4. 16. Assuming that the weight gain amplitude is due to the selective oxidation of all the remaining Al in the core of the particles according to Eq. (4.1), then the weight gain can be calculated. This mass change is close to the observed mass gain amplitude of particle encapsulated in pO_2 of 5×10^{-10} atm. as indicated in Figure 4. 16.
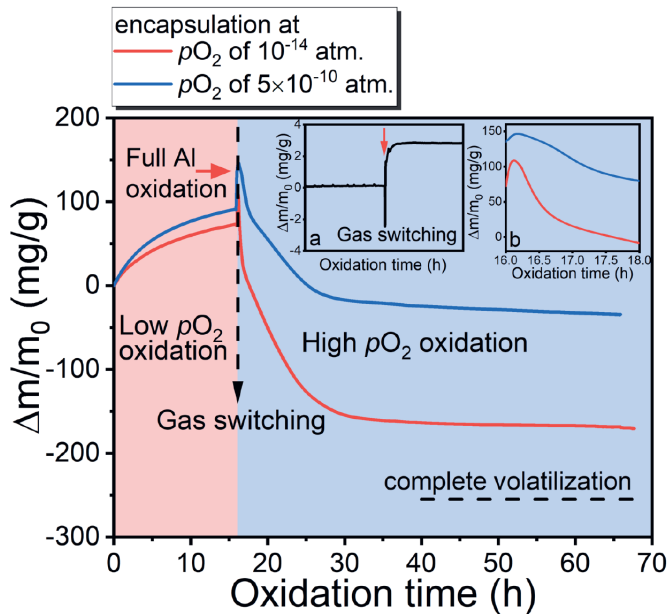
Figure 4. 16. Mass change of Mo(Al$_{0.40}$Si$_{0.60}$)$_2$ particle during isothermal exposure at 1100 ℃. First to low oxygen partial pressure (i.e., pO_2 of 10^{-14} atm. and pO_2 of 5×10^{-10} atm., respectively) for 16 hours. Subsequently, exposure to high oxygen partial pressure (i.e., Ar with 20 vol.% O$_2$) for 50 hours. The insert (a) shows the mass change amplitude caused by switching the gas composition and insert (b) shows the initial oxidation upon gas switching. The dash line corresponds with the mass change of complete oxidation, i.e., when all Mo(Al$_{0.40}$Si$_{0.60}$)$_2$ is oxidized into Al$_2$O$_3$, SiO$_2$ and volatile MoO$_3$.

The subsequent gradual weight loss is due to the formation of volatile MoO_3. Some whisker-shaped MoO_3 crystals were found in the outlet of the gas path after oxidation in Ar with 20 vol.% O_2 at 1100 °C of the $Mo(Al_{0.40}Si_{0.60})_2$; see Figure 4. 17a. These MoO_3 crystals were not observed after pre-oxidation with both pO_2 of 10^{-14} atm. and 5×10^{-10} atm., suggesting that then the formation of MoO_3 crystal was mitigated by selective oxidation of aluminium. The XRD pattern of the MoO_3 crystals deposited by thermal evaporation corresponds with orthorhombic α-MoO_3 [49]; see Figure 4. 17b. Thus, the α-MoO_3 crystals grow with a strong (0 k 0) preferred orientation [50, 51].
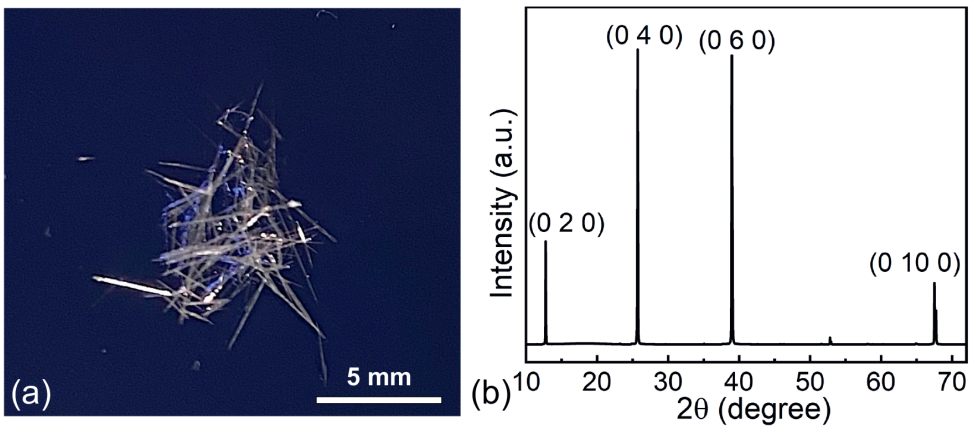
Figure 4. 17. (a) MoO_3 deposited by thermal evaporation and (b) XRD pattern of the MoO_3. The strong diffraction lines at 12.75 ± 0.03, 25.65 ± 0.03, 39.00 ± 0.03 and 67.50 ± 0.03 ° correspond with the (0 2 0), (0 4 0), (0 6 0) and (0 10 0) planes of orthorhombic α-MoO_3, respectively.

The formation of MoO_3 is likely due to particles that were not fully sealed by an alumina shell. Particles encapsulated in the pO_2 of 5×10^{-10} atm. exhibit slower mass loss after gas switching than those encapsulated in the pO_2 of 10^{-14} atm., indicating a better protection provided by the encapsulation in the pO_2 of 5×10^{-10} atm.; see insert b of Figure 4. 16. After about 15 hours of exposure to high pO_2 of 0.2 atm. the mass change ceases, suggesting that the remaining particles will be preserved after long-time exposure to high temperature and high oxygen partial pressure. The particles encapsulated with a pO_2 of 10^{-14} atm. exhibit larger weight loss than those encapsulated with a pO_2 of 5×10^{-10} atm. The MoO_3 will act as a catalyst to promote the reaction between silica and alumina to form mullite ($3Al_2O_3 \cdot 2SiO_2$)

and lowers the mullitization temperature [52, 53], which explains the presence of mullite on the particles after exposure to Ar with 20 vol.% O_2 at 1100 °C. Note that mullite is also capable to preserve the $MoSi_2$ core, although the diffusion coefficient of oxygen D in mullite ($D_O^{lattice} \sim 10^{-21}$ m^2/s and $D_O^{gb} \sim 10^{-17}$ m^2/s at 1100 °C [54]) is higher than α-Al_2O_3 ($D_O^{lattice} \sim 10^{-26}$ $m^2 \cdot s^{-1}$ and $D_O^{gb} \sim 10^{-19}$ $m^2 \cdot s^{-1}$ at 1100 °C). For comparison the oxygen diffusion coefficients of ZrO_2 and amorphous SiO_2 are $D_O^{lattice} \sim 10^{-11}$ $m^2 \cdot s^{-1}$ [15, 55] and $D_{O2} \sim 10^{-12}$ $m^2 \cdot s^{-1}$ [56], respectively.

Comparing the mass change behaviour of particles during exposure to Ar with 20 vol.% O_2 at 1100 °C, after the pre-oxidation with pO_2 of 10^{-14} atm. and 5×10^{-10} atm. for 16 h, respectively, then a large difference in weight loss is observed; see Figure 4. 16. The weight loss, with respect to the value when the Mo(Al$_x$Si$_{1-x}$)$_2$ particles are completely oxidized into Al_2O_3, SiO_2 and MoO_3, is about 86 % and 30 % for the particles after pre-oxidation with pO_2 of 10^{-14} atm. and 5×10^{-10} atm. for 16 h, respectively.

4

Conclusions

Encapsulation of Mo(Al$_x$Si$_{1-x}$)$_2$ healing particles is designed in terms of alumina shell thickness, particle size and fraction Al dissolved. The conditions for the selective oxidation of Al to form a dense α-Al_2O_3 shell are determined based on thermodynamic and kinetic data.

Encapsulation with alumina of these sacrificial particles envisioned for self-healing yttria partially stabilized zirconia (YPSZ) thermal barrier coatings (TBCs) has been realized by selective oxidation of Al in Mo(Al$_x$Si$_{1-x}$)$_2$ particles with x between 0.35 to 0.65 and an on average size of about 30 µm. By replacing Si by Al in $MoSi_2$ still a strong crack damage healing ability is maintained (relative volume expansion not less than 40 %).

A closed shell of exclusively α-Al_2O_3 with thickness of about 0.8 ± 0.3 µm was formed after oxidation in a low oxygen partial pressure gas ambient of 10^{-14} atm. at 1100 °C for 16 hours, whereby the formation of volatile molybdenum oxide species was mitigated. A two-layered structure, comprising of an equiaxed layer consists of fine grains and a thin columnar layer underneath, was observed in the α-Al_2O_3 scale which is ascribed to a counter-diffusion mechanism.

Increasing the oxygen partial pressure to 5×10^{-10} atm. still results in a shell of exclusively α-Al_2O_3 when oxidizing the Mo(Al$_x$Si$_{1-x}$)$_2$ particles at 1100 °C for 16 hours, but with a larger thickness of about 1.3 ± 0.2 µm. This higher oxygen partial pressure promotes the grain growth in both equiaxed and columnar layer and results in a dense α-Al_2O_3 scale.

The conversion from Al to Al_2O_3 does not increase with increasing the Al content of the original $Mo(Al_xSi_{1-x})_2$ particles. The growth of the alumina oxide shell by selective oxidation is captured with a 3-D diffusion-Jander (D3) reaction model. The conversion from Al to Al_2O_3 is practically independent of the Al content of the original $Mo(Al_xSi_{1-x})_2$ particles. The activation energy required for oxidation of the $Mo(Al_xSi_{1-x})_2$ particles with pO_2 of 10^{-14} atm. and 5×10^{-10} atm. equals 84 ± 11 kJ/mol and 184 ± 22 kJ/mol, respectively, which is much lower than for the oxidation of alumina forming alloys with a flat surface (about 250 kJ/mol).

The $Mo(Al_{0.4}Si_{0.6})_2$ particles encapsulated by selective oxidation of Al with a pO_2 of 5×10^{-10} atm. at 1100 °C for 16 hours are the most promising to prevent premature full oxidation in a self-healing thermal barrier coating system. After exposure to Ar with 20 vol.% O_2 at 1100 °C for 50 hours, a core of pure $MoSi_2$ with a rim of Mo_5Si_3 is enveloped by a robust oxide shell of α-Al_2O_3. This encapsulation provides $MoSi_2$ particles with 86 % less weight loss upon oxidation preserving the healing capacity of the particles.

4

References

[1] N.P. Padture, M. Gell, E.H. Jordan, Thermal barrier coatings for gas-turbine engine applications, Science 296(5566) (2002) 280-284.

[2] X.Q. Cao, R. Vassen, D. Stoever, Ceramic materials for thermal barrier coatings, Journal of the European Ceramic Society 24(1) (2004) 1-10.

[3] D.R. Clarke, S.R. Phillpot, Thermal barrier coating materials, Materials Today 8(6) (2005) 22-29.

[4] Z. Derelioglu, A.L. Carabat, G.M. Song, S. van der Zwaag, W.G. Sloof, On the use of B-alloyed $MoSi_2$ particles as crack healing agents in yttria stabilized zirconia thermal barrier coatings, Journal of the European Ceramic Society 35(16) (2015) 4507-4511.

[5] L.B. Chen, Yttria-stabilized zirconia thermal barrier coatings—a review, Surface review and letters 13 (2006) 535-544.

[6] A. Rabiei, A.G. Evans, Failure mechanisms associated with the thermally grown oxide in plasma-sprayed thermal barrier coatings, Acta Materialia 48 (2000) 3963-3976.

[7] Y. Chen, X. Zhang, S. van der Zwaag, W.G. Sloof, P. Xiao, Damage evolution in a self-healing air plasma sprayed thermal barrier coating containing self-shielding $MoSi_2$ particles, Journal of the American Ceramic Society 102(8) (2019) 4899-4910.

[8] J. Krishnasamy, S.A. Ponnusami, S. Turteltaub, S. van der Zwaag, Modelling the fracture behaviour of thermal barrier coatings containing healing particles, Materials & Design 157 (2018) 75-86.

[9] S.A. Ponnusami, J. Krishnasamy, S. Turteltaub, S. van der Zwaag, A cohesive-zone crack healing model for self-healing materials, International Journal of Solids and Structures 134 (2018) 249-263.

[10] T.S. Hille, T.J. Nijdam, A.S.J. Suiker, S. Turteltaub, W.G. Sloof, Damage growth triggered by interface irregularities in thermal barrier coatings, Acta Materialia 57(9) (2009) 2624-2630.

[11] A. Kumthekar, S.A. Ponnusami, S. van der Zwaag, S. Turteltaub, Uncertainty quantification of the lifetime of self-healing thermal barrier coatings based on surrogate modelling of thermal cyclic fracture and healing, Materials & Design 221 (2022).

[12] A.G. Evans, D.R. Mumm, J.W. Hutchinson, G.H. Meier, F.S. Pettit, Mechanisms controlling the durability of thermal barrier coatings, Progress in Materials Science 46 (2001) 505-553.

[13] J. Aktaa, K. Sfar, D. Munz, Assessment of TBC systems failure mechanisms using a fracture mechanics approach, Acta Materialia 53(16) (2005) 4399-4413.

[14] J. Krishnasamy, S.A. Ponnusami, S. Turteltaub, S. van der Zwaag, Thermal cyclic behavior and lifetime prediction of self-healing thermal barrier coatings, International Journal of Solids and Structures 222-223 (2021).

[15] F. Nozahic, C. Estournès, A.L. Carabat, W.G. Sloof, S. van der Zwaag, D. Monceau, Self-healing thermal barrier coating systems fabricated by spark plasma sintering, Materials & Design 143 (2018) 204-213.

[16] D. Koch, D.E. Mack, R. Vaßen, Degradation and lifetime of self-healing thermal barrier coatings containing $MoSi_2$ as self-healing particles in thermo-cycling testing, Surface and Coatings Technology 437 (2022).

[17] F. Nozahic, A.L. Carabat, W. Mao, D. Monceau, C. Estournes, C. Kwakernaak, S. van der Zwaag, W.G. Sloof, Kinetics of zircon formation in yttria partially stabilized zirconia as a result of oxidation of embedded molybdenum disilicide, Acta Materialia 174 (2019) 206-216.

[18] X.-P. Zhang, J.-H. Ouyang, Z.-G. Liu, Y.-J. Wang, Y.-M. Wang, Crack-healing behavior and strength recovery of hot-pressed TZ3Y20A–$MoSi_2$ ceramics, Materials Science and Engineering: A 648 (2015) 299-304.

[19] M. Yuan, L. Liu, J. Wang, Q. Hu, H. Zhang, S. Zhang, X. Zhou, Crack-healing behaviour of $MoSi_2$ dispersed $Yb_2Si_2O_7$ environmental barrier coatings, Ceramics International 48(20) (2022) 29919-29928.

[20] A.H. Heuer, T. Nakagawa, M.Z. Azar, D.B. Hovis, J.L. Smialek, B. Gleeson, N.D.M. Hine, H. Guhl, H.S. Lee, P. Tangney, W.M.C. Foulkes, M.W. Finnis, On the growth of Al_2O_3 scales, Acta Materialia 61(18) (2013) 6670-6683.

[21] A.H. Heuer, Oxygen and aluminum diffusion in α-Al2O3: How much do we really understand?, Journal of the European Ceramic Society 28(7) (2008) 1495-1507.

[22] D.J. Young, High temperature oxidation and corrosion of metals, Elsevier2016.

[23] A.L. Carabat, S. Zwaag, W.G. Sloof, T. Troczynski, Creating a protective shell for reactive $MoSi_2$ particles in high‑temperature ceramics, Journal of the American Ceramic Society 98(8) (2015) 2609-2616.

[24] A.L. Carabat, M.J. Meijerink, J.C. Brouwer, E.M. Kelder, J.R. van Ommen, S. van der Zwaag, W.G. Sloof, Protecting the $MoSi_2$ healing particles for thermal barrier coatings using a sol-gel produced Al_2O_3 coating, Journal of the European Ceramic Society 38(7) (2018) 2728-2734.

[25] T.J. Nijdam, L.P.H. Jeurgens, W.G. Sloof, Promoting exclusive α-Al_2O_3 growth upon high-temperature oxidation of NiCrAl alloys: experiment versus model predictions, Acta Materialia 53(6) (2005) 1643-1653.

[26] T.J. Nijdam, L.P.H. Jeurgens, W.G. Sloof, Modelling the thermal oxidation of ternary alloys—compositional changes in the alloy and the development of oxide phases, Acta Materialia 51(18) (2003) 5295-5307.

[27] M. Białas, Finite element analysis of stress distribution in thermal barrier coatings, Surface and Coatings Technology 202(24) (2008) 6002-6010.

4

[28] M. Ranjbar-Far, J. Absi, S. Shahidi, G. Mariaux, Impact of the non-homogenous temperature distribution and the coatings process modeling on the thermal barrier coatings system, Materials & Design 32(2) (2011) 728-735.

[29] L. Ingemarsson, K. Hellström, S. Canovic, T. Jonsson, M. Halvarsson, L.G. Johansson, J.E. Svensson, Oxidation behavior of a Mo(Si,Al)$_2$ composite at 900–1600 °C in dry air, Journal of Materials Science 48(4) (2012) 1511-1523.

[30] A. Khawam, D.R. Flanagan, Solid-state kinetic models: basics and mathematical fundamentals, The Journal of Physical Chemistry B 110 (2006) 17315-17328.

[31] C. Rozycki, M. Maciejewski, Method of the selection of the g(α) function based on the reduced-time plot, Thermochimica Acta 122 (1987) 339-364.

[32] W.B. Gong, C.K. Sha, D.Q. Sun, W.Q. Wang, Microstructures and thermal insulation capability of plasma-sprayed nanostructured ceria stabilized zirconia coatings, Surface and Coatings Technology 201(6) (2006) 3109-3115.

[33] M.R. Loghman-Estarki, M. Pourbafrany, R. Shoja Razavi, H. Edris, S.R. Bakhshi, M. Erfanmanesh, H. Jamali, S.N. Hosseini, M. Hajizadeh-Oghaz, Preparation of nanostructured YSZ granules by the spray drying method, Ceramics International 40(2) (2014) 3721-3729.

[34] K. Prabhakaran, M.O. Beigh, J. Lakra, N.M. Gokhale, S.C. Sharma, Characteristics of 8 mol% yttria stabilized zirconia powder prepared by spray drying process, Journal of Materials Processing Technology 189(1-3) (2007) 178-181.

[35] A.A. Sharif, High-temperature oxidation of MoSi$_2$, Journal of Materials Science 45(4) (2010) 865-870.

[36] Z. Ding, J.C. Brouwer, C. Kwakernaak, M.J.M. Hermans, V. Popovich, W.J. Quadakkers, W.G. Sloof, Selective oxidation of aluminium in Mo(Al,Si)$_2$, Corrosion Science 211 (2023) 110844.

[37] T. Maruyama, K. Yanagihara, High temperature oxidation and pesting of Mo(Si,Al)$_2$, Materials Science and Engineering A 230-240 (1997) 828-841.

[38] D.J. Tallman, B. Anasori, M.W. Barsoum, A Critical Review of the Oxidation of Ti$_2$AlC, Ti$_3$AlC$_2$ and Cr$_2$AlC in Air, Materials Research Letters 1(3) (2013) 115-125.

[39] R.H. Doremus, Oxidation of alloys containing aluminum and diffusion in Al$_2$O$_3$, Journal of Applied Physics 95(6) (2004) 3217-3222.

[40] L. Boatemaa, J.C. Brouwer, S. van der Zwaag, W.G. Sloof, The effect of the TiC particle size on the preferred oxidation temperature for self-healing of oxide ceramic matrix materials, Journal of Materials Science 53(8) (2018) 5973-5986.

[41] J. Šesták, Rationale and fallacy of thermoanalytical kinetic patterns, Journal of Thermal Analysis and Calorimetry 110(1) (2011) 5-16.

[42] A.H. Heuer, D.B. Hovis, J.L. Smialek, B. Gleeson, Alumina scale formation: a new perspective, Journal of the American Ceramic Society 94 (2011) s146-s153.

4

[43] V.K. Tolpygo, D.R. Clarke, Microstructural evidence for counter-diffusion of aluminum and oxygen during the growth of alumina scales, Materials at High Temperatures 20(3) (2014) 261-271.

[44] H.J. Yang, Y.T. Pei, J.T.M. De Hosson, Oxide-scale growth on Cr_2AlC ceramic and its consequence for self-healing, Scripta Materialia 69(2) (2013) 203-206.

[45] J.A. Nychka, D.R. Clarke, Quantification of aluminum outward diffusion during oxidation of FeCrAl alloys, Oxidation of Metals 63(5-6) (2005) 325-352.

[46] P. Vomacka, O. Babushkin, R. Warren, Zirconia as a nucleating agent in a yttria-alumiina-silica glass, Journal of the European Ceramic Society 15 (1995) 1111-1117.

[47] N. Sadiki, J.P. Coutures, C. Fillet, J.L. Dussossoy, Crystallization of lanthanum and yttrium aluminosilicate glasses, Journal of Nuclear Materials 348(1-2) (2006) 70-78.

[48] T. Ohashi, T. Harada, High-temperature oxidation of Fe-Cr-Al-Si alloys extruded into honeycomb structures, Oxidation of Metals 46 (1996) 235-254.

[49] L. Zhu, Y. Dong, S. Hampshire, S. Cerneaux, L. Winnubst, Waste-to-resource preparation of a porous ceramic membrane support featuring elongated mullite whiskers with enhanced porosity and permeance, Journal of the European Ceramic Society 35(2) (2015) 711–721,

[50] M.B. Rahmani, S.H. Keshmiri, J. Yu, A.Z. Sadek, L. Al-Mashat, A. Moafi, K. Latham, Y.X. Li, W. Wlodarski, K. Kalantar-zadeh, Gas sensing properties of thermally evaporated lamellar MoO_3, Sensors and Actuators B: Chemical 145(1) (2010) 13-19.

[51] Q.P. Ding, H.B. Huang, J.H. Duan, J.F. Gong, S.G. Yang, X.N. Zhao, Y.W. Du, Molybdenum trioxide nanostructures prepared by thermal oxidization of molybdenum, Journal of Crystal Growth 294(2) (2006) 304-308.

[52] L. Zhu, Y. Dong, S. Hampshire, S. Cerneaux, L. Winnubst, Waste-to-resource preparation of a porous ceramic membrane support featuring elongated mullite whiskers with enhanced porosity and permeance, Journal of the European Ceramic Society 35(2) (2015) 711-721.

[53] Z. Zhu, Z. Wei, J. Shen, L. Zhu, L. Xu, Y. Zhang, S. Wang, T. Liu, Fabrication and catalytic growth mechanism of mullite ceramic whiskers using molybdenum oxide as catalyst, Ceramics International 43(2) (2017) 2871-2875.

[54] P. Fielitz, G. Borchardt, Oxygen grain-boundary diffusion in polycrystalline mullite ceramics, Journal of American Ceramic Society 87(12) (2004) 2232-2236.

[55] A. Madeysk, W.W. Smeltzer, Oxygen diffusion in monoclinic zirconia, Materials Research Bulletin 3 (1968) 369-376.

[56] M.A. Lamkin, F.L. Riley, R.J. Fordham, Oxygen mobility in silicon dioxide and silicate glasses: a review, Journal of the European Ceramic Society 10 (1992) 347-367.

4

4

5.

Effects of boron addition on the high temperature oxidation of MoSi₂ alloys

Zhaoying Ding, Johannes C. Brouwer, Jia-Ning Zhu, Vera Popovich, Marcel J.M. Hermans and Willem G. Sloof. "Effects of boron addition on the high temperature oxidation of MoSi₂ alloys." *Scripta Materialia* 234 (2023): 115580.

Abstract

Boron containing $MoSi_2$ is a promising material for applications at high temperature, but the oxidation mechanism is still unclear. In this work, the high temperature (1100 °C) oxidation of B doped $MoSi_2$ in synthetic air has been investigated. A (boro)silicate layer is formed on the surface of the alloy, which features a mixture of amorphous SiO_2 and cristobalite. After an initial transient period, the oxidation kinetics follows a parabolic growth rate law. The growth rate constant of the oxide layer is enhanced by the boron in the alloy by 90 % per at.% B. The increase in growth rate is associated with boron mitigating the formation of cristobalite thereby promoting the formation of amorphous SiO_2.

5.1. Introduction

With a high melting point of over 2000 °C, moderate density (6.24 g/cm^3) and outstanding oxidation resistance, molybdenum disilicide ($MoSi_2$) is one of the most promising high-temperature material used as furnace elements, high-temperature heat exchangers and filters, gas burners, components for hot-section jet engines and gas turbines [1, 2]. However, it suffers from pest oxidation at temperatures of 400–600 °C [3] through the diffusion of oxygen along grain boundaries [4], resulting in rapid fragmentation and disintegration. It is suggested that having crystalline cristobalite as the oxide scale for $MoSi_2$ can also accelerate the pest oxidation. To resolve this problem, a minor amount of boron is added to $MoSi_2$, which also allows to enhance the fracture toughness of the alloy [1]. A borosilicate layer with a lower viscosity than silica is formed on the surface of Mo–Si–B alloy upon oxidation [4, 5], which promotes a faster coverage and provides a self-healing effect on the surface of the alloy [6]. Also B-containing $MoSi_2$ particles are used for crack-healing in yttria partially stabilized zirconia (YPSZ) [7], where the presence of B significantly facilitates the formation of borosilicate as crack-filling agent and thereby promotes the subsequent formation of the mechanical load bearing phase of zircon [8].

Although the oxidation kinetics of $MoSi_2$ with and without boron addition has been studied [9-15], the effect of boron on the high temperature oxidation of $MoSi_2$ is still debated [3, 9]. Moreover, electron beam induced damage caused by high diffuse electron scattering as in electron microscopy may result in transformation of crystalline into amorphous SiO_2 hindering detailed microstructure analysis [16, 17]. To date, the evolution of the microstructure on an atomic scale to reveal the oxidation mechanism of $MoSi_2$ with boron

5

addition is still lacking [18]. Thus, the present study aims at understanding the effect of boron addition on the oxidation of $MoSi_2$ at elevated temperature.

5.2. Materials and Methods

5.2.1. Materials

Pure $MoSi_2$ powder (<50 μm, ChemPUR GmbH, Germany) and $MoSi_2$ with boron addition powder (<45 μm, nominal 2 wt.% boron, ChemPUR GmbH, Germany) were used as the starting material. Also, a mixture of both powders, i.e., $MoSi_2$ without and with 2 wt.% B, with a ratio of 1:1 was prepared to obtain $MoSi_2$ with 1 wt.% B particles. The starting powders and their mixtures were milled using a planetary ball mill (PM100, Retsch GmbH, Germany) to refine the microstructure of molybdenum boride. The ball-milling of the powders was conducted in around 20 ml isopropanol using ZrO_2 balls (100 and 8 balls with diameter of 5 mm and 10 mm, respectively) and a 50 ml ZrO_2 jar. The weight ratio of balls and powder was about 20:1. In order to confirm the boron content of the material, the ball milled powders were analysed using inductively couple plasma optical emission spectroscopy (ICP-OES, iCAP 6500 Duo Thermo Fisher Scientific). The dissolution of these powders was specifically designed for the Mo–Si–B system [19]. The measured content of boron in the ball milled powders are 0 wt.%, 0.66 wt.% (3 at.%) and 1.29 wt.% (6 at.%), respectively; see Table 5. 1.

Table 5. 1. Boron content of Mo–Si–(B) powders used for spark plasma sintering (SPS) as obtained by ICP-OES.

Nominal composition (-)	Pre-treatment (-)	Boron content (wt.%)
$MoSi_2$	/	/
$MoSi_2$-1 wt.%B	Ball-milled	0.66
$MoSi_2$-2 wt.%B	Ball-milled	1.29

Next, the above ball milled powders were densified by means of spark plasma sintering (SPS) using a HP D 25 SD furnace (FCT Systeme GmbH, Germany) with a sintering pressure of 50 MPa at 1500 °C for 30 minutes in a flowing argon atmosphere. The heating rate was 20 °C/min, while natural cooling was used to cool down from the maximum temperature.

The prepared alloys with 0, 3 and 6 at.% boron are denoted as Mo–67Si, Mo–64Si–3B and Mo–61Si–6B, respectively.

5.2.2. Isothermal high temperature oxidation

The isothermal oxidation kinetics of the Mo–Si–B material in dry synthetic air (N_2 with 20 vol.% O_2) at a temperature of 1100 °C in terms of mass change was assessed via thermogravimetric analyses, using a dual furnace balance (Setaram TAG 16/18, France). To this end, the sintered discs were cut into rectangular bars of $15 \times 8 \times 2$ mm^3 via electric discharge machining (EDM). The initial mass of the sample was weighed using a Mettler Toledo balance (accuracy ± 1 µg). A dummy sample of alumina with the same dimensions was mounted onto a sapphire rod of the counter part of the balance to eliminate any buoyancy effect. The gas mixture was admitted to the TGA analyser via mass flow controllers (Bronkhorst, the Netherlands) such that the total gas flow matches 50 sccm, which was equally divided over both furnace tubes, i.e., 25 sccm gas in each furnace. To flush the gas lines, balance and furnaces, the TGA system was pumped to vacuum (< 50 Pa) and refilled with Ar three times. Then, the dual furnaces were heated up from room temperature to the target temperature with 10 °C/min. When the target temperature for isothermal oxidation was reached, the gas composition was switched to the oxidation atmosphere while maintaining a total gas flow of 50 sccm for 20 hours. After oxidation, the furnace was cooled down to room temperature with 10 °C/min while flushing with pure Ar.

5.2.3. Characterization of the oxide scale

The phase composition of the alloy before oxidation was determined with X-ray diffractometry (XRD) using a D8 advance diffractometer (Bruker, Germany) in the Bragg-Brentano geometry operated with Co Kα radiation. Diffractograms were recorded in the 2θ range of 10 to 90° with a step size of 0.030° and a counting time per step of 2 s. The phase composition of the alloy after oxidation was determined in the grazing incidence geometry with the same diffractometer in the same 2θ range but with a fixed observation angle of 3°. The incident beam size is 4 mm in height and 2 mm in width. A step size of 0.03° 2θ and a counting time of 5 s per step were applied to identify the oxide phases present at the sample surface. These diffractograms were evaluated using the Bruker Diffrac EVA software (version 3.1).

Raman spectra were recorded with a Horiba LabRAM HR device equipped with an argon-ion laser operating at 514 nm wavelength. The surface morphology in terms of the Mo–Si–B alloy before and after oxidation was observed with scanning electron microscopy (SEM, JEOL JSM6500F) operated at 15 keV. In addition, SEM combined with a xenon plasma focused ion beam (Helios G4 PFIB UXe, Thermo Fisher Scientific, USA) was used to prepare and characterize cross-sections of the oxide scales. Lamella for transmission electron microscopy (TEM) from selected area in the oxide scale were prepared with the plasma focused ion beam and subsequently lifted. The cross-section of the oxide scale was observed with scanning transmission electron microscopy (STEM) within the dual beam microscope (Helios G4 PFIB UXe, Thermo Fisher Scientific, USA) operated with a 30 keV electron beam. Next, the thin lamellas were analysed with TEM using a JEOL JEM-1400 plus (JEOL, Japan) operated with a 120 keV electron beam. High resolution TEM (HRTEM) and X-ray microanalysis were performed using a FEI Cs-corrected cubed Titan (FEI, USA) operating at 300 keV. X-ray emission elemental mapping in STEM mode was performed using the super-X in the ChemiSTEM^{TM} configuration. HREM lattice images were collected with a Thermo Scientific Ceta^{TM} 16M.

5.3. Results and Discussion

The Mo–67Si alloy features a microstructure with a matrix of $MoSi_2$ and small SiO_2 inclusions, see Figure 5. 1a, while Mo–64Si–3B and Mo–61Si–6B feature a microstructure also with a matrix of $MoSi_2$ and homogeneous distributed MoB precipitates but with more SiO_2 inclusions; see Figure 5. 1b and c. The diffractograms of the densified materials with different amount of boron addition clearly show peaks of tetragonal $MoSi_2$ as the main phase and small peaks of tetragonal MoB as the minor second phase; see Figure 5. 1d. The inclusions of SiO_2 are not seen in the diffractogram due to their amorphous nature; see Figure 5. 1e–f. The elemental mapping, shown in Figure 5. 1g, confirms the indicated phases and the contamination of Zr from the ball milling.
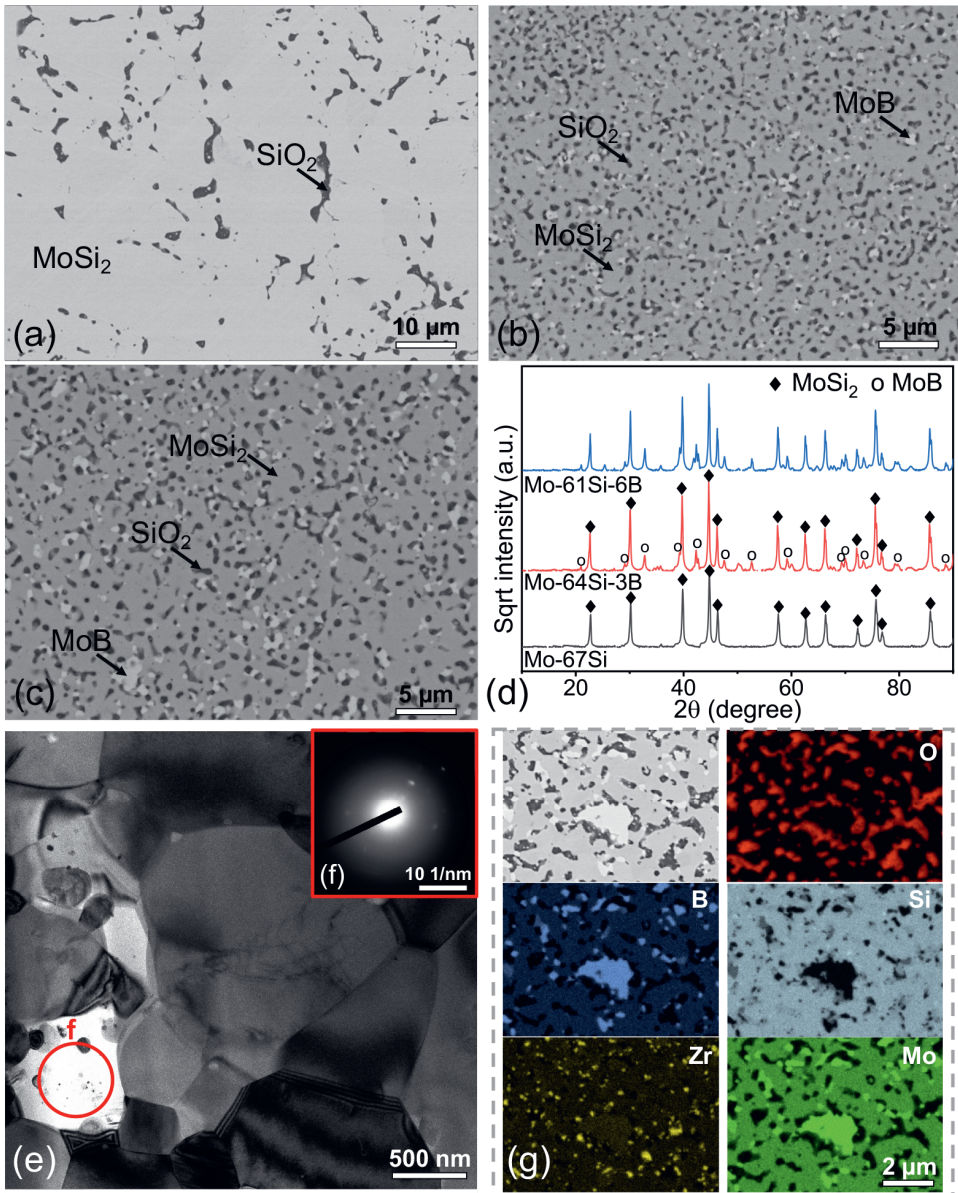
Figure 5. 1. SEM back scattered electron images of the microstructure of Mo–Si–B alloys: (a) Mo–67Si, (b) Mo–64Si–3B and (c) Mo–61Si–6B; (d) X-ray diffraction patterns of the Mo–Si–B alloys; (e) bright-field TEM image of Mo–61Si–6B; (f) SAED pattern of the area in (e) showing amorphous SiO_2; (g) X-ray emission maps of the elements in Mo–61Si–6B.

111

The weight gain per unit surface area of the Mo–Si–B alloys recorded during oxidation at 1100 °C in synthetic air is shown in Figure 5. 2a. Although the weight gain during this oxidation process is very small, it can be observed clearly that the weight gain increases with increasing boron content of the Mo–Si–(B) alloys. The linear fits of the mass gain versus oxidation time in Figure 5. 2b suggest that the oxide layer growth obeys a parabolic growth rate law after an initial transient oxidation period. This indicates that the oxidation is dominated by diffusion during the steady state regime. The growth of the silica or borosilicate layer occurs by diffusion of oxygen through the developing layer. It has been reported that two main mechanisms are possible: O_2 permeation through the structure and O^{2-} self-diffusion through the network of bonded oxygen via point defects, respectively [20]. Thus, the rate-limiting step in the oxidation of $MoSi_2$ is the inward diffusion of O^{2-} or O_2 through the developing continuous SiO_2 layer [8, 18].

In an attempt to describe the oxidation process quantitatively, the oxidation kinetics was formulated as a power law with exponent n [21]:

$$\left(\frac{\Delta m}{A}\right)^n = k_m t \tag{5.1},$$

where Δm is the weight change; A is the surface area of the sample and t the isothermal oxidation time; k_m denotes the oxidation rate constant. The exponent n versus time t can be derived from the mass change data with [22]:

$$\frac{1}{n} = \frac{\partial \log(\frac{\Delta m}{A})}{\partial \log(t)} \tag{5.2}.$$

Analysis of the exponent n as a function of oxidation time of the oxide growth curves shows that the oxide growth proceeds a transition from an initial linear growth rate to a parabolic growth rate regime; see Figure 5. 2c. A slightly shortened transient stage in the Mo–61Si–6B than Mo–67Si alloy can be seen in Figure 5. 2c, indicating a faster complete coverage of boron doped SiO_2 (borosilicate). The parabolic growth rate constant increases proportional with the boron content of Mo–Si–(B) alloy; see Figure 5. 2d. In practice, the enhanced rate is still acceptable, since it promotes the complete coverage of the $MoSi_2$ alloy by a protective oxide scale which is the key to oxidation resistance.
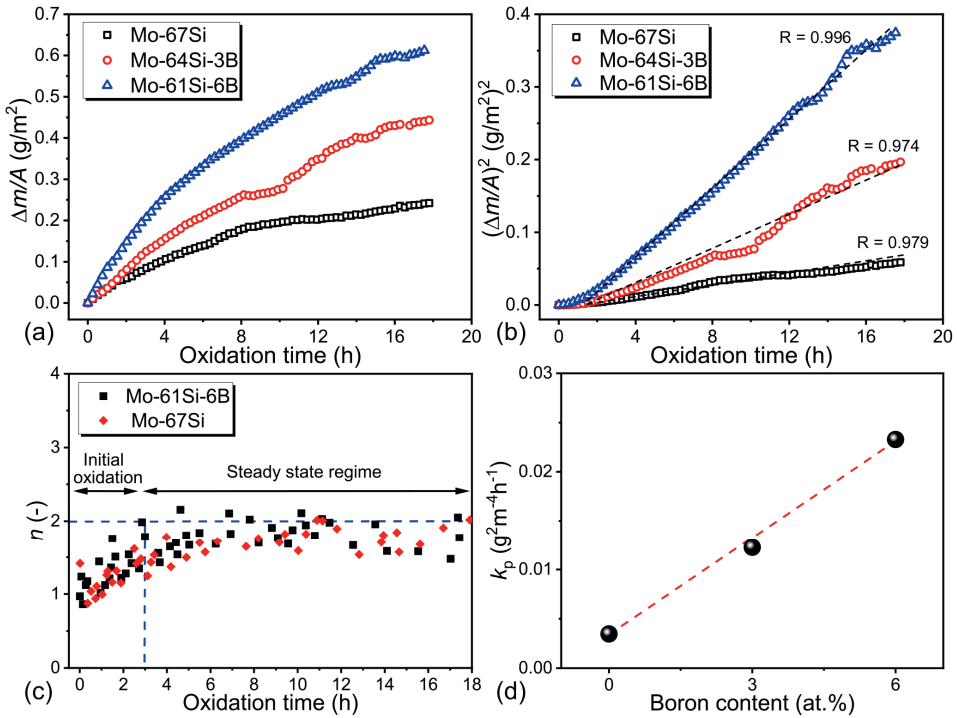
Figure 5. 2. Thermogravimetric analysis of the oxidation of Mo–Si–B at 1100 ºC in synthetic air as a function of oxidation time in terms of (a) weight gain per unit area; (b) squared weight gain per unit area; (c) exponent n of a power law (cf. Eq. (5.1)); and (d) parabolic oxide growth rate constant k_p as a function of the alloy boron content (red dashed line only to guide the eyes).

After oxidation of the alloys in dry synthetic air at 1100 °C for 20 hours, their surfaces are covered with an oxide scale of SiO_2; see Figure 5. 3. It can be observed that the boron promotes the formation of a smooth and glassy film on Mo–Si–B at the surface. The bright protuberances are Zr containing species according to X-ray microanalysis, which stems from the ball milling process. Some needle like oxide can be observed on the oxide scale of pure $MoSi_2$ after oxidation, which is apparently MoO_3 condensate at the surface.

5

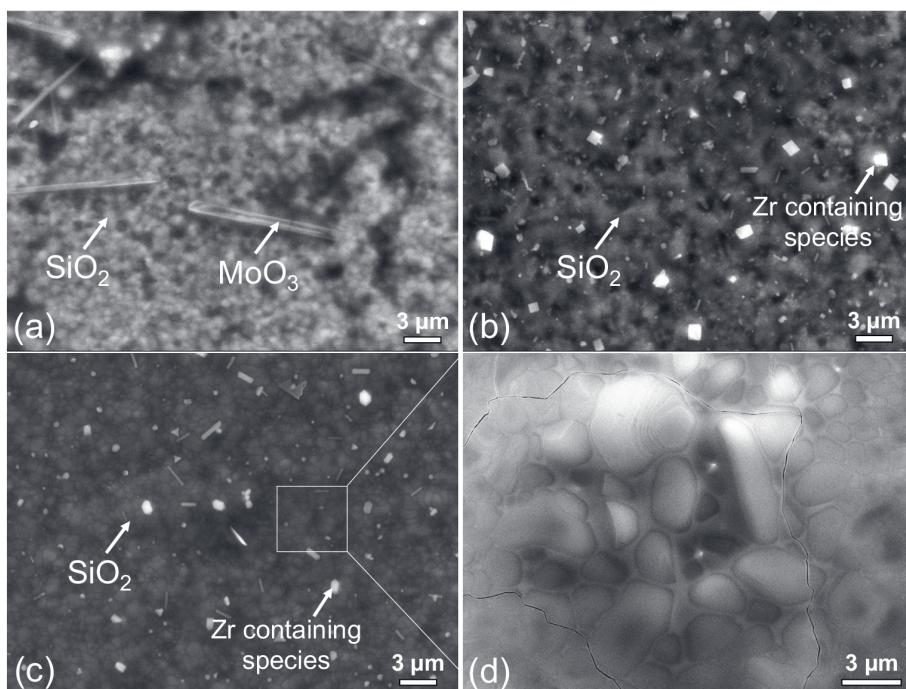Figure 5. 3. Surface morphologies of the Mo–Si–B alloys after oxidation at 1100 °C in synthetic air for 20 hours: (a) Mo–67Si; (b) Mo–64Si–3B; (c) and (d) Mo–61Si–6B.

Cristobalite with a tetragonal crystal lattice in the silica layer formed on Mo–Si–(B) alloys was identified with XRD using a grazing incidence geometry; see Figure 5. 4a. In addition, the peaks at 230 and 410 cm^{-1} in the Raman spectra (Figure 5. 4b) of the oxidized Mo–Si–(B) alloys can be assigned to the A_1 modes from cristobalite [23, 24]. Further, two Raman active lattice modes are clearly seen in Figure 5. 4b, namely an A_{1g} mode and an E_g mode at 326 and 440 cm^{-1}, respectively, both pertaining to t-MoSi$_2$ [25]. A significant band in the 610–680 cm^{-1} region can be observed in the Raman spectra of the oxidized Mo–64Si–3B and Mo–61Si–6B alloys, but not in the spectrum of oxidized pure MoSi$_2$; see Figure 5. 4b. The band in the 610–630 cm^{-1} region is associated to vibrations of metaborate anions of the ring type [26]. The band near 680 cm^{-1} is associated with the bending motion of oxygen bonds contributing to defect structures [26]. These defect structures have been reported to consist of broken oxygen bridges within the silicate network, which hints at an amorphous structure of the oxide formed on the alloys with boron.
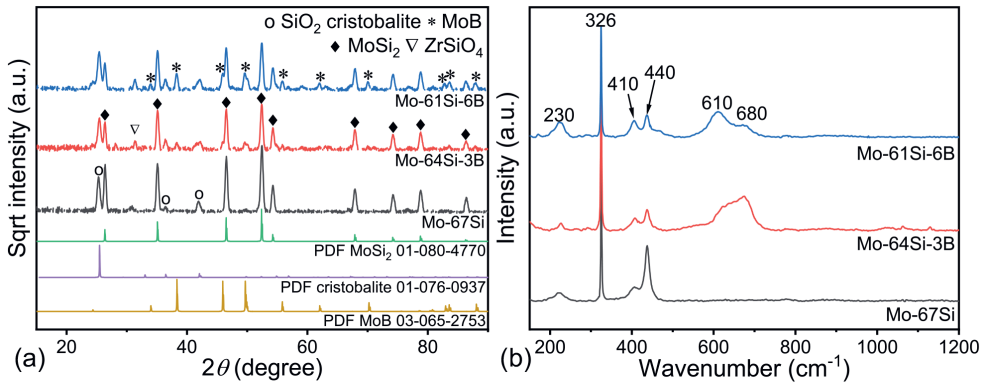
Figure 5. 4. (a) XRD patterns recorded with grazing incidence geometry and (b) Raman spectra of Mo–Si–B alloys after oxidation at 1100 °C in synthetic air for 20 hours.

Cross-sections of the oxidized alloys confirm a continuous and dense SiO_2 film of which the thickness increases with alloy B content; see Figure 5. 5a–c. In the oxide layer grown on the Mo–64Si–3B and Mo–61Si–6B alloys, inclusions with a size of about 40 nm can be seen near the interface with the alloy; see Figure 5. 5b and c. Local composition analysis with X-ray micro analysis (XMA) indicates that these inclusions are a mix of MoB and MoO_3; see Figure 5. 5d–g.

5

Figure 5. 5. STEM image (HAADF) of cross-section of Mo–Si–B alloys after oxidation at 1100 °C in synthetic air for 20 hours: (a) Mo–67Si, (b) Mo–64Si–3B and (c) Mo–61Si–6B; and (d) image of area indicated by the red box in (c) with (e), (f) and (g) the corresponding X-ray emission maps of B, Mo and O, respectively.

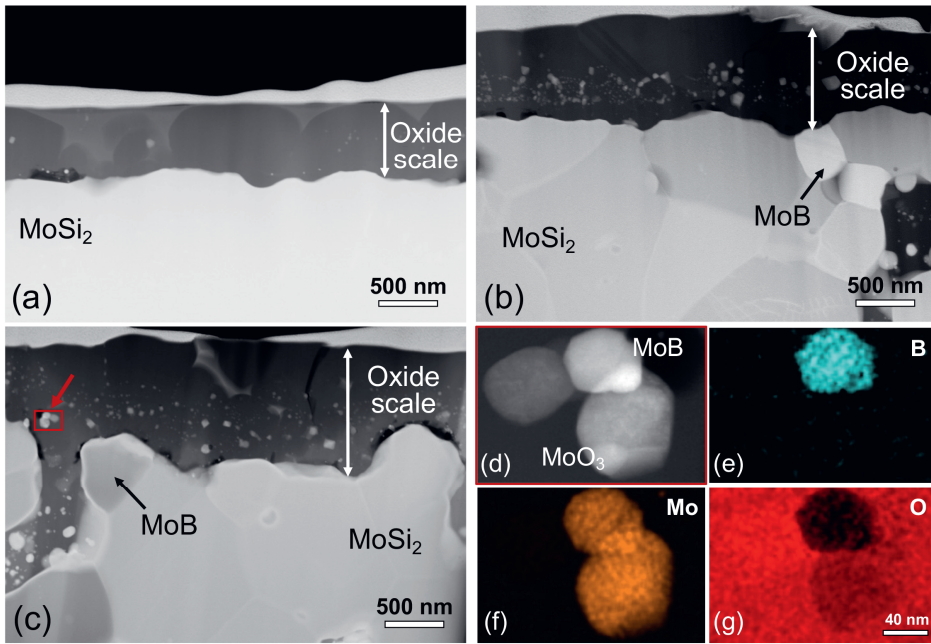High-resolution transmission electron microscopy (HRTEM) of the oxide scale formed on Mo–67Si alloy show crystalline fragments in the SiO_2 scale; see Figure 5. 6a. The d-spacing of these crystalline fragments are 0.49 and 0.28 nm, respectively, which can be assigned to (100) and (012) lattice planes of cristobalite having a tetragonal structure; see Figure 5. 6b. The diffraction pattern obtained by Fast Fourier transformation (FFT) of the HRTEM image confirms that the crystalline phase is tetragonal cristobalite; see Figure 5. 5c. SiO_2 with an amorphous structure surrounding the cristobalite fragments was also observed in the silica scale on pure $MoSi_2$ (see Figure 5. 6a), which is likely ascribed to high diffuse electron scattering intensities (DSIs) [16, 17].

Such crystalline SiO_2 fragments can hardly be found in the oxide scale formed on Mo–64Si–3B and Mo–61Si–6B. Only near the interface with MoB small orderly arranged atoms clusters were observed within the amorphous oxide scale of SiO_2; see Figure 5. 6d. FFT of these regions in the HRTEM image shows that the pattern matches well with the simulated

diffraction pattern of teragonal cristobalite. Thus, the presence of B promotes the formation of amorphous structure in the SiO_2 scale. As a reference, the FFT of the lattice fringes in the HRTEM image pertaining to the MoB phase was also performed and the pattern matches well with the simulated SAED pattern of tetragonal MoB. The amount of cristobalite in the SiO_2 layer reduces with increasing boron content in the Mo–Si–B alloy which also indicates that boron effectively promotes the formation of amorphous SiO_2.

Upon oxidation, the MoB in the alloy is oxidized resulting in B_2O_3, which dissolves in SiO_2 as a network modifier [27]. Then, some Si–O bonds are broken, which is beneficial for vitrification and hinders crystallization of SiO_2 [28]. This change of the local order of SiO_2 enhances the diffusivity of oxygen. Since the diffusion channels in cristobalite are smaller in size than the mean of those in amorphous SiO_2, the O_2 permeation is heavily suppressed in a crystalline SiO_2 when compared to the enlarged ring channels in SiO_2 glass [29, 30]. It has been reported that the diffusivity of oxygen in amorphous SiO_2 is about five times greater than that in cristobalite at high temperature [20], which explains the enhanced diffusion-controlled oxidation of Mo–Si–(B) alloys with increasing boron addition.

5
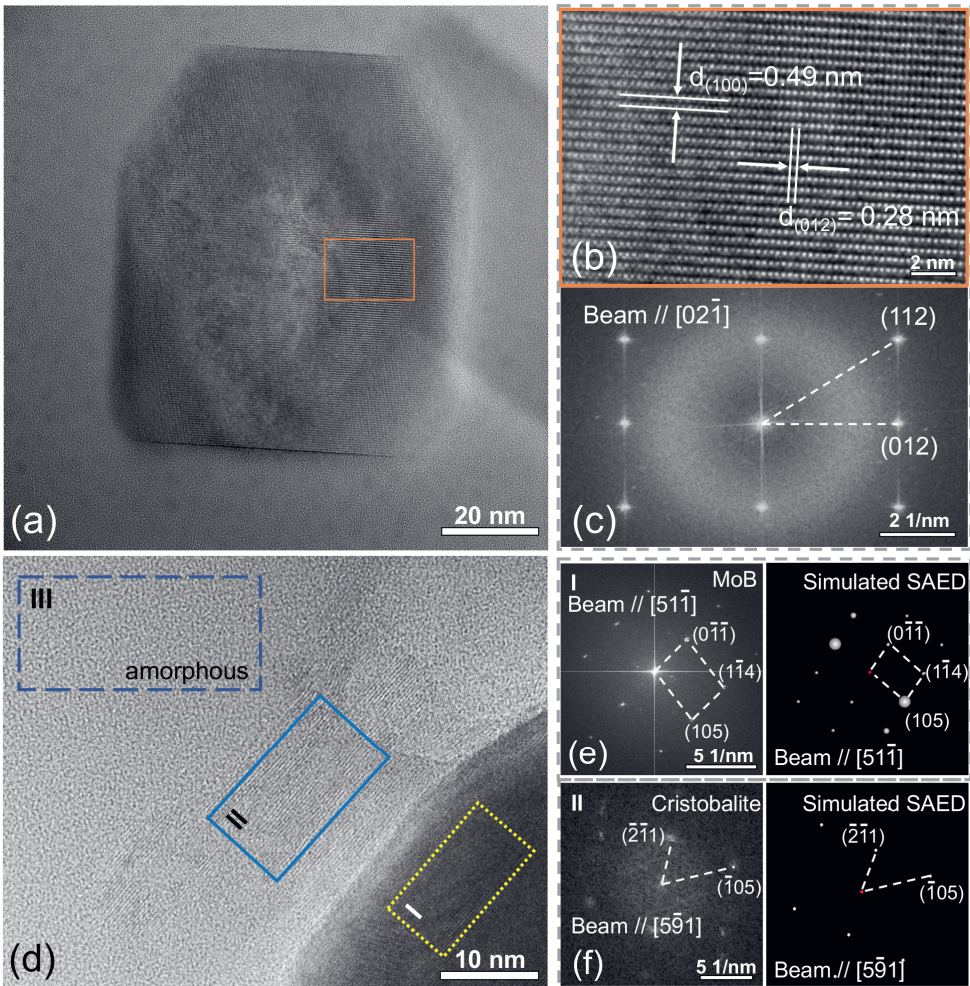
Figure 5. 6. Evidence of cristobalite nanocrystals from HRTEM after oxidation at 1100 °C in synthetic air for 20 hours: (a)–(c) belongs to Mo–67Si and (d)–(f) belongs to Mo–61Si–6B; (a) HRTEM image of the oxide scale grown on Mo–67Si showing crystalline SiO_2 patch in the amorphous SiO_2; (b) HRTEM image of the frame area in (a); (c) FFT of image (b); (d) HRTEM image of MoB-SiO_2 edge in the oxide scale on Mo–61Si–6B; (e) FFT of region I in HRTEM image (d) and simulated SAED by PDF-4+ software (version 2023) showing the orientation of MoB atomic layers; (f) FFT of region II in HRTEM image (d) and simulated SAED of cristobalite SiO_2. Region III in HRTEM image (d) shows amorphous SiO_2.

5.4. Conclusions

In conclusion, the high temperature oxidation in air of Mo–Si alloys is accelerated by addition of boron. The parabolic growth rate constant of the silica oxide layer increases proportional with the alloy boron content by 90% per at.%B; with respect to the alloy without boron. The addition of boron effectively mitigates the formation of cristobalite and promotes the formation of amorphous SiO_2, which provides enlarged channels for oxygen diffusivity. The enhanced rate caused by boron addition is acceptable since it promotes the formation of a smooth protective oxide scale and prevents other accelerated degradation like pesting.

5

References

[1] J.A. Lemberg, R.O. Ritchie, Mo-Si-B alloys for ultrahigh-temperature structural applications, Advanced Materials 24(26) (2012) 3445-80.

[2] J. Petrovic, MoSi$_2$-based high-temperature structural silicides, MRS Bulletin 18 (1993) 35-41.

[3] S.H. Wen, J.B. Sha, Isothermal and cyclic oxidation behaviours of MoSi$_2$ with additions of B at 1250 °C prepared by spark plasma sintering, Materials Characterization 139 (2018) 134-143.

[4] S.H. Wen, C.G. Zhou, J.B. Sha, Improvement of oxidation resistance of a Mo-62Si-5B (at.%) alloy at 1250 °C and 1350 °C via an in situ pre-formed SiO$_2$ fabricated by spark plasma sintering, Corrosion Science 127 (2017) 175-185.

[5] J.S. Park, R. Sakidja, J.H. Perepezko, Coating designs for oxidation control of Mo–Si–B alloys, Scripta Materialia 46 (2002) 765-770.

[6] F.A. Rioult, S.D. Imhoff, R. Sakidja, J.H. Perepezko, Transient oxidation of Mo–Si–B alloys: Effect of the microstructure size scale, Acta Materialia 57(15) (2009) 4600-4613.

[7] Z. Derelioglu, A.L. Carabat, G.M. Song, S.v.d. Zwaag, W.G. Sloof, On the use of B-alloyed MoSi$_2$ particles as crack healing agents in yttria stabilized zirconia thermal barrier coatings, Journal of the European Ceramic Society 35(16) (2015) 4507-4511.

[8] F. Nozahic, A.L. Carabat, W. Mao, D. Monceau, C. Estournes, C. Kwakernaak, S. van der Zwaag, W.G. Sloof, Kinetics of zircon formation in yttria partially stabilized zirconia as a result of oxidation of embedded molybdenum disilicide, Acta Materialia 174 (2019) 206-216.

[9] Z. Chen, W. Shao, M. Li, Z. Wu, P. Peng, C. Zhou, Effect of minor B modification on the oxidation behavior of MoSi$_2$ alloy at high temperature, Corrosion Science 216 (2023).

[10] X.Q. Liu, Z.M. Guo, C. Ma, T. Lin, Microstructure of MoSi$_2$ coating with B addition prepared by vacuum cladding, Advanced Materials Research 468-471 (2012) 2111-2114.

[11] J. Pang, W. Wang, C. Zhou, Microstructure evolution and oxidation behavior of B modified MoSi$_2$ coating on Nb–Si based alloys, Corrosion Science 105 (2016) 1-7.

[12] A.Y. Potanin, Y.S. Pogozhev, E.A. Levashov, A.V. Novikov, N.V. Shvindina, T.A. Sviridova, Kinetics and oxidation mechanism of MoSi$_2$–MoB ceramics in the 600–1200 °C temperature range, Ceramics International 43(13) (2017) 10478-10486.

[13] P.R. Taleghani, S.R. Bakhshi, M. Erfanmanesh, G.H. Borhani, R. Vafaei, Improvement of MoSi$_2$ oxidation resistance via boron addition: Fabrication of MoB/MoSi$_2$ composite by mechanical alloying and subsequent reactive sintering, Powder Technology 254 (2014) 241-247.

[14] C.D. Wirkus, D.R. Wilder, High-temperature oxidation of molybdenum disilicide, Journal of the American Ceramic Society 49(4) (1966) 173-177.

5

[15] D.A. Berztiss, R.R. Cerchiara, E.A. Gulbransen, F.S. Pettit, G.H. Meier, Oxidation of $MoSi_2$ and comparison with other silicide materials, Materials Science and Engineering A 155 (1992) 165-181.

[16] A. Cernok, K. Marquardt, R. Caracas, E. Bykova, G. Habler, H.P. Liermann, M. Hanfland, M. Mezouar, E. Bobocioiu, L. Dubrovinsky, Compressional pathways of alpha-cristobalite, structure of cristobalite X-I, and towards the understanding of seifertite formation, Nature Communication 8 (2017) 15647.

[17] C.-H. Chao, H.-y. Lu, β-Cristobalite stabilization in (Na2O + Al2O3)-added silica, Metallurgical and Materials Transactions A 33A (2002) 2703-2711.

[18] S. Knittel, S. Mathieu, M. Vilasi, The oxidation behaviour of uniaxial hot pressed MoSi2 in air from 400 to 1400 °C, Intermetallics 19(8) (2011) 1207-1215.

[19] Y. Danzaki, K. Wagatsuma, T. Syoji, K. Yoshimi, Dissolution of molybdenum-silicon (-boron) alloys using a mixture of sulfuric, nitric and hydrofluoric acids and a sequential correction method for ICP-AES analysis, Fresenius' Journal of Analytical Chemistry 369 (2001) 184-186.

[20] J. Rodríguez‐Viejo, F. Sibieude, M.T. Clavaguera‐Mora, C. Monty, [18]O diffusion through amorphous SiO_2 and cristobalite, Applied Physics Letters 63(14) (1993) 1906-1908.

[21] D.J. Young, High temperature oxidation and corrosion of metals, Elsevier2008.

[22] Z. Ding, J.C. Brouwer, C. Kwakernaak, M.J.M. Hermans, V. Popovich, W.J. Quadakkers, W.G. Sloof, Selective oxidation of aluminium in $Mo(Al,Si)_2$, Corrosion Science 211 (2023).

[23] J. Etchepare, M. Merian, P. Kaplan, Vibrational normal modes of SiO_2. II. Cristobalite and tridymite, The Journal of Chemical Physics 68(4) (1978) 1531-1537.

[24] J.B. Bates, Raman spectra of α and β cristobalite, The Journal of Chemical Physics 57 (1972) 4042-4047.

[25] G.A. Yakaboylu, T. Yumak, K. Sabolsky, E.M. Sabolsky, Effect of high temperature preoxidation treatment on the oxidation behavior of $MoSi_2$- and WSi_2–Al_2O_3 composites, Journal of Alloys and Compounds 816 (2020).

[26] J. Kline, M. Tangstad, G. Tranell, A raman spectroscopic study of the structural modifications associated with the addition of calcium oxide and boron oxide to silica, Metallurgical and Materials Transactions B 46(1) (2014) 62-73.

[27] B. Liang, Z.-H. Yang, D.-C. Jia, J.-C. Rao, D.-L. Yu, Y.-J. Tian, Q. Li, Y. Miao, Q.-S. Zhu, Y. Zhou, Amorphous silicoboron carbonitride monoliths resistant to flowing air up to 1800 °C, Corrosion Science 109 (2016) 162-173.

[28] M.I. Ojovan, W.E. Lee, 17-Immobilisation of radioactive waste in glass, in: M.I. Ojovan, W.E. Lee (Eds.), An Introduction to Nuclear Waste Immobilisation (Second Edition), Elsevier, Oxford, 2014, pp. 245-282.

5

[29] M.I. Heggie, R. Jones, C.D. Latham, S.C.P. Maynard, P. Tole, Molecular diffusion of oxygen and water in crystalline and amorphous silica, Philosophical Magazine B 65(3) (2006) 463-471.

[30] M.A. Lamkin, F.L. Riley, Oxygen mobility in silicon dioxide and silicate glasses: a review, Journal of the European Ceramic Society 10 (1992) 347-367.

5

6.

On the high temperature oxidation of MoSi₂ particles with boron addition

Abstract

Boron doped $MoSi_2$ particles have been envisioned as sacrificial particles for self-healing thermal barrier coatings (TBCs) but their oxidation behaviour is yet not well understood. In this work, oxidation of $MoSi_2$ based particle is studied in the temperature range of 1050 to 1200 °C. The oxidation proceeds from a transient to a steady-state oxidation stage. The kinetics during steady-state oxidation is captured with a thermal diffusion-based model. As compared to the oxidation of pure $MoSi_2$ particles, the addition of boron strongly enhances the silica formation. Also, a finer dispersion of MoB_x in the $MoSi_2$ matrix accelerates the formation of silica. The oxide growth rate constant increases proportional with the boron content of the $MoSi_2$ particles. This enhanced oxidation is related to the microstructure of the oxide scale. Boron promotes the formation of amorphous borosilicate mitigating the formation of crystalline SiO_2, consequently accelerating the migration of oxygen within the oxide scale.

6.1. Introduction

With a melting point over 2000 °C, moderate density (6.3 g cm^{-3}), and outstanding oxidation resistance, molybdenum disilicide ($MoSi_2$) is an attractive material for high-temperature applications such as heating elements, protective coatings, engines parts, *etc* [1-3]. Moreover, particles of $MoSi_2$ with small amounts of boron are envisioned as sacrificial particles for self-healing thermal barrier coatings (TBCs) [4-6]. Then, these particles are embedded in yttria partially stabilized zirconia (YPSZ) [4]. Once intercepted by cracks [7, 8], the $MoSi_2$ based particles oxidize preferentially and the oxidation product of amorphous SiO_2 fills the crack gaps and subsequently reacts with ZrO_2 of the YPSZ matrix to form $ZrSiO_4$ at the crack face surfaces restoring the mechanical integrity [4-6, 9]. In this context, the presence of boron in the $MoSi_2$ particles is paramount for crack healing since it increases the fluidity of the SiO_2 [4] and promotes the subsequent reaction with ZrO_2 to form the load-bearing phase of $ZrSiO_4$ [9]. Therefore, adding a small amount of boron in $MoSi_2$ particle becomes imperative in a self-healing TBC system, where the precise amount of boron addition holds the key to regulating the healing rate [10, 11].

The oxidation behaviour of bulk $MoSi_2$ in the temperature range of 400 to 1800 °C has been well documented [2, 3, 12-16]. However, the oxidation behaviour of $MoSi_2$ particles is rarely reported. In contrast with the oxidation of the bulk $MoSi_2$ [17, 18], the oxidation process of $MoSi_2$ based particles is much more complex due to stronger element depletion,

larger specific surface area and associated higher defect density of particles [19, 20]. When boron is added to $MoSi_2$ particles, knowledge about their oxidation behaviour is lacking. However, for the high temperature oxidation of bulk Mo–Si–B alloys [21-26], it has been reported that the oxidation significantly accelerated by adding a small trace of B [27].

This work focuses on the oxidation of two-phase $MoSi_2$–MoB_x particles. The oxidation of $MoSi_2$ particles with and without boron doping was investigated in the temperature range from 1050 up to 1200 °C. The effects of particle size, boron content and microstructure on the oxidation kinetics were studied at 1100 °C. The microstructure evolution of the oxide scale was investigated to reveal the oxidation mechanism.

6.2. Materials and methods

6.2.1. Particle preparation

6.2.1.1. Starting material

$MoSi_2$ powders with and without boron (< 45 μm, ChemPUR GmbH, Germany) were used as the starting material. This starting material is wind-sifted to eliminate the extremely fine fraction of the particles; see the particle size distribution in Figure 6. 1. Wind sifting was performed using an Alpine 100 MRZ laboratory zig-zag classifier (Alpine Multi-Plex 100 MRZ, Hosokawa Micron Powder System, USA) with the airflow fixed at 15 m^3 h^{-1} and the classifier rotational speed kept at 5000 rpm. To confirm the boron content of the material, the wind-sifted particles were analysed using inductively couple plasma optical emission spectroscopy (ICP-OES, using iCAP 6500 Duo, Thermo Fisher Scientific). The dissolution process was specifically designed for the Mo–Si–B system [28]. The measured content of boron is 1.3 wt% (6 at.%), which is lower than the nominal 2 wt%; see Table 6. 1. Henceforth, the particles are denoted as wind-sifted Mo–67Si and wind-sifted Mo–58Si–7B, respectively.
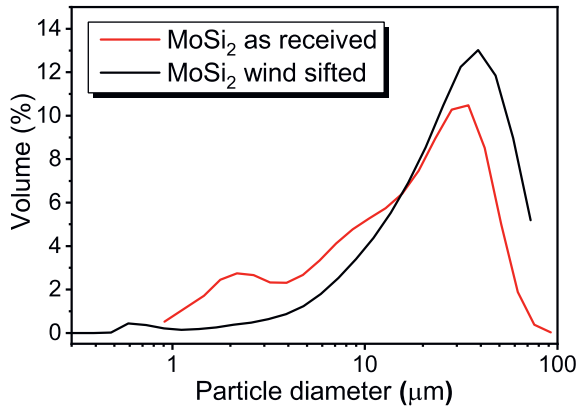
Figure 6. 1. Particle size distribution of $MoSi_2$ healing particles in as received conditions (black solid line) and after wind sifting (red solid line).

6.2.1.2. Particles with different sizes

To investigate the influence of particle size on the oxidation kinetics, different size fractions of the wind-sifted Mo–58Si–6B particles were prepared via sieving the particles through 20 and 50 µm sieves (Analysensieb, DIN-ISO 3310-1, Retsch, Germany). Thus, fine particles with a size of $d < 20$ µm and particles with a size of $20 < d < 50$ µm were obtained. The coarse particles ($d > 50$ µm) were discarded. In the end, three batches of particles with different sizes distribution were prepared, namely wind-sifted particles containing a mixture of fine and coarse particles, fine fraction of the sieved particles with particle size of $d < 20$ µm and sieved particles with particle size of $20 < d < 50$ µm. Their morphologies and size distribution are shown in Figure 6. 2a–f.

In order to confirm the boron content of the particles with different sizes, ICP-OES analysis was conducted according to the same procedure as mentioned in Section 6.2.1.1; see Table 6. 1. The boron content of particles with different sizes do not differ much.

6
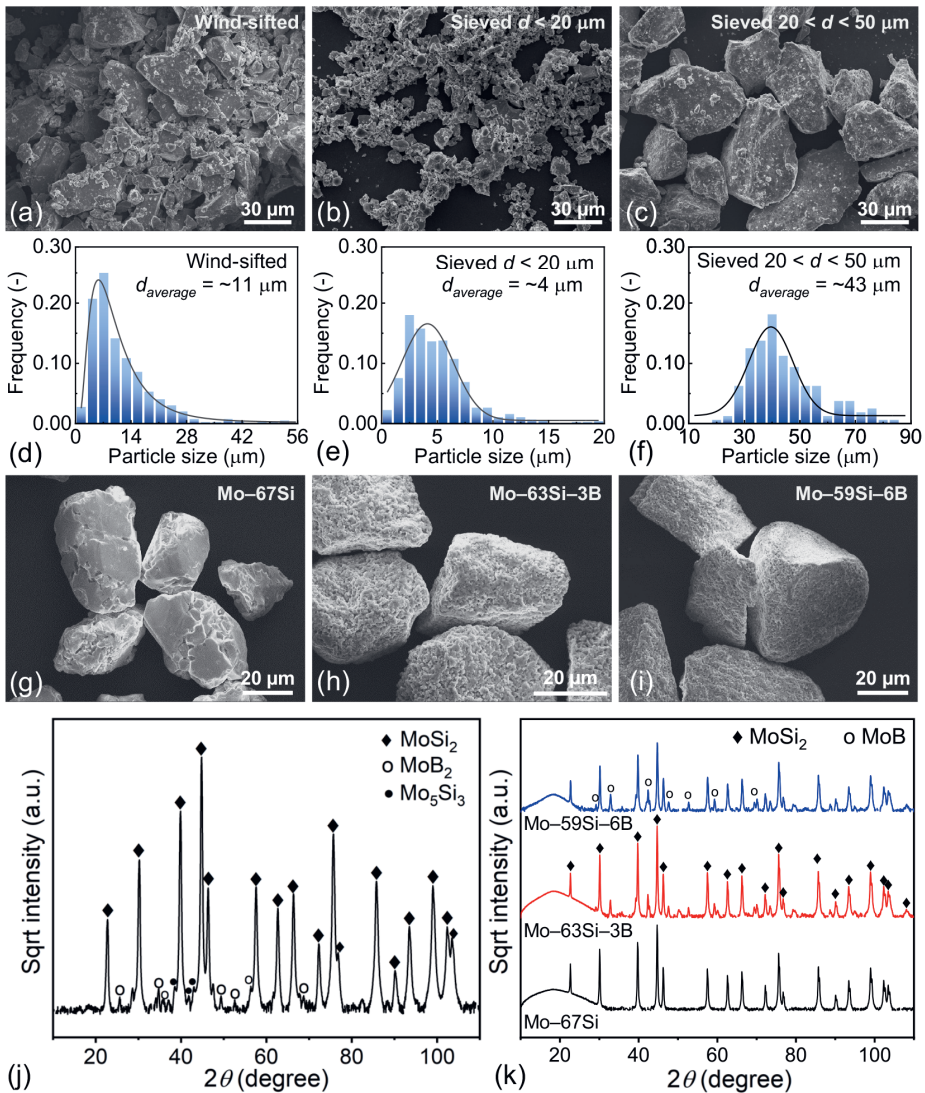
Figure 6. 2. (a)–(c) SEM images of the morphology of MoSi2 particles with boron addition and different sizes: (a) wind-sifted particles contain a mixture of fine and coarse particles; (b) fine fraction of the sieved particle with particle size of $d < 20$ µm; (c) sieved particle with a uniform particle size of $20 < d < 50$ µm and (d)–(f) the corresponding particle size distribution; (g)–(i) SEM images of the morphology of spheroidized Mo–Si based particles prepared from crunching a SPS tablet and a gentle ball milling and polishing process afterwards; XRD patterns of (j) wind-sifted Mo–58Si–6B particles and (k) spheroidized Mo–Si based particles.

6.2.1.3. Particles with various boron content

A mixture of the starting powders, i.e., $MoSi_2$ without and with 6 at.% B, with a ratio of 1:1 were prepared to obtain $MoSi_2$ with 3 at.% B particles. To refine the dispersion of the MoB phase in the particles, the starting powders and their mixtures were milled using a planetary ball mill (PM100, Retsch GmbH, Germany). Wet ball-milling of the powders was conducted in isopropanol using zirconia balls (100 and 8 balls with diameter of 5 and 10 mm, respectively) and a zirconia jar (50 ml). The weight ratio between balls and powder was about 5:1. The milling speed was 300 rpm and the milling time was 3 hours with cycles of 20 minutes running and 10 minutes pause, i.e., the effective milling time was 2 hours. Subsequently, the milled powder was dried in the oven for 12 hours at 80 °C. The dried powder was then sieved with a 200 μm mesh sieve. ICP-OES analysis was conducted according to the same procedure as mentioned in Section 6.2.1.1 and the as determined boron content of the ball milled powders was 3 and 6 at.% respectively, demonstrating that there is no significant loss of boron in the ball milling process; see Table 6. 1.

Table 6. 1. Summary of prepared particles and their corresponding processing conditions.

Nominal composition (-)	Pre-treatment (-)	Boron content (wt%)	Actual composition (-)
$MoSi_2$	Wind-sifted	0.0	Mo–67Si
	Wind-sifted	1.3	Mo–58Si–6B
$MoSi_2$-2 wt% B	Sieved $20 < d < 50$ μm	1.4	Mo–58Si–7B
	Sieved $d < 20$ μm	1.5	Mo–57Si–7B
$MoSi_2$	Refined and spheroidized	/	Mo–67Si
$MoSi_2$-1 wt% B	Refined and spheroidized	0.7	Mo–63Si–3B
$MoSi_2$-2 wt% B	Refined and spheroidized	1.3	Mo–59Si–6B

6

Next, the above ball milled powders were densified by means of spark plasma sintering (SPS) with a HP D 25 SD furnace (FCT Systeme GmbH, Germany) at 1500 °C for 30 minutes in a flowing argon atmosphere with a pressure of 50 MPa. The heating was 20 °C min^{-1}, while natural cooling was used to cool down from the sintering temperature to room temperature.
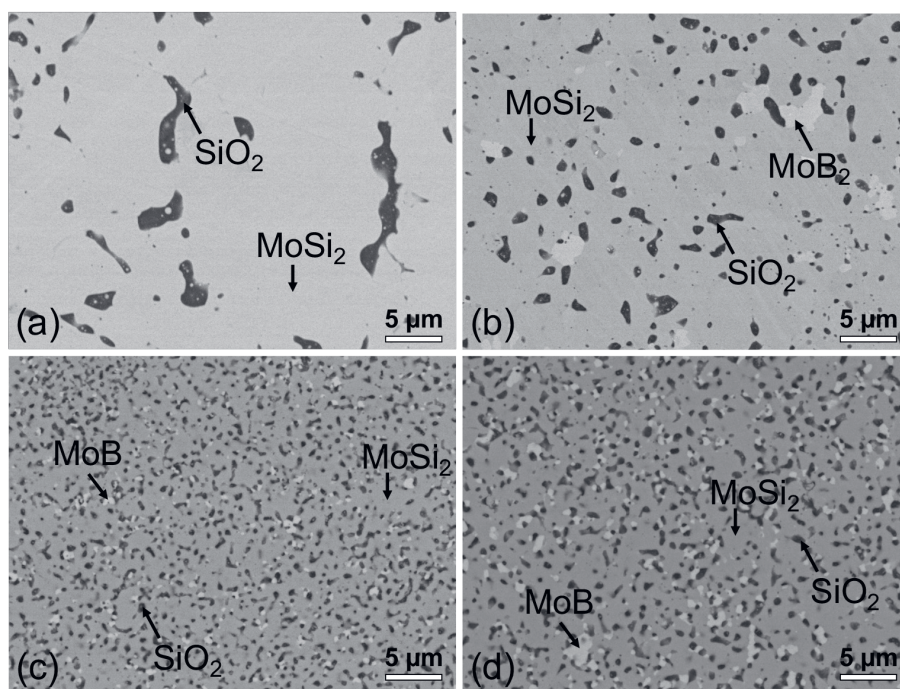
Figure 6. 3. SEM back scattered electron images of the microstructure of different Mo–Si based bulk materials prepared with SPS from: (a) Mo–67Si particles, (b) as-received Mo–58Si–6B particles, (c) ball milled Mo–64Si–3B particles and (d) ball milled Mo–59Si–6B particles.

6

The microstructure of the densified material prepared by SPS of the as received and ball milled $MoSi_2$ based powders is shown in Figure 6. 3. It is evident that the ball milling treatment of the $MoSi_2$ based powders promotes an even and fine distribution of the boride phase; comparing Figure 6. 3c and 2d with Figure 6. 3b. Inclusion of SiO_2 can be observed in the microstructures in Figure 6. 3 but cannot be seen in the diffractograms, indicating an amorphous nature.

The dense materials prepared were pulverized and sieved. The pulverizing was done using a Fritsch Pulverisette (type P-0150, Germany) with a steel ball (diameter 70 mm). To spheroidize the crushed powders, a combined ball milling and polishing process was executed. Full details of the particle processing procedure can be found in [18]. The morphology of the spheroidized particles is shown in Figure 6. 2g–i. As compared with the

starting powders, the size of these particles is more uniform and their shape is more spherical. Transition from MoB_2 to MoB was observed in the microstructure refinement since MoB phase exhibits the lowest energy of formation among all the molybdenum borides [29]; see the diffractograms in Figure 6. 2j–k. This observation is in agreement with the isothermal section of the Mo–Si–B ternary phase diagram at 1450 °C [30] (close to the sintering temperature of 1500 °C).

6.2.2. Isothermal high temperature oxidation

The isothermal oxidation kinetics of the $MoSi_2$ based particles at temperatures in the range of 1050 to 1200 °C in terms of mass change was assessed via thermogravimetric analyses, using a dual furnace balance (Seteram TAG 16/18, France) which allows automatic correction for buoyancy effects. The alumina furnace tubes have an inner diameter of 15 mm. This analyser is equipped with Pt/Pt-10%Rh (S-type) thermocouples. The mass change of the particles was recorded upon oxidation in dry synthetic air (N_2 with 20 vol.% O_2). The gas mixture was admitted to the TGA analyser via mass flow controllers (Bronkhorst, The Netherlands) operated with Labview (version 2020) such that the total gas flow matches 100 sccm, which was equally divided over both furnace tubes. Prior to admitting the gas mixture to the furnace, each gas, i.e., both oxygen and nitrogen (Linde Gas Benelux BV, purity better than 5N), were filtered to remove any residual moisture and hydrocarbons, with Hydrosorb (< 20 ppb H_2O) and Accosorb (< 10 ppb hydrocarbons) filters (Messer Griesheim, Germany), respectively. The nitrogen gas was additionally filtered to remove residual oxygen with an Oxysorb filter (< 5 ppb O_2).

Approximately 200 mg particles were loaded into a 100 μL alumina crucible. The initial mass of the particles was weighed using a Mettler Toledo mechanical balance (AG-204, Switzerland, accuracy $\pm$ 1 μg). The crucible with the particles was mounted at one side of the balance and an identical but empty crucible was mounted at the other side of the balance. Both furnaces, each at one side of the balance, were heated simultaneously with 10 °C min^{-1} in a flow of pure nitrogen. When both furnaces of the thermogravimetric analyser reached the target temperature, oxygen was added to the nitrogen gas flow to create dry synthetic air during the isothermal hold.

6

6.2.3. Characterization

The phase composition of the materials was determined with X-ray diffractometry (XRD) using a D8 advance diffractometer (Bruker, Germany) operated with Co Ka radiation. Diffractograms were recorded in the 2θ range of 10 to 110° with a 2θ step size of 0.030° and a counting time per step of 2 s. These diffractograms were evaluated using the Bruker Diffrac EVA software (version 3.1). The microstructure in terms of boron distribution of the sintered tablets and the morphology of the particles was observed with scanning electron microscopy (SEM) using a JEOL JSM 6500F (JEOL, Japan). To study the mechanism of boron accelerated $MoSi_2$ particle oxidation, scanning electron microscopy combined with a Xenon plasma focused ion beam (Helios G4 PFIB UXe, Thermo Fisher Scientific, USA) was performed to create cross-sections of the spheroidized particles after oxidation in dry synthetic air for 20 hours. First, the particles to be investigated were put on a silicon wafer (Si-<100> p-type, University Wafer, USA). Next, one of the particles was covered with about 2 μm layer of Pt added with some C using the electron beam operated at 12 keV. Then, the particle was cut with the Xenon plasma focused ion beam operated at 30 keV. Lamella for transmission electron microscopy (TEM) from selected areas in the oxide scale were also prepared with the plasma focused ion beam and subsequently lifted. Next, the thin lamellas were analysed with TEM using a Cs-corrected Titan ETEM G2 apparatus (FEI/Thermo Fisher Scientific, USA) operated at 300 keV, which was equipped with a Gatan K3 camera for performing electron energy loss spectroscopy (EELS). The elemental mapping and energy-dispersive spectroscopy (EDS) spectra were carried out with a Talos F200X field-emission TEM (FEI/Thermo Fisher Scientific, USA) operated at 200 keV, equipped with a high-brightness field emission gun (X-FEG) and a Super-X G2 EDX detector.
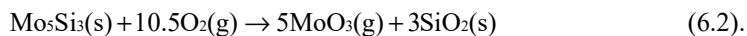
6.3. Results and discussion

6.3.1. Thermodynamic considerations

The oxidation of pure $MoSi_2$ particles proceeds according to [19]:

$$5MoSi_2(s) + 7O_2 \rightarrow Mo_5Si_3(s) + 7SiO_2(s) \tag{6.1};$$
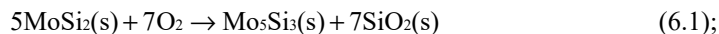
and Mo_5Si_3 subsequently oxidizes according to [13, 19]:

$$Mo_5Si_3(s) + 10.5O_2(g) \rightarrow 5MoO_3(g) + 3SiO_2(s) \tag{6.2}.$$

In the early stage of oxidation, the two reactions are considered to occur simultaneously rather than consecutively [19]. In the following stage, when a continuous SiO_2 passive layer is formed on the surface, the oxidation of Mo_5Si_3, i.e. Eq. (6.2), is suppressed [19]. This two-step oxidation process of pure $MoSi_2$ particles is consistent with what is generally accepted for the oxidation of bulk $MoSi_2$ [14]. Then, MoO_3 forms initially and evaporates quickly before the formation of a continuous SiO_2 film on $MoSi_2$.

The oxidation of boron in the system considered here proceeds according to [31]:

$$4MoB(s) + 7O_2 \rightarrow 4MoO_2(g) + 2B_2O_3(g) \qquad (6.3).$$
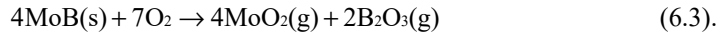
Given that the free energies of formation of B_2O_3 and SiO_2 are very close [32], Si and B tend oxidize simultaneously. Once these two oxides are formed (according to Eq. (6.1) and (6.3)), B_2O_3 and SiO_2 merge rapidly to form amorphous borosilicate.

The Mo–O, Si–O, and B–O stability diagrams pertaining to 1100 °C are presented in Figure 6. 4. It can be seen that the dissociation oxygen partial pressure of the oxides increases in of order SiO_2, B_2O_3, MoO_2, and MoO_3 (10^{-25}, 10^{-23}, 10^{-13} and 10^{-6} atm., respectively). Thus, SiO_2 is the most stable oxide, more than B_2O_3, which is more stable than MoO_2 and MoO_3. According to these stability diagrams (Figure 6. 4), the major volatile species are the higher order oxides of molybdenum, i.e. $(MoO_3)_2$. During the initial oxidation of pure $MoSi_2$ particles besides silica also volatile Mo-oxides are formed. Once the surfaces of these particles are fully covered with silica, the formation of Mo-oxides is terminated. Then, the oxidation proceeds from the early transient stage to the subsequent steady-state oxidation, during which only Si is selectively oxidized and the oxygen partial pressure at the oxide interface is governed by the equilibrium between Si in the alloy at the interface with the oxide scale composed of SiO_2 (about 10^{-25} atm. at 1100 °C). Therefore, the formation of a continuous SiO_2 or borosilicate scale on the surface marks the transition from a fast initial to a steady-state oxidation of $MoSi_2$ based particles.
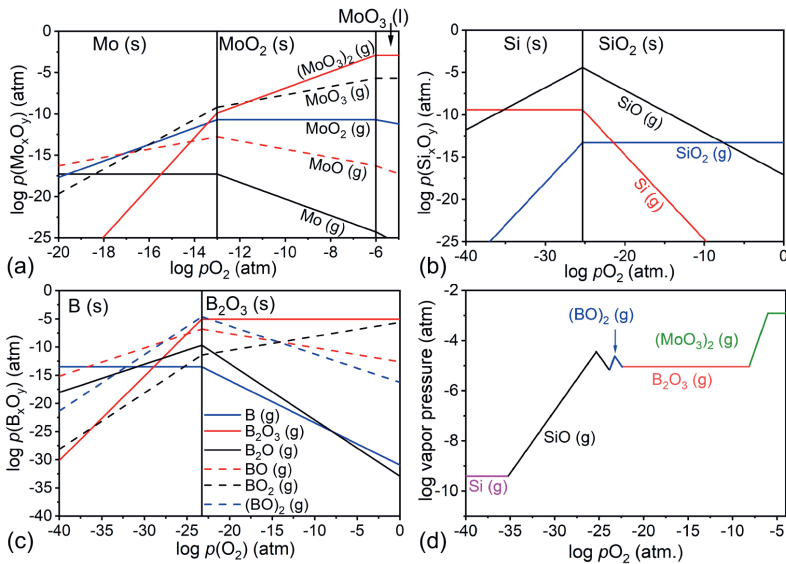
6

Figure 6. 4. Stability diagrams at 1100 °C for: (a) Mo–O, (b) Si–O, (c) B–O systems and (d) combined diagram presenting the species with the highest vapour pressure versus pO_2.

6.3.2. Oxidation kinetics

6.3.2.1. Effect of boron addition

The converted fraction (a) of wind-sifted Mo–67Si particles from $MoSi_2$ to SiO_2 is rather small during oxidation in the temperature range of 1050 up to 1200 °C; see Figure 6. 5a. But an increased conversion with increasing temperature can be clearly observed; see Figure 6. 5a.

The wind-sifted Mo–58Si–6B particles results in a much larger amount of silica formed upon oxidation in the temperature range of 1050 up to 1200 °C; see Figure 6. 5b. As compared to the oxidation of the Mo–67Si particles (Figure 6. 5a), the oxidation kinetics of the Mo–58Si–6B particles is strongly promoted by the addition of boron. Note that some weight loss can be observed at the initial oxidation stage of the boron doped $MoSi_2$ particles when oxidized at 1050 and 1100 °C; see Figure 6. 5b. This weight loss may also have happened at the higher oxidation temperatures, but is not seen because of the net weight increase. The weight loss during the initial stage of oxidation is associate with the formation of volatile species of MoO_3, which indicates that then the surface of the particles was not yet fully covered by a layer of SiO_2 (or borosilicate).
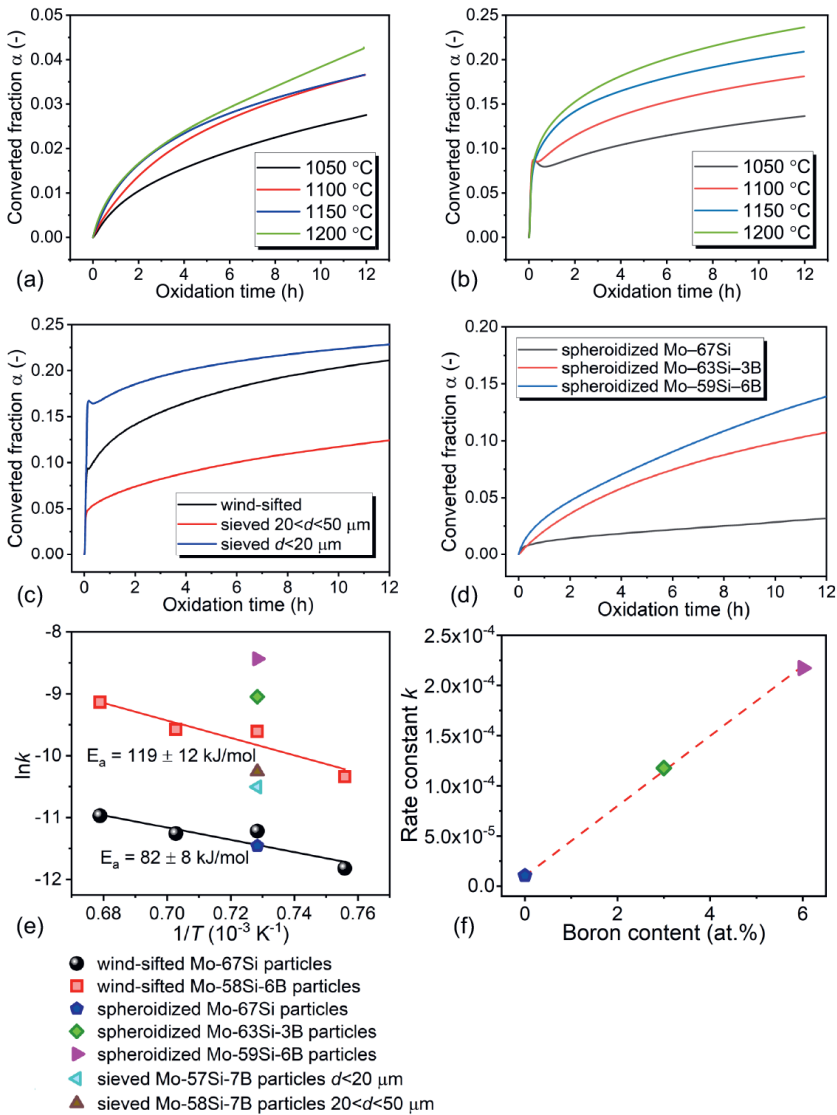
Figure 6. 5. Converted fraction α of (a) wind-sifted Mo–67Si particles and (b) wind-sifted Mo–58Si–6B particles after isothermal oxidation at between 1050 and 1200 °C in dry synthetic air for 12 hours; Converted fraction α of (c) Mo–Si–B particles with different particle sizes and (d) spheroidized Mo–Si based particles after isothermal oxidation at 1100 °C in dry synthetic air for 12 hours; the rate constant (e) ln k versus the inverse of absolute temperature ($1/T$) for all tested Mo–Si based particles and (f) k as a function of the boron content in the spheroidized Mo–Si based particles.

6.3.2.2. Effect of particle size

The converted fraction of the Mo–Si–B particles with different particle sizes upon oxidation in dry synthetic air in the temperature of 1100 °C is shown in Figure 6. 5c. As can be seen, the particles size has a significant effect on the initial oxidation; see Figure 6. 5c. The fine particles ($d < 20$ mm) exhibit largest conversion during the oxidation process with the fastest initial weight gain followed by a weight loss during the initial stage. Particles with size distribution of $20 < d < 50$ μm shows the least conversion and a weight loss cannot be observed anymore. This suggests that the surface of the particles is rapidly fully covered with silica and sealing the alloy, preventing volatile species to form. Thus, the transition from the initial to the steady oxidation state is enhanced by reducing the particle surface area corresponding with increasing particle size.

6.3.2.3. Effect of boron content

The isothermal oxidation kinetics of the spheroidized Mo–Si–B particles with different boron addition, at 1100 °C in dry synthetic air, in terms of the conversion of $MoSi_2$ upon oxidation is displayed in Figure 6. 5d. The conversion increased with increasing of boron addition, which further demonstrated the enhanced oxidation of $MoSi_2$ by a minor addition of boron.

6.3.2.4. Effect of particle microstructure

It is remarkable that the quick weight gain and the subsequent weight loss stage cannot be observed for these spherical particles with refined microstructure; cf. Figure 6. 5d. Apparently, the protective silica or borosilicate layer is rapidly formed, which suggests that when the boron containing phase is homogeneously distributed and particles are spherical and smooth. Hence, the transition from the initial fast to the steady-state oxidation state is further promoted.

6.3.3. Kinetic model

The rate of conversion into oxides upon thermal oxidation of the solid particles can be described with [33]:

$$\frac{d\alpha}{dt} = Ae^{-\left(\frac{E_a}{RT}\right)}f(\alpha) \qquad (6.4),$$

where A is the pre-exponential factor of the Arrhenius relation, E_a is the activation energy (J/mol), T is absolute temperature (K), R is the gas constant, $f(\alpha)$ represents the reaction model, and α is the conversion fraction. In a gravimetric measurement, α is defined by:

$$\alpha = \frac{m_t - m_0}{m_\infty - m_0} \qquad (6.5),$$

where m_0 denotes the initial mass, m_t is the mass at time t, and m_∞ is the mass after full conversion of the particles. Separating variables and integrating Eq. (6.4) gives the integral form of the isothermal rate law [33]:

$$g(\alpha) = kt \qquad (6.6),$$

$$\text{where } g(\alpha) = \int_0^\alpha \frac{d(\alpha)}{f(\alpha)} \qquad (6.7),$$

$$\text{and } k = Ae^{\left(-\frac{E_a}{RT}\right)} \qquad (6.8),$$

wherein $g(\alpha)$ is the integral reaction model and k being the rate constant. An experimental value for the rate constant k at different temperatures can be obtained from plotting $g(\alpha)$ versus t, once the kinetic model is established. The activation energy E_a and the frequency factor A can be estimated from ln k versus the reciprocal temperature (1/T).

The relative mass change ($\Delta m/m_0$) as recorded with thermogravimetry during the isothermal high temperature oxidation was used to determine the fraction of $MoSi_2$ based particles converted into oxidation products as a function of temperature and time. After the surface of the $MoSi_2$ based particles is covered with an oxide layer, the chemical reaction according to Eq. (6.1) is dominant [13, 14, 19]. Then, it holds that:

$$m_\infty / m_0 = (M_{Mo5Si3} + 7M_{SiO_2}) / 5M_{SiO_2} \qquad (6.9),$$

where M is the corresponding molar mass.

When a continuous oxide scale is formed on the surface of the particles, two possible oxygen migration mechanism may occur in the oxide scale [34]; namely: (i) molecular permeation through the channels of open space in the low-density structures and (ii) atomic oxygen self-diffusion through the network of bonded oxygen by making use of lattice

6

vacancies and interstitial positions. At high temperatures, these two kinds of diffusions can act simultaneously, which is a so called "interstitialcy diffusion" process. In this process, the presence of O_2 is required as an interstitial defect or "carrier" for the self-diffusion of oxygen. For diffusion-controlled solid-state reactions, the thermally activated oxidation process can be described best with the 3-D diffusion-Jander (D3) model [18, 33, 35] based on the assumption of spherical solid particles:

$$g(\alpha) = (1 - (1 - \alpha)^{1/3})^2 \qquad (6.10).$$

When combining Eq. (6.4)–(6.6) and Eq. (6.10), then the expression representing the converted fraction α can be calculated as:

$$\alpha = 1 - (1 - \sqrt{kt})^3 \qquad (6.11).$$

The D3 model was fitted to the conversion data pertaining to the steady-state oxidation stage; see Figure 6. 6. Comparison between the model and experimental data confirms that the D3 model describes well the oxidation kinetics of the MoSi$_2$ based particles in the steady-state oxidation.

The rate constant k is determined form a linear least-square fitting of Eq. (6.4) and (6.6) to the kinetic data at each isothermal oxidation; see Figure 6. 5e. The activation energy of the oxidation reaction of wind-sifted particles with and without boron addition is evaluated from the slope of a line a linear least-square fitted through the data of ln k versus the reciprocal of absolute temperature (1/T); see Figure 6. 5e. The activation energy equals to 82 ± 8 kJ/mol for the oxidation in the steady state of wind-sifted Mo–67Si particles, which is the same to the reported activation energy of oxygen transport through pure SiO$_2$ prepared by a gel process [36]. For the wind-sifted Mo–58Si–6B particles, the oxidation activation energy equals to 119 ± 12 kJ/mol, which corresponds well to the activation energy of oxygen diffusion in boron containing glasses (118 kJ/mol for low boron content) [36]. These values are close to the activation energies of the "interstitialcy diffusion" process (85–121 kJ/mol) [34], indication a simultaneous diffusion process of molecular O_2 and atomic O in the oxide scale formed on Mo–Si(–B) particles. The increased activation energy is likely related to the changing of the SiO$_2$ structure by boron addition [27, 36]. Large B$_5$O$_6$-ring segments build up inside the silica network, which increases the oxygen permeation [27, 34, 36]. The diffusion behavior by the exchange of network oxygen with interstitially dissolved O_2 is therefore also increased, which requires a higher activation energy [34, 37]. By increasing the boron content from 0 to 3 and 6 at.% of the spheroidized Mo–Si–B particles, the rate

constant in the steady-state oxidation increases proportionally; see Figure 6. 5f. This demonstrate that the accelerated oxidation can be attributed to the addition of boron.
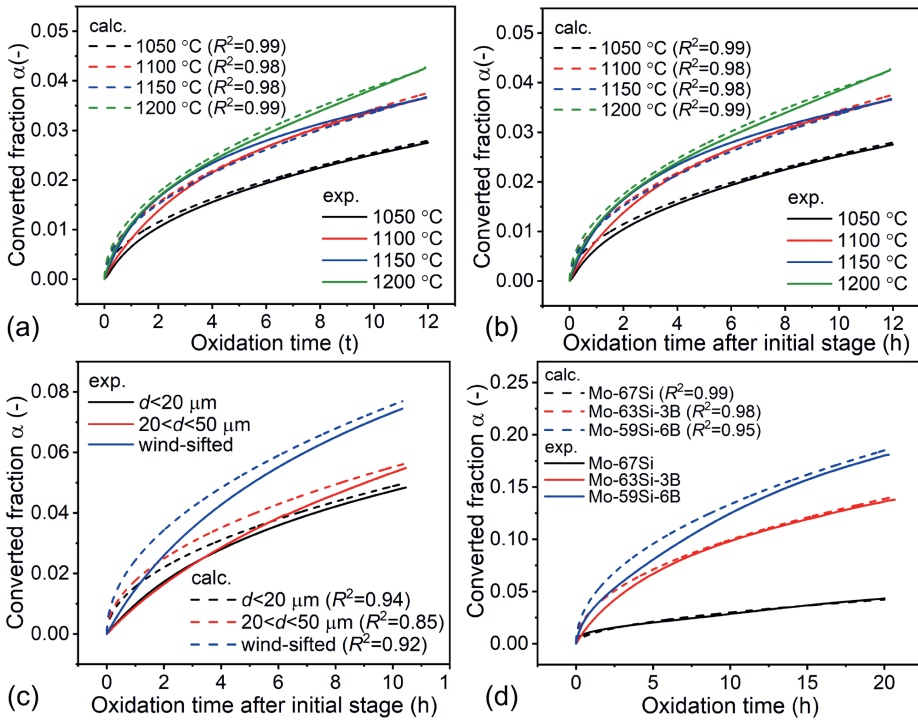

Figure 6. 6. Converted fraction α in the steady state of oxidation calculated using the integral form of Eq. (6.3) – (6.5) and the experimental data of isothermal oxidation of (a) wind-sifted Mo–67Si particles, (b) wind-sifted Mo–58Si–6B particles; (c) Mo–Si–B particles with different particle sizes; (d) spheroidized Mo–Si based particles. The starting time of (b) and (c) are set at t = 1.5 hours to skip the violent initial oxidation stage.

Although particle size has shown a significant effect on the initial oxidation, it has little effect on the steady-state oxidation of the MoSi$_2$ based particles. The oxide growth rate constant k is almost the same for the Mo–67Si particles after spheroidization and the wind-sifted Mo–67Si particles with irregular shape; see Figure 6. 5e. Also, not many differences can be observed among the oxide growth rate constant k of Mo–Si–B particles with different

139

particle sizes, namely wind-sifted particle with various particle size, fine particles with $d <$ 20 mm and particles with $20 < d < 50$ mm.

The microstructure of the $MoSi_2$ particles with boron addition, on the contrary, has a significant effect on the rate constant of steady-state oxidation. The rate constant of oxidation of Mo–Si–B particles increased from 3.5×10^{-5} s^{-1} (sieved Mo–58Si–7B particles with $20 < d < 50$ mm) to 2.2×10^{-4} s^{-1} (spheroidization Mo–59Si–6B particles, $20 < d < 50$ mm) by refining the boron distribution. For this reason, the diffusion distances of boron are reduced and the boron contained in the borosilicate covering the particles will diffuse more quickly into the structure and promote the formation of continuous passive layer. A shortened transient oxidation stage of Mo–Si–B alloy by a refined microstructure was also observed; cf. [38].

6.3.4. Oxide scale microstructure

After oxidation at 1100 °C for 20 hours in dry synthetic air, the oxide scale was formed around the core particles in the spheroidized particles; see Figure 6. 7a–c. The surface of the particles with B addition has a smoother appearance than that of the spheroidized Mo–67Si particles after oxidation; see Figure 6. 7d–f.

Cross-sections of spheroidized Mo–67Si particles after oxidation at 1100 °C for 20 hours in dry synthetic air show that a thin but uniform layer of silica was formed; see Figure 6. 7g. After similar oxidation of $MoSi_2$ particles with boron addition, thicker oxide layers were observed indicating an enhanced oxidation by the boron addition, which is consistent with the oxidation kinetics captured by TGA in Section 6.3.2.3. The chemical composition and microstructure of the core of all the particles remained the same as before oxidation.

The enhanced oxidation by boron addition to the $MoSi_2$ particles is also manifest in the recorded diffractograms; see Figure 6. 8. With increasing boron content, the intensity of the $MoSi_2$ diffraction lines decreases, while the intensity of the Mo_5Si_3 diffraction lines increases due to Si depletion. In addition, diffraction lines associated with cristobalite were observed in the diffractogram of spheroidized Mo–67Si particles after oxidation at 1100 °C in dry synthetic air for 20 hours, but not in the diffractograms of particles with boron addition. This indicates that the structure of the oxide scale is changed by the introduction of boron.
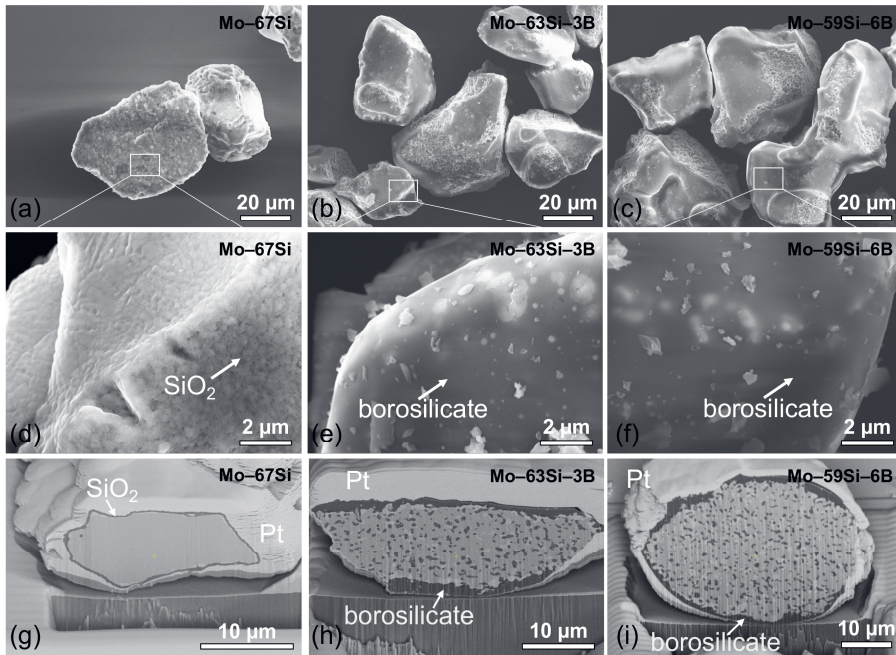
Figure 6. 7. SEM images of the surface and cross-section of spheroidized Mo–Si based particles after isothermal exposure at 1100 ° C for 20 hours in synthetic air: (a)(d)(g) Mo–67Si particles, (b)(e)(h) Mo–63Si–3B particles and (c)(f)(i) Mo–59Si–6B particles.
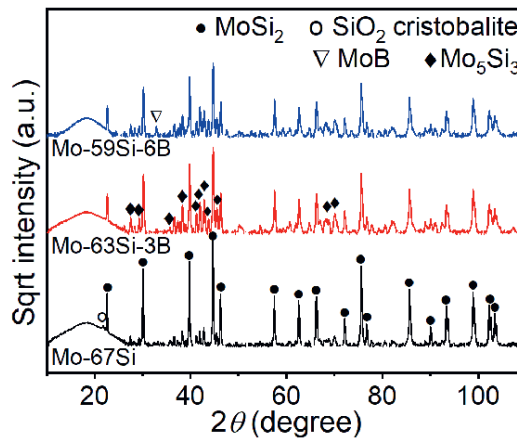

Figure 6. 8. X-ray diffraction patterns of the spheroidized Mo–Si based particles after isothermal exposure at 1100 ºC for 20 hours in dry synthetic air.

141

A crystalline structure with twin lamellae can be seen clearly in the oxide scale formed on spheroidized Mo–67Si particles (cf. Figure 6. 9a), while the crystalline structure cannot be observed in the oxide scale formed on spheroidized Mo–59Si–6B particles (cf. Figure 6. 9b). The twin lamellae structure is a characteristic microstructural features of cristobalite [39]. However, a selected area diffraction pattern cannot be obtained of these cristobalite areas due to high diffuse electron scattering intensities [39]. Evidence of such a transition from crystalline to amorphous structure of the oxide scale was captured with TEM, while operating with the electron beam at 200 keV. In order to confirm the crystalline structure, lattice plane imaging was performed quickly with high resolution TEM (HRTEM) near the interface of the oxide scale and the $MoSi_2$ substrate; see Figure 6. 9c. Fast Fourier Transformation (FFT) was performed on the lattice fringes and the obtained pattern matches well with the simulated diffraction pattern of tetragonal cristobalite; see Figure 6. 9d. The glassy oxide scales formed on spheroidized Mo–58Si–6B particles contains inclusions near the interface of the oxide scale and the inner core material; see Figure 6. 9b and e. The bright nano particles are Mo rich and likely composed of MoO_3. The presence of boron in these inclusions was confirmed by Electron Energy Loss Spectroscopy (EELS); see Figure 6. 9 i and Figure 6. 9 j. As can be seen, the peak associated with boron is clearly present in the EELS spectrum (Figure 6. 9j). The distribution of boron in the oxide scale corresponds with the dark inclusions; see Figure 6. 9e and i.
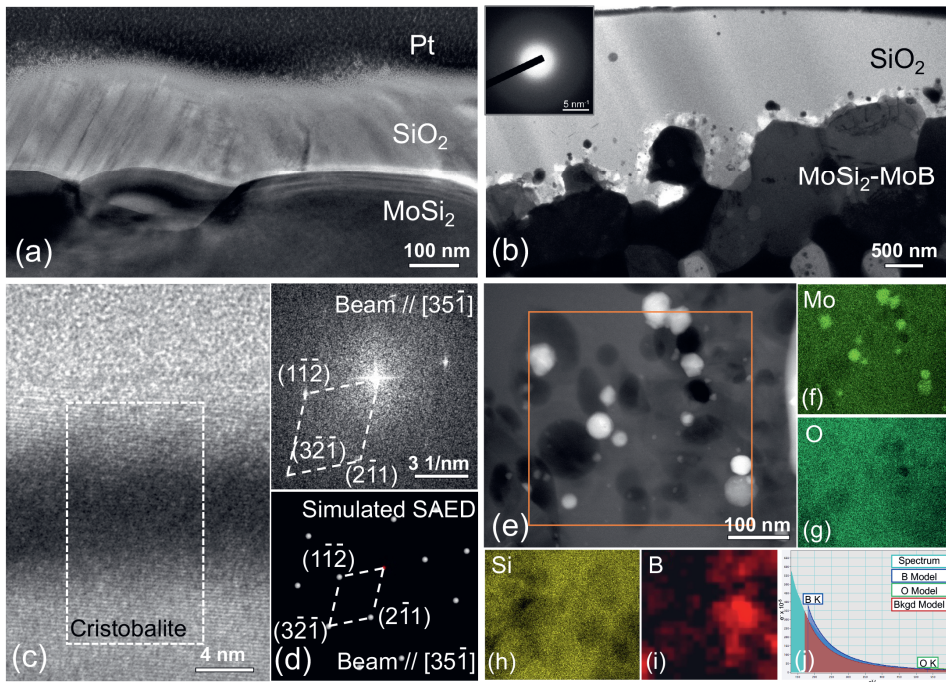
6

Figure 6. 9. TEM image of the oxide scale grown on (a) spheroidized Mo–67Si particles; (b) spheroidized Mo–59Si–6B particles; (c) HRTEM image of SiO$_2$-MoSi$_2$ interface on spheroidized Mo–67Si particle; (d) FFT of white box in (c) and simulated SAED by PDF-4+ software (version 2023) showing the orientation of cristobalite atomic layers; (e) HAADF image of the inclusion near the interface of the oxide scale and substrate in (b) and (f)–(h) the corresponding X-ray emission maps of Mo, O and Si respectively; EELS (i) elemental map and (j) spectrum of boron corresponding to the reduced area in (e).

6.3.5. Oxygen transport through the oxide scale

Upon oxidation, the MoB$_x$ in the alloy is oxidized resulting in B$_2$O$_3$, which dissolves in SiO$_2$ as a network modifier. Then, some Si–O bonds are broken and borosilicate is formed, which is beneficial for vitrification and hinders crystallization of SiO$_2$. Easier transport of oxygen through amorphous borosilicate makes it less passive than the crystalline silica scale formed on pure MoSi$_2$ [34, 40], which explains the accelerated oxidation by boron addition to MoSi$_2$ during the steady-state oxidation.

Two relations were reported to present the oxygen migration in an amorphous oxide scale at high temperatures, viz.: (i) Stokes-Einstein and Eyring equation [34, 41, 42]. Stokes-Einstein equation, expressed as Eq. (6.12), which was used to estimate the diffusion of oxygen molecule in SiO_4 tetrahedral network and (ii) Eyring equation, expressed as Eq. (6.13), considers oxygen diffused in the form of ions.

$$D = \frac{kT}{6\pi r \eta} \tag{6.12},$$

$$D = \frac{kT}{\lambda \eta} \tag{6.13},$$

where k is the Boltzmann constant, T the thermodynamic temperature and r is particle radius through glass (0.121 nm, the distance of O–O bond in O_2) and λ is the average jump distance of diffusion species (0.159 nm, the distance of Si–O bond in SiO_2) [34, 41]. As mentioned in Section 6.3.3, these two kinds of diffusion types act simultaneously and are linked to each other through so-called "interstitialcy diffusion" [20].
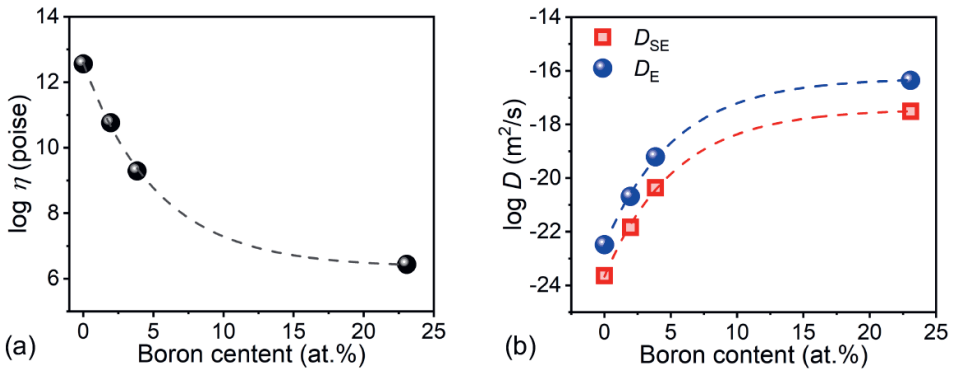

Figure 6. 10. (a) Viscosity of SiO_2–B_2O_3 glass as a function of boron content at 1100 °C estimated using viscosity data reported by Yan *et al.* [41]; (b) oxygen diffusivity calculated with Stokes-Einstein (D_{SE}) and Eyring equation (D_E).

Both the Stokes-Einstein and the Eyring equation express that the oxygen permeability is inversely proportional to the glass viscosity. Yan *et al.* measured the viscosity of a series of silica with different B contents in their sintering study [43]. Using their viscosity data, the

relationship of the change in viscosity of borosilicate glass as a function of B content at 1100 °C is constructed in Figure 6. 10a and the diffusivity of oxygen was calculated using the Stokes-Einstein as well as the Eyring equation, respectively; see Figure 6. 10b. It can be seen that the introduction of a trace amount of boron can reduce the viscosity of SiO_2 by several orders of magnitude (see Figure 6. 10a), which makes the diffusion coefficient of oxygen to increases by several orders of magnitude; see Figure 6. 10b. This increase of the oxygen diffusion coefficient explains the enhanced growth of the oxide scale on the $MoSi_2$ particles by the B addition.

6.4. Conclusions

The oxidation of $MoSi_2$ and $MoSi_2$–MoB_x particles follows a two-step oxidation process, namely an initial fast oxidation followed by a relatively slow steady-state oxidation. The formation of a continuous protective scale on the surface marks the transition from the initial fast to the steady-state oxidation of $MoSi_2$ based particles. The oxidation kinetics in the steady-state stage can be described with a 3-D diffusion-Jander (D3) reaction model.

The high temperature oxidation kinetics of $MoSi_2$ particles is significantly enhanced when Boron is added. The oxidation rate constant pertaining to the steady-state stage of the $MoSi_2$ based particles increases proportional with their boron content (observed at 1100 °C).

The particles size of Mo–Si–B particles has a significant effect on the initial fast oxidation but has little effect on the steady-state of the oxidation at 1100 °C in dry synthetic air. The transition from the initial to steady-state oxidation state is accelerated when the particles become larger due to the reduced surface area. The transition from the initial to steady-state oxidation is further promoted when the boron containing phase is finer dispersed.

Microstructure analysis of the oxide scaled formed on these particles reveals that the formation of crystalline SiO_2 is mitigated while amorphous borosilicate is promoted by the addition of boron. The MoB phase in the particle alloy is oxidized to B_2O_3, which dissolves into SiO_2 as a network modifier causing vitrification of the oxide scale.

The enhanced oxidation of $MoSi_2$ particles by boron addition is due to an increase of the diffusion coefficient of oxygen in the borosilicate oxide scale, which is inversely proportional to its viscosity.

6

References

[1] J.H. Perepezko, Surface engineering of Mo-Base alloys for elevated-temperature environmental resistance, Annual Review of Materials Research 45(1) (2015) 519-542.

[2] X.D. Tian, X.P. Guo, Z.P. Sun, J.L. Qu, L.J. Wang, Oxidation resistance comparison of $MoSi_2$ and B-modified $MoSi_2$ coatings on pure Mo prepared through pack cementation, Materials and Corrosion 66(7) (2015) 681-687.

[3] K. Nagata, S.C. Deevi, Oxidation behavior of molybdenum silicides and their composites, Intermetallics 8 (2000) 1147-1158.

[4] Z. Derelioglu, A.L. Carabat, G.M. Song, S.v.d. Zwaag, W.G. Sloof, On the use of B-alloyed $MoSi_2$ particles as crack healing agents in yttria stabilized zirconia thermal barrier coatings, Journal of the European Ceramic Society 35(16) (2015) 4507-4511.

[5] F. Nozahic, C. Estournès, A.L. Carabat, W.G. Sloof, S. van der Zwaag, D. Monceau, Self-healing thermal barrier coating systems fabricated by spark plasma sintering, Journal of the European Ceramic Society 143 (2018) 204-213.

[6] Y. Chen, X. Zhang, S. van der Zwaag, W.G. Sloof, P. Xiao, Damage evolution in a self-healing air plasma sprayed thermal barrier coating containing self-shielding $MoSi_2$ particles, Journal of the American Ceramic Society 102(8) (2019) 4899-4910.

[7] J. Krishnasamy, S.A. Ponnusami, S. Turteltaub, S. van der Zwaag, Modelling the fracture behaviour of thermal barrier coatings containing healing particles, Materials & Design 157 (2018) 75-86.

[8] S.A. Ponnusami, J. Krishnasamy, S. Turteltaub, S. Zwaag, A micromechanical fracture analysis to investigate the effect of healing particles on the overall mechanical response of a self-healing particulate composite, Fatigue & Fracture of Engineering Materials & Structures 42(2) (2018) 533-545.

[9] F. Nozahic, A.L. Carabat, W. Mao, D. Monceau, C. Estournes, C. Kwakernaak, S. van der Zwaag, W.G. Sloof, Kinetics of zircon formation in yttria partially stabilized zirconia as a result of oxidation of embedded molybdenum disilicide, Acta Materialia 174 (2019) 206-216.

[10] P. Greil, Generic principles of crack-healing ceramics, Journal of Advanced Ceramics 1(4) (2012) 249-267.

[11] T. Osada, K. Kamoda, M. Mitome, T. Hara, T. Abe, Y. Tamagawa, W. Nakao, T. Ohmura, A novel design approach for self-crack-healing structural ceramics with 3D networks of healing activator, Scientific Reports 7(1) (2017) 17853.

[12] J. Chen, C. Li, Z. Fu, X. Tu, M. Sundberg, R. Pompe, Low temperature oxidation behavior of a $MoSi_2$-based material, Materials Science and Engineering: A 261 (1999) 239-244.

[13] Y.Q. Liu, G. Shao, P. Tsakiropoulos, On the oxidation behaviour of $MoSi_2$, Intermetallics 9 (2001) 125-136.

6

[14] S. Knittel, S. Mathieu, M. Vilasi, The oxidation behaviour of uniaxial hot pressed $MoSi_2$ in air from 400 to 1400 °C, Intermetallics 19(8) (2011) 1207-1215.

[15] Y. Yang, M. Li, L. Xu, J. Xu, Y. Qian, J. Zuo, T. Li, Oxidation behaviours of ZrB_2-SiC-$MoSi_2$ composites at 1800 °C in air with different pressures, Corrosion Science 157 (2019) 87-97.

[16] M. Samadzadeh, C. Oprea, H. Karimi Sharif, T. Troczynski, Comparative studies of the oxidation of $MoSi_2$ based materials: High-temperature oxidation (1000–1600 °C), International Journal of Refractory Metals and Hard Materials 69 (2017) 31-39.

[17] Z. Ding, J.C. Brouwer, C. Kwakernaak, M.J.M. Hermans, V. Popovich, W.J. Quadakkers, W.G. Sloof, Selective oxidation of aluminium in $Mo(Al,Si)_2$, Corrosion Science 211 (2023).

[18] Z. Ding, J.C. Brouwer, C. Kwakernaak, J.-N. Zhu, V. Popovich, M.J.M. Hermans, W.G. Sloof, $Mo(Al_xSi_{1−x})_2$ healing particles for high temperature ceramics and encapsulation by selective oxidation of aluminium, Materials & Design 225 (2023).

[19] Y.T. Zhu, M. Stan, S.D. Conzone, D.P. Butt, Thermal oxidation kinetics of $MoSi_2$-based powders, Journal of American Ceramic Society 82(10) (1999) 2785-2790.

[20] Y.T. Zhu, L. Shu, Kinetics and products of molybdenum disilicide powder oxidation, Journal of American Ceramic Society 85(2) (2002) 507-509.

[21] J.A. Lemberg, R.O. Ritchie, Mo-Si-B alloys for ultrahigh-temperature structural applications, Advanced Materials 24(26) (2012) 3445-80.

[22] A. Lange, R. Braun, Magnetron-sputtered oxidation protection coatings for Mo–Si–B alloys, Corrosion Science 84 (2014) 74-84.

[23] S. Majumdar, B. Dönges, B. Gorr, H.-J. Christ, D. Schliephake, M. Heilmaier, Mechanisms of oxide scale formation on yttrium-alloyed Mo–Si–B containing fine-grained microstructure, Corrosion Science 90 (2015) 76-88.

[24] H. Yokota, T. Kudoh, T. Suzuki, Oxidation resistance of boronized $MoSi_2$, Surface and Coatings Technology 169-170 (2003) 171-173.

[25] A. Lange, M. Heilmaier, T.A. Sossamann, J.H. Perepezko, Oxidation behavior of pack-cemented Si–B oxidation protection coatings for Mo–Si–B alloys at 1300 °C, Surface and Coatings Technology 266 (2015) 57-63.

[26] S.H. Wen, C.G. Zhou, J.B. Sha, Improvement of oxidation resistance of a Mo-62Si-5B (at.%) alloy at 1250 °C and 1350 °C via an in situ pre-formed SiO_2 fabricated by spark plasma sintering, Corrosion Science 127 (2017) 175-185.

[27] Z. Ding, J.C. Brouwer, J.-N. Zhu, V. Popovich, M.J.M. Hermans, W.G. Sloof, Effects of boron addition on the high temperature oxidation of $MoSi_2$ alloys, Scripta Materialia 234 (2023).

[28] Y. Danzaki, K. Wagatsuma, T. Syoji, K. Yoshimi, Dissolution of molybdenum-silicon (-boron) alloys using a mixture of sulfuric, nitric and hydrofluoric acids and a sequential

6

correction method for ICP-AES analysis, Fresenius' Journal of Analytical Chemistry 369 (2001) 184-186.

[29] D.V. Rybkovskiy, A.G. Kvashnin, Y.A. Kvashnina, A.R. Oganov, Structure, stability, and mechanical properties of Boron-rich Mo-B Phases: A computational study, Journal of Physical Chemistry Letters 11(7) (2020) 2393-2401.

[30] M.J. Kriegel, W. Foerster, D. Chmelik, O. Fabrichnaya, J. Januschewsky, M. Kathrein, L.S. Sigl, D. Rafaja, Diffusion path and growth of intermediate phases in Mo/(Si,B) diffusion couples, 18th Plansee Seminar (2013).

[31] P.R. Taleghani, S.R. Bakhshi, M. Erfanmanesh, G.H. Borhani, R. Vafaei, Improvement of MoSi$_2$ oxidation resistance via boron addition: Fabrication of MoB/MoSi$_2$ composite by mechanical alloying and subsequent reactive sintering, Powder Technology 254 (2014) 241-247.

[32] M.D. Johnston, L.T. Khajavi, M. Li, S. Sokhanvaran, M. Barati, High-temperature refining of metallurgical-grade silicon: a review, JOM 64(8) (2012) 935-945.

[33] A. Khawam, D.R. Flanagan, Solid-state kinetic models: basics and mathematical fundamentals, Journal of Physical Chemistry B 110(35) (2006) 17315-17328.

[34] M.A. Lamkin, F.L. Riley, Oxygen mobility in silicon dioxide and silicate glasses: a review, Journal of the European Ceramic Society 10 (1992) 347-367.

[35] L. Boatemaa, J.C. Brouwer, S. van der Zwaag, W.G. Sloof, The effect of the TiC particle size on the preferred oxidation temperature for self-healing of oxide ceramic matrix materials, Journal of Materials Science 53(8) (2018) 5973-5986.

[36] J. Schlichting, Oxygen transport through glass layers fromed by a gel process, Journal of Non-Crystalline Solids 63 (1984) 173-181.

[37] Z. Chen, W. Shao, M. Li, Z. Wu, P. Peng, C. Zhou, Effect of minor B modification on the oxidation behavior of MoSi$_2$ alloy at high temperature, Corrosion Science 216 (2023).

[38] F.A. Rioult, S.D. Imhoff, R. Sakidja, J.H. Perepezko, Transient oxidation of Mo–Si–B alloys: effect of the microstructure size scale, Acta Materialia 57(15) (2009) 4600-4613.

[39] C.-h. Chao, H.-y. Lu, β-Cristobalite stabilization in (Na$_2$O + Al$_2$O$_3$)-added silica, Metallurgical and Materials Transactions A 33 (2002) 2703–2711.

[40] J.S. Park, R. Sakidja, J.H. Perepezko, Coating designs for oxidation control of Mo-Si-B alloys, Scripta Materialia 46 (2002) 765-770.

[41] L. Wang, W. Wang, Q. Fu, The improvement of the self-healing ability of MoSi$_2$ coatings at 900–1200 °C by introducing SiB$_6$, Journal of the European Ceramic Society 40(8) (2020) 2896-2906.

[42] M.L.F. Nascimento, E.D. Zanotto, Mechanisms and dynamics of crystal growth, viscous flow, and self-diffusion in silica glass, Physical Review B 73(2) (2006).

[43] M.F. Yan, S.R. Macchesney, S.R. Nagel, W.W. Rhodes, Sintering of optical wave-guide glasses, Jounal of Materials Science 15 (1980) 1371-1378.

6

7.

On the use of Mo(Al,Si)$_2$ particles with boron addition as sacrificial particles in yttria stabilized zirconia ceramics designed for self-healing thermal barrier coatings

Abstract

Avoiding the premature oxidation of healing particles and maximizing crack healing efficiency are the main challenges for realizing a self-healing thermal barrier coating system. Here a self-healing ceramic has been fabricated, envisioned for self-healing thermal barrier coatings. This ceramic is composed of partially yttria-stabilized zirconia (YSZ) with embedded $Mo(Al,Si)_2$ particles with boron addition designed for optimized self-healing performance. Utilizing selective oxidation of Al, a shell composed of dense α-Al_2O_3 was formed in-situ after exposing the ceramic composite to a gaseous ambient with a low oxygen partial pressure of 5×10^{-10} atm. at 1100 °C for 16 hours. After further exposing the ceramic composite to Ar with 20 vol.% O_2 for 16 hours, a core of $MoSi_2$ with MoB as a fine distributed second phase is enveloped by a robust shell of α-Al_2O_3 that effectively prevents premature oxidation. Finally, the envisioned crack healing of the self-healing YSZ composite with encapsulated $MoSi_2(B)$ has been demonstrated.

7.1. Introduction

Thermal barrier coating (TBC) systems are employed on metallic components to furnish thermal insulation against the hot gas stream in gas-turbine and jet engines [1-3]. The incorporation of a TBC allows contemporary gas-turbine engines to function at gas temperatures considerably surpassing the melting points of nickel- or cobalt-based structural superalloys (around 1300 °C), which enhances both efficiency and overall performance of an engine [1-3].

Yttria partially stabilized zirconia (YSZ) is the state-of-art material for TBCs because of its low thermal conductivity at high temperatures (2.3 $W \cdot m^{-1} \cdot °C^{-1}$ at 1000 °C) in conjunction with high "strain tolerance" and chemical stability [1-4]. Nonetheless, these coatings experience thermal cycles spanning between operational temperatures and room temperature [1-3, 5]. Therefore, significant stresses (2–6 GPa) arises due to the difference in thermal expansion coefficients (CTEs) of the ceramic coating of YSZ ($11–13 \times 10^{-6} °C^{-1}$) and the metal substrate ($18–20 \times 10^{-6} °C^{-1}$) [6] and give rise to the formation of microcracks, which propagate and eventually coalesce, ultimately leading to TBC spallation [5]. Hence, a TBC that is capable of autonomic crack repair and structural integrity recovery in a high-temperature oxidizing environment is highly desirable [6].

A new self-healing TBC system has been introduced with the aim of extending its operational lifetime [6-8]; see Figure 7. 1. This approach has been effectively implemented

7

in an actual TBC system, utilizing the oxidation process of boron-doped molybdenum disilicide ($MoSi_2$–B) particles that are incorporated within the YSZ–TBC [6-8]. When intercepted by cracks [9, 10], the $MoSi_2$ healing particles oxidize preferentially, leading to the formation of amorphous SiO_2, which fills the crack gap and establishes direct contact with the crack faces [6-8]; see Figure 7. 1. Consequently, the amorphous SiO_2 engages in a subsequent reaction with the ZrO_2 of the matrix, culminating in the development of a load-bearing $ZrSiO_4$ phase, ensuring effective wetting of the crack faces [11].

The incorporation of aluminium and boron into the sacrificial $MoSi_2$ particle is of paramount importance for encapsulating these sacrificial particles to prevent premature oxidation and effectively promote the rate of the healing reaction [6-8, 12, 13]. As can be seen in Figure 7. 1, the concept of self-healing TBC involves creating an inert and oxygen impenetrable shell of α-Al_2O_3 around the sacrificial healing particle ($MoSi_2$) [7, 8, 14, 15]. Various methods have been utilized for the encapsulation of $MoSi_2$ based particles [7, 12, 14, 15], among which an in-situ encapsulation method is the most promising [7, 12]. Instead of $MoSi_2$ particles, Al alloyed $MoSi_2$ particles are embedded in the matrix of YSZ. The encapsulation process is carried out prior to the application of the system under operational conditions [7, 12] and accomplished in-situ by annealing the system in an appropriate ambient based on selective oxidation of Al in Mo(Al,Si)$_2$ particles [12, 16].

It has been reported that the addition of boron can effectively mitigate the formation of cristobalite (crystalline SiO_2) and promotes the formation of amorphous SiO_2 upon high temperature oxidation of $MoSi_2$ [13, 17]. Therefore, alloying the sacrificial $MoSi_2$ particle with B in a self-healing TBC system is expected to increase the fluidity of the healing agent of SiO_2 by forming (boro)silicate glass at the intended temperature, which will facilitate the filling of cracks [6, 13, 18, 19]. Furthermore, the formation of desired amorphous (boro)silicate promoted by boron addition will accelerate the zircon formation in the subsequent healing reaction[11].

The concept of a self-healing TBC system has already been proven successful [6-8]. However, these studies also indicated that further development is still needed to improve the protectiveness of the Al_2O_3 shells and maximise crack healing efficiency [7]. In this work, a complete self-healing YSZ system is presented with optimized design features of the embedded Mo(Al,Si)$_2$ particles with boron addition, i.e., their Al content, boron content and sphericity. A crack was introduced in the optimized self-healing YSZ composite to study the crack healing at 1100°C in an oxidizing gaseous atmosphere.
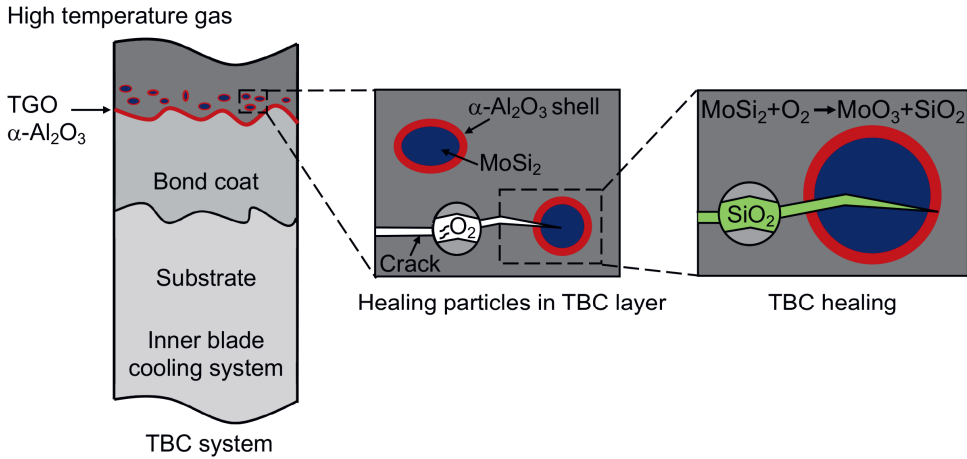
Figure 7. 1. Schematic of the crack-healing mechanism in a thermal barrier coating (TBC) with encapsulated Mo–Si based sacrificial particles.

7.2. Materials and methods

7.2.1. Preparation of Mo(Al,Si)$_2$ with B particles

Elemental powder of molybdenum (2–5 µm and 99.95$^+$ % purity, Chempur, Germany), silicon (45 µm and 99.99% purity, TLS Technik GmbH, Germany), aluminium (45 µm and 99.8 % purity, TLS Technik GmbH, Germany) and boron (100 nm and 99.99 % purity, Shanghai ST-NANO SCIENCE & TECHNOLOGY Co., LTD, China) were mixed in the desired molar ratios and milled using a planetary ball mill (PM100, Retsch GmbH, Germany). Wet ball-milling of the powders was conducted in hexane (VWR Chemicals, The Netherlands) using zirconia balls (100 and 30 balls with a diameter of 3 and 5 mm, respectively) in a zirconia jar (50 ml). The weight ratio between balls and powder was about 5:1. About 10 g of powder was milled with a rotation speed of 150 rpm for 2 hours, which was realized by cycles of milling and pause for 20 and 10 minutes, respectively. The milled particles were dried in a fume hood for 5 hours. Then, the particles were passed through a 50 µm sieve (Analysensieb, DIN-ISO 3310-1, Retsch, Germany) to attain a homogeneous mixture.

The Mo–Si–Al–B alloys were prepared by a one-step sintering process with the above prepared powder mixture. To this end, about 6.5 g powder was loaded into a graphite die with an inner diameter of 20 mm (ISO-68, Toyo Tanso, Japan). Graphite foils (Permafoil,

PF20-HP, Toyo Tanso, Thailand) were used to prevent a possible reaction between the powder and the graphite die and punches. Thin layers of BN (Henze, Lauben, Germany) were sprayed onto both sides of the graphite foils for easy removal of the composite sample from the die and punches after sintering. The punches and die assembly with the elemental powder mixture was mounted into the SPS furnace. Then, this furnace was evacuated and flushed two times with Ar-gas of 5N purity (Linde, The Netherlands). Next, the furnace was heated up to 1773 K with a heating rate of 20 °C min^{-1}. The electric current was applied following a 15/5 on/off 3 ms pulse sequence. First, a pressure of 50 MPa was applied till the temperature reached 600 °C. Next, the pressure was released to avoid leakage of melted Al. When the temperature reached to 1500 °C, a pressure of 50 MPa was applied again to promote alloying and densification. The sample was kept for 30 minutes at the sintering temperature and thereafter cooled naturally to room temperature. The sintered discs with a diameter of 20 mm and a thickness of about 3 mm were ground with SiC emery paper starting with 80 mesh grit size to finally 1500 mesh grit size to obtain a smooth surface finish. Hereafter, the disc was thoroughly cleaned ultrasonically with isopropanol.

After sintering, the discs were crushed with a Fritsch Pulverisette (type P-0150, Germany). Two different size fractions of the particles were prepared by sieving (Analysensieb, DIN-ISO 3310-1, Retsch, Germany), namely fine particles of size $d < 20$ μm and coarse particles of size $d > 20$ μm. The fine powder fraction was discarded. To polish away the sharp edges of the crushed particles with a size of $d > 20$ μm, a planetary ball mill (PM100, Retsch GmbH, Germany) was used. To this end, a 50 ml zirconia jar with 200 and 90 balls with diameters of 3 and 5 mm zirconia balls were used. As polishing medium SiC (1 μm and 99.8 % purity, Alfa Aesar, Germany) was used and mixed with about 25 ml iso-propanol. Several batches of about 5.5 g of powder were milled with a rotation speed of 100 rpm for 100 minutes, which was realized by cycles of milling and pausing for 25 and 5 minutes, respectively. Next, the milled particles were washed with deionized water (Milli Q, 18.2 MΩ.cm at 25 °C) and sieved with a 20 μm mesh sieve to remove the fine particles and the milling media. The remaining particles were dried in an oven at 80 ºC overnight. Then, the particles were passed through a 50 μm sieve to eliminate the coarse fraction. Finally, particles with a size of $20 < d < 50$ μm were obtained.

7.2.2. Encapsulation of sacrificial particles

Free Mo(Al,Si)$_2$ with B particles were encapsulated with an alumina (α-Al$_2$O$_3$) shell by selective oxidation of Al [12]. To this end, these particles were mixed with yttria partially

stabilized zirconia (YSZ, Amprit 827, H.C. Starck, Germany) with a mass ratio of 1:3 to avoid bonding and sintering at high temperature ensuring uniform oxidation of all particles. Then, the alloy particles were oxidized in gas mixtures of Ar + 8 vol.% CO_2 + 50 vol.% CO and Ar + 95 vol.% CO_2 + 2.5 vol.% CO at 1100 ºC, corresponding with oxygen partial pressures (pO_2) of 10^{-14} and 5×10^{-10} atm., respectively. The kinetics of isothermal oxidation was monitored with thermogravimetric analysis (TGA) using a dual furnace balance (Seteram TAG 16/18, France), which allows automatic correction for buoyancy effects.

7.2.3. Fabrication of YSZ composite with sacrificial particles and in-situ encapsulation

Commercially available YSZ powder (ZrO_2 with 3 mol.% Y_2O_3) with an average particle size of 0.7 μm (TZ-3Y-E, 99.9 wt% purity, Tosoh, Japan) was employed to prepare a composite with a 'sandwich architecture' via spark plasma sintering (FCT SPS system, type KCE-FCT HP D-25-SI, Germany). The sandwich architecture involves two layers of pure YSZ with a composite layer of YSZ and Mo(Al,Si)$_2$ with B particles in between; see Figure 7. 2. This sandwich was fabricated as follows: First, 2.60 g of YSZ powder was evenly loaded into the graphite die (20 mm inner diameter) on a vibrator plate (Henry Schein, Vibrator L, Germany) as the bottom layer. Then, the middle layer, consisting of 0.80 g of YSZ mixed with 10 vol.% of Mo(Al,Si)$_2$ with B particles, was poured on top of the first layer. Finally, for the third layer another 2.60 g of YSZ powder was loaded as the top layer. Graphite foils (Papyrex Mersen, France) sprayed with a thin layer of BN were used to prevent possible reaction between the powders and the graphite die and also for easy removal of the composite sample from the die and the punches after sintering. SPS was performed with a heating rate of 20 °C min^{-1} up to 1200 °C and kept at this temperature for 1 hour, while applying a uniaxial pressure of 50 MPa from the beginning of the sintering cycle and flushing the furnace with Ar (purity better than 5N). Finally, after releasing the pressure to the material, it was cooled naturally from the sintering temperature to room temperature. The sintered discs with a diameter of 20 mm and a thickness of about 3 mm were ground with SiC emery paper starting with 80 mesh grit size to finally 1500 mesh grit size obtaining a smooth surface finish. Hereafter, the discs were thoroughly cleaned ultrasonically with isopropanol.

The in-situ encapsulation was carried out via annealing the ceramic composite in a horizontal quartz tube furnace (Carbolite MTF 12/38/850, UK) at 1100 ºC. The temperature in the furnace tube was measured with a NiCr / NiAl (type K) thermocouple at the sample location. Gas mixtures of Ar + 8 vol.% CO_2 + 50 vol.% CO, Ar + 95 vol.% CO_2 + 2.5 vol.%

7

CO and Ar + 20 vol.% O_2 at 1100 °C, corresponding with pO_2 of 10^{-14}, 5×10^{-10} atm. and 0.2 atm. respectively, were passed the furnace tube at atmospheric pressure. The quartz tube inner diameter was 30 mm and the total gas flow was 200 sccm. Before annealing, the furnace was closed and flushed with the Ar for more than 30 minutes. The heating and cooling of the sample was about 20 °C min^{-1}.
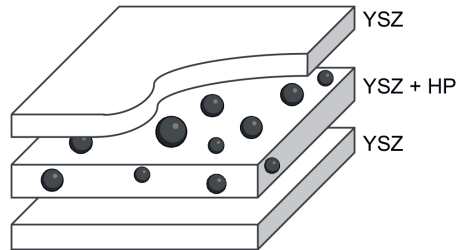

Figure 7. 2. Sample configuration of yttria partially stabilized zirconia (YSZ) with embedded Mo(Al,Si)$_2$ with B particles.

7.2.4. Crack introduction and healing

To introduce a crack into the composite material (cf. Section 7.2.3) in a controlled manner, the following procedure was followed. First, the YSZ composite with the Mo(Al,Si)$_2$ with B particles embedded was cut into rectangular specimens with dimensions of $10 \times 5 \times 2$ mm^3 using a diamond wafering blade of 0.3 mm thickness and an IsoMet low speed saw (Beuhler, USA). Next, the composite was glued onto a rectangular DP800 steel substrate of $50 \times 10 \times 1.5$ mm^3 using an epoxy adhesive (Bison Combi metal–metal). Subsequently, a notch with a length of about 1.3 mm was cut in the middle of the adhered samples using a 0.15 mm thick diamond blade. Then, a crack with a length of about 3 mm was generated using a tensile micro-tester (Deben, Woolpit, UK) with maximum load of 5 kN and 0.1 mm/min crosshead speed. In order to monitor the crack initiation and growth dynamically, acoustic emission (AE) was utilized during the loading process [20]. To this end, two microphones (type PICO S/N 4926 and 4928, nominal frequency 500 kHz) were mounted on the steel substrate with paraffin wax to each end of the sample to allow registration of acoustic emission signals during the experiments. Registration and post-processing were executed with the Physical Acoustics AEWin 1.70 (2005) software module. An acoustic event was recorded if the signal level of any microphone exceeded 5 mV. Every event was separately

recorded as a waveform file containing 2048 points at 0.5 μs intervals. The energies recorded varied in a wide range between 1 aJ to 1 nJ. A cumulative energy as a function of time, termed the "acoustic energy", was obtained through post-processing of the acoustic events. Here, the total acoustic energy is assumed to be proportional to the total amount of fracture introduced in the specimen. When acoustic events with peak frequency higher than 10^8 Hz were observed, the loading was stopped after holding the force for a few seconds.

To separate the cracked ceramic composites from the steel strip, the sample was annealed in a furnace at 300 °C in air for 30 minutes. Under these conditions the epoxy adhesive is burned. Next, the ceramic with a crack was collected and placed in a quartz boat crucible (Frialit - Degussit Technical Ceramics, Mannheim, Germany) in the hot-zone of an open horizontal alumina tube furnace (Lenton PTF 16/75/610 with an inner diameter of 75 mm, Hope Valley, UK) at 1100 °C for 16 hours.

7.2.5. Characterization

The phase composition of the materials was determined with X-ray diffractometry (XRD) using a D8 advance diffractometer (Bruker, Germany) operated with Cu K☐ radiation. Diffractograms were recorded in the 2θ range of 10 to 110° with a 2θ step size of 0.030° and a counting time per step of 2 s. These diffractograms were evaluated using the Bruker Diffrac EVA software (version 3.1).

The microstructure and morphology of the particles were observed with scanning electron microscopy (SEM) using a JEOL JSM 6500F (JEOL, Japan). This instrument is equipped with an ultra-dry energy dispersive spectrometer (EDS) for X-ray micro analysis (XMA) using System 7, Thermo Fisher Noran, USA. In addition, SEM combined with a Xenon plasma focused ion beam (Helios G4 PFIB UXe, Thermo Fisher Scientific, USA) was performed to create cross-sections of the oxidized particles. This instrument is equipped with an EDAX system for energy dispersive X-ray micro analysis (XMA) with an Octane Elite plus detector, using APEX acquisition and analysis software (version 4.5). Transmission electron microscopy (TEM) lamella from selected area were lifted with the plasma focused ion beam. Scanning transmission electron microscope (STEM) images were taken within the dual beam microscope operated with a 30 keV electron beam.

7

7.3. Results and discussion

7.3.1. Composition of Mo(Al,Si)$_2$ with B alloy

In order to maximize the robustness of the alumina shell for encapsulation of the healing particle to be created by selective oxidation of Mo(Al_xSi_{1-x})$_2$, the amount of Al dissolved must be as much as possible while maintaining the hexagonal (C40) crystal lattice structure as of MoSi$_2$ [16]. Mo(Al_xSi_{1-x})$_2$ alloys with various Al content (x) can be prepared by a one-step spark plasma sintering process at 1500 °C [12, 16]. The maximum solubility of Al in Mo(Al_xSi_{1-x})$_2$ particle with a hexagonal (C40) crystal lattice structure by replacing Si by Al in MoSi$_2$ is about 26.4 at.% ($x = 0.40$) [12, 16]. Then, particles with size between 20 to 50 μm will upon selective oxidation be enveloped by an a-Al$_2$O$_3$ shell of 1.3 to 3.1 mm thickness, respectively, when Al is fully depleted from their core [11].

Concerning the B addition, it has been reported that the parabolic growth rate constant of the silica formation in MoSi$_2$ oxidation increases proportional with the alloy boron content by 90 % per at.% B; with respect to the alloy without boron [16]. Thus, adding trace amounts of boron to sacrificial particles can significantly accelerate the healing reaction rate.

Hence, based on the above referred research, particles with a composition of Mo($Al_{0.4}Si_{0.6}$)$_2$ containing 1 wt% B will be used as sacrificial particles in the present work, which correspond to the composition of Mo–24Al–36Si–5B and are denoted as Mo(Al,Si)$_2$ with B particles.

The alloy fabricated by sintering of elemental powder mixtures exhibit uniform two-phase microstructures consisting of Mo(Al,Si)$_2$ as the matrix and MoB as second phase; see Figure 7. 3a and b. Small patches of alumina were observed as well; see Figure 7. 3a. The MoB phase demonstrates a finely dispersed distribution (Figure 7. 3a), which has been reported to effectively accelerated the oxidation kinetics of MoSi$_2$ at 1100 °C [12].
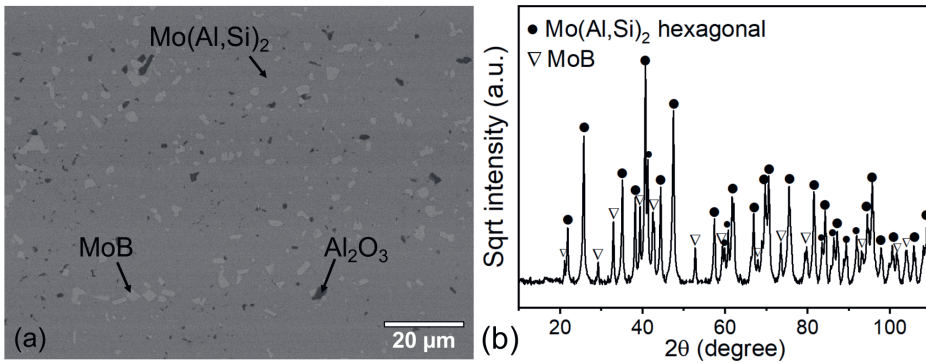
7

Figure 7. 3. (a) SEM back scattered electron images of the microstructure of Mo(Al,Si)$_2$ with B alloys prepared with SPS; (b) X-ray diffraction patterns of the Mo(Al,Si)$_2$ with B alloys.

7.3.2. Encapsulation of Mo(Al,Si)$_2$ with B free particles

The encapsulation of the Mo(Al,Si)$_2$ particles at a temperature of 1100 °C has been studied [11]. In the Mo–Si–Al system, Al-oxides exhibit the lowest dissociation oxygen partial pressure and Al is selectively oxidized in the low pO_2 gaseous ambient of 10^{-14} and 5×10^{-10} atm. at 1100 °C. When boron is added, Al$_2$O$_3$ still exhibits the lowest dissociation oxygen partial pressure of about 10^{-31} atm. in the Mo–Si–Al–B system and thus Al will be preferentially oxidized; see Figure 7. 4. Both B$_2$O$_3$(g) and MoO$_3$(g) may occur when the oxygen partial pressure pO_2 amounts 5×10^{-10} atm. in the gaseous ambient at 1100 °C; see Figure 7. 4. Under this condition the vapour pressure of B$_2$O$_3$(g) and MoO$_3$(g) corresponds to 10^{-5} and 10^{-6} atm., respectively. However, once the surface is fully covered with a close layer of a-Al$_2$O$_3$, volatile species will cease to form.

7
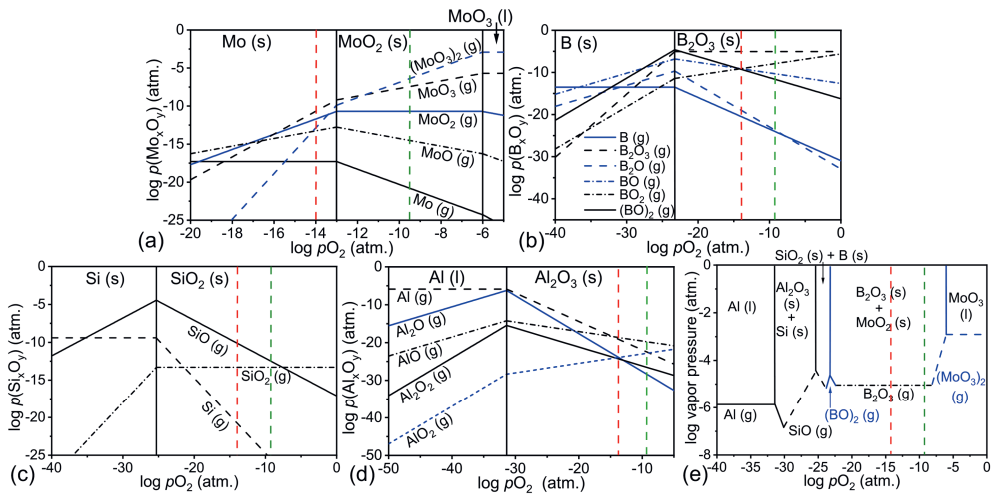
Figure 7. 4. Stability diagrams at 1100 °C for: (a) Mo–O; (b) B–O; (c) Si–O; (d) Al–O; and (e) combined diagram presenting the species with the highest vapour pressure as a function of pO_2. Vertical dashed lines indicate an oxygen partial pressure of 10^{-14} atm. (red) and 5×10^{-10} atm. (green).

The mass change during exposure of the Mo(Al,Si)$_2$ with B particles to the pO_2 of 10^{-14} atm. and 5×10^{-10} atm. at 1100 °C for 16 hours recorded with TGA is shown in Figure 7. 5. As a reference, the mass change is plotted of Mo(Al,Si)$_2$ particles without boron and with the same Al content during oxidation also in pO_2 of 10^{-14} atm. at 1100 °C for 16 hours. Fast oxidation during the initial stage of oxidation can be observed for all the particles followed by a slow steady mass increase. A higher mass gain was observed during the initial stage of oxidation when exposing Mo(Al,Si)$_2$ with B particles to the pO_2 of 5×10^{-10} atm. comparison to the mass gain observed at pO_2 of 10^{-14} atm. The Mo(Al,Si)$_2$ particles with and without B show nearly identical mass change during oxidation in pO_2 of 10^{-14} atm. at 1100 °C; see Figure 7. 5. This observation suggests that only Al is selectively oxidized.

7
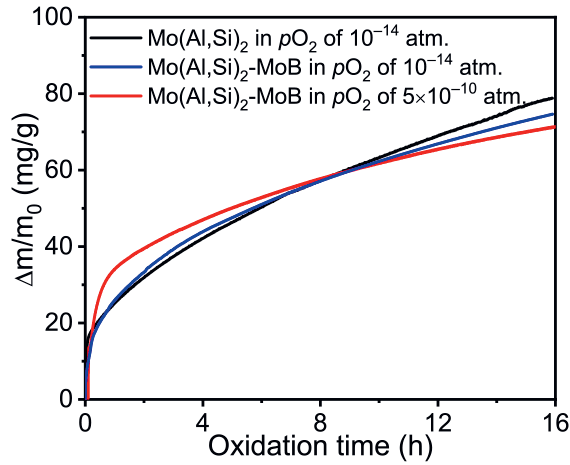
Figure 7. 5. Mass change of Mo(Al,Si)$_2$ with B particles during isothermal exposure with pO_2 of of 10^{-14} atm. and 5×10^{-10} atm. at 1100 °C for 16 hours. Mass change of Mo(Al,Si)$_2$ particles with the same Al content oxidized in pO_2 of 10^{-14} atm. at 1100 °C for 16 hours was plotted as a reference.

The surface of the free particle is covered with a thermally grown oxide after oxidation in the gaseous ambient with pO_2 of 10^{-14} atm. at 1100 °C for 16 hours; see Figure 7. 6a. The cross-sectional morphology and the corresponding XMA reveals that the particles are enveloped by an Al$_2$O$_3$ shell with a Mo(Al,Si)$_2$ core and MoB as the second phase, preserving the initial microstructure before oxidation; see Figure 7. 3b. Grain boundary ridges can be found in the surface of the Al$_2$O$_3$ shell (Figure 7. 6c), indicating a counter-diffusion process along the grain boundaries [11]. More equiaxed grains were formed at the surface of the Al$_2$O$_3$ shell in contact with the gaseous ambient, which corresponds with a dominant Al outward-diffusion process.

7
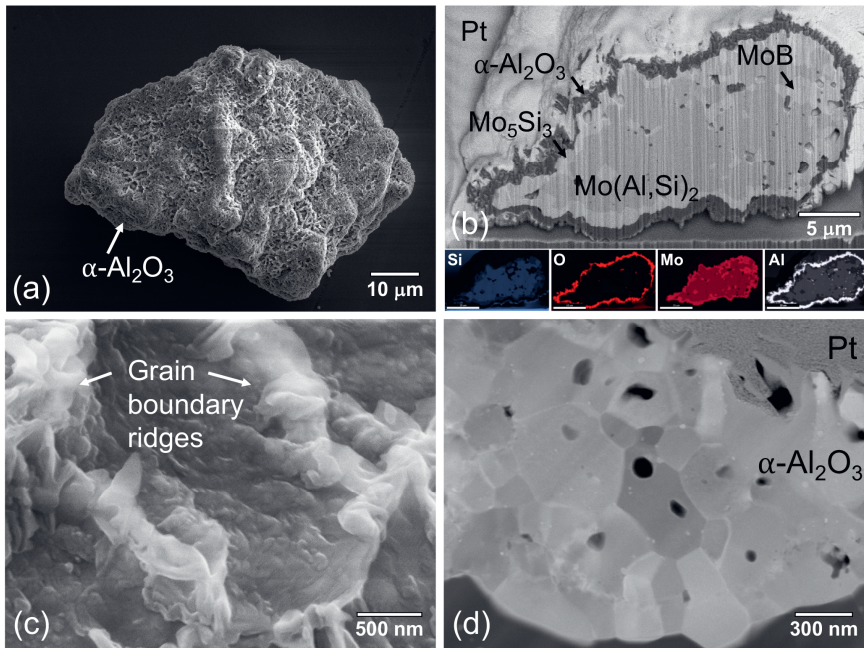
Figure 7. 6. Mo(Al,Si)$_2$ with B particle after oxidation with an oxygen partial pressure of 10^{-14} atm.: (a) SEM images showing surface morphology; (b) SEM images showing cross-section with X-ray emission maps of Si, O, Mo and Al, respectively; (c) detail observation of surface oxides; (d) STEM image of the oxide shell of α-Al$_2$O$_3$.

A denser thermally grown oxide was observed in the surface of the free particles when oxidized at 1100 °C with a pO_2 of 5×10^{-10} atm. for 16 h; see Figure 7. 7a. The surface is covered by granular oxide (Figure 7. 7c) and grain boundary ridges (Figure 7. 7c) cannot be observed. The cross-sectional morphology and the corresponding XMA confirm that the MoB phase is still intact in the core of Mo(Al,Si)$_2$ and an Al$_2$O$_3$ shell is formed around the particles; see Figure 7. 7b. The oxide layer features a distinct two-layered structure, comprising a dense equiaxed layer on top of dense columnar layer; see Figure 7. 7d. This structure arises from the counter-diffusion process involving the outward-diffusion of Al and inward-diffusion of O. This oxide scale formed by exposing the particles to gaseous ambient in the pO_2 of 5×10^{-10} atm. is denser than the oxide scale formed in gaseous ambient in the pO_2 of 10^{-14} atm.; cf. Figure 7. 6d and Figure 7. 7d. The dense oxide scale formed will effectively inhibit the diffusion of oxygen or silicon through the oxide scale and thus serve as a protective shell for the core material [15].
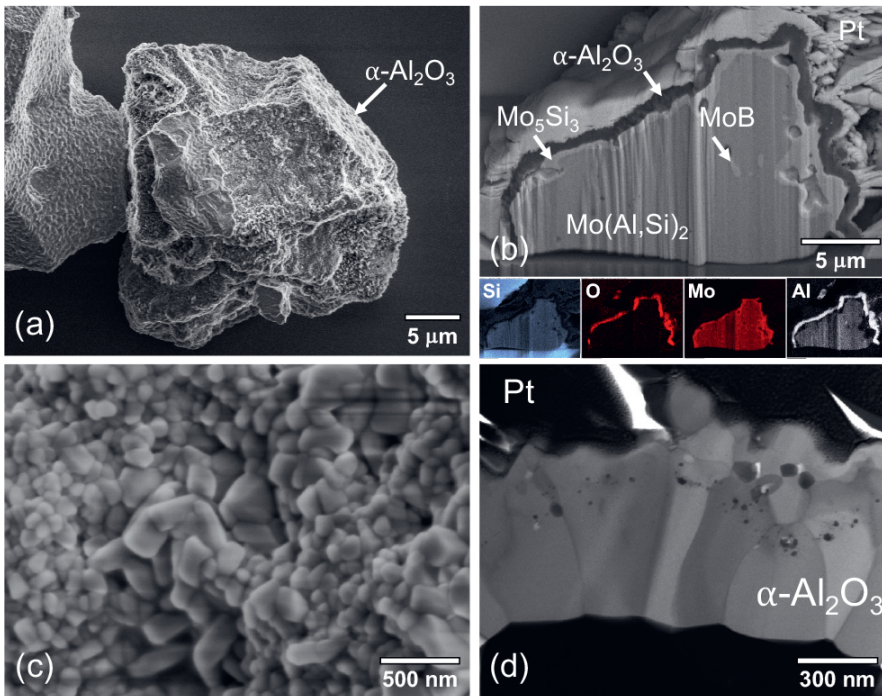
Figure 7. 7. Mo(Al,Si)$_2$ with B particle after oxidation with an oxygen partial pressure of 5 × 10^{-10} atm.: (a) SEM images showing surface morphology; (b) SEM images showing cross-section with X-ray emission maps of Si, O, Mo and Al, respectively; (c) detail observation of surface oxides; (d) STEM image of the oxide shell of α-Al$_2$O$_3$.

7.3.3. In-situ encapsulation of Mo(Al,Si)$_2$ with B particles in YSZ

In the cross-section of an as-sintered YSZ ceramic with the Mo(Al,Si)$_2$ with B particles embedded, a thin layer of Al$_2$O$_3$ in the thickness of about 330 nm can be observed (Figure 7. 8a), which is attribute to the residual pO_2 in the SPS furnace when sintering. The thickness of the Al$_2$O$_3$ layer increased to about 650 nm and 710 nm after oxidation in the gaseous ambient with pO_2 of 10^{-14} atm. and 5 × 10^{-10} atm. at 1100 °C for 16 hours, respectively, enveloping the core of the Mo(Al,Si)$_2$ particles with MoB still existing as second phase; see Figure 7. 8b and 8c. However, when exposing the ceramic composite directly to synthetic air with a pO_2 of 0.2 atm., internal oxidation was observed where the MoB phase originally was present; see Figure 7. 8d. Composition analysis with XMA showed that still a high amount of Al is present in the centre of the particle (Figure 7. 8d and 8f), namely: 24.0 at.% compared

7

with 26.4 at.% initially. Apparently, beside Al also boron is oxidized. Thus, the Al_2O_3 does not protect the MoB in the core of the particle from oxidation when the ceramic composite is exposed directly to gaseous ambient with high pO_2. Hence, oxidation in a low pO_2 ambient as a precursor for the formation of an exclusive Al_2O_3 scale is paramount.

The cross-section of the YSZ ceramic with embedded Mo(Al,Si)$_2$ with B particles after oxidation in first a low pO_2 of 5×10^{-10} atm. for 16 hours and then a high pO_2 of 0.2 atm. for another 16 hours is shown in Figure 7. 8e. It can be seen that the thickness of Al_2O_3 is significantly increased to about 2.4 μm enveloping the core of the healing particles. Composition analysis with XMA shows that the remnant core of the particles is fully depleted of Al and is composed of pure $MoSi_2$ as matrix and MoB as second phase; see Figure 7. 8e and 8f. This suggests that the in-situ encapsulation with pO_2 of 5×10^{-10} atm. at 1100 °C for 16 h acts as a robust protection of the particle core material and the subsequent exposure to gaseous ambient in high pO_2 can effectively release all the Al in the core material. The thickness of the Al_2O_3 shell formed after oxidation in first a low pO_2 of 5×10^{-10} atm. for 16 hours and then a high pO_2 of 0.2 atm. for another 16 hours of the particle observed equals 2.4 μm; see Figure 7. 8e. This thickness is very close to thickness calculated [11] when all Al is consumed by selective oxidation of an original healing particle of about 40 μm in diameter.
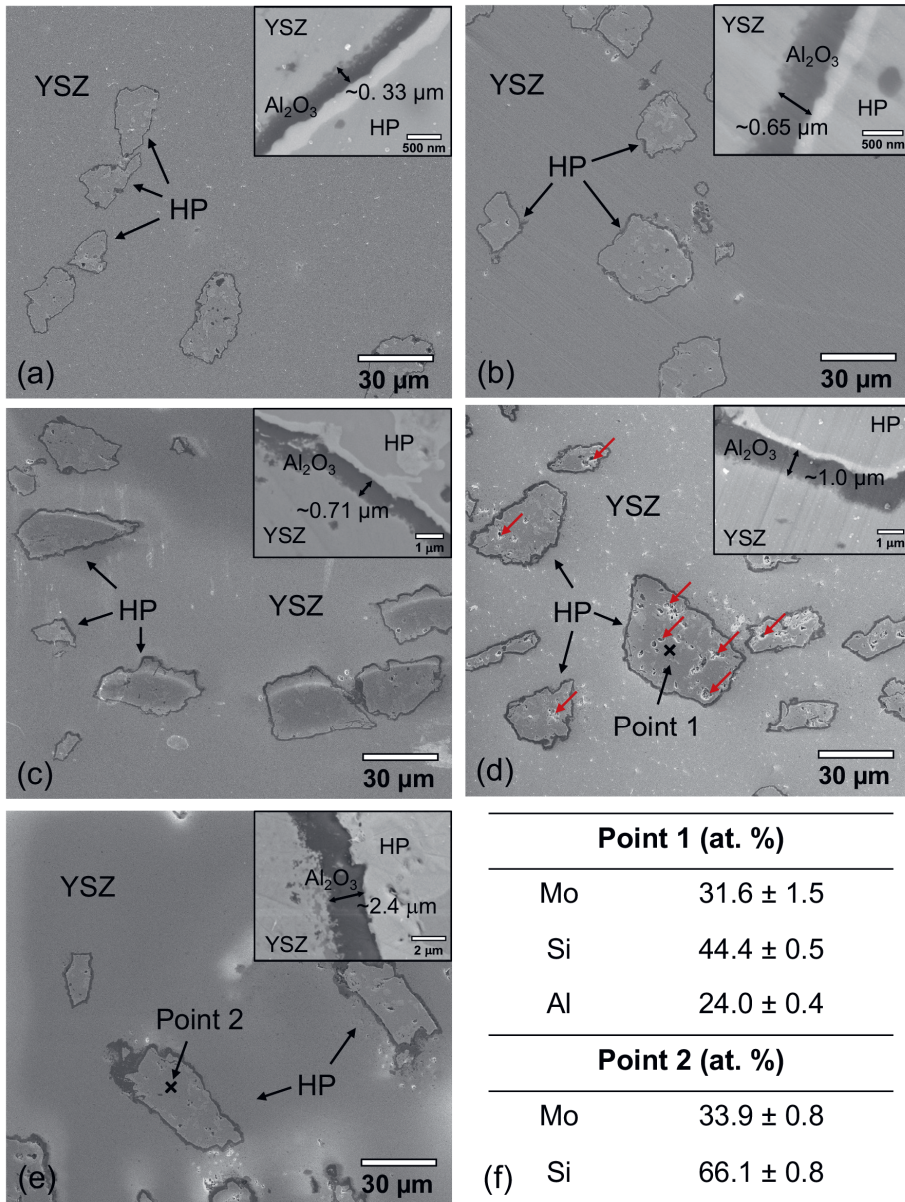
7

Figure 7. 8. Cross-section image of Mo(Al,Si)$_2$ with B particles embedded in in yttria partially stabilized zirconia (YPSZ): (a) as-sintered material; after oxidation in (b) pO_2 of 10^{-14} atm. (c) pO_2 of 5×10^{-10} atm. and (d) synthetic air at 1100 °C for 16 hours; (e) after oxidation first in pO_2 of 5×10^{-10} atm. for 16 hours and then in synthetic air for 16 hours at 1100 °C; (f) results of EDS point analysis of point 1 in (d) and point 2 in (e).

7.3.4. Crack healing in YSZ

A crack was initiated in the composite with the embedded and encapsulated sacrificial MoSi$_2$ particles with MoB (cf. Section 7.2.3 and 7.3.3) using a tensile micro-tester; cf. Section 7.2.4 and Figure 7. 9a. After 6 minutes of loading, acoustic emission detected local abnormal events, providing clear evidence of tearing the sample; see Figure 7. 9b. Crack–particle interaction can be observed along the crack path shown in Figure 7. 9c. The straight crack intersected particles on its path instead of being deflected or ran along the edge of a particle. The latter could lead to an interface debonding between the healing particle and the YSZ ceramic matrix rather than fracturing the particle [8].
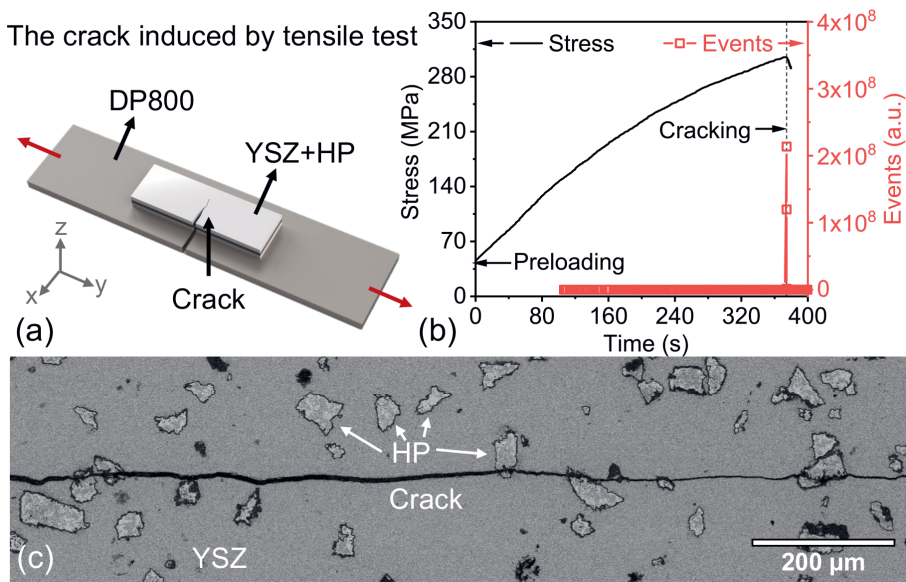

Figure 7. 9. (a) Sample configuration of teared yttria partially stabilized zirconia (YSZ) ceramic with Mo(Al,Si)$_2$ with B healing particles embedded in the middle layer; (b) Sample fracture monitored by acoustic emission; (c) Crack path in the composite layer.

After annealing at 1100 °C for 16 hours in synthetic air, filling of the crack tip with (boro)silicate was observed, which had migrated along the crack over more than 30 μm away from the MoSi$_2$ with MoB particles of addition; see Figure 7. 10a. ZrSiO$_4$ (zircon) was developed within the interface layer connecting the crack face and the YSZ ceramic, serving

as the intended load-bearing phase in the crack healing concept [5]; see the elemental maps of characteristic regions of the healed crack in Figure 7. 10b. The STEM image along the crack path confirms that the crack was fully healed by amorphous SiO_2 and zircon with large grains of about 1.5 µm formed between the amorphous SiO_2 and the matrix of YSZ ceramic; see Figure 7. 10c and 10d.
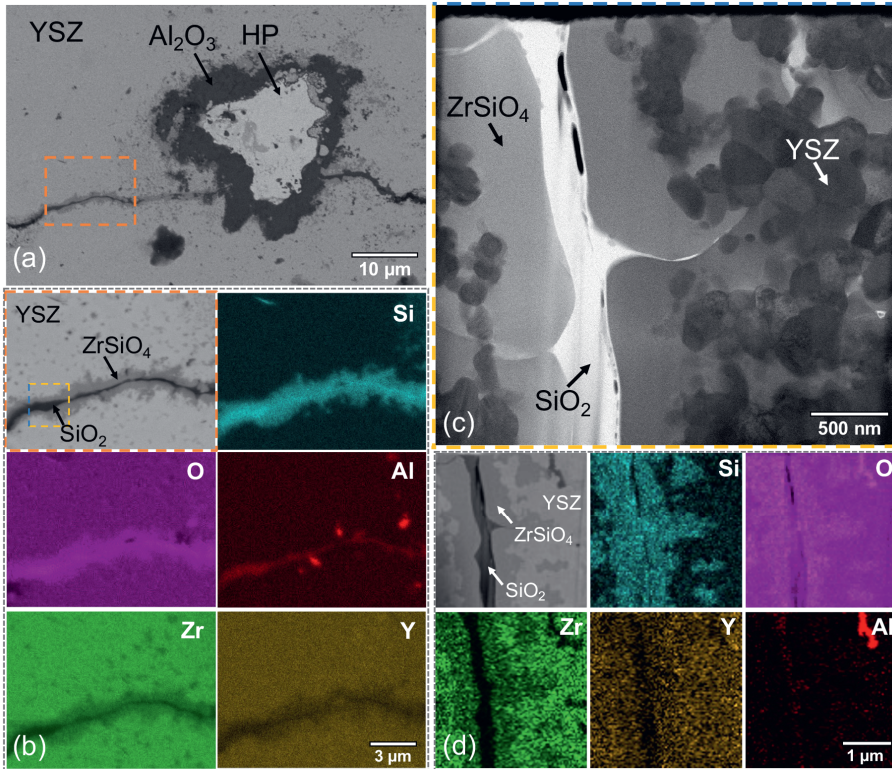

Figure 7. 10. Crack healing in yttria stabilized zirconia (YPSZ) composite with embedded encapsulated with α-Al_2O_3 healing particles (HP) of $MoSi_2$ with MoB after exposure at 1100 °C for 20 h in air: (a) backscattered electron image of cross section; (b) enlargement of region indicated in (a) and the corresponding X-ray emission maps of Si, O, Al, Zr and Y, respectively; (c) STEM image along the healed crack using planar-view FIB lift-out in the region indicated in (b) and (d) the corresponding X-ray emission maps of Si, O, Al, Zr and Y, respectively.

7.4. Conclusion

An autonomous self-healing ceramic system, composed of yttria partially stabilized zirconia (YSZ) with embedded Mo(Al,Si)$_2$ with B particles as sacrificial particles, was fabricated. This system incorporates optimized design features of sacrificial particles, including the alloying of aluminium and boron, as well as particle spheroidization.

Based on selective oxidation of Al, a shell of α-Al$_2$O$_3$ was formed exclusively by exposing the free Mo(Al,Si)$_2$ with B particles in gaseous ambient with oxygen partial pressure of 10^{-14} atm. at 1100 °C for 16 hours. Increasing the oxygen partial pressure to 5×10^{-10} atm. still resulted in a shell of exclusively α-Al$_2$O$_3$ when oxidizing the Mo(Al,Si)$_2$ with B particles at 1100 °C for 16 hours. This higher oxygen partial pressure promotes the large grains in both the equiaxed and columnar part of the oxide layer and resulted in a dense α-Al$_2$O$_3$ shell.

In-situ encapsulation with an α-Al$_2$O$_3$ shell around the original Mo(Al,Si)$_2$ with B healing particles was realized by annealing the yttria partially stabilized zirconia (YSZ) ceramic composite in an oxidizing ambient with an oxygen partial pressure of 5×10^{-10} atm. at 1100 °C for 16 hours. Further annealing the composite in a high oxygen partial pressure gaseous ambient (Ar with 20 vol.% O$_2$) at 1100 °C for 16 hours fully depleted the healing particles from Al leaving a core of MoSi$_2$ with MoB as fine distributed second phase enveloped by a robust shell of α-Al$_2$O$_3$ which effectively preventing premature oxidation.

Full crack healing of the yttria partially stabilized zirconia (YSZ) composite with embedded and encapsulated sacrificial MoSi$_2$ particles with MoB has been demonstrated. A crack intercepting the healing particles was filled with amorphous SiO$_2$ (promoted by the boron addition) wetting the crack surfaces and forming a loadbearing ZrSiO$_4$ (zircon) at the interface with the yttria partially stabilized zirconia (YSZ) matrix.

7

References

[1] D.R. Clarke, S.R. Phillpot, Thermal barrier coating materials, Materials Today 8(6) (2005) 22-29.

[2] N.P. Padture, M. Gell, E.H. Jordan, Thermal Barrier Coatings for Gas-Turbine Engine Applications, Science 296(5566) (2002) 280-284.

[3] R. Vaßen, M.O. Jarligo, T. Steinke, D.E. Mack, D. Stöver, Overview on advanced thermal barrier coatings, Surface and Coatings Technology 205(4) (2010) 938-942.

[4] F. Cernuschi, J. Kulczyk-Malecka, X. Zhang, F. Nozahic, C. Estournès, W.G. Sloof, Thermal conductivity of binary ceramic composites made of insulating and conducting materials comprising full composition range – Applied to yttria partially stabilized zirconia and molybdenum disilicide, Journal of the European Ceramic Society 43(14) (2023) 6296-6307.

[5] E. Tzimas, H. Müllejans, S.D. Peteves, J. Bressers, W. Stamm, Failure of thermal barrier coating systems under cyclic thermomechanical loading, Acta Materialia 48(18) (2000) 4699-4707.

[6] Z. Derelioglu, A.L. Carabat, G.M. Song, S.v.d. Zwaag, W.G. Sloof, On the use of B-alloyed $MoSi_2$ particles as crack healing agents in yttria stabilized zirconia thermal barrier coatings, Journal of the European Ceramic Society 35(16) (2015) 4507-4511.

[7] Y. Chen, X. Zhang, S. van der Zwaag, W.G. Sloof, P. Xiao, Damage evolution in a self-healing air plasma sprayed thermal barrier coating containing self-shielding $MoSi_2$ particles, Journal of the American Ceramic Society 102(8) (2019) 4899-4910.

[8] F. Nozahic, C. Estournès, A.L. Carabat, W.G. Sloof, S. van der Zwaag, D. Monceau, Self-healing thermal barrier coating systems fabricated by spark plasma sintering, Materials & Design 143 (2018) 204-213.

[9] S.A. Ponnusami, S. Turteltaub, S. van der Zwaag, Cohesive-zone modelling of crack nucleation and propagation in particulate composites, Engineering Fracture Mechanics 149 (2015) 170-190.

[10] S.A. Ponnusami, J. Krishnasamy, S. Turteltaub, S. van der Zwaag, A cohesive-zone crack healing model for self-healing materials, International Journal of Solids and Structures 134 (2018) 249-263.

[11] F. Nozahic, A.L. Carabat, W. Mao, D. Monceau, C. Estournes, C. Kwakernaak, S. van der Zwaag, W.G. Sloof, Kinetics of zircon formation in yttria partially stabilized zirconia as a result of oxidation of embedded molybdenum disilicide, Acta Materialia 174 (2019) 206-216.

[12] Z. Ding, J.C. Brouwer, C. Kwakernaak, J.-N. Zhu, V. Popovich, M.J.M. Hermans, W.G. Sloof, $Mo(Al_xSi_{1-x})_2$ healing particles for high temperature ceramics and encapsulation by selective oxidation of aluminium, Mater. Des. 225 (2023) 111577.

[13] Z. Ding, J.C. Brouwer, X. Yao, J.-N. Zhu, M.J.M. Hermans, V. Popovich, W.G. Sloof, On the high temperature oxidation of $MoSi_2$ particles with boron, Submitted.

7

[14] A.L. Carabat, S. van der Zwaag, W.G. Sloof, Creating a Protective Shell for Reactive MoSi$_2$ Particles in High-Temperature Ceramics, Journal of the American Ceramic Society 98(8) (2015) 2609-2616.

[15] A.L. Carabat, M.J. Meijerink, J.C. Brouwer, E.M. Kelder, J.R. van Ommen, S. van der Zwaag, W.G. Sloof, Protecting the MoSi$_2$ healing particles for thermal barrier coatings using a sol-gel produced Al$_2$O3 coating, Journal of the European Ceramic Society 38(7) (2018) 2728-2734.

[16] Z. Ding, J.C. Brouwer, C. Kwakernaak, M.J.M. Hermans, V. Popovich, W.J. Quadakkers, W.G. Sloof, Selective oxidation of aluminium in Mo(Al,Si)$_2$, Corrosion Science 211 (2023) 110884.

[17] Z. Ding, J.C. Brouwer, J.-N. Zhu, V. Popovich, M.J.M. Hermans, W.G. Sloof, Effects of boron addition on the high temperature oxidation of MoSi$_2$ alloys, Scripta Materialia 234 (2023) 115580.

[18] T. Osada, K. Kamoda, M. Mitome, T. Hara, T. Abe, Y. Tamagawa, W. Nakao, T. Ohmura, A novel design approach for self-crack-healing structural ceramics with 3D networks of healing activator, Scientific Reports 7(1) (2017) 17853.

[19] P. Greil, Generic principles of crack-healing ceramics, Journal of Advanced Ceramics 1(4) (2012) 249-267.

[20] T. Osada, A. Watabe, J. Yamamoto, J.C. Brouwer, C. Kwakernaak, S. Ozaki, S. van der Zwaag, W.G. Sloof, Full strength and toughness recovery after repeated cracking and healing in bone-like high temperature ceramics, Scientific Reports 10(1) (2020) 18990.

7

8.

General Discussion and Conclusions

In the initiation of this doctoral project, the sacrificial particle employed in the research of self-healing TBCs relies on commercially available $MoSi_2$-based particles. However, the action-readiness of this material falls out of meeting the specified requirements, despite the proven effectiveness of the self-healing concept in extending the lifetime of YSZ-based TBCs. Therefore, the objective of this research was to fill this gap by developing $MoSi_2$-based sacrificial particles for self-healing TBCs that meet all designed features. Substantial efforts throughout this research were dedicated to addressing the prevailing issue of premature oxidation in sacrificial particles and fine-tuning the efficiency of the healing reaction. Finally, a microcapsule system, comprising a robust alumina shell and a boron-doped $MoSi_2$ core, was developed and implemented in YSZ ceramics designed for self-healing TBCs.

Finding a protocol to optimize the shape of the sacrificial particles was the first step in this research. A simple and cost-effective method to prepare spherical $MoSi_2$ based particles is proposed in this work. It was demonstrated that $MoSi_2$-based particles with irregular shape can be made more spherical by a combination of ball milling and polishing process while their size is hardly reduced. This spheroidization is essential for a good flowability which is required for many applications such as plasma spraying. In particular for high melting point materials as $MoSi_2$ alternative routes appeared to be difficult and expensive.

Building upon the particle processing parameters, a systematic investigation has been conducted on the in-situ encapsulation of $MoSi_2$-based particle with alumina shell based on the Al selective oxidation in Al-alloyed $MoSi_2$. Taking the size effect into the gas-solid interactions, the study commenced with bulk $Mo(Al_xSi_{1-x})_2$ material with the aim of diving into the mechanism of Al selective oxidation in $Mo(Al_xSi_{1-x})_2$. $Mo(Al_xSi_{1-x})_2$ bulk materials was successfully fabricated by a one-step spark plasma sintering process. The growth kinetic and mechanism of α-Al_2O_3 scale on Al-depleted $Mo(Al_xSi_{1-x})_2$ were investigated in a low oxygen partial pressure (pO_2) ambient of 10^{-14} atm. at 1100 °C to avoid formation of volatile Mo-oxides. It was found that a counter-diffusion process of O and Al along grain boundaries of oxide scale is responsible for the columnar and equiaxed grain growth of α-Al_2O_3 based on a two-layered microstructure. Direct exposure to a high pO_2 ambient (0.2 atm.) leads to a more protective α-Al_2O_3 scale with excellent high temperature oxidation resistance.

After gaining insights into the selective oxidation of Al in bulk $Mo(Al,Si)_2$, the investigation delved into the design of Al-containing $MoSi_2$ particles for self-healing TBCs. For this purpose, $Mo(Al_xSi_{1-x})_2$ particles with various Al content were obtained by crunching of bulk $Mo(Al,Si)_2$ and subsequently processed using the developed particle processing method. Under a designed oxidation ambient with oxygen partial pressures of 5×10^{-10} atm., exclusive growth of α-Al_2O_3 scale around the particles was obtained, which inhibits the

formation of volatile Mo−O oxides. The dense α-Al$_2$O$_3$ scale (~1.3 μm thickness) contributes to around 86% less volatilization loss upon exposing the particle to high pO_2 ambient (0.2 atm.) at 1100 °C for 50 hours than complete oxidation. The particles thus encapsulated features an inner core of MoSi$_2$ with Al completely consumed and an oxide shell of α-Al$_2$O$_3$, which is desired as the encapsulated sacrificial particles in self-healing TBC system. It is noted that the oxidation behaviour of the particle is completely different compared with oxidation of bulk Mo(Al$_{0.40}$Si$_{0.60}$)$_2$ under the same conditions, indicating that the size effect has a significant impact on the oxidation process. The findings and method from this part of the study are a leap forwards in the developing of self-healing TBC material and can be utilized to achieve a robust design of a self-healing system for other high temperature ceramics.

In addition to aluminium doping for in-situ encapsulation, the incorporation of boron also plays a pivotal role in controlling the healing efficiency in MoSi$_2$-based sacrificial particles. Observations of this study revealed that the high temperature oxidation in air of Mo–Si alloys is accelerated by the addition of boron. The parabolic growth rate constant of the silica oxide layer increases proportional with the alloy boron content by 90% per at.%B; with respect to the alloy without boron. The addition of boron effectively mitigates the formation of cristobalite and promotes the formation of amorphous SiO$_2$, which provides enlarged channels for oxygen diffusivity.

Building upon the study on the Mo–Si–B bulk material, a systematic investigation into the high-temperature oxidation of MoSi$_2$ and MoSi$_2$–MoB$_x$ particles, across different size ranges and microstructure, has been conducted. These particles are envisioned as sacrificial particles to promote amorphous SiO$_2$ in the self-healing TBC system. The results of this study show that the oxidation of MoSi$_2$ and MoSi$_2$–MoB$_x$ particles follows a two-step oxidation process, namely an initial fast oxidation followed by a relatively slow steady-state oxidation. The particle size, boron addition and the microstructure each exert distinct effects on the high-temperature oxidation of Mo–Si–B particles at different stages. By describing the oxidation kinetics using a 3-D diffusion-Jander (D3) reaction model, it was observed that the oxidation rate constant pertaining to the steady-state stage of the MoSi$_2$-based particles increases proportional with their boron content (observed at 1100 °C). Microstructure analysis of the oxide scaled formed on these particles reveals that the formation of crystalline SiO$_2$ is mitigated while the desirable amorphous borosilicate is promoted by the addition of boron. This can be attribute to the oxidation of MoB phase into B$_2$O$_3$, which dissolves into SiO$_2$ as a network modifier causing vitrification of the oxide scale. Consequently, the

8

increased diffusion coefficient of oxygen in the borosilicate oxide scale, inversely proportional to its viscosity, enhances the oxidation of $MoSi_2$ with the addition of boron.

Finally, an autonomous self-healing ceramic system, composed of yttria partially stabilized zirconia (YSZ) with embedded $Mo(Al,Si)_2$ with MoB as sacrificial particles, was fabricated. This system incorporates optimized design features of sacrificial particles, including the alloying of aluminium and boron, as well as particle spheroidization. A microcapsule system was established by in-situ encapsulation leaving a core of $MoSi_2$ with MoB as fine distributed second phase enveloped by a robust shell of α-Al_2O_3. Full crack healing of the YSZ composite with embedded and encapsulated sacrificial $MoSi_2$ particles with MoB has been demonstrated. A crack intercepting the healing particles was filled with amorphous SiO_2 (promoted by the boron addition) wetting the crack surfaces and forming a loadbearing $ZrSiO_4$ (zircon) at the interface with the yttria partially stabilized zirconia (YSZ) matrix.

This research endeavours to optimize sacrificial particles for self-healing thermal barrier coatings. Although significant progress has been made, further research is still required before the practical implementation in thermal barrier coatings. From a manufacturing standpoint, the utilization of dual-injection APS has effectively introduced healing particles into the bottom part of the ceramic layer within the thermal barrier coating. However, defects in the coating and the splat shape of the particles have significantly increased the complexity of the system. Moreover, while the in-situ encapsulation method outlined in this study notably enhances the high-temperature stability of the particles, the cumulative thermal stress within the shell may lead to exfoliation, thereby compromising the particles' high-temperature stability under prolonged thermal cycling in operational conditions. Furthermore, the evaluation of life extension in self-healing thermal barrier coatings remains a crucial area for further development.

The results presented in this research establish a robust foundation for future progress in self-healing TBCs. The methodologies applied in this research facilitated a systematic exploration of the smart material, including material design, advanced preparation, and evaluation of its service behavior. This holds significant implications for material safety, product performance and enhanced fatigue lifetime. The insights derived from this research are transferable to other high-temperature materials and self-healing systems, offering the potential for the development of a broader range of smart materials endowed with advanced functionalities.

8

8

9.

Recommendations

The study has undertaken the development of MoSi$_2$-based sacrificial particles for self-healing thermal barrier coatings (TBCs). A microcapsule system composed of a robust alumina shell and boron doped MoSi$_2$ core was established. This system has been demonstrated able to heal cracks effectively in a partially yttria stabilized zirconia system designed for self-healing TBCs. Upon the outcomes of this research, the following recommendations are formulated:

1. The optimized sacrificial particles have been demonstrated crack healing ability in YPSZ ceramics fabricated by spark plasma sintering (SPS) but it was still yet far from the real application in air plasma sprayed (APS) TBCs. While the behavior of the sacrificial particle in a real TBC coating system is beyond the scope of the present work, it is strongly recommended that further research be conducted on the application of particles into real TBC coatings through spraying methods. A systematic lifetime assessment and failure analysis is highly desired, the focus of which can be on the damage evolution in TBCs upon thermal cycling and on the extension of lifetime by self-healing. For this purpose, the manufacturing of the self-healing top coat with MoSi$_2$ particle can be achieved through a dual injection system in APS. In this process, the Al- and B-alloyed MoSi$_2$ particle are recommended to be injected in the self-healing interlayer in close proximity to the bond coat, the location where crack propagation typically takes place in TBC systems. Typically, short (1 to 2 hours cycle) and long (about 24 hours cycle) dwell times promote thermal fatigue and TGO induced damage, respectively. Furthermore, the self-healing mechanism itself could be affected differently by the cycle dwell time as well. Thus, standardized furnace cycle tests are recommended to be executed with both short and long dwell times. When increasing the temperature, the lifetime of the TBC will be shorter. Then, the crack damage increases, but also the crack gap filling kinetics will be enhanced and thus the self-healing promoted. To align the tests more closely with practical application, thermal cycle tests are recommended to be executed with two temperatures for the hot dwell period.

2. Traditionally, investigations into the microstructures at interfaces and the causes of failure in thermal barrier coatings have relied on 2D methodologies, which often fall short in capturing the full scope of their 3D nature. Furthermore, the anisotropic nature of thermal-physical properties within these coatings presents an unexplored opportunity to examine the relationship between 3D crystallographic orientations and failure modes. Thus, correlative characterization methods based on 3D

9

tomography and 3D EBSD are recommended to be employed to gain a more comprehensive understanding of high-temperature reactions at the interface and the modes of coating failure. This approach promises to yield invaluable insights into the field of thermal barrier coatings and open up new avenues for further exploration.

3. Today, the demand for more efficient and environmentally friendly propulsion and energy generation systems drives the application of environmental barrier coatings (EBCs) and ceramic matrix composite (CMCs). Rare-earth silicates of Yb_2SiO_5 and $Yb_2Si_2O_7$ have been recognized as promising candidates for EBCs applications. Due to the low fracture toughness of EBC materials, cracks inevitably form when thermal stress accumulates to a critical value. It has been reported that cracks and holes in rare earth silicate coatings will become channels for high-temperature gas to corrode the coating and the substrate. Therefore, a coating with self-healing capability is highly desirable for maintaining the protective properties and mechanical stability of the EBCs. The success of self-healing TBCs serves as both inspiration and guidance for designing and preparing EBCs with a self-healing function.

9

Curriculum Vitae

Zhaoying Ding

Born on 03 October 1992, Zhejiang

03. 2023 – present	Application Scientist DualBeam
	Thermo Fisher Scientific, Eindhoven, the Netherlands
09. 2018 – present	PhD researcher in Materials Science and Engineering
	Delft University of Technology, Delft, the Netherlands
03. 2017 – 06. 2018	Research Associate
	Harbin Institute of Technology, Harbin, China
09. 2014 – 07. 2016	MSc in Materials Science and Engineering
	Delft University of Technology, Delft, the Netherlands
09. 2010 – 06. 2014	BSc in Materials Science and Engineering
	Southwest Jiaotong University, Chengdu, China

List of Publications

Journal papers

1. **Z. Ding,** J.C. Brouwer, J.N. Zhu, V. Popovich, M.J.M. Hermans, W.G. Sloof, Effects of boron addition on the high temperature oxidation of $MoSi_2$ alloys, *Scripta Materialia* 234 (2023) 115580.

2. **Z. Ding,** J.C. Brouwer, C. Kwakernaak, M.J.M. Hermans, V. Popovich, W.J. Quadakkers, W.G. Sloof, Selective oxidation of aluminium in $Mo(Al,Si)_2$, *Corrosion Science* 211 (2023) 110884.

3. **Z. Ding**, J.C. Brouwer, C. Kwakernaak, J.N. Zhu, V. Popovich, M.J.M. Hermans, W.G. Sloof, $Mo(Al_xSi_{1-x})_2$ healing particles for high temperature ceramics and encapsulation by selective oxidation of aluminium, *Materials & Design* 225 (2023) 111577.

4. **Z. Ding,** J.C. Brouwer**,** X. Yao**,** J.N. Zhu, M.J.M. Hermans, V. Popovich, W.G. Sloof, On the high temperature oxidation of $MoSi_2$ particles with boron addition. *Journal of European Ceramic Society,* Revision.

5. **Z. Ding**, C. Kwakernaak, J.C. Brouwer, J.N. Zhu, V. Popovich, M.J.M. Hermans, W.G. Sloof, On the use of $Mo(Al,Si)_2$ particles with boron addition as sacrificial particles in yttria stabilized zirconia ceramics designed for self-healing thermal barrier coatings. In preparation.

Other journal papers

1. J.N. Zhu, **Z. Ding**, E. Borisov, X. Yao, J.C. Brouwer, A. Popovich, M. Hermans, V. Popovich, Healing cracks in additively manufactured NiTi shape memory alloys, *Virtual and Physical Prototyping* 18(1) (2023) e2246437.

2. Q. Liu, A. Muralidharan, A. Saateh, **Z. Ding**, P. ten Dijke, P.E. Boukany, A Programmable Multifunctional 3D Cancer Cell Invasion Micro Platform, *Small* 18(20) (2022) 2107757.

3. **Z.Y. Ding**, Y.H. Wang, J.H. Ouyang, Z.G. Liu, Y.M. Wang, Y.J. Wang, Influence of Al_2O_3 addition in $NaAlO_2$ electrolyte on microstructure and high-temperature properties of plasma electrolytic oxidation ceramic coatings on Ti_2AlNb alloy, *Surface and Coatings Technology* 370 (2019) 187-195.

4. **Z.Y. Ding**, Y.H. Wang, J.H. Ouyang, Z.G. Liu, Y.M. Wang, Y.J. Wang, Insights into structure and high-temperature oxidation behavior of plasma electrolytic oxidation ceramic coatings formed in $NaAlO_2$–Na_2CrO_4 electrolyte, *Journal of Materials Science* 53(14) (2018) 9978-9987.

Acknowledgment

I would like to thank all my friends in Delft for their companionship and support during my stay here. The greatest appreciation goes to my collaborator Jia-Ning, who is smart and helpful. I really benefit a lot from his expertise. I owe gratitude to my colleagues, present and past, Marcel (Sluiter), Chen, Soroush, Meng (Zhao), Qian, Guoping, Yuliu, Weichen, Yucheng and Fei for the relaxing discussion. I would like to thank Xiaohui, Dingshan, Yifan, Zhaorui, Wei, Keer, Gaojie, Jiaxiang, Quanxin, Kai, Ziyu and Yaqi for the pleasant time we spent together. I would like to extend my thanks to Renan, Yuxuan, Rui, Jiahui, Min, Xiujie, Huan, Jun, Meng (Zhang), Hongpeng and Langzi for the enjoyable holiday time and the happy moments we shared. Additionally, I must also thank Nan and Tianchi for repeatedly inviting me for dinner, which was so sweet for someone who doesn't like to cook.

I would like to thank Yuzhang for encouraging me to pursue a PhD, without whom I would not have this incredible journey, and the support he and his parents offered. I would like to express my gratitude to Prof. Ouyang for introducing me to the realm of high temperature materials. I deeply appreciate your guidance during my initial foray into the world of research. My cats Julie and Felix deserve special recognition for being with me through the tough times in my PhD life. I would like to thank Renan, Yuxuan and Jia-Ning once more for their encouragement, which helped me navigate the most challenging period of my PhD studies.

I thank my family, my parents and brother, for their faith in me.

Zhaoying in Eindhoven

March 2024